SEABED FLUID FLOW-RELATED PROCESSES

EVIDENCE AND QUANTIFICATION

BASED ON HIGH-RESOLUTION IMAGING TECHNIQUES AND GIS ANALYSES

Dissertation

zur Erlangung des

Doktorgrades der Naturwissenschaften

(Dr. rer. nat.)

am Fachbereich Geowissenschaften

der Universität Bremen

vorgelegt von

Yann Marcon

Bremen, Dezember 2012

Gutachter:

Prof. Dr. Gerhard Bohrmann

Prof. Dr. Achim Kopf

Preface

This work was conducted within the Geosciences department at the University of Bremen and the MARUM institute, from January 2010 until December 2012. It was supported by the European Commission under the EU Framework 7 funded Marie Curie Initial Training Network (ITN) SENSEnet (contract nº237868), and funded through DFG Research Center / Excellence Cluster "The Ocean in the Earth System".

The data used in this thesis were acquired during the *RV MARIA S. MERIAN* cruise MSM15/2 (2010) to Black Sea mud volcanoes, the *RV METEOR* cruise M82/3 (2010) to the Menez Gwen hydrothermal volcano on the Mid-Atlantic Ridge, and the *RV POURQUOI PAS?* cruise WACS (2011) to cold seeps in the deep-sea Congo fan.

This thesis comprises seven chapters, including one technical and three scientific manuscripts, and is aimed at improving the current knowledge of deep-sea seabed fluid flow processes using state-of-the-art high-resolution imaging techniques. The first chapter provides an introduction to seabed fluid flow features in general, with a focus on hydrothermal vent and cold seep systems, and presents the motivation and objectives of this study. The second chapter presents the main imaging techniques used in this thesis, as well as the main technical achievement of this project; it corresponds to the first manuscript, which describes a new mosaicking tool (*LAPM Toolbox*) that was developed in (and for) this project. The third chapter gives an overview of the two main study areas of this work. The fourth, fifth, and sixth chapters correspond to the three main scientific manuscripts produced during this thesis; these chapters present the main scientific part of the work. The seventh chapter closes the thesis by summarizing the main results and highlights the importance of high-resolution imaging techniques for future deep-sea studies.

Contents

PREFACE ..... **III**

CONTENTS ..... **IV**

ABBREVIATIONS ..... **V**

ABSTRACT ..... **VI**

KURZFASSUNG ..... **VIII**

CHAPTER 1 INTRODUCTION **1**

1.1 Seabed Fluid Flow 1
1.2 Anaerobic Oxidation of Methane (AOM) 9
1.3 Chemosynthetic fauna 9
1.4 Authigenic carbonates 10
1.5 Methane hydrates 12
1.6 Motivation and objectives 15

CHAPTER 2 METHODS AND DATA **19**

2.1 Image-mosaicking 19
2.2 Hydroacoustic mapping 22
2.3 LAPM: A MATLAB Toolbox for Underwater Large-Area Photo-Mosaicking (**Manuscript 1**) 24

CHAPTER 3 STUDY AREAS **39**

3.1 Menez Gwen hydrothermal vent 39
3.2 Regab pockmark 41

CHAPTER 4 MEGAFAUNAL DISTRIBUTION AND ASSESSMENT OF TOTAL METHANE AND SULFIDE CONSUMPTION BY MUSSEL BEDS AT MENEZ GWEN HYDROTHERMAL VENT, BASED ON GEO-REFERENCED PHOTO-MOSAICS (MANUSCRIPT 2) **45**

CHAPTER 5 DISTRIBUTION AND TEMPORAL EVOLUTION OF MEGA-FAUNA AT THE REGAB POCKMARK (NORTHERN CONGO FAN), BASED ON A COMPARISON OF VIDEO-MOSAICS AND GIS ANALYSES (MANUSCRIPT 3) **75**

CHAPTER 6 FLUID FLOW REGIMES AND GROWTH OF A GIANT POCKMARK (MANUSCRIPT 4) **99**

CHAPTER 7 CONCLUSION AND OUTLOOK **111**

ACKNOWLEDGEMENTS **117**

REFERENCES **119**

APPENDIX A: REVIEW OF COMMONLY USED MOSAICKING TECHNIQUES ..... **A-i**

ERKLÄRUNG ..... **B-i**

Abbreviations

AOM	Anaerobic oxidation of methane
AUV	Autonomous underwater vehicle
DOF	Degree of freedom
DVL	Doppler velocity log
FOV	Field of view
GHSZ	Gas hydrate stability zone
GIS	Geographic information system
LBL	Long-baseline
LMedS	Least median of squares
MAR	Mid-Atlantic Ridge
MBES	Multibeam echosounder
MDAC	Methane derive authigenic carbonates
RANSAC	Random sample consensus
ROV	Remotely operated vehicle
SFM	Structure-from-motion
SIFT	Scale invariant feature transform
SMI	Sulfate-methane interface
SURF	Speeded up robust features
USBL	Ultra-short-baseline

Abstract

The overall aim of this thesis is to provide better insights on different aspects of seabed fluid flow processes based on seafloor observations. The methods used in this work entirely rely on high-resolution imaging and mapping techniques, either optical, acoustic or both. All high-resolution data were acquired during seafloor surveys with remotely operated vehicles. Optical data were used to produce visual maps of the seafloor, in the form of geo-referenced video- and photo-mosaics, whereas acoustic techniques allowed mapping the detailed topography of the seabed, i.e. the micro-bathymetry, as well as the signal reflectivity of the sediment surface and of the water column. Therefore, this work also highlights how valuable high-resolution mapping techniques are, and to what extent they can contribute to increasing our knowledge of deep-sea environments.

Some of the high-resolution techniques used in this thesis are not commonly used by the marine scientific community. This is particularly the case for large-area photo-mosaics. Although the interest in mosaicking is growing, there are still no tools freely and readily available to scientists to routinely construct accurate and large-area photo-mosaics.

Manuscript 1 presents a MATLAB toolbox for large-area photo-mosaicking (*LAPM toolbox*), which was developed as part of this thesis. The toolbox allows constructing photo-mosaics of any size, on any recent computer, and from any set of images. Images can be registered either with feature-matching methods, navigation data, or both. Final mosaics are geo-referenced and can be imported directly into geographic information systems. The LAPM toolbox will ultimately be available for download on the internet.

The first case study (**manuscript 2**) was conducted at the *Menez Gwen* hydrothermal vent volcano, located at about 800 m water depth on the Mid-Atlantic Ridge. The overall aim of this study was to assess how significant methane and sulfide consumption by the fauna is in comparison to natural release of gas from the system. Several sites of venting activity were intensively surveyed and four were fully imaged with geo-referenced photo-mosaics. Based on spatial analyses, total biomasses and abundances of the dominant megafaunal chemosynthetic species were assessed at all imaged sites. These calculations served as bases for quantifying the total annual consumption of methane and sulfide by the dominant species at the scale of the sites. Results were then compared to natural methane and sulfide fluxes from the system, which were estimated from the imagery data. This study concluded that the faunal consumption of dissolved gases at hydrothermal vents is low in comparison to natural release from the system, both focused and diffuse. This is unlike in cold seep environments where chemosynthetic fauna has been shown to act as a benthic filter for dissolved methane release to the hydrosphere.

The second case study (**manuscript 3**) focused on the giant *Regab pockmark*, located at 3160 m water depth in the Lower Congo basin. This study investigated the distribution of the chemosynthetic fauna and its 10-year temporal evolution, based on spatial analyses of large

video-mosaics of the most populated area of the pockmark. Discrete patterns in the faunal distribution were observed that indicated that the intensity of seepage is very heterogeneous across the pockmark, and a model was proposed, in which the dominant megafaunal species are structured around zones of intense fluid advection. Furthermore, results revealed very little changes in the fauna distribution, suggesting that the seepage activity at Regab has been stable over the past ten years.

In the third case study (**manuscript 4**), the Regab pockmark was entirely mapped with ROV-based micro-bathymetry and backscatter data, which gives an unprecedented detailed view of the entire structure. Furthermore, this dataset is completed by a 105,000 m^2-large photo-mosaic of the most active area in terms of seepage activity, and by a sidescan mapping of the gas emissions over the whole pockmark. This is the most detailed and comprehensive imaging dataset ever published for a giant methane pockmark. This data was used to better understand the mechanisms of formation and evolution of giant pockmarks. In particular, results revealed that the pockmark is constituted of more than a thousand sub-pockmarks of very various sizes and shapes. The distribution of these sub-pockmarks allowed identifying two distinct areas, representative of two very different fluid flow regimes. The first area is characterized by discrete and focused seepage activity, associated to the presence of preferential pathways in the subsurface, such as fractures. The second area is related to diffuse flow within porous and non-fractured sediments.

Kurzfassung

Das übergeordnete Ziel dieser Arbeit ist es, basierend auf Meeresbodenbeobachtungen, bessere Einblicke in verschiedene Aspekte der Fluidzirkulation zu gewinnen. Die in dieser Arbeit verwendeten Methoden basieren ausschließlich auf hochauflösenden optischen und/ oder hydroakustischen Kartierungstechniken. Alle hochauflösenden Daten wurden unter Einsatz von ferngesteuerten Unterwasserfahrzeugen (‚remotely operated vehicles', ROV) gewonnen. Optische Daten wurden verwendet, um visuelle Karten des Meeresbodens in Form von georeferenzierten Video- und Fotomosaiken zu produzieren. Hydroakustische Techniken erlaubten die Abbildung der detaillierten Topographie des Meeresbodens, der Mikrobathymetrie. Darüber hinaus gibt die Rückstreuintensität des akustischen Signals Hinweise auf die Sedimentbeschaffenheit und Gasblasen in der Wassersäule. Diese Arbeit zeigt wie wertvoll hochauflösende Kartierungstechniken sind und in wie fern diese zu einer verbesserten Kenntnis der Tiefsee beitragen können.

Einige der hochauflösenden Techniken die in dieser Arbeit verwendet wurden, sind noch nicht in der wissenschaftlichen Meeresforschung etabliert. Dies gilt besonders für großflächige Fotomosaike. Obwohl das Interesse und der Bedarf an Mosaiken wachsen, gibt es noch keine frei oder kommerziell verfügbaren Programme, die es Wissenschaftlern erlauben routinemäßig präzise und großflächige Fotomosaike zu konstruieren.

Manuskript 1 stellt eine MATLAB-Toolbox für die Erzeugung großflächiger Fotomosaike (*LAPM Toolbox*) dar, die im Rahmen dieser Arbeit entwickelt wurde. Die Toolbox funktioniert auf jedem modernen Computer und ermöglicht die Konstruktion von Fotomosaiken jeglicher Größe mit einem beliebigen Satz von Bildern. Die Bildregistrierung erfolgt entweder mittels *feature-matching* Methoden, anhand von Navigationsdaten oder beidem. Die endgültigen Mosaike sind georeferenziert und können direkt in Geoinformationssysteme importiert werden. Die *LAPM Toolbox* soll in Zukunft im Internet frei zugänglich gemacht werden.

Die erste Fallstudie (**Manuskript 2**) wurde am hydrothermalen *Menez Gwen* Vulkan am Mittelatlantischen Rücken in 800 m Wassertiefe durchgeführt. Das übergeordnete Ziel dieser Studie war es zu beurteilen, wie bedeutend der Umsatz von Methan und Schwefelwasserstoff durch Fauna im Vergleich zu natürlichen Freisetzung von Gas aus dem System ist. Mehrere Gebiete aktiver Entgasung wurden detailliert untersucht; vier wurden komplett durch georeferenzierte Fotomosaike abgebildet. Die Gesamtbiomasse und Abundanz der chemosynthetischen Megafauna wurde, basierend auf räumlicher Analyse der Mosaike, bestimmt. Diese Berechnungen dienten als Grundlage für die Quantifizierung des jährlichen Gesamtverbrauchs von Methan und Schwefelwasserstoff durch die dominante chemosynthetische Art im kartierten Gebiet. Diese Umsatzraten wurden dann mit den Methan- und Schwefelwasserstoffflüssen des Systems verglichen, die ebenfalls anhand der Mosaike bestimmt wurden. Diese Studie ergab, dass der Verbrauch gelösten Gases durch Fauna an Hydrothermalquellen niedrig ist im Vergleich zu diffusen und fokussierten

Emissionen. Dies steht im Gegensatz zu Beobachtungen an kalten Quellen, die zeigen, dass chemosynthetischen Organismen einen benthischen Filter für die Emission gelösten Methans in die Wassersäule bilden.

Die zweite Fallstudie (**Manuskript 3**) wurde an der großen *Regab Pockmark* in 3160 m Wassertiefe, im Kongobecken durchgeführt. *Pockmarks* sind Depressionen im Meeresboden die verschiedenen Formen und Tiefen annehmen können. Im Allgemeinen wird die Bildung solcher Strukturen durch Fluidemissionen erklärt. Die Studie untersuchte die Verteilung chemosynthetischer Fauna und deren Entwicklung über zehn Jahre, basierend auf der räumlichen Analyse von Videomosaiken, die das am dichtesten besiedelte Gebiet der Pockmark abdecken. Es wurden diskrete Verteilungsmuster der Fauna beobachtet, die zeigen, dass Gasflussintensitäten im kartierten Gebiet sehr heterogen sind. Aufgrund dieser Beobachtungen wurde ein Modell entwickelt, in dem die vorherrschende megafaunale Art auf Bereiche intensivster Fluidadvektion konzentriert ist. Des Weiteren, zeigte die Studie, dass sich die Verteilung der Fauna innerhalb der letzten zehn Jahre nur minimal geändert hat, was auf stabile Fluidflüsse in diesem Zeitraum hindeutet.

In der dritten Fallstudie (**Manuskript 4**), werden Mikrobathymetrie und Rückstreukarten des gesamten Gebiets der Regab Pockmark gezeigt. Die Daten wurden mit einem ROV aufgezeichnet und zeigen eine sehr detaillierte Ansicht der gesamten Struktur. Die geophysikalischen Daten werden durch ein 105.000 m2 großes Fotomosaik, dass den aktivsten Teil der Pockmark abdeckt, ergänzt. Eine detaillierte Kartierung von Gasemissionen, anhand von Seitensichtsonardaten komplimentiert den Datensatz. Diese Studie stellt die umfassendste und detaillierteste publizierte Kartierung einer solch großen Pockmark dar. Diese Daten wurden verwendet, um ein besseres Verständnis der Entstehungs- und Entwicklungsmechanismen von großen Pockmarks zu entwickeln. Die Ergebnisse zeigen, dass sich die Regab Struktur aus mehr als 1000 kleineren Pockmarks, unterschiedlicher Größe und Form, zusammensetzt. Die Verteilung dieser Subpockmarks erlaubte die Identifizierung von zwei Bereichen, die durch unterschiedliche Fluidflüsse charakterisiert sind. Der erste Bereich ist durch diskrete, fokussierte Fluidemissionen charakterisiert, die durch Fluidmigrationswege, wie z.B. Störungen, kontrolliert werden. Der zweite Bereich ist durch diffuse Fluidflüsse in porösem, ungestörtem Sediment gekennzeichnet.

Chapter 1 Introduction

1.1 Seabed Fluid Flow

Seabed fluid flow generally refers to the upward flow of liquids and gases through the seafloor (Judd & Hovland 2007). It is a widespread phenomenon in the marine environment, which has been observed all around the world (Figure 1.1). Rising fluids can have very different chemical compositions and temperatures, depending on their origin and on the geological context. Commonly, seabed fluid flow features are divided in two categories, based on the temperature of the escaping fluids: hot vents and cold seeps. Hot vents, also known as hydrothermal vents, are associated to ocean spreading centers, whereas cold seeps occur primarily along convergent or passive continental margins (Campbell 2006, Figure 1.1). Therefore, origins of the fluids, flow mechanisms and surficial expressions between vents and seeps are very different.

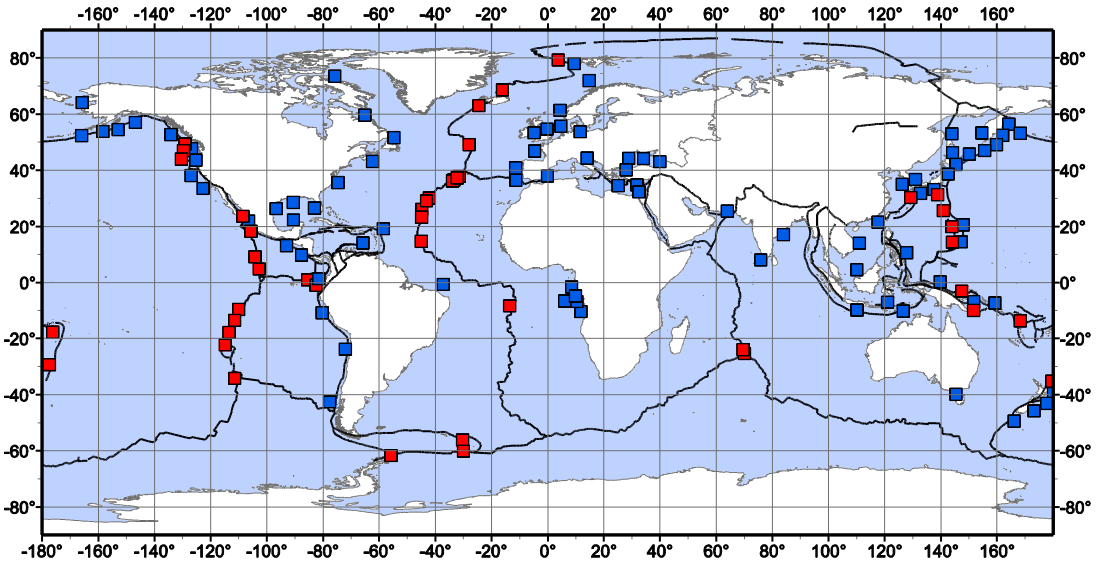

Figure 1.1: Distribution map of known hydrothermal vent (red squares) and cold seep (blue squares) systems. Adapted from Campbell (2006) and Suess (2010), including additional locations from Dover et al. (2001), Ondréas et al. (2005), Yoerger et al. (2007), Sahling et al. (2008a), Westbrook et al. (2009), Rogers et al. (2012).

1.1.1 Hydrothermal vent systems

Hot hydrothermal vents have been discovered in 1977 (Ballard 1977, Corliss et al. 1979) and occur along mid-ocean ridges and back-arc basins in all oceans (Campbell 2006, Figure 1.1). Their occurrence can be considered as a side-effect of plate tectonics, and specifically of seafloor spreading processes. Mid-ocean ridges, also known as ocean spreading centers, are underwater mountain ranges that are generated by the rise and surface crystallization of magma from the Earth's lithosphere. On its way to the surface, the rising magma is stored in

magmatic chambers a few kilometers under the seabed. Related cooling and shrinkage of the magma allows cold seawater to infiltrate along cracks in the seafloor (Figure 1.2). At the contact with the magma, the water becomes heated up to temperatures in excess of 300 °C and rises towards the surface due to an increase in pressure (Edmond et al. 1982, Baross & Hoffman 1985).

The increased solubility of heated water facilitates its enrichment in metallic ions and dissolved gases by interacting with the oceanic crust. Therefore, the composition of end-member fluids depends on the initial temperature of the fluids and on the type of rocks encountered (Damm 1995, Charlou et al. 2000, 2002, Douville et al. 2002). End-member hydrothermal fluids are usually enriched relatively to seawater in volatiles such as hydrogen (H_2), helium (He), carbon dioxide (CO_2), methane (CH_4) and hydrogen sulfide (H_2S). Most these gas originate from direct degassing from the magma chamber or high temperature abiogenic fluid-rock interactions (Welhan 1988, Shanks et al. 1995, Kelley et al. 2002). However, other mechanisms occur that can contribute significantly to gas enrichment of hydrothermal fluids. For instance, isotopic analyses showed that H_2S in hydrothermal fluids is mostly related to the reduction of seawater sulfate to sulfide (Damm 1995, Shanks et al. 1995). Similarly, CH_4, which is in very variable concentrations in hydrothermal fluids of basaltic systems (Welhan 1988, Jean-Baptiste et al. 1991, Charlou & Donval 1993, Lilley et al. 1993, Charlou et al. 2000, Lilley & Olson 2001), is generally very enriched within fluids of mafic and ultramafic-hosted systems, due to serpentinization processes (Kelley 1996, Charlou et al. 1998, 2002, Kelley et al. 2001, Douville et al. 2002).

During ascent to the seafloor, the composition of rising fluids can be altered by condensation and boiling processes (Kelley et al. 2002). Such processes occur mainly in high-temperature systems and trigger a phase separation, in which rising fluids are separated into a gas-rich fluid and a saline, metal-enriched brine (Butterfield et al. 1994, 1997, Charlou et al. 1996, Lilley et al. 2003, Foustoukos & Seyfried Jr. 2007). Furthermore, hot fluids may undergo various amounts of dilution due to mixing with ambient seawater (2 °C) in the subsurface (Edmond et al. 1982).

As they reach the seafloor, hydrothermal fluids are reduced, enriched in metals, and exhibit temperatures up to 400 °C. The sudden mixing with oxygenated cold seawater causes precipitation and deposition of minerals such as anhydrite, barite, pyrite, chalcopyrite, or sphalerite (Kelley et al. 2002), thus forming chimneys and mound structures around the emissions of vent fluid.

The particular physicochemical conditions of hydrothermal environment generally allow sustaining very diverse microbial and faunal communities (Lutz & Kennish 1993, Dover 2000, Desbruyères et al. 2006) that are dependent on reduced compounds such as hydrogen, methane, and hydrogen sulfide (Dubilier et al. 2008, Petersen et al. 2011).

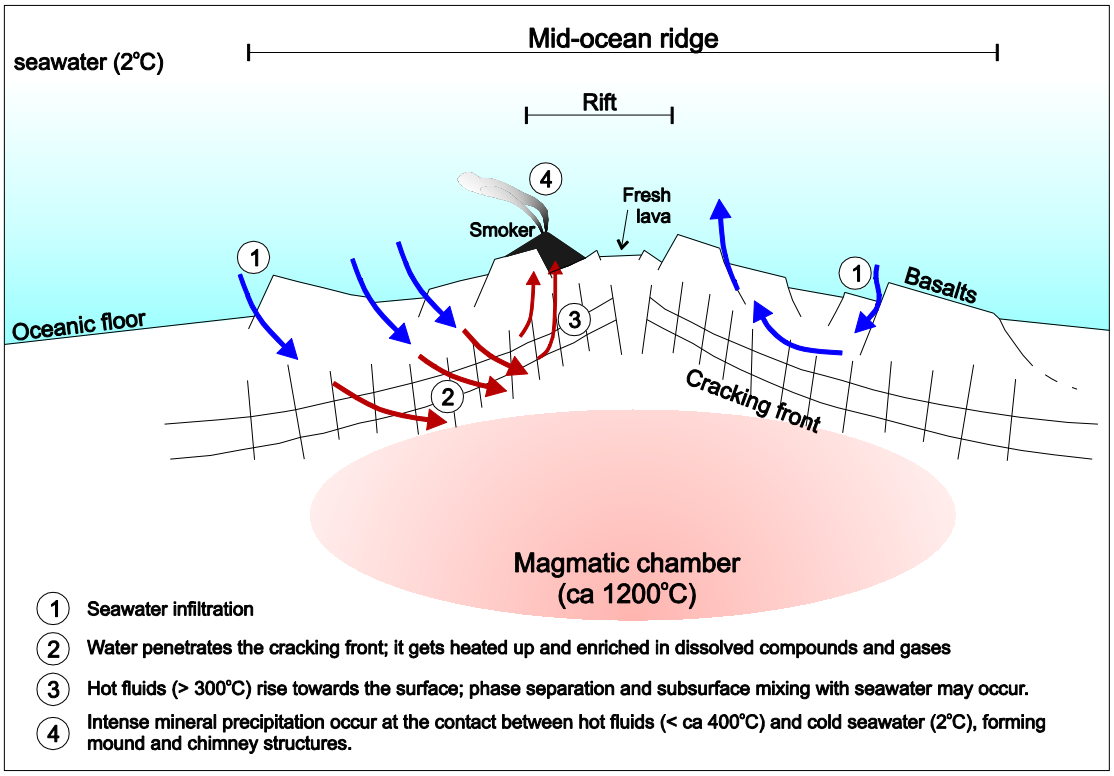

Figure 1.2: Schematic illustrating the general geological context of hydrothermal vent systems.

1.1.2 Hydrocarbon cold seeps

The term 'cold seep' refers to the escape of fluids, involving transport of gas, water or sediments at ambient seawater temperature and slow emission rates in comparison to hot vents (Parnell 2002, Talukder 2012). This definition can apply to several sorts of fluid discharges, e.g. groundwater discharge, brine discharge, or hydrocarbon seepage. However, only hydrocarbon seeps will be considered in this work. Unlike hydrothermal vent systems, which occur along divergent plate margins, cold seep systems occur mainly at convergent and passive continental margins (Campbell 2006, Suess 2010, Figure 1.1). Hence, the processes involved in the fluid expulsion at cold seeps are radically different to those that occur at hydrothermal vent systems. Indeed, fluid advection at cold seeps is mainly driven by compressional tectonics and fluid density gradients, whereas it is generally temperature-driven in hydrothermal systems. Numerous cold seeps have been discovered to date (Figure 1.1), and their distribution suggest that they are widespread along all continental margins, both active and passive (Campbell 2006, Judd & Hovland 2007, Suess 2010).

Geological contexts of marine cold seeps

An active continental margin is a plate boundary where a dense oceanic crust gets subducted beneath a lighter crust, made of continental or island arc material (Von Huene & Scholl 1991). During the subduction process, the upper crust acts as a buttress against the underthrusting

plate. Depending on the effect of such a buttress onto the subducting plate, active margins can be divided in two categories: the accretionary margins and the erosive margins. At accretionary margins, the sedimentary deposits of the oceanic crust are being scrapped off and piled up in slices against the bedrock of the upper crust. Such piling of sliced sedimentary masses results in the formation of accretionary prisms. Von Huene & Scholl (1991) estimated that up to 30 % of the incoming sediment can be scrapped off a decollement surface and accreted to the accretionary prism. In response to the lateral compression of the subduction process, pore water is expelled from accreting sediments and driven to the surface though thrust faults in the accretionary prism (Suess 2010). Conversely, erosive margins are characterized by the absence of a significant accretionary prism. In this case, the sediments are carried down with the oceanic crust. At both accretionary and erosive margins, with depth subducted sediments undergo increasing conditions of pressure and temperature, and subsequent dewatering. Expelled pore water is driven to the surface along the decollement surface (Moore 1989, Mascle & Moore 1990, Le Pichon et al. 1993, Talukder 2012) or through deep-penetrating faults across the upper plate (Ranero et al. 2008, Sahling et al. 2008b, Suess 2010).

Conversely, a passive continental margin is characterized by the absence of subduction. In this context, the expulsion and origin of fluids is not necessarily related to compressional tectonics, and can be very varied (Gay et al. 2007, Suess 2010). Especially in the case of hydrocarbon seep systems, fluids are driven upwards from a reservoir to the surface by buoyancy and diffusion through fractures, or pore spaces (Floodgate & Judd 1992, Clennell et al. 2000, Etiope & Martinelli 2002). (Gay et al. 2007) proposed a schematic model to illustrate and summarize the different seep-related processes that can be observed at the West African passive margin (Figure 1.3).

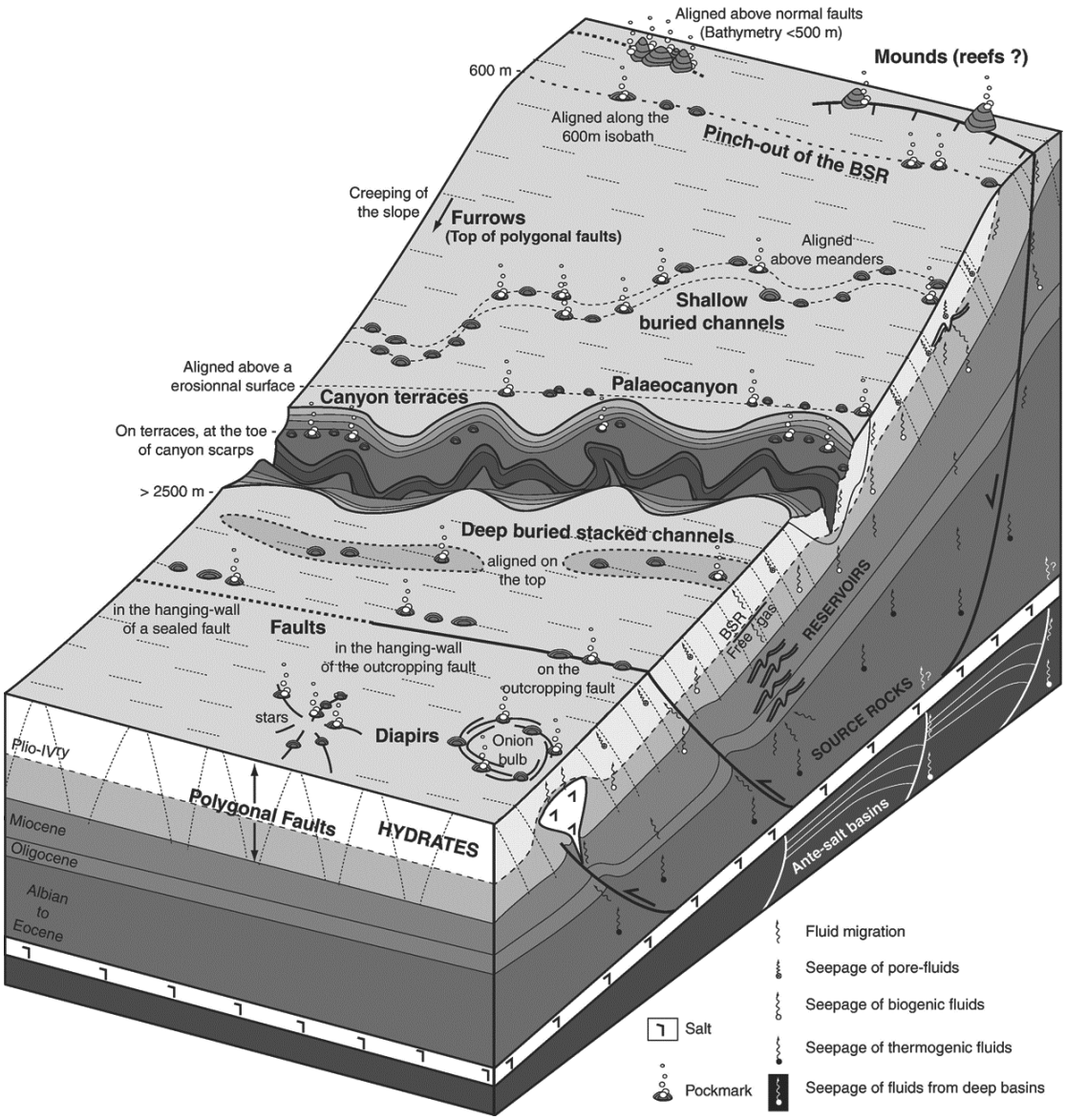

Figure 1.3: 3D block diagram illustrating the geological controls of cold seep-related processes that occur on the East-Atlantic passive margin. From Gay et al. (2007).

1.1.2.1 Origins of methane and other gases in hydrocarbon cold seeps

The presence of gases in shallow sediments is common and can involve the presence of hydrocarbon gases, of carbon dioxide (CO_2) or also of hydrogen sulfide (H_2S). Nevertheless, methane (CH_4) is by far the most abundant of these gases (Claypool & Kvenvolden 1983, Floodgate & Judd 1992). The formation of methane, and of hydrocarbons in general, results from the alteration of organic matter deposits in sediments. Therefore, hydrocarbon reservoirs normally occur in sediments with of high organic carbon content. The origin of methane in such sediments is, thus, considered as *biogenic* (i.e. from organic material), as opposed to

the mostly *abiogenic* origin* (i.e. from inorganic substances) of methane in hydrothermal vent systems (Floodgate & Judd 1992, Judd & Hovland 2007).

The accumulation of large volumes of organic matter in sediments requires (1) high primary productivity, (2) low bottom-water oxygen (O_2) concentrations and (3) high burial rates (i.e. high sedimentation rates). A high productivity allows abundant deposition of organic matter on the seafloor, while low oxygen concentrations and rapid burial prevent the oxidation of organic carbon to CO_2 (Tissot & Welte 1978). With increasing burial depth, organic matter then undergoes several transformation stages, which are function of temperature and pressure conditions: diagenesis, catagenesis and metagenesis.

Sediment diagenesis occurs at relatively low temperatures (<50 °C) and shallow depths (<1 km). During this stage, the organic matter is anaerobically degraded by microbes. Dominant reactions include denitrification, sulfate reduction and methanogenesis, and lead to the formation of gases such as nitrogen (N_2), hydrogen sulfide (H_2S) and methane (CH_4) (Tissot & Welte 1978, Floodgate & Judd 1992). Methane produced during methanogenesis is referred to as *microbial** methane. Methanogenesis occurs under the sulfate reduction zone (Claypool & Kvenvolden 1983) and involves the following reactions:

$$CO_2 + 4H_2 \rightarrow CH_4 + 2H_2O \ (CO_2\ reduction) \quad (1)$$

$$CH_3COOH \rightarrow CO_2 + CH_4 \ (acetate\ fermentation) \quad (2)$$

However, because acetate is preferentially used in sulfate reduction reactions, CO_2 reduction is the dominant methanogenesis reaction in marine sediments (Whiticar 1999, Reeburgh 2007).

At deeper depths (>1 km), catagenesis (60 to 200 °C) and metagenesis (>200 °C) reactions occur. In particular during early catagenesis, the remaining organic material is converted into heavy kerogen complexes. With increasing temperatures, those complexes are progressively broken down into shorter-chain hydrocarbons, producing successively crude oil (C_{15+}), condensate (C_8-C_{15}), wet gas (C_2-C_7) and, ultimately, dry gas, i.e. methane (C_1) (Floodgate & Judd 1992, Figure 1.4). The methane produced during catagenesis is known as *thermogenic** methane. During metagenesis, temperatures (>200 °C) become too elevated to allow for hydrocarbon formation, and kerogens are turned into inert carbon (Durand 1980, Floodgate & Judd 1992).

* The terms ‘biogenic’ and ‘abiogenic’ are here used to refer to the source of carbon (i.e. organic or inorganic), while the terms ‘microbial’ and ‘thermogenic’ will be used to refer to the degradation process (i.e. microbial or thermal). Indeed, the term ‘biogenic’ is often used erroneously to refer to the microbial degradation of organic matter (Judd & Hovland 2007). This work being about both hydrothermal- and cold seep-related processes, this distinction was necessary.

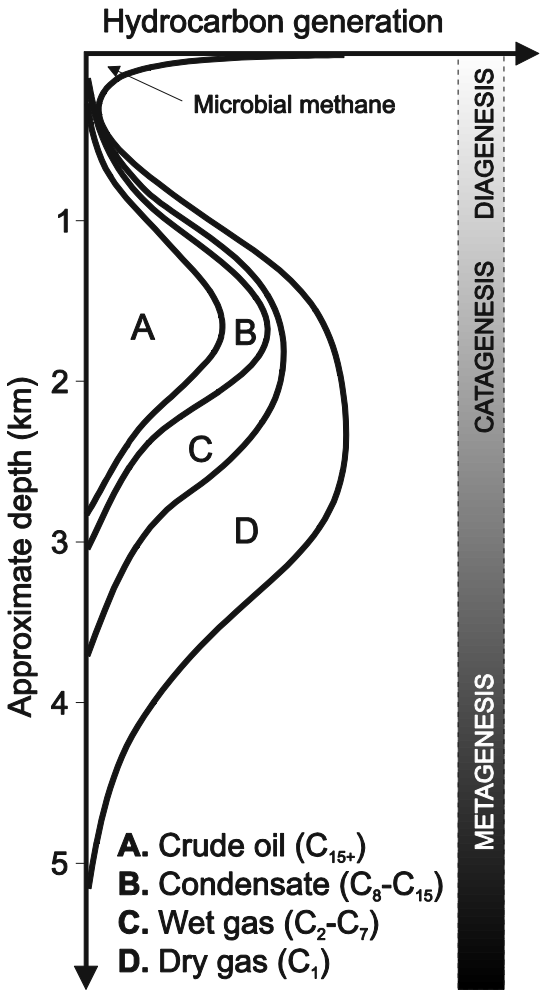

Figure 1.4: Schematic of hydrocarbons generation with depth; the depth scale varies with the geothermal gradient. Adapted from Floodgate & Judd (1992).

The driving forces for upward fluid migration are (1) overpressure caused by tectonic (active margins) and burial (active and passive margins) compaction of source-rocks, (2) density gradient or buoyancy of light hydrocarbons (mostly methane and ethane), and (3) fluid diffusion (concentration gradient) (Floodgate & Judd 1992, Clennell et al. 2000, Etiope & Martinelli 2002). Upon leaking from their source rock, hydrocarbons migrate through permeable or fractured rocks. On the way to the surface, rising hydrocarbons may become trapped under impermeable rocks layers (i.e. shales). Over time, large volumes of hydrocarbons can accumulate in such reservoirs, leading to an increase in pore fluid pressure. From there, lateral migration occurs until an escape pathway is found, which will allow fluids enriched in light hydrocarbons (mostly methane and ethane) to seep through to the surface. Escape pathways can be varied (Figure 1.3): higher permeability strata, presence of faults, diapirism, or also buried channel/levee systems (Floodgate & Judd 1992, Gay & Lopez 2004, Ondréas et al. 2005, Gay et al. 2006b, c, a, 2007).

1.1.2.2 Surficial expression of hydrocarbon cold seeps

Due to the lowest density of methane, methane cold seeps are the most abundant hydrocarbon cold seeps (Judd & Hovland 2007). The surficial expression of seafloor fluid

seepage can be very varied, and depends on several factors such as fluid flow type (gas, pore water or both) and rate (slow or vigorous), sediment type and grain size, pore pressure conditions, driving forces (buoyancy, compressional tectonics), faulting system, or also duration of seeping activity (Loncke et al. 2004, Judd & Hovland 2007). The main common expressions of hydrocarbon seeps include pockmarks (King & MacLean 1970, Hovland et al. 2002, Gay et al. 2003, Ussler III et al. 2003, Ondréas et al. 2005, Pilcher & Argent 2007), mud volcanoes (Vogt et al. 1999, Milkov 2000, Somoza et al. 2003, Bohrmann et al. 2003, Sahling et al. 2009), gas hydrate pingoes (Hovland & Svensen 2006, Paull et al. 2008, Serié et al. 2012), carbonate pavements (Suess et al. 1999, Paull et al. 2008), and carbonate chimneys (Peckmann et al. 2001, Loncke et al. 2004, Bayon et al. 2009).

For instance, mud volcanoes involve the strong, sometimes violent, advection of fluids (water and gas) and fluidized sediments, whereas pockmarks are generally considered to be related to lower fluid advection rates and gas-dominated fluids (Judd & Hovland 2007). To illustrate these features, Figure 1.5 shows the detailed morphologies of a mud volcano and of a large pockmark.

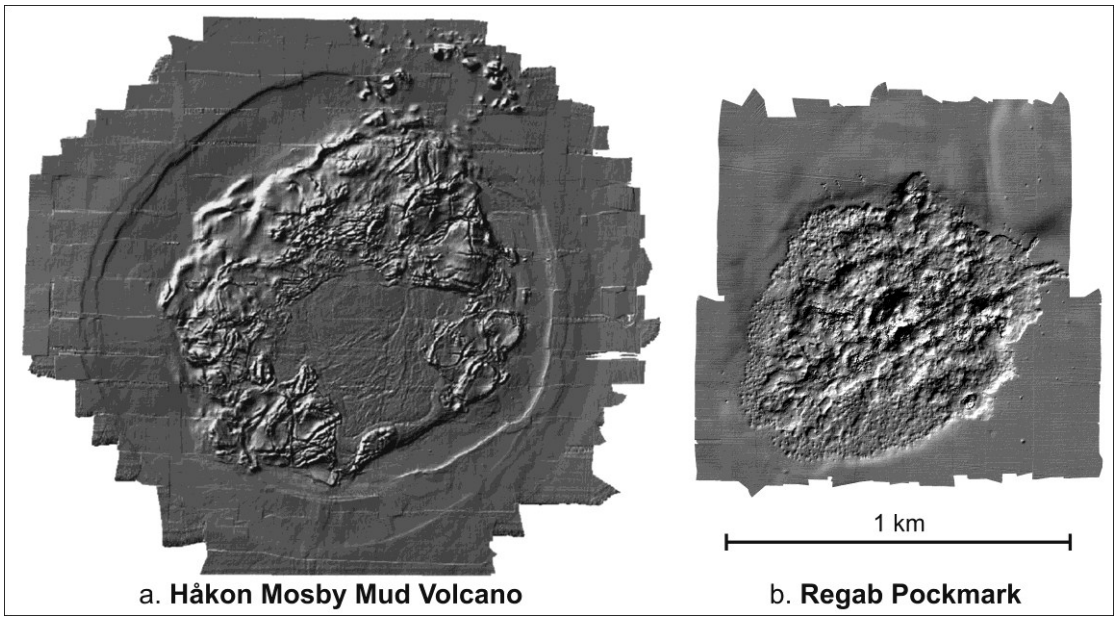

Figure 1.5: Detailed morphology of (a) the Håkon Mosby Mud Volcano (HMMV) (Jerosch et al. 2007b) and (b) the Regab pockmark (© Ifremer, WACS 2011). Both datasets were acquired with the ROV Victor 6000 (Ifremer). The HMMV is mostly a positive feature, characterized by a large hummocky mound located within a flat and shallow circular depression; a depression filled with fresh mud (main crater) occurs in the center of the volcano. The Regab pockmarck is mostly a negative feature; it is composed of a main circular depression slightly elongated in a N70 direction; the bottom of the pockmark is very rugged and shows the presence of a myriad of sub-depressions of various sizes and depths. The scale bar applies to both datasets. Maximum elevation differences between high and low points are of 16 m at HMMV and 13 m at Regab.

The several types of surficial expressions, therefore, reflect the variety of fluid expulsion regimes. Especially, methane can escape as free gas, as dissolved gas into advecting pore

water, or by diffusion due to a gas concentration gradient between the pore fluids and ambient seawater (Luff & Wallmann 2003, Luff et al. 2004, Sommer et al. 2006, Naudts et al. 2010).

1.2 Anaerobic Oxidation of Methane (AOM)

The anaerobic oxidation of methane (AOM) is considered to be an important sink in oceanic methane geochemistry (Reeburgh 2007). Its existence and mechanism were observed and postulated since many years (Reeburgh 1976, Barnes & Goldberg 1976, Martens & Berner 1977), but the agents of the AOM were unknown until recently (Hoehler et al. 1994, Boetius et al. 2000). In particular, the AOM appeared to be mediated by a microbial consortium within the shallow sediments (Boetius et al. 2000) and to be a major process at hydrocarbon seep systems, where it efficiently removes methane before it reaches the sediment-water interface (Hinrichs & Boetius 2002). The consortium comprises sulfate-reducing bacteria and methane-oxidizing archaea and achieves the following net reaction:

$$CH_4 + SO_4^{2-} \rightarrow HCO_3^- + HS^- + H_2O \quad (3)$$

The anaerobic oxidation of methane occurs mainly within the sediments, at the sulfate-methane interface (SMI) (Devol & Ahmed 1981, Iversen & Jørgensen 1985, Borowski et al. 1999), and has been shown to play a major part in the reduction of seawater sulfates (Treude et al. 2005). It is notably responsible for the production of hydrogen sulfide, iron sulfide (pyrite) and bicarbonate ions, which, by reacting mainly with seawater calcium and magnesium, cause the precipitation of carbonates (Kulm et al. 1986, Ritger et al. 1987, Burton 1993, Bohrmann et al. 1998, Aloisi et al. 2002). The main factors controlling the AOM rate are the availabilities of methane and sulfide (Knittel & Boetius 2009).

Thereby, AOM is a very important process at seep systems, where it allows sustaining rich endemic sulfide-dependent microbial and faunal populations. To a lesser extent, AOM also occurs at hydrothermal vents, but in very small niches because the lack of sediments seems to hinder the development of the microbial consortium (Knittel & Boetius 2009).

1.3 Chemosynthetic fauna

Chemosynthetic fauna refers to organisms that rely on reduced compounds such as hydrogen, hydrogen sulfide, and methane as primary energy source. The term ‘chemosynthesis’ is here opposed to ‘photosynthesis’, for which the sunlight is the primary energy source. Chemosynthetic organisms possess endosymbionts, mostly in their gills, that oxidize the reduced compounds into organic carbon (Dubilier et al. 2008, Petersen et al. 2011).

The first chemosynthetic organisms were discovered together with hydrothermal vents at the Galapagos Rift in 1977. Since then chemosynthetic fauna have been shown to be widespread and to occur in many different habitats (Figure 1.6). They were in particular observed at

hydrothermal vents (Lutz & Kennish 1993, Dover 2000, Desbruyères et al. 2006), deep-sea cold seeps (Fisher et al. 1997, Sibuet & Olu 1998, Hinrichs & Boetius 2002, Cordes et al. 2009) and whale falls (Smith & Baco 2003). Numerous species have been discovered and chemosynthetic fauna have proved to be very rich and diverse. In many cases, hydrothermal and cold seep faunal assemblages are dominated by various combinations of sulfur-oxidizing bacteria, bivalves (mussels and clams), vestimentiferan tubeworms, shrimps or crabs. Nevertheless, chemosynthetic fauna are very endemic species, and their distribution is directly linked to the availability of reduced compounds and to the tolerance thresholds of each organism (Olu et al. 1996a, b, 1997, Sibuet & Olu 1998, Bergquist et al. 2003a, Olu-Le Roy et al. 2007a, Cuvelier et al. 2009, Podowski et al. 2009).

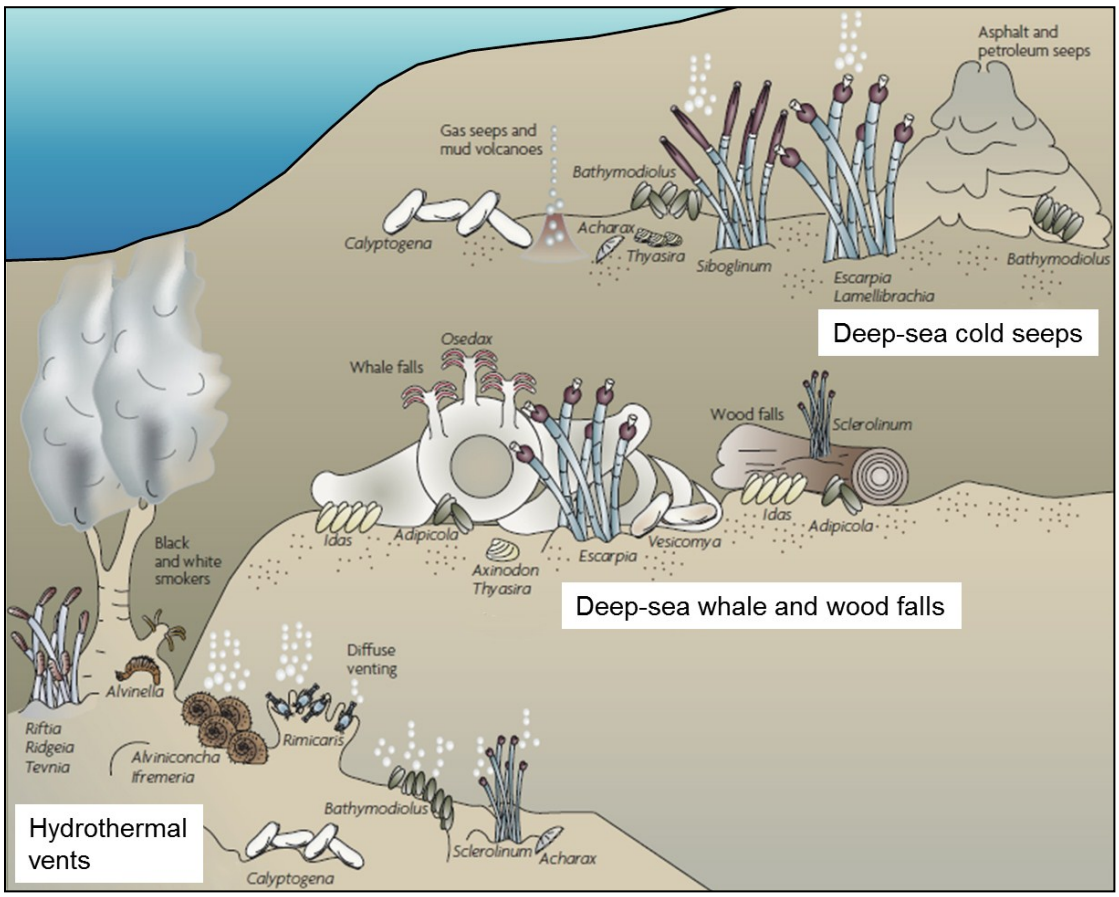

Figure 1.6: Overview of the different chemosynthetic marine habitats of the deep-sea, and of the chemosynthetic organisms that are typically observed. Adapted from Dubilier et al. (2008).

1.4 Authigenic carbonates

By producing bicarbonate ions, the anaerobic oxidation of methane causes pore water alkalinity to increase. This process results in the precipitation of carbonates (Kulm et al. 1986, Ritger et al. 1987, Aloisi et al. 2002). The main reaction for precipitation of methane-derived carbonates is:

$$2HCO_3^- + Ca^{2+} \rightarrow CaCO_3 + CO_2 + H_2O \quad (4)$$

However, the mineralogy of such carbonates can be varied, including magnesium-rich calcite ($MgCO_3$), aragonite ($CaCO_3$) or dolomite ($CaMg(CO_3)_2$) (Ritger et al. 1987, Burton 1993, Bohrmann et al. 1998). The precise controls on the carbonate mineralogy are still not fully understood, but could be related to the pore water sulfate concentrations (Burton 1993, Aloisi et al. 2002, Luff & Wallmann 2003).

Such carbonates are called methane-derived authigenic carbonates (MDAC) and are widespread on continental margins, and in particular at hydrocarbon seeps (Baker & Burns 1985, Bohrmann et al. 1998, Judd & Hovland 2007, Naehr et al. 2007). They form mostly in anoxic layers of sediments or at the sediment surface in anoxic seawaters like the Black Sea (Peckmann et al. 2001). However, there are some suggestions that AOM-derived carbonate mounds could be able to grow in oxic seawaters too (Teichert et al. 2005).

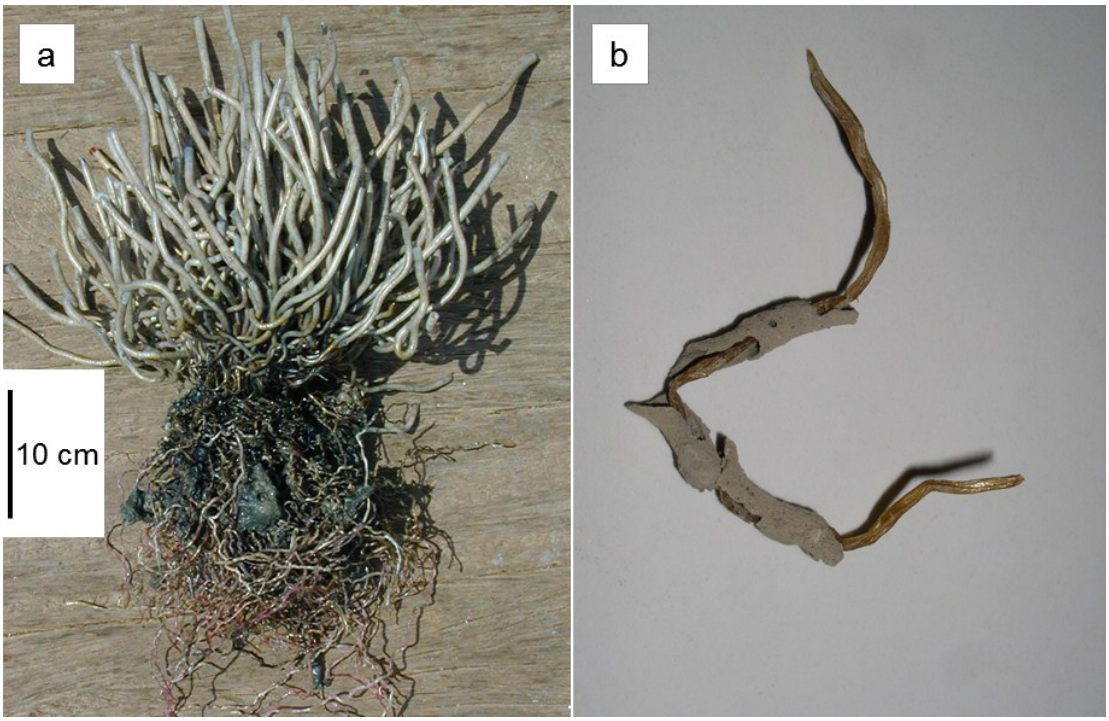

Figure 1.7: Photos illustrating the close link between tubeworms and methane-derived authigenic carbonates, at cold seeps of the West-African passive margin. (a) Bush of juvenile tubeworms; the roots of the tubeworms are closely intertwined with authigenic carbonates. From Sahling et al. (2008a). (b) A single tubeworm root within a carbonated sheathing (Cruise M56, 2002).

Methane-derived authigenic carbonates can form extensive and thick crusts, slabs, concretions, or chimneys depending on the places and conditions in which they form and on the duration of the seeping activity (Judd & Hovland 2007, Haas et al. 2010). Little is known about the timescales of carbonate formation. Current available age estimations are in order of thousand to hundreds of thousands of years for thick carbonate crusts (Luff & Wallmann 2003, Teichert et al. 2003). Nonetheless, a few recent studies imply that some faunal communities, to a certain extent, enhance the rate of the anaerobic oxidation of methane,

which could possibly boost the precipitation of MDAC (Figure 1.7). For instance, by releasing seawater sulfate through their roots, tubeworms can contribute to maintain a high AOM activity even under thick carbonate pavements (Cordes et al. 2005a, Dattagupta et al. 2008, Haas et al. 2009). A similar mechanism has been postulated for vesicomyid clams (Wallmann et al. 1997, Fischer et al. 2011). However, it is unclear to what extent such faunal influence could reduce timescales of carbonate formation.

1.5 Methane hydrates

Gas hydrates, also called clathrates, are ice-like compounds that entrap light gas molecules under specific conditions of temperature and pressure. Gas hydrates form solid cages of water molecules, each of which contains a guest molecule. They can crystalize with three different structures (types I, II and H), each made of a combination of hydrate cages of various sizes and shapes (Figure 1.8). Depending on the type of cages, hydrates can imprison molecules of various sizes. However, when all cages are filled with a guest molecule, all crystal structures have similar concentrations of water (about 85%) and gas (about 15%) (Sloan 1998, 2003, Bohrmann & Torres 2006).

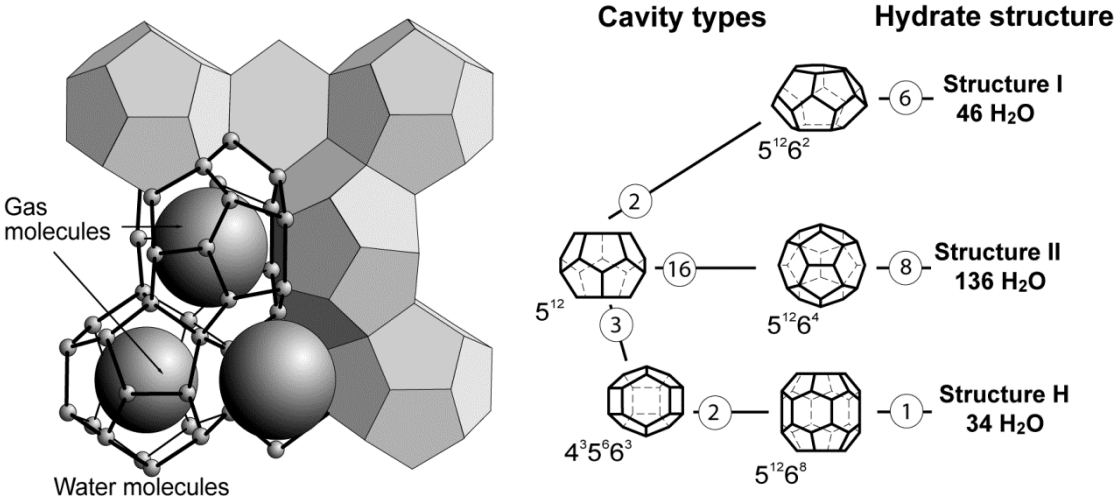

Figure 1.8: Illustration of the cages (cavities) and crystal structures of gas hydrates. Left: example of the hydrate structure type I. Right: illustration of the cages that form each hydrate structure. From Bohrmann & Torres (2006).

The hydrate structure type I, which can contain only relatively small molecules, is by far the most common in marine sediments. Indeed, it can form with most gases present in the sediments (CH_4, CO_2, and H_2S).

However, the formation and stability of gas hydrates is bound to specific physicochemical conditions. It requires in particular high hydrostatic pressure, low water temperature and concentrations in low molecular weight gases above saturation; in addition, salinity is influencing the stability conditions (Figure 1.9). These conditions are often met in the marine

sediments (Figure 1.10), in a shallow zone called the gas hydrate stability zone (GHSZ). Nevertheless, the thickness of this zone is variable, and depends on the water depth and on the geothermal gradient (Figure 1.9). Within the GHSZ, hydrates will form and be stable only if the water is oversaturated in a certain dissolved gas.

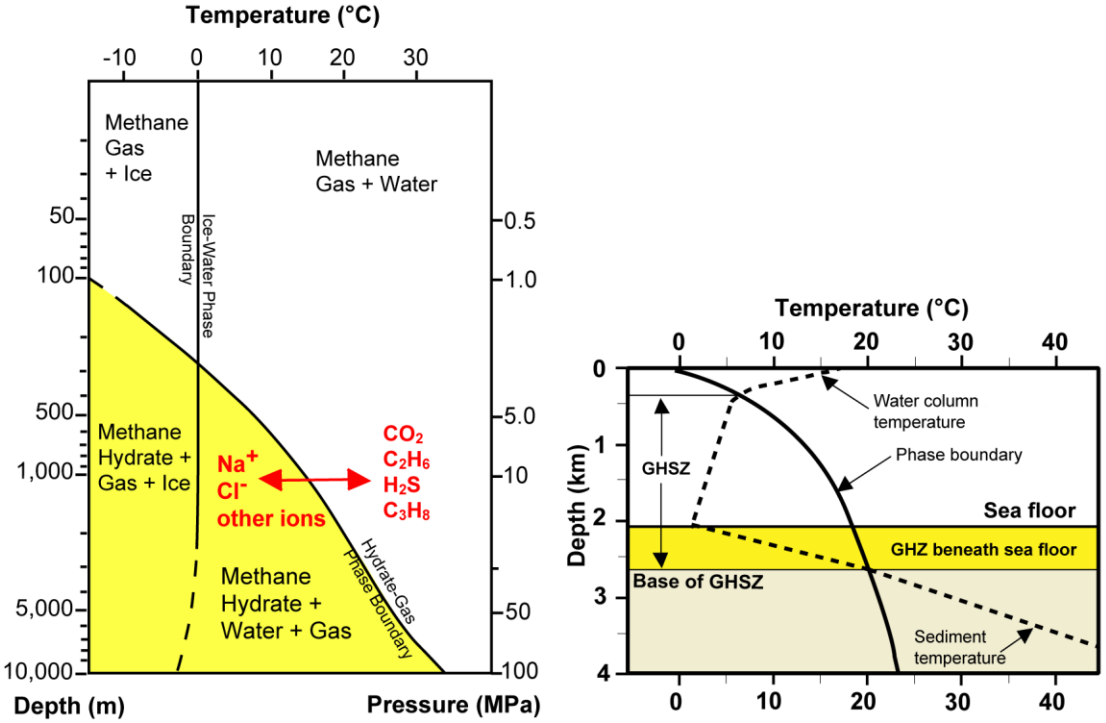

Figure 1.9: Left: Phase diagram showing the limit between free gas and hydrate, for a pure methane/H_2O system; the red arrows show the direction towards which the boundary is shifted in the addition of ions or other gases. Right: Definition of the gas hydrate stability zone (GHSZ) as a function of depth and temperature (at a normal seawater salinity). After Bohrmann & Torres (2006).

Gas hydrates are considered to play a major role in the formation and evolution of some methane seep systems. For instance, mechanisms involving hydrate dissolution or buoyancy-driven hydrate rafting have been proposed to explain pockmark and mound formation on the seafloor (Suess et al. 2001, Sultan et al. 2010, Pape et al. 2011). Furthermore, slow dissociation of hydrate deposits in shallow sediments can allow a stable release of methane into the overlying sediments, thus ensuring a stable supply to methane-dependent microbes and organisms (Sahling et al. 2002, 2008a). In such a case, hydrate deposits act as a 'capacitor' to buffer transient fluid seepages (Dickens 2003, Sahling et al. 2008a).

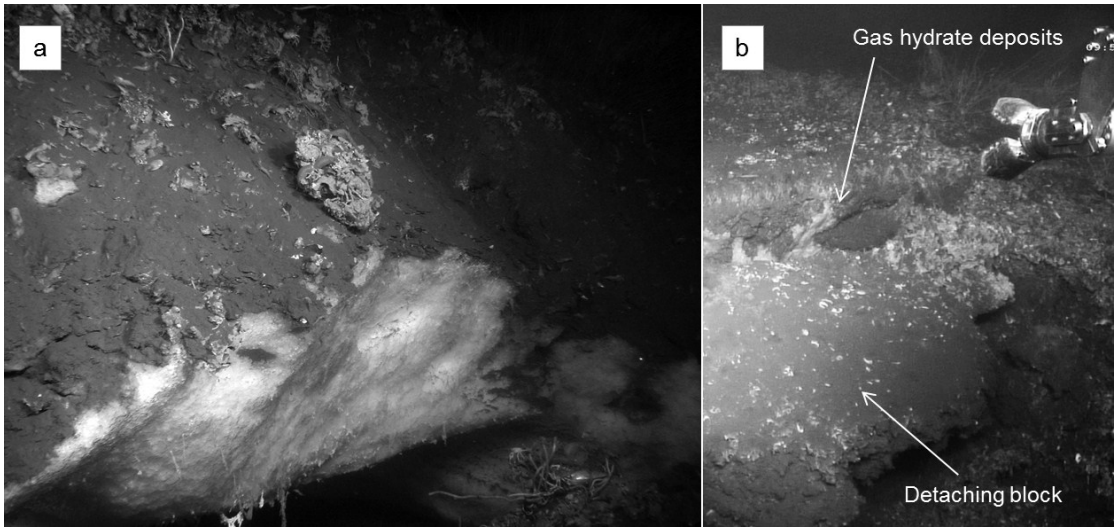

Figure 1.10: Outcrops of gas hydrate deposits within sediments at the giant Regab pockmark (© Ifremer). (a) Massive gas hydrates occur at the surface under a crust of carbonates and indurated sediments. From Olu-Le Roy et al. (2007a). (b) Gas hydrate deposits under carbonate crusts (Cruise WACS, 2011); the gas hydrate outcrop occurs within a fracture between the carbonated seafloor and a collapsing block; the hydrate formation could be responsible for the break-up of the overlying crust.

Indeed, gas hydrates in marine sediments (Figure 1.10) can contain significant volumes of gases. For instance, when dissociating at surface conditions of temperature and pressure, 1 m^3 of methane hydrate can release up to 164 m^3 of methane (Kvenvolden 1993). For this reason, marine structure I gas hydrates are simultaneously regarded as new potential resources of natural gases (Collett 2002, Makogon et al. 2007), potential geohazards (Maslin et al. 2004, 2010, Sultan et al. 2004), and major actors in global climate changes (MacDonald 1990, Buffett & Archer 2004, Archer & Buffett 2005, Reagan & Moridis 2007).

1.6 Motivation and objectives

The overall aim of this work is to determine to what extent the use of state-of-the-art high-resolution imaging and mapping techniques can help better understanding seabed fluid flow-related processes.

The deep marine environment is hardly accessible and most part has remained largely unknown. One reason is that available underwater vehicles for deep ocean exploration have limited range and that surveys and investigations are still much localized, and must focus on small areas of the seafloor only. One of the main focuses of deep sea studies are areas where seabed fluid flow occur, both in hot vent and cold seep systems. However, the challenging conditions prevailing in the deep sea constrain the exploration to rely on the use of a range of sensors and sampling devices, both ship-borne and transported by underwater platforms. These tools are very diverse, from sediment corers to *in-situ* sensors, but are mainly restricted to local measurements. Therefore, most studies of seep-related processes are based either on discrete observations and measurements at the sediment surface or within the first few meters, or on ship-borne seismic and acoustic mapping surveys of the seabed morphology and sub-seafloor structure. Also, deep-tow surveys using sidescan sonar systems, TV-sled observations and video-guided sampling represent important steps on the way to map and sample discrete seepage structures (Bohrmann et al. 2003, Klaucke et al. 2006, Sahling et al. 2008a, b).

However, very few works have carried out systematic ROV- or AUV-borne mapping and provided high-resolution maps of entire features of seabed fluid flow. To date, very few micro-bathymetry maps of entire vent and seep systems have been published (Hovland et al. 2005, Jerosch et al. 2007b, Dupré et al. 2008, Feseker et al. 2010, Bell et al. 2012, Römer et al. 2012). Furthermore, high-resolution visual maps of such features are even scarcer (Escartín et al. 2008, Barreyre et al. 2012). Hence it is often difficult to visualize large areas of the seabed, and spatial dimensions and morphologies remain difficult to comprehend. A better insight on these environments would be a key step towards getting a better understanding of the deep ocean communities and geology.

This fact highlighted the current need for high-resolution imaging techniques and motivated the decision to use optical- and acoustic-mapping techniques in this work. Optical mapping was carried out using ROV-borne cameras and the final maps were produced in the form of ‘areal’ photo- and video-mosaics of the seafloor. Acoustic surveys relied on multibeam echosounders and sidescan sonars both to produce micro-bathymetry maps and to map backscatter anomalies on the seafloor and in the water column. Therefore, this work had a very strong technical side, and required the development of dedicated tools and workflows, in particular for the construction of geo-referenced mosaics (cf. Chapter 2.3). These high-resolution imaging techniques were then used to better understand seabed fluid flow-related processes.

Notably, spatial imaging techniques provide the missing link that relates large-scale geological processes to local-scale observations such as surficial features and endemic fauna distribution and biomass. For instance, most studies on vent and seep fauna focus on getting a better knowledge of the habitats and physiology of the organisms or on their relations to the environment (Dubilier et al. 2008, Cordes et al. 2009, Podowski et al. 2009). Although several local measurements of biomasses or estimations of population densities have been published (e.g. Colaço et al. 1998), there is virtually not any information available about total biomasses or population estimations at the scale of a vent or seep site, and only few works provide faunal coverage estimations at cold seep ecosystems (Olu et al. 1996a, b, Sibuet & Olu-Le Roy 2002, Jerosch et al. 2006, Olu-Le Roy et al. 2007a). It is now commonly accepted that the presence of chemosynthetic communities is an indication for seabed fluid flow (e.g. Olu et al. 1997). However, it seems that chemosynthetic fauna has never been used as a proxy to assess chemical fluxes, even within orders of magnitude. Assessing the faunal consumption of dissolved gases (e.g. methane or sulfide) at the scale of an entire site of fluid flow could indeed provide minimum estimations of mass flows.

Sommer et al. (2006) introduced the term ‘benthic filter’ to describe the impact of microbial and faunal populations on the diffuse fluxes of dissolved methane at the Hydrate Ridge cold seep system, on the Cascadia margin. There, both sulfide-oxidizing bacteria and clams appeared to consume significant portions (respectively 66% and 83%) of the natural release of dissolved methane, suggesting that seep fauna plays a significant role in controlling methane effluxes to the hydrosphere and, possibly, to the atmosphere. In a context where seabed methane emissions are considered to contribute noticeably to the global carbon budget (Judd, 2003), it is important to evaluate the relative significance of faunal methane consumption against natural methane effluxes. Similar estimations would, therefore, be necessary for hydrothermal vent systems. Indeed, compared to cold seeps, fluid release at hydrothermal vent systems is generally more vigorous and focused; hence methane fluxes are more likely to bypass the benthic filter. However it is currently unclear, whether the chemical consumption by vent fauna is significant compared to the focused chemical fluxes at hydrothermal vents. This leads to the first questions of this work:

(1) At the scale of a hydrothermal vent site, how significant is the chemical consumption by vent fauna in comparison to the natural release in dissolved gas? Do benthic vent fauna exert a noticeable control on the methane and sulfide effluxes to the hydrosphere?

Several studies used mosaics to describe the faunal composition and to map its distribution in relation to the environment (Grehan & Juniper 1996, Jerosch et al. 2006, 2007b, Olu-Le Roy et al. 2007a, Podowski et al. 2009, Lessard-Pilon et al. 2010a). These studies generally suggested that the fauna distribution is controlled by the ambient physicochemical conditions, which expectedly depend on the fluid flow regime. However, those mosaics provided either full coverage (= ‘areal’ mosaic) over small areas (up to 110 m^2) (Grehan & Juniper 1996,

Podowski et al. 2009, Lessard-Pilon et al. 2010a), or partial coverage over larger areas (Jerosch et al. 2006, 2007b, Olu-Le Roy et al. 2007a); therefore, they could not always allow reliable identification of large-scale distribution patterns. In this work, for the first time, the faunal distribution of the Regab pockmark was mapped over a 14,000 m^2-large area, based on a fully covering 'areal' video-mosaic (i.e. without gaps between mosaic lines), in order to answer the following questions:

(2) Is there any distinct pattern in the distribution of seep fauna? If so, what does it reveal about the seepage activity and plumbing system of the pockmark?

Video- and photo-mosaics can also be seen as large-scale snapshots, in that they provide views of entire scenes at a specific point in time. Digging this idea further, the comparison of snapshots of a same site but from different times could allow identifying temporal changes. The range of possibilities offered by such method is still largely unexplored, since it was used for the first times only very recently, either to identify small-scale changes in the micro-distribution of benthic fauna (Lessard-Pilon et al. 2010b, Cuvelier et al. 2011), or to describe the temporal evolution of the venting activity in parts of the Lucky Strike hydrothermal vent (Barreyre et al. 2012). It is generally accepted that cold seeps provide more stable environments than hydrothermal vents. Indeed, seep fauna are known to be extremely long-lived (Nix et al. 1995, Fisher et al. 1997, Smith et al. 2000, Bergquist et al. 2000). Therefore studies about temporal evolution of seep fauna micro-distribution are very scarce and usually focused on very small areas (up to 110 m^2) (Lessard-Pilon et al. 2010b). Currently there is not any information available about larger-scale distribution changes at cold seeps. Such information is of importance since distribution changes can reflect changes in the seeping activity. In this work, two large-scale video-mosaics (4600 m^2), representing the same scene with a 10-year interval, were used to describe the temporal evolution of cold seep fauna and to answer the following questions:

(3) How dynamic are cold seep communities? What can be inferred about the temporal evolution of the seepage activity?

Processes involved in the formation and evolution of giant pockmarks are still subject to discussion, and several mechanisms have been proposed that are partly based on interpretations from surficial observations (Hovland et al. 1984, 2005, Harrington 1985, Sultan et al. 2010). However, apart from a few published high-resolution ROV-bathymetry maps (Hovland et al. 2005), most available bathymetry datasets of entire pockmark features are ship-based and, thus, too coarse for detailed interpretations of pockmark structures. More generally, published micro-bathymetry (i.e. ROV-borne) maps of entire vent and seep systems are scarce. One of the largest and most studied of them is certainly the map of Håkon Mosby Mud Volcano (Jerosch et al. 2007b) (Figure 1.5), which provided valuable information to

improve the understanding of mud volcanoes. Interestingly, up to now, a comparably large dataset did not exist for giant pockmarks.

To fill this gap, a comprehensive dataset was acquired at the giant Regab pockmark. This dataset combines for the first time high-resolution micro-bathymetry and backscatter maps, extensive and high-definition photo-mosaics, and comprehensive mapping of gas bubbles in the water column over the entire pockmark. Such dataset, together with GIS mapping of fauna distribution and carbonate occurrence, and observations of outcropping gas hydrates, were used to understand the fluid flow pattern across the pockmark, and to answer the following question:

(4) What are the main mechanisms driving the growth of the Regab pockmark?

And finally, the last question is based on all case studies:

(5) To what extent do high-resolution acoustic and optical datasets allow understanding vent- and seep-related processes?

Chapter 2 Methods and data

2.1 Image-mosaicking

As evidenced in Chapter 1.6, the deep marine environment is hardly accessible and most part has remained largely unknown. One reason is that light in the deep-sea undergoes strong attenuation and high backscattering, which constrains seafloor observations to be carried out from few meters only from the scene of interest. Such short distances severely limit the field of view of the cameras (Figure 2.1). Hence, representing extended scenes of the seafloor requires several images to be taken and assembled together.

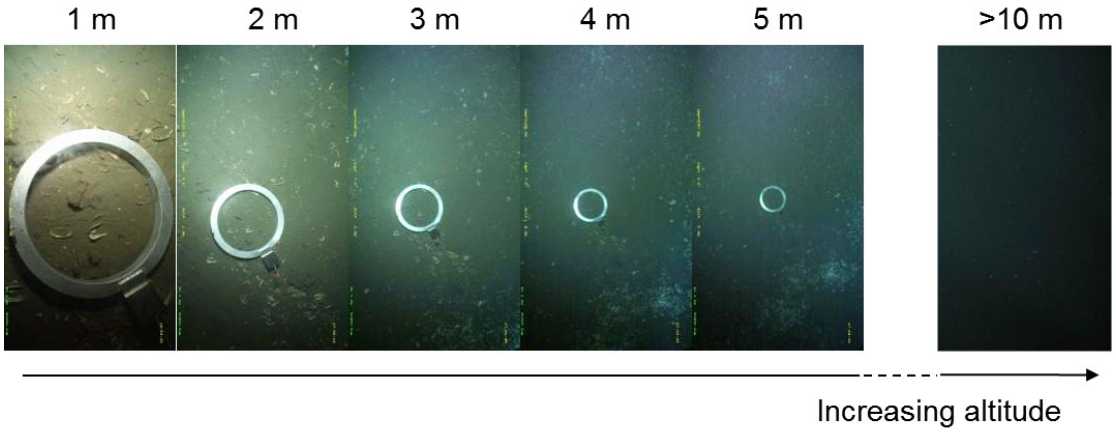

Figure 2.1: Effects of the altitude of survey on the visibility and on the field of view (the ring has an inner diameter of 49 cm); the level of details and the lighting quality decrease sharply with the altitude; at 10 meters the ring is not visible at all. These images were taken at about 3600 m water depth.

Such method is called *mosaicking*. Video- or photo-mosaicking consists in aligning and stitching frames or photographs together to form a large composite picture. This is a widely used technique in photography, in particular for the production of panoramas, for which many dedicated open-source and commercial programs are available. Several programs were tested during this work, which all failed to cope with underwater imagery correctly. The main reason for failure is not so much the heterogeneity of lighting as the lack of contrasts and the perspective distortions caused by features with relief. Unlike traditional scenery photography, deep-sea optical surveys must be conducted a few meters away from the scene, commonly less than five meters. In this context, a feature protruding slightly from the scene would cause a strong perspective change between consecutive images.

Efforts have been made in several institutes to develop tools to generate photo- and video-mosaics of the seafloor (Gracias & Santos-Victor 2001, Eustice et al. 2002, Vincent et al. 2003, Pizarro & Singh 2003, Allais et al. 2004, Ferrer et al. 2007, Escartín et al. 2008). Those tools cope better, although variously well, with underwater images. Details on the different mosaicking techniques available are presented in Appendix A. Based on this review, the

routines and programs that were deemed most appropriate for underwater imagery were selected and used with different datasets to assemble mosaics. The chosen methods include both video- and photo-mosaicking techniques, depending on the types of cameras available on the ROVs.

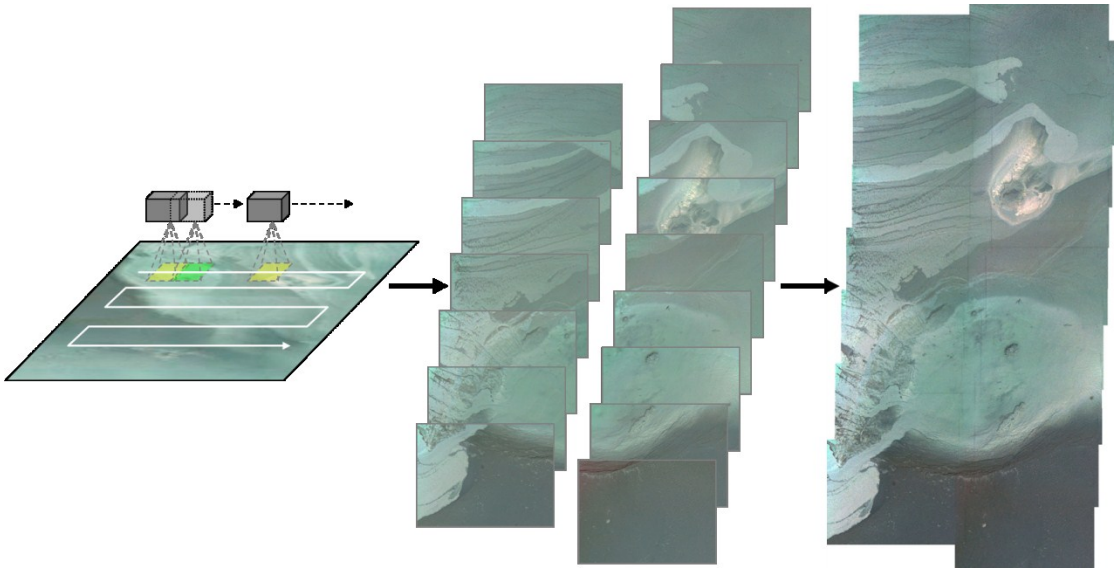

Figure 2.2: Illustration of the photo-mosaicking process; this example shows a photo-mosaic of mud flows in the Black Sea. The scene was surveyed by conducting several parallel transects with an ROV flying at low altitude (3 to 4 meters); photos of the seabed were taken at regular intervals to ensure sufficient overlap between consecutive images (each image is about 3.4 m wide); to further constrain the global registration error, spacing between adjacent lines was chosen so as to ensure a minimum overlap between transects too. The final photo-mosaic was constructed with the LAPM toolbox (Individual photos: © Marum).

2.1.1 Video-mosaicking

The video-mosaics were constructed with the Ifremer MATISSE program. MATISSE was developed to construct lines of mosaic based the ROV navigation data and on pictorial information (Vincent et al. 2003, Allais et al. 2004). This method offers the great advantage of producing lines of mosaic at the speed of the video feed, i.e. in real-time. Mosaic segments are geo-referenced based on the navigation data and can be directly loaded into GIS programs.

The only downside of video-mosaicking techniques is that minor local imprecisions generally add up and can lead to larger global errors (drift, image distortion) over long lines of mosaic. Indeed, such techniques do not consider potential overlaps between the different lines of mosaics in order to constrain the global registration error.

To limit such errors, the video-mosaics were constructed in short segments. These segments were then loaded into a GIS and geo-referenced together based on the information provided by the overlapping areas. This allowed creating a high-resolution video-mosaic of a 14,000 m^2-large area with only limited drift-related errors (cf. Chapter 5).

2.1.2 Photo-mosaicking

Photo-mosaics generally achieved better results and higher definition than video-mosaics. Indeed, the chosen methods allowed considering all information gained from all overlaps between any pair of images in order to minimize a cost function, i.e. to compute for every image the best position and transformation that are required to obtain the lowest possible global error (Figure 2.2). Therefore, such photo-mosaicking methods are in general very slow, memory-demanding and applicable to a limited amount of images; hence, they are often limited to relatively small areas.

Therefore, a MATLAB toolbox for large-area photo-mosaicking (LAPM toolbox) was created (cf. Chapter 2.3). The main strength of this tool lies in its ability to generate photo-mosaics of any size and on virtually any recent computer. To achieve such capability, large mosaics are automatically divided in several square tiles (Figure 2.3), which are then constructed successively. The size of individual tiles is limited by the computing resources, but the amount of tiles is unlimited. Tiles are automatically given geographic attributes and can be directly imported into GIS, where the entire mosaic will be displayed. More technical details about this toolbox are given in Chapter 2.3.

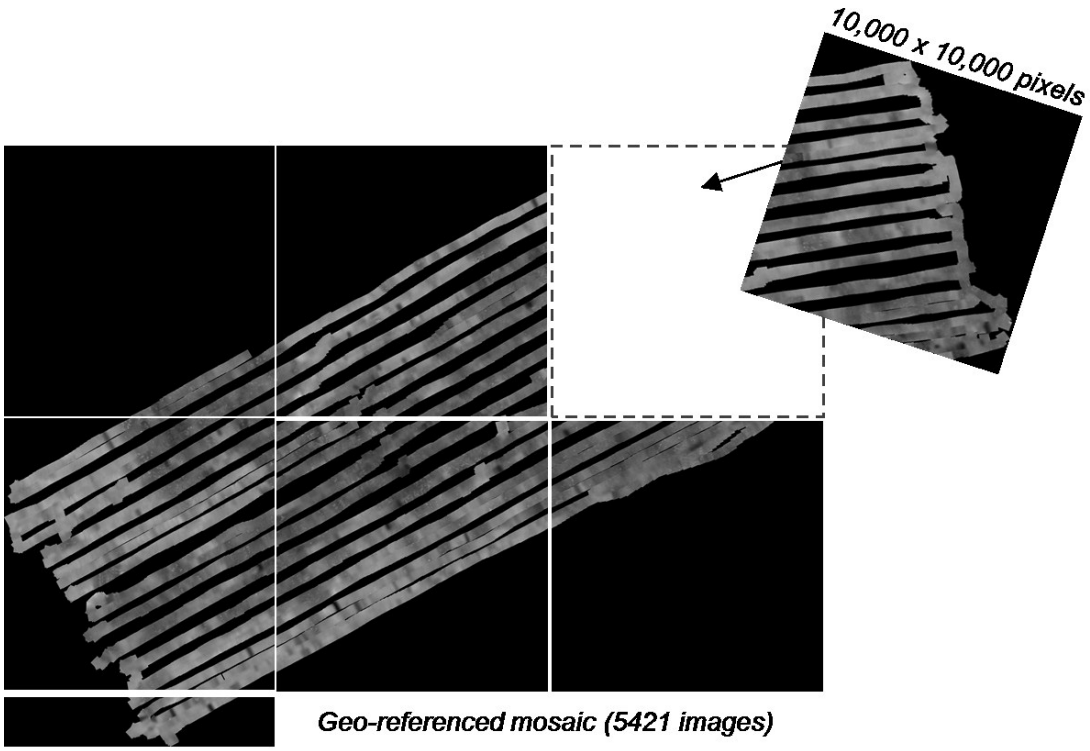

Figure 2.3: Illustration of the mosaic tiles as produced by the LAPM toolbox (in this example, each square tile covers about 100,000 m^2); individual tiles are constructed separately in order not to exceed the computing resources; tiles are geo-referenced, hence, loading them into a GIS allows visualizing the entire photo-mosaic; GIS analyses can then be performed.

2.2 Hydroacoustic mapping

Bathymetry and micro-bathymetry data were acquired using multibeam echosounders (MBES) mounted either on ships (bathymetry) or on underwater vehicles (micro-bathymetry), such as ROV and AUV. The systems used in this work include the hull-mounted Kongsberg Simrad EM122 (RV METEOR), and an ROV-borne Reson Seabat 7125 (ROV VICTOR 6000).

A MBES not only allows mapping the seafloor topography, but can also provide information on the intensity of the signal reflection, also known as signal backscattering. The backscattering intensity of the acoustic signal can be influenced by many parameters (Figure 2.4), and is generally enhanced by the presence of hard substrata, such as hard rock or bivalve shells. Such capability is very useful at hydrocarbon seeps, where high backscatter intensity can help identifying carbonate crust occurrences or faunal presence (Figure 2.4), i.e. areas of past or present seepage activity.

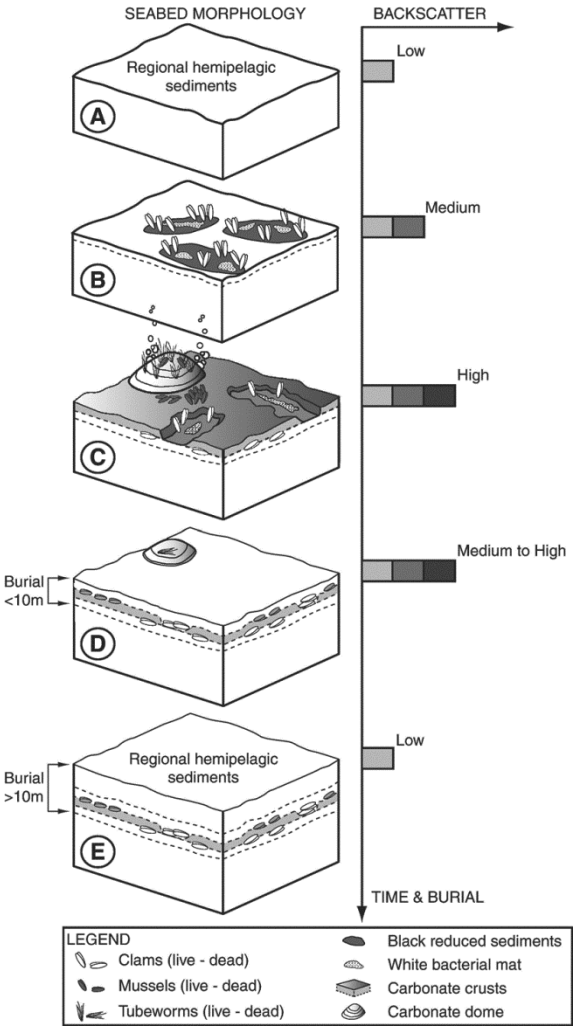

Figure 2.4: Block diagrams showing the impact of the bottom fauna and substratum type on the intensity of signal backscattering. From Gay et al. (2007).

At high frequencies, acoustic methods can also be used to detect the presence of free gas in the water column (Greinert et al. 2006, Nikolovska et al. 2008). Indeed, the acoustic signature of free gas bubbles is characterized by a very strong and much localized backscatter

anomaly. The most common application of such characteristic is for the detection of gas plumes at hydrocarbon seeps. Gas induced acoustic anomalies are known as *flares*. Flares can be imaged in various ways, for instance with sub-bottom profilers, multibeam echosounders, or also sidescan sonars (Figure 2.5).

The flare mapping survey conducted in this work used a MBES Reson Seabat 7125 mounted on a ROV. The system was running at very high frequency (400 kHz) and was therefore very sensitive to the presence of gas in the water column. However, because of the widespread occurrence of highly reflective carbonate crusts within the surveyed area, gas emissions could not be reliably identified on the MBES swath view, and the side-scan view was used instead. The sidescan view consists in plotting the raw (i.e. unprocessed) sonar data against time, i.e. in the sequence in which it is received. The presence of gas bubbles in the water column can then be detected before the first echo of the seabed is received and, thus, generates a strong backscatter anomaly within the water column section of the sidescan view (Figure 2.5c).

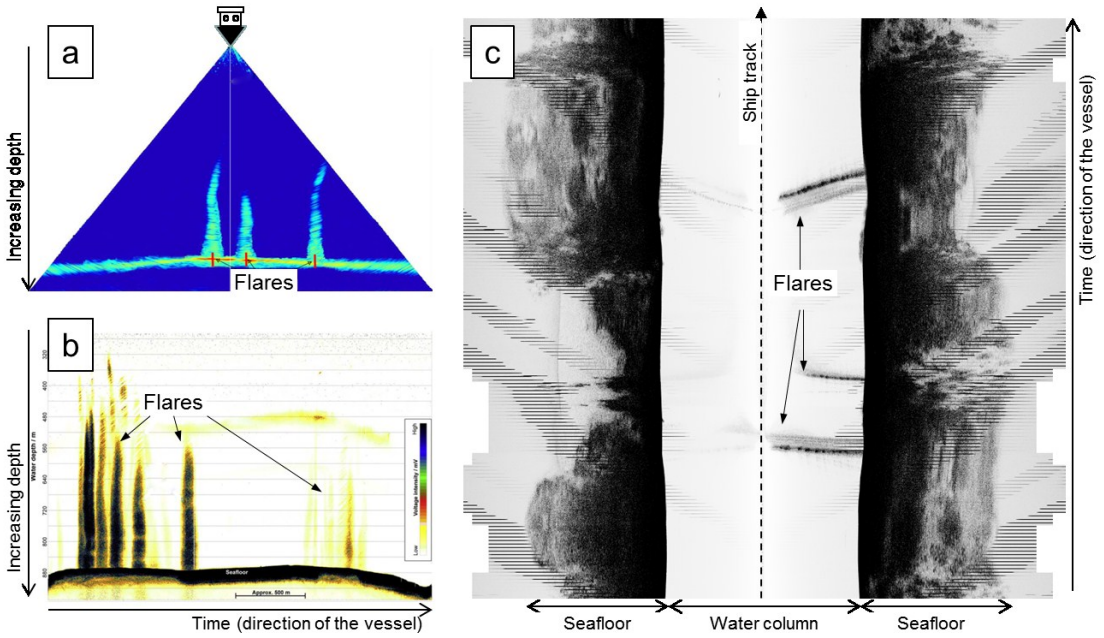

Figure 2.5: Illustration of several flare-mapping techniques. (a) View of the swath of a multibeam echosounder representing flares on the seafloor; the swath provides a view perpendicular to the ship direction and is relatively suited to map large areas. (b) Along-track view from a sub-bottom profiler showing several flares; because of the narrow angle of sub-bottom profilers, flares must be close to the ship track to be detectable with this method. (c) Sidescan view of three large flares; the across-track axis represents time; this method allows mapping large areas, but the localization of flare origin is less precise than with other techniques. (a) and (b) from Nikolovska et al. (2008).

2.3 LAPM: A MATLAB Toolbox for Underwater Large-Area Photo-Mosaicking

LAPM: A MATLAB Toolbox for Underwater Large-Area Photo-Mosaicking

Yann Marcon, Heiko Sahling, Gerhard Bohrmann

MARUM – Center for Marine Environmental Sciences and Faculty of Geosciences, University of Bremen, Klagenfurter Straße, D-28359 Bremen, Germany

MANUSCRIPT 1

In preparation for submission to *Environmental Modelling & Software*.

2.3.1 Abstract

This paper presents a new MATLAB toolbox for large-area photo-mosaicking (LAPM toolbox). This toolbox was developed specifically for the purpose of underwater mosaicking, and it is aimed at providing end-user scientists with an easy and robust way to construct large photo-mosaics from any set of images. It is notably capable of constructing mosaic with an unlimited amount of images and on any recent computer. The mosaicking process can rely on both feature matching and navigation data. This is complemented by an intuitive graphical user interface, which gives the user full control over the feature matches between any pair of overlapping images. Finally, mosaics are given geographic attributes that allow direct import into ArcGIS. So far, the LAPM toolbox was successfully used to construct geo-referenced photo-mosaics with photo and video material from several scientific cruises. The largest photo-mosaic contained more than 5000 images for a total area of about 105,000 m^2.

2.3.2 Introduction

Low visibility in the deep-sea constrains images of the seafloor to be taken from a very short distance only (<10 m) to the scene. Such low altitude severely limits the field of view of individual images. Hence, imaging extended areas requires many images.

Photo-mosaicking consists in aligning and stitching photographs together to form a large composite picture. This technique is widely used in photography for the production of panoramas. However, the interest in mosaics to map deep-sea environments is growing among the scientific community, and several works have focused on developing algorithms to reliably build underwater mosaics (Gracias & Santos-Victor 2001, Eustice et al. 2002, Vincent et al. 2003, Pizarro & Singh 2003, Allais et al. 2004, Ferrer et al. 2007, Escartín et al. 2008). Indeed, traditional panorama-dedicated programs usually fail to cope with underwater imagery correctly. The deep sea is a very challenging environment, and the reasons for failure are manifold; strong lighting heterogeneities, low contrasts, perspective distortions, poor accuracy of camera positioning data, or adverse camera motions due to bottom currents are many hindrances to the construction of large and low-distorted photo-mosaics.

Efforts have been made in several institutes of physics, robotics or computer vision sciences to develop tools to generate photo-mosaics of the seafloor (Eustice et al. 2002, Pizarro & Singh 2003, Ferrer et al. 2007, Escartín et al. 2008), and impressive results were achieved. However, applying those techniques often requires strong mathematics, physics and programming skills, which the end-user of deep-sea mosaics does not necessarily possesses. Indeed, published works about mosaicking techniques are generally aimed at improving known techniques rather than on developing a robust end-user product for potential deep-sea scientists. It is interesting to note that recent mosaicking works now concentrate on 3-dimensional imaging and mosaicking techniques (Nicosevici et al. 2006, 2009, Brandou et al. 2007, Pizarro et al. 2009), whereas no freely available tool exists for end-users to routinely produce 2-dimensional areal mosaics.

The MATLAB large-area photo-mosaicking toolbox (LAPM toolbox) was developed to palliate this lack. The main strength of this tool lies in its ability to generate photo-mosaics of any size and on virtually any recent computer. Furthermore, mosaic files are given geographic attributes and can be directly imported into a geographic information system (GIS). Finally, the toolbox has an intuitive interface, which makes it easy to use for end users without requiring detailed mathematics, physics and programming knowledge.

2.3.3 Mosaicking process

2.3.3.1 Photo-mosaicking background

Two main sorts of photo-mosaicking techniques exist. The first consists in geo-referencing

each individual photograph based on navigation (easting, northing, and altitude) and attitude (pitch, roll, and yaw) data of a remotely operated vehicle (ROV) or autonomous underwater vehicle (AUV). The method is fast and low demanding in terms of computing resources, but the quality of the mosaic suffers from the inaccuracies of the navigation data (Figure 2.6a). The other method consists in using pictorial information to infer the motion between two images. Such method requires each image to overlap with the next and has higher computing requirements, but it generally yields better results (Figure 2.6b). However, the second technique may not be able to register images if the overlap area is too small or if the scene is featureless.

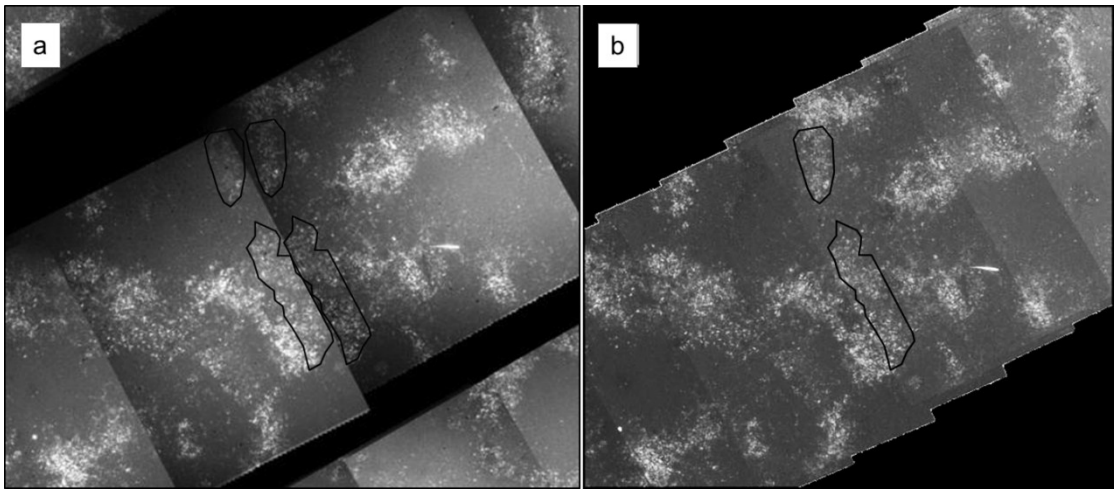

Figure 2.6: Two photo-mosaics of a same area, constructed with different methods. (a) Navigation-based photo-mosaic; mismatches occur between consecutive images. (b) Feature-based photo-mosaic; better fit between consecutive images; however, more images are required to cover the same area.

Therefore, a robust underwater mosaic tool must rely on feature tracking methods to ensure best registration accuracy. However, it should also be able to use navigation data in areas were feature mapping is not possible.

2.3.3.2 Graphical user interface

The LAPM toolbox was developed so as to be easy to use for an end-user without prior knowledge of the techniques involved. Therefore, it has a graphical user interface (GUI) to guide the user through the several stages of mosaic creation (Figure 2.7). Depending on the available data, mosaics can be constructed in three different ways: with feature tracking and navigation data, with feature tracking only, or with navigation data only.

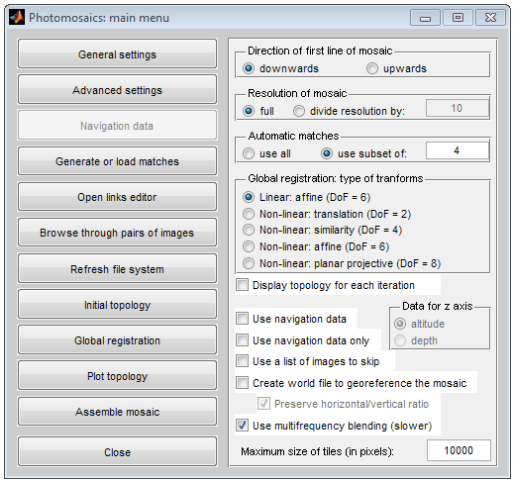

Figure 2.7: Graphical user interface (GUI) of the large-area photo-mosaicking (LAPM) toolbox; the column of buttons is designed to guide the user through the mosaicking process.

2.3.3.3 Feature tracking

If used, feature tracking is the first step of the mosaicking process. It consists in detecting and matching features between each pair of the image sequence. The feature tracking is based on the VLFeat toolbox (Vedaldi & Fulkerson 2008, 2010), which includes an open-source implementation of the Scale Invariant Feature Transform (SIFT) method (Lowe 1999, 2004). With this method, a set of features is computed for every image and tracked onto the next image of the sequence in order to compute the transform matrix, or *homography*, that explains the motion. In addition, an outlier rejection (Pizarro & Singh 2003) is performed in order to remove erroneous matches from the set of positive matches, which ensures that the best possible homography is computed.

In some cases, the feature tracking may also fail to compute matches. This happens generally if the overlap between the images is insufficient, if the scene is featureless, or if the relief causes perspective distortions. Such failure can be overcome by user intervention, i.e. by creating a few links between the unmatched images (Figure 2.8). Alternatively, navigation data can be used to estimate the motion between unmatched images.

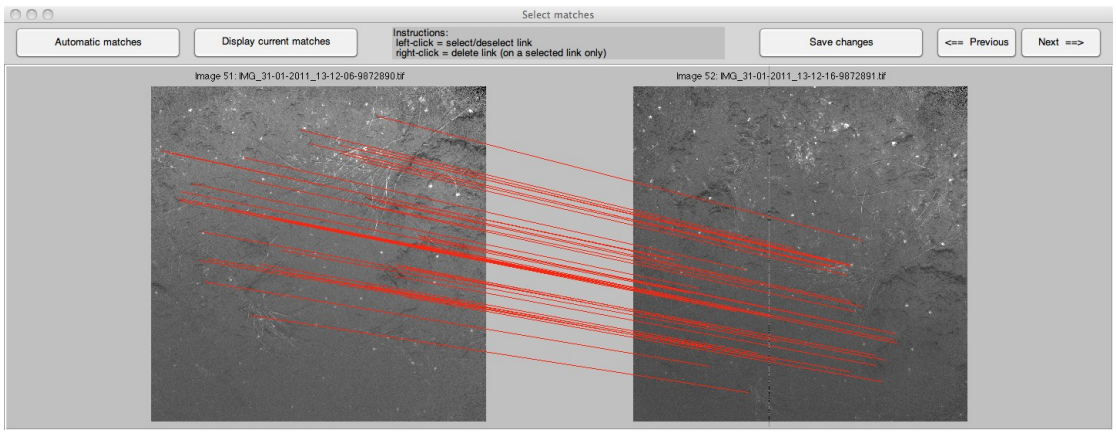

Figure 2.8: The interface of the match selector allows browsing through each pair of images and visualizing the computed matches; erroneous matches can be removed and new matches can be manually created.

2.3.3.4 *Initial topology and crossover*

In mosaicking terms, the *topology* is the estimation of the position and orientation of every image onto the 2D plane of the mosaic (Figure 2.9). The projection of an image onto the 2D plane of the mosaic is called *image registration*. Computing the topology is the next main step of the mosaicking process and a pre-requisite for the actual construction of the mosaic.

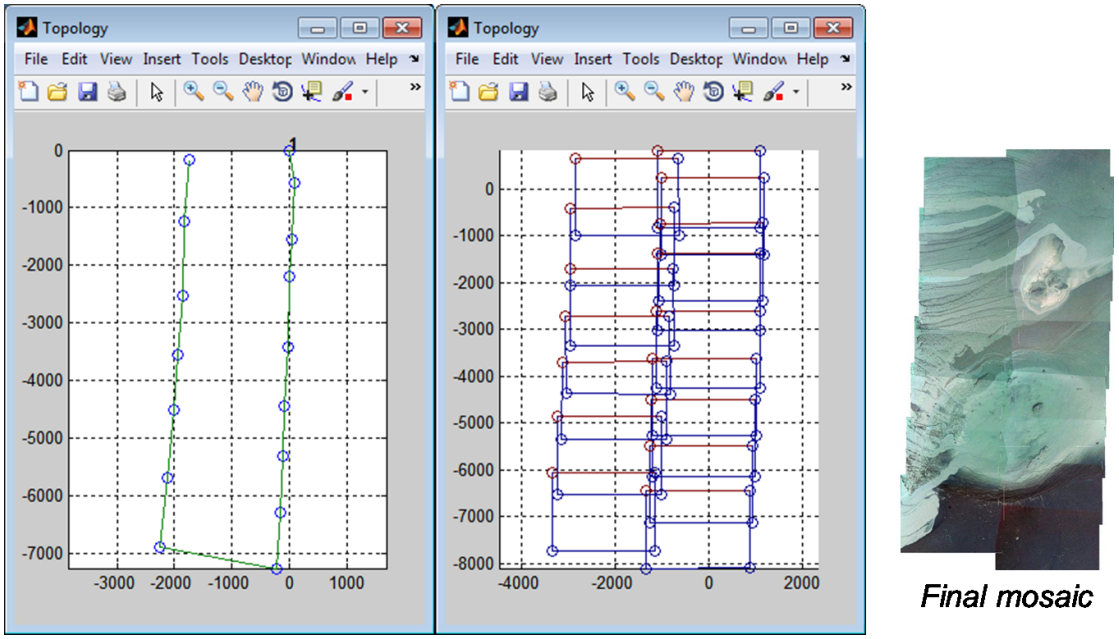

Figure 2.9: Illustration of the initial topology. Left: estimation of the center position of each image. Middle: estimation of the projection of the image frames onto the 2D plane of the mosaic. Right: corresponding mosaic.

The initial topology step consists in estimating the position of each image onto the mosaic plane from the homographies. In this step, the image registration is done successively from the first image to the last in the order of the image sequence. In such context, minor registration errors tend to add up from a pair to the next and to lead to a larger global error. The use of overlaps between nonconsecutive images can help limiting the error by providing additional positioning constraints (Figure 2.10), also known as *crossover points* (Fleischer et al. 1996, 1997, Fleischer & Rock 1998). However, overlaps between nonconsecutive images must be planned at the image acquisition stage; they can be of two types: *crossover path* and *sidelap* (Figure 2.11).

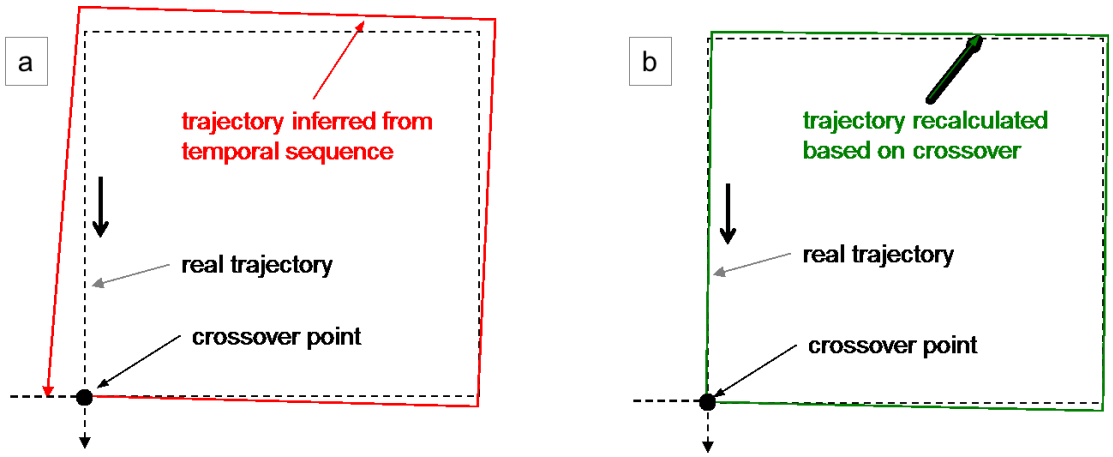

Figure 2.10: Illustration of the contribution of crossover points in limiting registration errors. (a) Small positioning errors add up along the trajectory and grow unbounded. (b) By forcing the trajectory to cross itself at a given point, the position of each point within the loop can be recalculated backward; the registration error of each image is reduced.

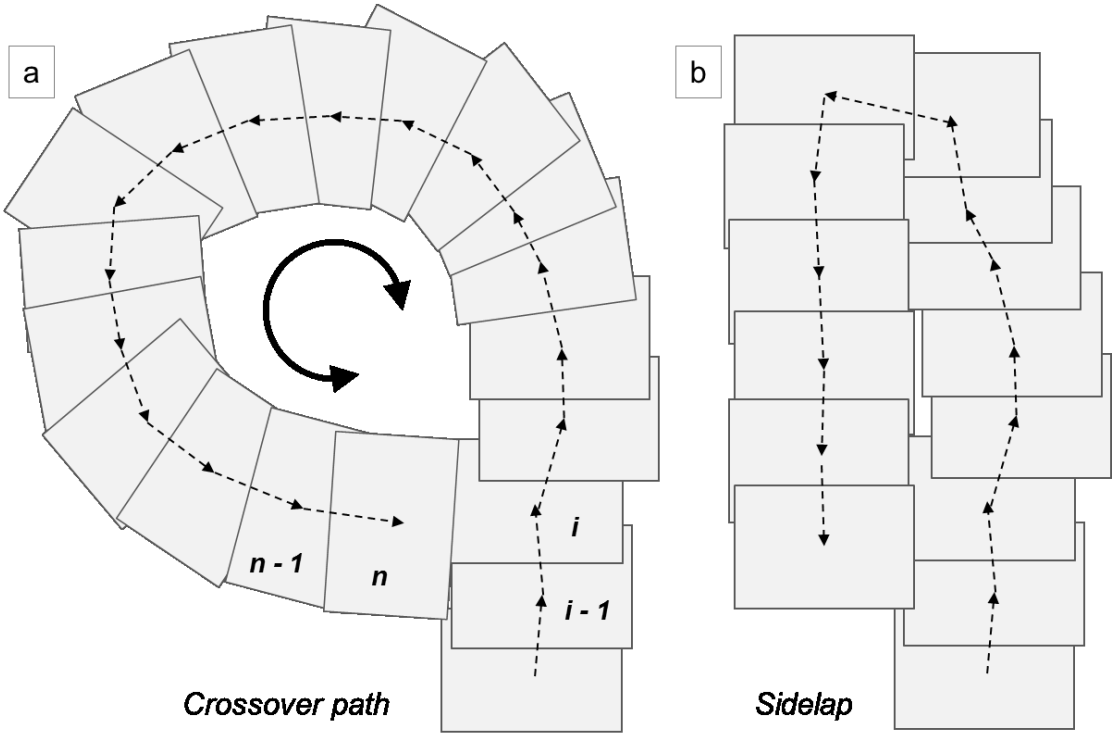

Figure 2.11: Examples of crossover trajectories. (a) A *crossover path* is a trajectory, in which the camera crosses its own trajectory and surveys a same point several times; adapted from Fleischer et al. (1996). (b) Side-overlap, or *sidelap*, occurs when parallel lines of mosaic overlap.

Concretely, implementing crossover information consists in computing or manually adding additional matches between pairs of adjacent (i.e. nonconsecutive) images. Crossover points have been used in previous mosaicking efforts, and in some cases in a fully automatized and iterative fashion (Pizarro & Singh 2003). In contrast, the LAPM toolbox gives to the user full

control over crossover matches. It includes a graphical interface, called links editor, to display all existing matches and to identify potential crossover points.

Crossover points are used in the computation of the initial topology after the pairwise registration of all images has been estimated. Starting again from the first image, whenever a crossover point is found, the registration parameters of all images within the loop are recalculated backward until the beginning of the loop or until the previous crossover point. The principle of this technique is comparable to the smoother-follower technique described by Fleischer et al. (1996).

The use of crossover points can significantly improve the quality of the topology and of the final mosaic (Figure 2.12). Crossover points can also be used to compensate for inaccuracies in the navigation data.

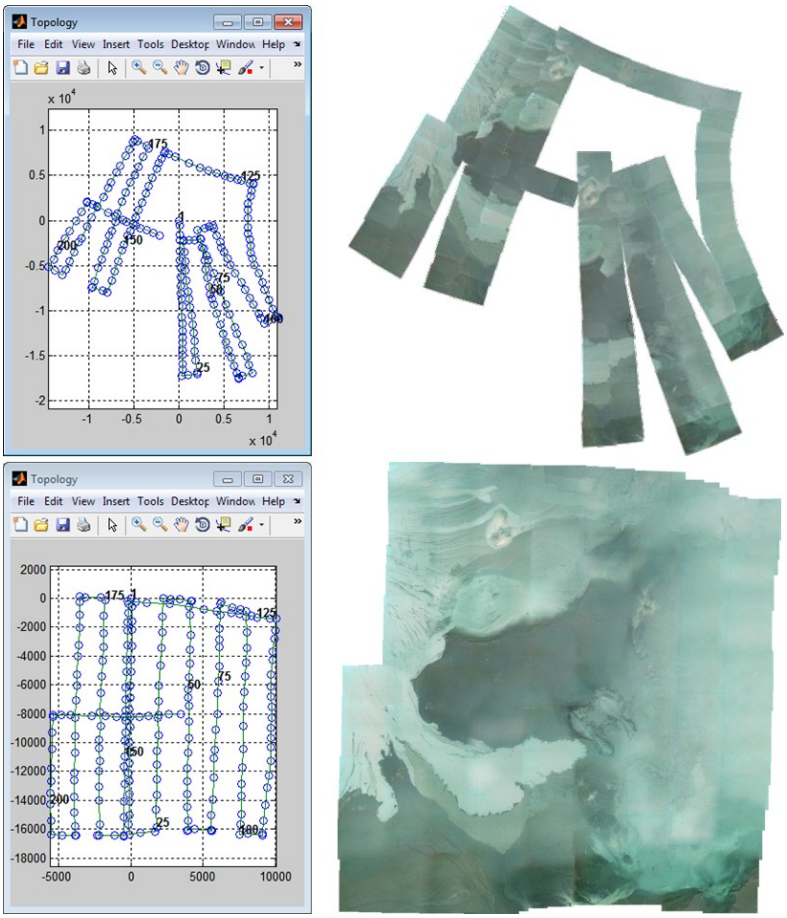

Figure 2.12: Illustration of the benefits of using crossover points. Top: pairwise registration errors add up and lead to a huge global error. In this example, the right line of the mosaic corresponds to a featureless area, and the pairwise image registration is impacted by large errors. Bottom: the use of crossover points allows constraining the error. The final mosaic is consistent.

2.3.3.5 Global registration

The global registration consists in computing for each image the optimal transformation matrix in order to obtain the smallest possible global error. This operation, also known as *bundle adjustment*, is done by minimizing a cost function, which simultaneously takes into account all matches from every matched pair of images.

The LAPM toolbox uses the cost function proposed by Pizarro & Singh (2003) to compute homographies. It is solved in one iteration by linear least squares. The global registration solves for affine (i.e. 6 degrees of freedom) homographies; hence, it generally results in a finer estimation of the topology than the initial topology. However, in some cases, it may produce less satisfying results than the initial topology estimation; this happens especially if the navigation data is used, or if the amount of matches between some images is too low to reliably compute a homography.

2.3.3.6 Mosaic construction

After all images have been registered, they are merged together to compose the actual mosaic. Several methods exist to optimize the rendering of the overlaps, which can be divided in two categories: clipping and blending methods (Burt & Adelson 1983, Marks et al. 1994, Eustice et al. 2002, Pizarro & Singh 2003, Ferrer et al. 2007, Lirman et al. 2007, Gracias et al. 2009).

Clipping methods consist in taking into account the pixels from one image of the overlapping images only; they are usually fast but clear seams are visible at the intersection between overlapping images. Conversely, blending methods combine pixels from the overlapping images; depending on the blending type, such technique can better render the mosaic, although at a higher computing cost.

Two rendering methods are available with the LAPM toolbox: a clipping method, in which the pixels that are closest to the center of their image are chosen (Lirman et al. 2007), and a blending method, known as *multi-resolution pyramidal blending* (Eustice et al. 2002, Pizarro & Singh 2003). The latter method is significantly slower but produces a seamless mosaic.

2.3.4 LAPM toolbox: Functions

The LAPM toolbox was developed specifically for the purpose of underwater mosaicking, and its main functions were designed to meet the needs of an end-user scientist, interested in building visual maps of the seafloor. The main requirements included the ability to (1) assemble large high-resolution image datasets on a regular computer, (2) to produce geo-referenced mosaics, (3) to give the user full control over feature matches, and (4) to produce mosaics in different resolutions.

2.3.4.1 Tiling the mosaic

Due to limited field of view in the deep sea, mosaicking large areas commonly requires hundreds to thousands of images. Most panorama-dedicated programs were usually not designed to cope with such large datasets, and computer resources are often exceeded.

For instance, a photo-mosaic image from a set of several thousand high-resolution

photographs can easily reach a few hundred million pixels. Most computers and operating systems cannot cope with such large files.

The main strength of the LAPM toolbox lies in its ability to generate photo-mosaics of any size and on any recent computer. To achieve such capability, large mosaics are automatically tiled in several square images (Figure 2.13), which are then constructed successively and independently.

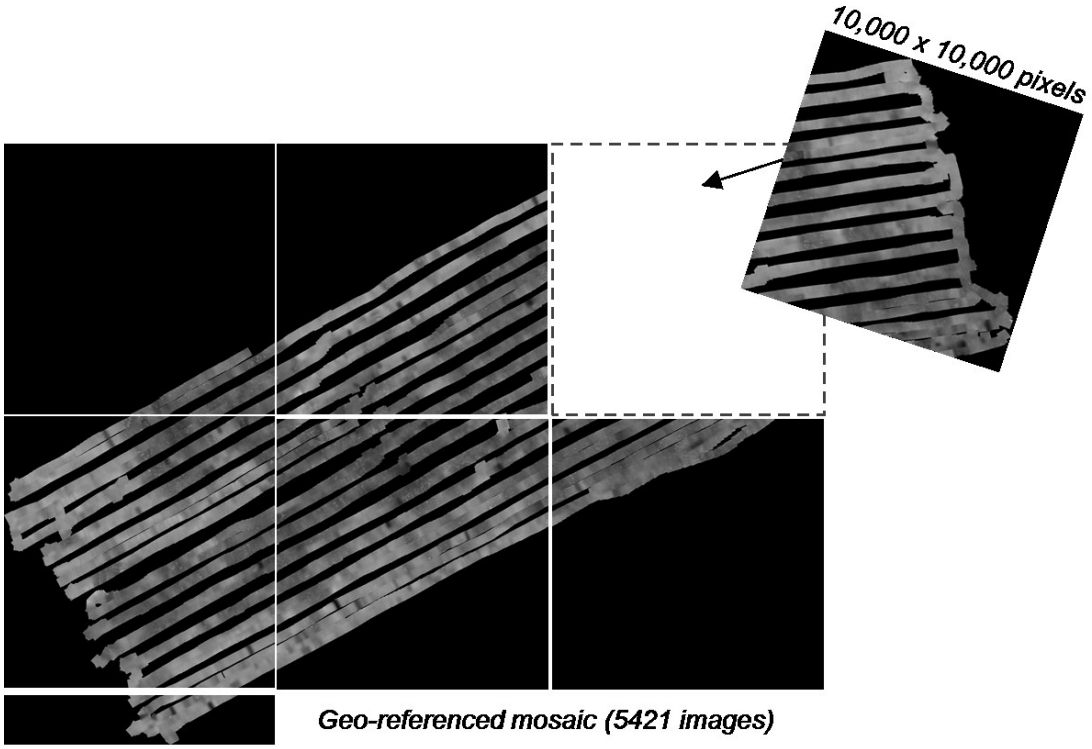

Figure 2.13: Illustration of the mosaic tiles as produced by the LAPM toolbox; in this example, each square tile covers about 100,000 m^2. Individual tiles are constructed separately in order not to exceed the computing resources; tiles are geo-referenced, hence, loading them into a GIS allows displaying the photo-mosaic entirely.

The size of individual tiles must be defined by the user and is limited by the computing resources available. Therefore, lower computing capabilities result in smaller tiles. However, because the amount of tiles is unlimited, photo-mosaics of any size can be constructed on any computer.

2.3.4.2 Geo-referencing the mosaic

If the navigation data is used, photo-mosaics can be geo-referenced. The geo-referencing data is written in a world file, which allows mosaics to be imported into a geographic information system (GIS) such as ArcGIS directly.

A world file is created for every tile of the mosaic. The final photo-mosaic can be visualized entirely by loading each tile into GIS (Figure 2.13). Therefore, spatial analyses can be

performed directly on the entire mosaic, instead of separately on each individual tiles.

A world file can also be produced when full navigation data is not available. In such case, the geo-referencing information is estimated from the position, orientation, and field of view of the first image of the mosaic. However, such method only gives a crude approximation of the true geographical data; its accuracy depends strongly on the morphology of the surveyed area and on the motion of the camera.

2.3.4.3 Editing feature matches

Although robust, feature tracking methods are not always foolproof and they sometimes fail to detect matches between overlapping images. This generally happens when the overlap is too small or when perspective distortions are too strong.

The toolbox includes graphical interfaces that provide the possibility to visualize current matches (Figure 2.14) and to manually edit them (Figure 2.8). If necessary, the user can select and delete individual links, or create new ones between any pair of images.

This function is particularly useful when reliable navigation data is not available, and that feature tracking fails. It is also very efficient to force the implementation of crossover points even between very low overlapping images.

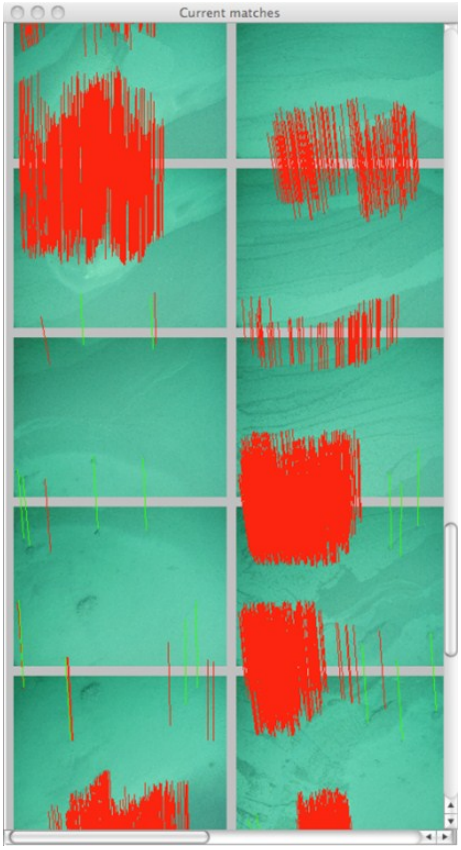

Figure 2.14: View of the link editor of the LAPM toolbox; it give the possibility to visualize all matches and to identify potential unmatched overlapping images.

2.3.4.4 Lowering the resolution

The LAPM toolbox includes the option to produce the final mosaics at several different resolutions. Lowering the resolution reduces computing times significantly. The construction of a high-resolution photo-mosaic is a very computer-intensive and slow process, and it may sometimes be advantageous to lower the resolution in order to speed up the process.

For instance, building large and accurate photo-mosaics can be an iterative process, for which the construction of low-resolution intermediary mosaics may be beneficial; a preliminary mosaic is indeed an efficient way of identifying crossover points in a set of images.

2.3.5 Results

The LAPM toolbox was used to create maps of several deep-sea features. In particular, it produced photo-mosaics with images datasets from different underwater vehicles (ROV and AUV) and from both video- and photo-cameras.

2.3.5.1 Helgoland mud volcano

The Helgoland mud volcano, in the Back Sea, was visited in 2010 during the MSM15/2 cruise (Bohrmann et al. 2011).

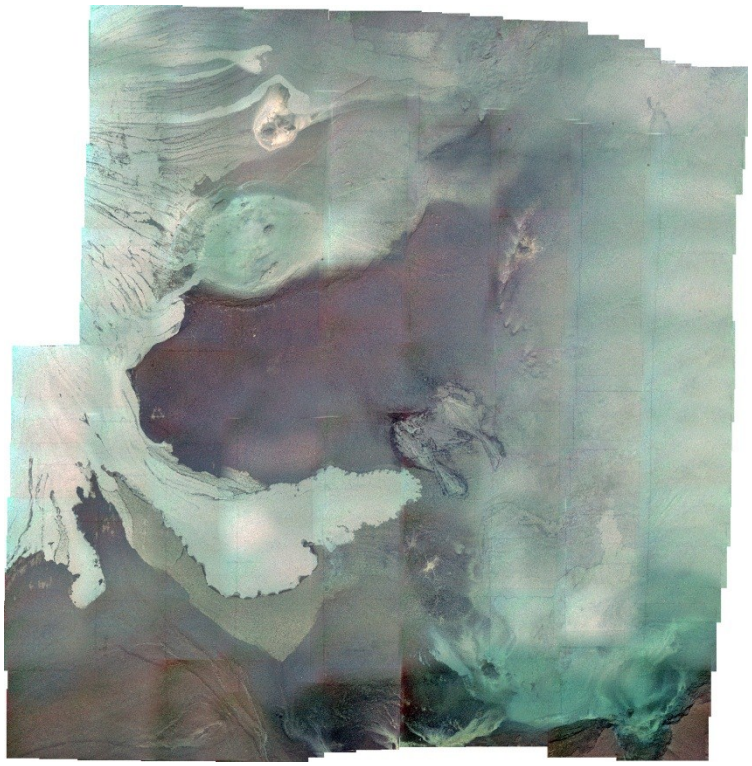

Figure 2.15: Photo-mosaic showing mud pool and mud flows at the Helgoland mud volcano; the mosaic was built with 218 images and covers a 400 m^2 area.

High-resolution images of the volcano center were acquired with a Canon Powershot G10 camera mounted on the MARUM ROV Quest 4000. The surveyed areas included both sharp topography and featureless areas, and reliable ROV-navigation data was not available. Nevertheless, photo-mosaics could be successfully constructed with the LAPM toolbox. The results include in particular a 400 m^2-large photo-mosaic of the center of the volcano (Figure 2.15).

2.3.5.2 Regab pockmark

The Regab pockmark, is a cold seep structure located at 3160 m water depth in the Congo deep-sea fan. It was intensively studied during the WACS cruise (2011) and large video and photo surveys were conducted with the Ifremer ROV Victor 6000. Datasets also include high quality ROV navigation data.

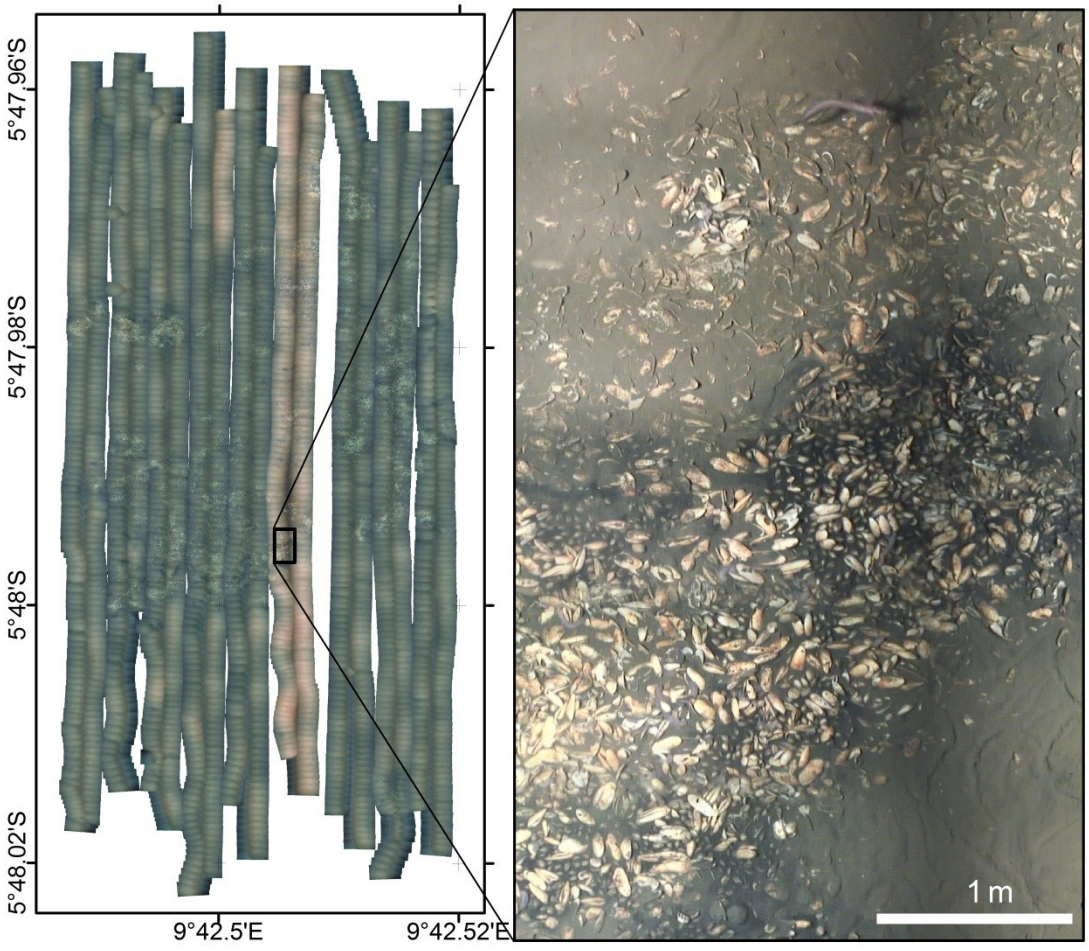

Figure 2.16: Geo-referenced photo-mosaic constructed from high-definition video material; the resolution of the mosaic allows distinguishing individual living and dead clams.

Results include notably a 105,000 m^2-large photo-mosaic of the most active area of the pockmark. Photos were obtained with the high-sensitivity OTUS camera (Simeoni et al. 2007) from an altitude of 8 m above seafloor. Illustration of this mosaic is given in Figure 2.13.

Photo-mosaics could also be constructed from video data. In such case, individual frames were extracted at regular interval (1 second) from the video files. Video images are usually of lower quality than photos from still cameras; however, the high frequency of frames (25 fps for PAL cameras) ensures large overlap areas between consecutive images. Therefore, a very high-definition 5,800 m^2-large mosaic could be constructed (Figure 2.16).

All mosaics are geo-referenced, thus enabling spatial analyses in a geographic information system.

2.3.5.3 Håkon-Mosby Mud Volcano

The Håkon-Mosby Mud Volcano (HMMV) is a 1.4 km-wide circular structure located at about 1250 m water depth in the Barents Sea (Jerosch et al. 2006). The HMMV has been intensively surveyed since its discovery, and high-resolution micro-bathymetry and video-mosaics are already available (Jerosch et al. 2006, 2007b).

Additional photo-mapping surveys were carried out during cruise MSM16/2 (Boetius et al. 2010), with the Sentry AUV from the Woods Hole Oceanic Institute. The largest of these surveys contains more than 5500 photos. The final photo-mosaic was built using both AUV navigation data and feature tracking, and almost fully covers a 75,000 m^2-large area of the volcano (Figure 2.17). It is geo-referenced and spatial analyses and area calculations can be performed in GIS.

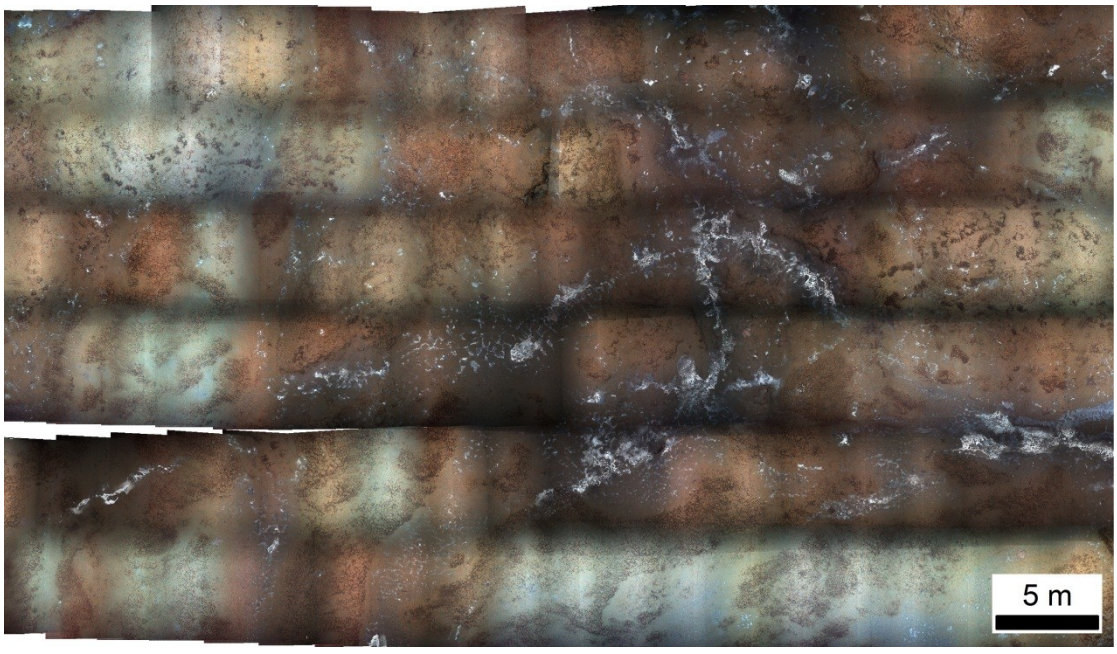

Figure 2.17: Excerpt of the photo-mosaic of Håkon-Mosby Mud Volcano; the continuity of the *Beggiatoa* mats and pogonophoran distribution across the mosaic indicates that images were accurately registered.

2.3.6 Conclusion

The MATLAB large-area photo-mosaicking (LAPM) toolbox was presented in this work. It allows end-users to easily construct large geo-referenced photo-mosaics without requiring in-depth knowledge of the technical aspect of the mosaicking process. The toolbox can be used with any imagery data, but its interface and functions were tailored specifically for the purpose of underwater mosaicking. However, in terms of quality and speed of execution, the LAPM toolbox does not claim to compete with the most advanced photo-mosaicking techniques. The development of this tool was instead motivated by the current lack of end-user underwater photo-mosaicking tools freely available to deep-sea scientists interested in seafloor mapping.

The LAPM toolbox is functional and has already been used successfully with photo and video material from several scientific cruises for the production of high quality and high-resolution photo-mosaics. It will be ultimately available for download online.

2.3.7 Acknowledgements

The author would like to thank the Ifremer for its collaboration and contribution during the WACS cruise, and Michaël Aron for his valuable help and encouragements in getting started with the LAPM toolbox.

Also thanks to Dirk de Beer (Max Plank Institute) and Dana Yoerger (Woods Hole Oceanographic Institute) for providing a large and high quality dataset of the Håkon-Mosby Mud Volcano in order to test the LAPM toolbox.

This work was supported by SENSEnet, a Marie Curie Initial Training Network (ITN) funded by the European Commission 7th Framework Programme, Contract No. PITN-GA-2009-237868.

Chapter 3 Study areas

This thesis focused on two different areas of seabed fluid flow: a hydrothermal vent and a cold seep area. The areas studied are the Menez Gwen volcano and the giant Regab pockmark, and are both located in the Atlantic Ocean (Figure 3.1).

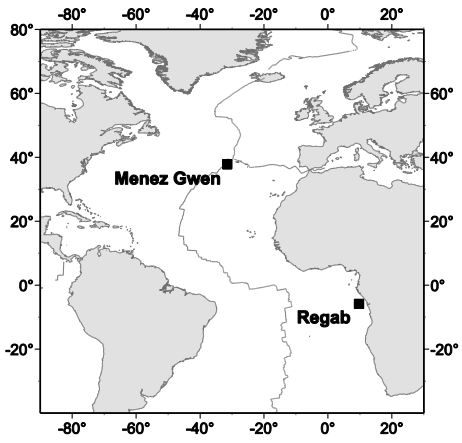

Figure 3.1: Overview map showing the location of the two study areas.

3.1 Menez Gwen hydrothermal vent

The Menez Gwen segment is 55 km long and is located immediately to the north of the Lucky Strike segment and south of the Azores Triple Junction (Figure 3.2a). In this area, the spreading rate of the Mid-Atlantic Ridge approaches 24 mm yr^{-1} (Parson et al. 2000). However, the segment is characterized by the absence of a central rift, and by the occurrence of fresh lava (Fouquet et al. 1994).

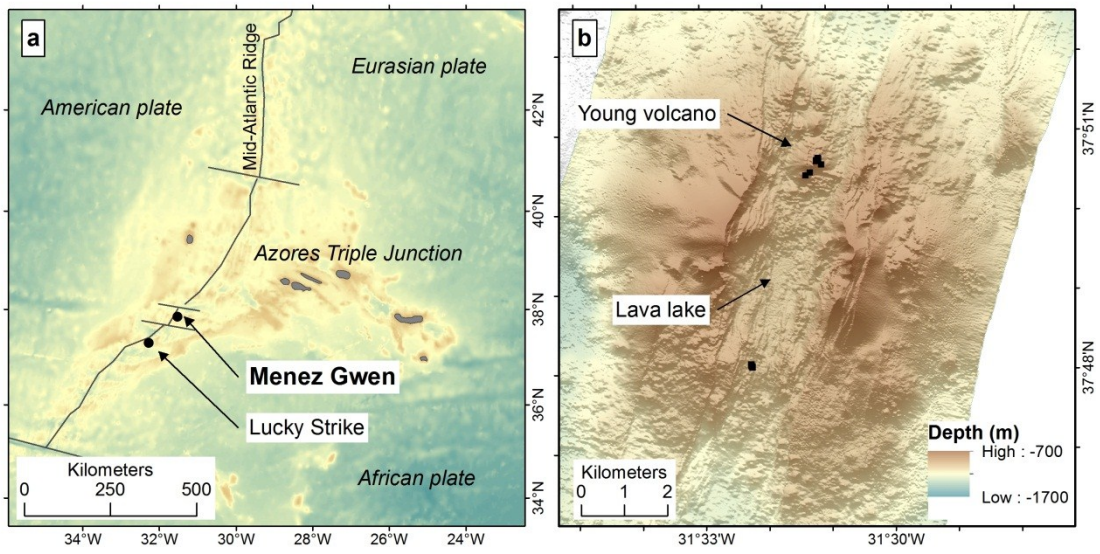

Figure 3.2: (a) Overview map showing the location of Menez Gwen in relation to Lucky Strike and the Azores Triple Junction; the bathymetry background (GEBCO data) shows the Mid-Atlantic Ridge and the tectonic plates. (b) Bathymetry of the Menez Gwen volcano acquired during cruise M82/3 in 2010; the black dots mark the location of known sites of active venting; the most southern site, named 'Bubbylon' was discovered during cruise M82/3 in 2010.

The Menez Gwen hydrothermal vent system is concentrated on a 15 km-large volcano structure (Figure 3.2b) that lies in the central part of the segment. The volcano is composed of basaltic boulders and is generally sediment-free. It is split into two halves by a 2 km-wide graben, globally in the same direction as the ridge segment. A large lava lake is present in the graben, which is surrounded by recent pillows and fresh lobate flows. A new 200 m-high volcano covered with extremely fresh pillows occurs within the graben, north of the lava lake (Fouquet et al. 1994, 1995). This recent volcano hosts most of the currently known hydrothermal vent fields of Menez Gwen (Desbruyères et al. 2001). The co-occurrence of a lava lake and hydrothermal fields in the graben is considered to indicate the presence of a shallow axial magma chamber (Fouquet et al. 1995).

The sites of hydrothermal activity are characterized by the absence of sediment cover and by unconsolidated anhydrite chimneys that grow on fresh pillows directly (Fouquet et al. 1994, Desbruyères et al. 2001). This suggests that the Menez Gwen system is very young in comparison, for instance, to the neighboring Lucky Strike system (Fouquet et al. 1994). Furthermore, emitted fluids are chlorite-depleted and much enriched in gases, especially in methane, indicating important phase separation processes (Fouquet et al. 1994, Charlou et al. 2000). The gas-enrichment of the fluids is an additional indication that the hydrothermal activity at Menez Gwen is recent (Butterfield et al. 1997).

Venting sites are not larger than 200 m^2 and host an abundant chemosynthetic fauna, largely dominated by mussels of the species *Bathymodiolus azoricus* (Fouquet et al. 1994, Desbruyères et al. 2001).

3.2 Regab pockmark

The Regab pockmark is an 800 m-large depression on the seafloor that is located on the West-African passive margin (Figure 3.3), at 3160 m water depth and about 10 km north of the Congo (Zaire) deep-sea canyon (Ondréas et al. 2005, Gay et al. 2006c).

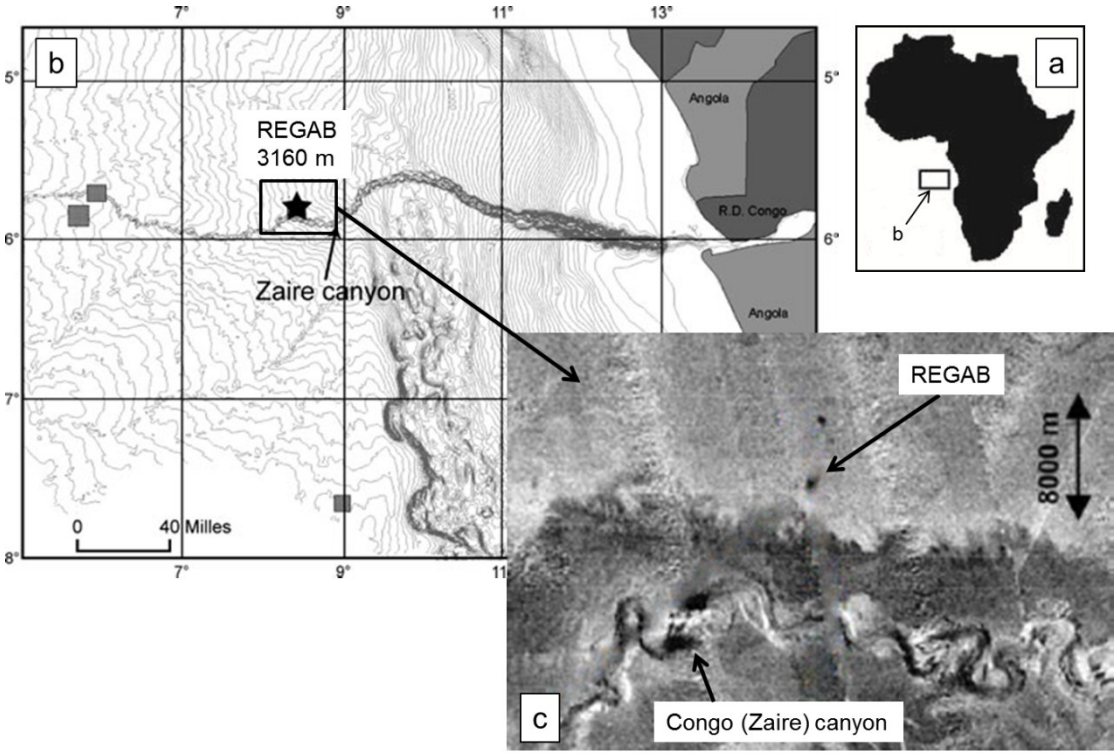

Figure 3.3: Location maps of the Regab pockmark. (a) Overview map showing the location of 'b'; adapted from Gay et al. (2006c). (b) Location of the pockmark in relation to the regional bathymetry; the pockmark is on the lower slope of the Congo deep-sea fan; the rectangle indicates the extent of 'c'; adapted from Olu-Le Roy et al. (2007a). (c) Backscatter map; the Regab pockmark appears as a strong backscatter anomaly; a similar anomaly occurs a few kilometers north of Regab, which correspond to a smaller pockmark; adapted from Ondréas et al. (2005).

The West-African continental margin was formed in the Early Cretaceous, about 130 Ma ago, with the opening of the Southern Atlantic Ocean (Jansen et al. 1984, Marton et al. 2000). After the deposition of a massive salt formation during the Aptian marine transgression, the sedimentation has been entirely marine (Fort et al. 2004). The two main post-salt sedimentary sequences are (1) an aggradation of carbonate/siliclastic deposits from Late Cretaceous to Early Oligocene, and (2) a progradation of silty/sandy turbiditic sediments during Post-Oligocene times. The Oligocene was characterized by a major erosional period, during which the large turbiditic Congo fan was formed, due to increased terrigenous input (Droz et al. 1996, Gay et al. 2006c).

The Congo fan is 1000 km long and extends down the slope to the abyssal plain at about 5000 m water depth (Droz et al. 1996). Numerous fossil channel/levee systems occur in the Quaternary fan, some of which are not connected to the present Congo main channel (Droz

et al. 1996, Savoye et al. 2000). The Regab pockmark is located towards the middle part of the fan, over oceanic crust, is and rooted to one of these fossil channels (Marton et al. 2000, Moulin et al. 2005, Ondréas et al. 2005).

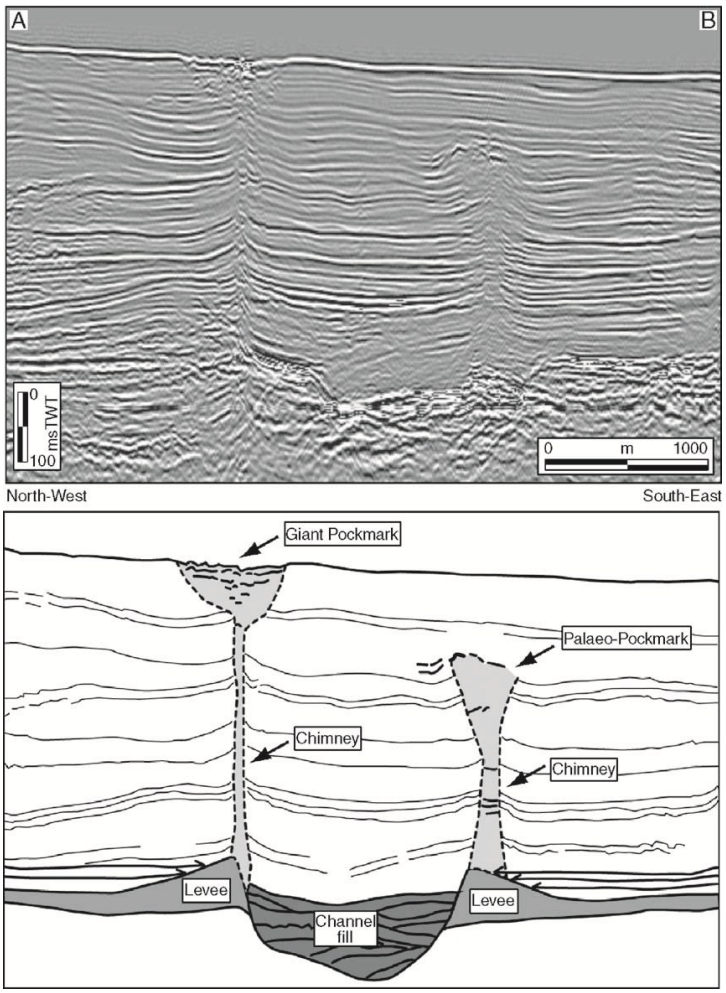

Figure 3.4: Seismic NW-SE transect crossing the Regab pockmark and corresponding interpretation; the pockmark is linked to a channel/levee system, which acts as a reservoir for mostly biogenic methane. A chimney is visible on the northern side of the channel that leads to a buried palaeo-channel. From Gay et al. (2006c).

Pockmark features are common in and around the Lower Congo Basin (Gay et al. 2003, 2006b, Sahling et al. 2008a), and are generally related to either tectonic structures (fault zones, salt diapirs, polygonal faults) or to buried sedimentary bodies (turbiditic channels, erosional surfaces) (Gay et al. 2007). However, with only one other pockmark in the vicinity, the Regab pockmark is rather isolated (Ondréas et al. 2005). Regab was shown to be related to a buried palaeochannel, which acts as a reservoir for mainly biogenic methane (Charlou et al. 2004, Ondréas et al. 2005, Gay et al. 2006c). The expulsion of fluids is triggered by the overpressure caused by the high sedimentation rate of the Congo fan, and occurs at the interface between the buried channel and its northern levee (Figure 3.4).

At the sediment surface, the Regab pockmark is characterized by extended crusts of

authigenic carbonates and the presence of very abundant fauna (Figure 3.5). Chemosynthetic fauna at Regab is dominated by siboglinid polychaetes (vestimentiferan tubeworms), mytilids (mussels), and vesicomyid clams (Olu-Le Roy et al. 2007a). Outcropping gas hydrate deposits and free gas emissions have been observed (Charlou et al. 2004, Ondréas et al. 2005).

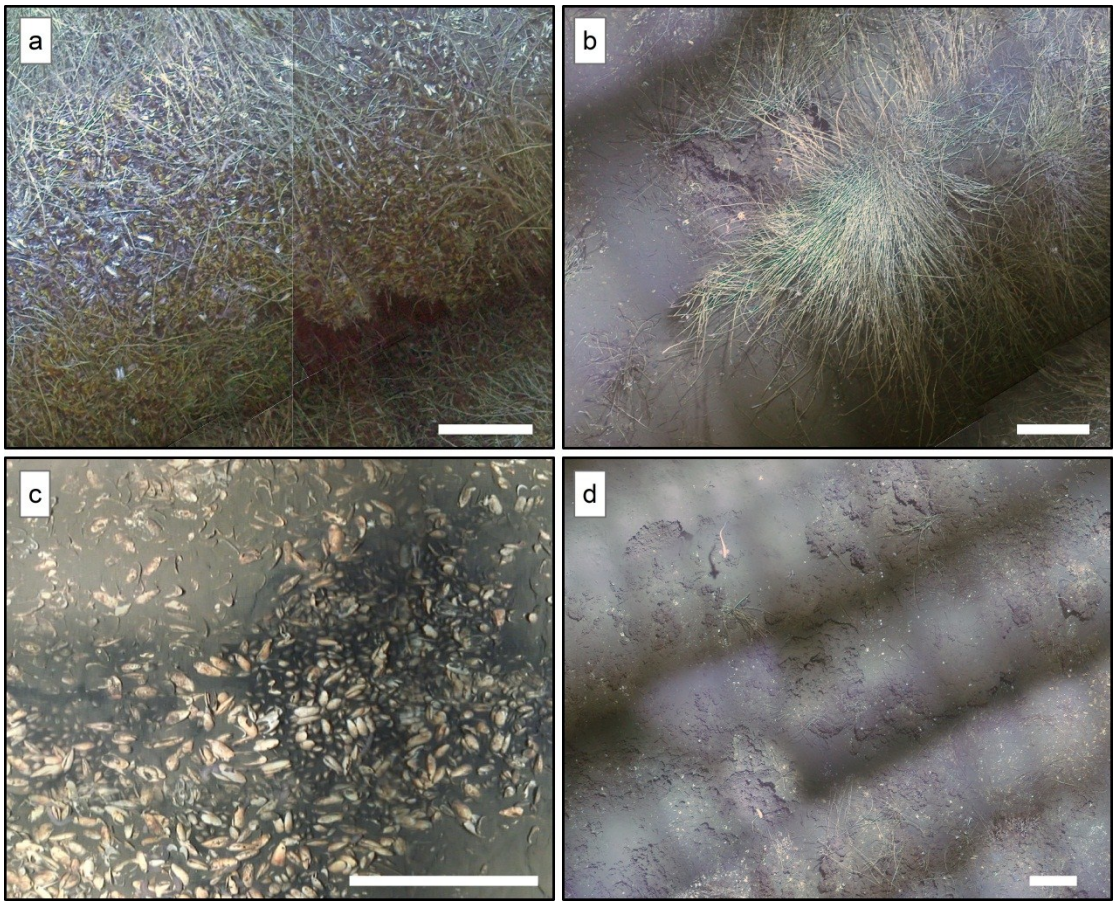

Figure 3.5: Excerpts of high-resolution photo-mosaics of the Regab pockmark. (a) Mussels between dense tubeworm bushes. (b) Large bush of adult tubeworms; these tubes are several meter long. (c) Dense aggregation of dead and living clams; dark sediments around the living clams indicate that sulfate reduction occurs. (d) Large pavement of authigenic carbonates. The white line represents 1 m on all images. Photo-mosaics constructed with the LAPM toolbox (Original images: © Ifremer).

Chapter 4

Megafaunal distribution and assessment of total methane and sulfide consumption by mussel beds at Menez Gwen hydrothermal vent, based on geo-referenced photo-mosaics

Yann Marcon[1], Heiko Sahling[1], Christian Borowski[2], Christian dos Santos Ferreira[1], Janis Thal[1], Gerhard Bohrmann[1]

[1] *MARUM – Center for Marine Environmental Sciences and Faculty of Geosciences, University of Bremen, Klagenfurter Straße, D-28359 Bremen, Germany*

[2] *Max Planck Institute for Marine Microbiology, Celsiusstraße 1, D-28359 Bremen, Germany*

MANUSCRIPT 2

In review at *Deep-Sea Research Part I: Oceanographic Research Papers*.

4.1 Abstract

The Menez Gwen hydrothermal vents, located on the flanks of a small young volcanic structure in the axial valley of the Menez Gwen seamount, are the shallowest known vent systems on the Mid-Atlantic Ridge that host chemosynthetic communities. Although visited several times by research cruises, very few images have been published of the active sites, and their spatial dimensions and morphologies remain difficult to comprehend. We visited the vents on the eastern flank of the small Menez Gwen volcano during cruises with RV Poseidon (POS402, 2010) and RV Meteor (M82/3, 2010), and used new bathymetry and imagery data to provide first detailed information on the extents, surface morphologies, spatial patterns of the hydrothermal discharge and the distribution of dominant megafauna of five active sites. The investigated sites were mostly covered by soft sediments and abundant white precipitates, and bordered by basaltic pillows. The hydrothermally-influenced areas of the sites ranged from 59 to 200 m^2. Geo-referenced photo-mosaics and video data revealed that the symbiotic mussel *Bathymodiolus azoricus* was the dominant species and present at all sites. Using literature data on average body sizes and biomasses of Menez Gwen *B. azoricus*, we estimated that the *B. azoricus* populations inhabiting the eastern flank sites of the small volcano range between 28,640 and 50,120 individuals with a total biomass of 50 to 380 kg wet weight. Based on modeled rates of chemical consumption by the symbionts, the annual methane and sulfide consumption by *B. azoricus* could reach 1760 mol CH_4 yr^{-1} and 11,060 mol H_2S yr^{-1}. We propose that the chemical consumption by *B. azoricus* over at the Menez Gwen sites is low compared to the natural release of methane and sulfide via venting fluids.

Keywords: photo-mosaic, *Bathymodiolus azoricus*, Menez Gwen, hydrothermal vent, biomass, chemical consumption, fluid flow.

4.2 Introduction

Hydrothermal vents were first discovered in 1977 and have been the focus of many studies since then (Lutz & Kennish 1993, Dover 2000). Especially the discovery of non-photosynthesis-fuelled ecosystems associated with these systems, with abundant and diverse endemic fauna, excited the interest of a multitude of scientists from various disciplines. However, hydrothermal vent systems are located in depths without natural sunlight where the field of view for researchers and cameras diving with submersibles or remotely operated vehicles (ROV) is extremely limited despite the use of powerful lights. Hence, more than 30 years after the first discovery, the overall structure of hydrothermal venting sites and the distribution of the associated fauna are often only known from images providing close-up views of limited sections of vents, while only very few detailed maps of entire sites have been published (Escartín et al. 2008, Bell et al. 2012, Barreyre et al. 2012).

Detailed descriptions of the distribution of the faunal assemblages at hydrothermal vent systems that are available in the literature are mostly based on drawings or geo-referenced GIS layers that are drawn from video data. Such data are available in particular from the Endeavour hydrothermal field on the Juan de Fuca Ridge (Sarrazin et al. 1997, Juniper et al. 1998), from the Broken Spur vent field (Copley et al. 1997) and the Logatchev site on the Mid-Atlantic Ridge (MAR) (Gebruk et al. 2000a), and from the Lucky Strike system, at which the faunal distribution on a large chimney structure was described (Cuvelier et al. 2009). Such maps give valuable qualitative information on the distribution of the faunal patches and the layout of the sites but they rely on hand drawings from observations of video material and precision of inferred areas of cover is likely to be limited. Some works (Sarrazin et al. 1997, Juniper et al. 1998, Durand et al. 2002), however, focused particularly on the issue of improving the accuracy of spatial measurements from video imaging by drawing the contours on a background geology map of the site. In those cases, geo-referencing data of the basemap were obtained either from passive reference markers that were captured on video images (Durand et al. 2002) or from long baseline (LBL) navigation data that were correlated to the images (Delaney et al. 1992, Sarrazin et al. 1997, Sarrazin & Juniper 1998). All these methods can be very efficient and can be applied in areas with sharp topographic contrasts.

An alternative approach is to use geo-referenced photo-mosaics to map the faunal distribution. Image mosaicking consists in assembling several overlapping images together to form a composite image of a larger scene. The mosaic is then geo-referenced into a geographic information system (GIS), and areas can be computed. Such a method can provide a significant gain of time to study areas with low to moderate relief but also, contours of features of interest can be drawn onto the geo-referenced image material directly. Similar methods have been used to successfully map faunal communities at different scales and in various types of environments. Examples include large-scale studies of faunal distribution at the Håkon Mosby Mud Volcano (Jerosch et al. 2006, 2007a) and at the Regab pockmark (Olu-Le Roy et al. 2007a), and small-scale studies at the Chowder Hill mound on the Juan de

Fuca Ridge (Grehan & Juniper 1996), at cold seeps in the Gulf of Mexico (Lessard-Pilon et al. 2010a, b) and at discrete sites of hydrothermal activity on the Eastern Lau Spreading Center (Podowski et al. 2009).

Analyses of hydrothermal fauna usually focus on the distribution of the assemblages or on population structure in relation to their environment, and sometimes give estimations of density and biomass estimations per unit areas (Lutz & Kennish 1993, Ramirez Llodra et al. 2007), but the overall spatial distributions of faunal assemblages and animal abundances or biomasses at entire vent sites have rarely been quantified (e.g. Gebruk et al. 2000a, Podowski et al. 2009). Such knowledge is valuable as it gives information on the size of hydrothermal faunal populations, and can be used to infer chemical consumption rates. In a context where seabed methane emissions are considered to contribute noticeably to the global carbon budget (Judd 2003), it is important to evaluate the relative significance of faunal methane consumption against methane effluxes in hot fluid emissions.

In this study, we use high-resolution bathymetry data together with areal photo-mosaics to provide for the first time detailed maps and descriptions of five sites of active venting from the Menez Gwen system in the area of the previously reported marker position PP30/31 (Desbruyères et al. 2001). The Menez Gwen hydrothermal vent field was chosen for this study because it is a volcano structure of the Azores region where hydrothermal activity was believed to be concentrated over small areas. It has been visited by several cruises and the faunal communities hosted by the vent field have been the focus of many biological studies (Fouquet et al. 1994, Comtet & Desbruyères 1998, Sarradin et al. 1999, 2001, Cosel et al. 1999, Dixon et al. 2001, Shank & Martin 2003, Riou et al. 2010). However, descriptions and images of the sites of venting activity remain poor and quantitative data on dimensions, size of populations and biomasses are scarce.

Ship- and autonomous underwater vehicle- (AUV) based bathymetry surveys were conducted in September-October 2010 during cruises POS402 and M82/3 to the Menez Gwen hydrothermal vent field on the Mid-Atlantic Ridge. Five sites of active venting activity were intensively studied during twenty ROV dives. Using GIS, we provide measurements of surfaces covered by dominant species of megafauna, and estimations of minimum biomass of *Bathymodiolus azoricus*. Also, we use published values of size, density and substrate uptake rates for *B. azoricus* at Menez Gwen to infer total methane and sulfide consumption rates at the scale of a vent site. The final goal of this study is to assess the significance of faunal methane and sulfide consumption against natural methane and sulfide release within vent fluids.

4.3 Site description

The Menez Gwen segment of the Mid-Atlantic Ridge is about 55 km long (Parson et al. 2000), and stretches from 38°03'N to 37°35'N in a S-SW to N-NE direction (Figure 4.1). A large

volcano with a mean diameter of 15 km is present near the center of the segment, and it reaches up to about 800 m above the surrounding seafloor (Figure 4.2a). The top part is divided into two halves by a 9-km long axial graben of similar orientation to the ridge segment that forms a 300 to 400-m deep and 2-km wide valley across the volcano.

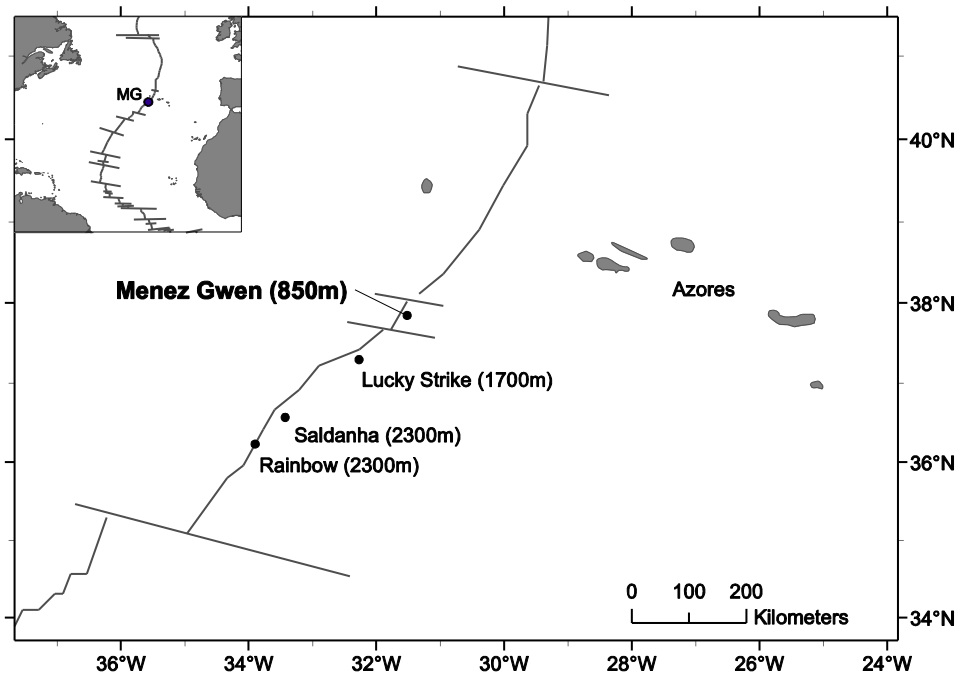

Figure 4.1: Location of the Menez Gwen volcano on the Mid-Atlantic Ridge.

Several recently formed minor volcanoes are scattered across the northern part of the graben. The largest of them is about 1 km wide, up to 200 m high (Figure 4.2b) and its highest point reaches up to 800 m water depth. The surface rocks of this young volcano are composed of fresh lava and some volcanic breccia (Fouquet et al. 1995, Ondréas et al. 1997). The lava has no sediment cover and it has been suggested that the entire small volcano built up during the latest eruptive episode (Ondréas et al. 1997). The hydrothermal activity at Menez Gwen is mainly concentrated on the southern and eastern flanks of this small volcano (Figure 4.2b) (Charlou et al. 2000, Desbruyères et al. 2001). Although the Menez Gwen hydrothermal vents have been visited several times by research cruises, information on the morphology and geological composition of active sites is scarce and concentrates on two locations on the southern flank of the volcano (Figure 4.2b). One of them (PP10/F11) is characterized as a low-elevated and 50-m wide mound with 2-m high anhydrite chimneys which are surrounded by barite-rich precipitates; the other (D9, PP11, F12) is an escarpment topped by a chimney, which is bordered by pillow lava and crumbled rock

(Fouquet et al. 1994, 1997, Charlou et al. 2000, Desbruyères et al. 2001). Such information is not available for sites on the eastern volcano flank.

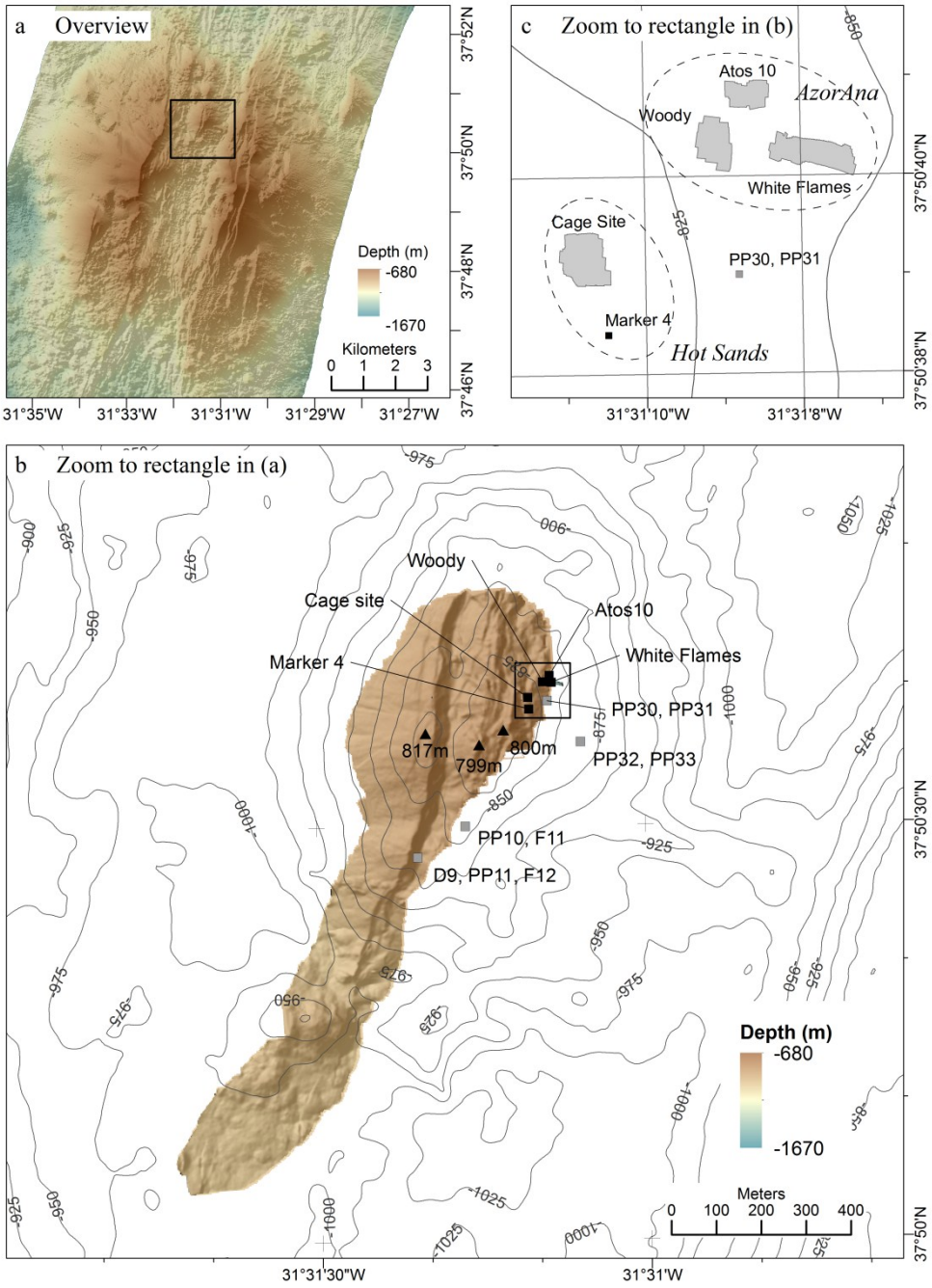

Figure 4.2: (a) Overview map of the Menez Gwen volcano; the rectangle indicates the location of the area shown in (b); (b) AUV-based micro-bathymetry of the young volcano (highest elevations are highlighted with black triangles) and individual sites of active venting during the M82/3 cruise (black squares); the sites described by Desbruyères et al. (2001) are also plotted (gray squares); the rectangle indicates the location of the area shown in (c); (c) outline and relative position of the photo-mosaics.

The sites of hydrothermal activity studied during the cruise M82/3 (2010) were therefore located in this area. Menez Gwen is part of the Azores Marine Park, and future potential access restrictions to the southern sites may lead future research interests at Menez Gwen to the eastern area. All visited sites are located on the eastern flank of the small volcano close to its summit (Figure 4.2b-c), and between 850 and 814 m depth. In 20 dives, five major sites were found in the area: Atos 10, Cage Site, Marker 4, White Flames, and Woody. The site names were those assigned during the cruise M82/3 in September-October 2010.

Large megafauna is composed of the bivalve species *Bathymodiolus azoricus*, the caridean shrimps *Chorocaris chacei*, *Mirocaris fortunata* and *Alvinocaris* sp. aff. *stactophila*, numerous gastropods, mainly *Lepetodrilus atlanticus* and *Protolira valvatoides*, the crab *Segonzacia mesatlantica* and the large non-hydrothermal crab *Chaceon affinis* (Cosel et al. 1999, Gebruk et al. 2000b, Ramirez Llodra et al. 2000, Desbruyères et al. 2001, Galkin & Goroslavskaya 2010). Smaller fauna is even more diverse (Galkin & Goroslavskaya 2010), but is not discernible in video and photo materials.

4.4 Methods

4.4.1 Bathymetric surveys

Swath-mapping surveys were conducted during the M82/3 cruise with the hull-mounted multibeam echosounder (MBES) EM122 from Kongsberg Maritime operating at 12 kHz with 432 beams. Micro-bathymetry was acquired during the POS402 cruise with the MARUM AUV SEAL 5000, using a RESON SeaBat 7125 multibeam echosounder operating at 400 kHz with 512 beams. Processing of the bathymetry data was done with MB-System (Caress & Chayes 2001).

4.4.2 Imagery, mosaicking and image processing

Imagery used for the production of mosaics was acquired with a DSPL SSC 6500 Colorzoom video camera with corrected optics to eliminate geometric and chromatic distortions. The DSPL camera was mounted on a pan-and-tilt head at the front of the ROV Quest 4000 m (MARUM). For mosaicking applications, the camera was positioned into the most possible vertical direction without having parts of the ROV within the view. In this position, the angle of the optical axis of the camera in relation to the vertical plane was 39 degrees; therefore every image was affected by the same perspective distortion. Laser pointers were used throughout the surveys to ensure that scale information is recorded with the imagery.

Images were obtained in a structured way by performing several parallel and overlapping transects at a constant speed and a steady altitude across each site. Photo-mosaics were constructed using consecutive frames from the video files, with an overlap of 25-30%. Individual transects of the mosaics were constructed using a MATLAB algorithm (Pizarro &

Singh 2003) provided by C. Fisher and E. Podowski. This algorithm was developed to cope with the peculiarities of the underwater environment (low lighting, adverse motion of the camera such as roll, pitch and yaw) and is relatively well suited to compensate for inaccuracies between consecutive images that would be related to the camera inclination. The final mosaics were constructed manually with Photoshop by assembling individual transects together. Drift-induced errors between transects were low (about 50 cm error every 10 m in flat areas, i.e. 5%) due to the small dimensions of the mosaics. Nevertheless, where possible, registration artifacts were positioned away from the main areas of interest in order to ensure the best possible matches in the most active areas of the study sites. For each mosaic, colors and contrasts were enhanced using ImageJ software (Abramoff et al. 2004).

Interpretation of the mosaics was supported by further images acquired with a high-definition camera “Insite Zeus Plus Colorzoom”, useful because images loose quality during the mosaicking procedure. This camera was mounted at the front of the ROV in a forward-looking orientation that gives a view of the scene from a different perspective, closer to the seafloor, and allowed observing the relief. Based on observations from videos of 20 dives, we identified high and low features and reconstructed 3D views directly on the mosaics. While such information is hard to scale and does not give exact values for altitude variations, it gives valuable insight on the overall site morphologies, which usually are difficult to comprehend from mosaics alone. At White Flames, altitude information provided by ROV sensors was used to estimate the height variation of the bottom topography.

4.4.3 GIS and spatial analyses

Mosaics were geo-referenced in ArcGIS using navigation data of the ROV Quest. Ultra-short baseline (USBL) data was used for the relative positioning of each site, whereas dead-reckoning navigation data from the Doppler Velocity Log (DVL) sensor was used for scaling and orientating the mosaics. Information from laser pointers was used to confirm correct scaling of the mosaics.

For all mosaics, bottom topography features were delineated and polygons were created in ArcGIS to map the spatial distribution of each feature. Mapped features include hard and soft substrata, patches of mussels or shells, and zones of intense whitish mineral precipitation. Total areas of each site were measured in ArcGIS and correspond to the limit of the hydrothermal deposits and fauna. The extent of mussel communities was delineated, areas and percentages of cover were calculated. All areas were measured using a Mollweide equal area projection.

Additional qualitative observations made from all high-resolution video and photo material from the cruise M82/3 were pinpointed onto the mosaics. Point features that were mapped include locations of the exit points of fluid emission, and qualitative assessments of abundance of some mobile fauna. Points of fluid emission were sorted depending on the presence or absence of chimney structure and, where relevant, on the height of the

chimneys. Additionally, wherever the videos showed the seafloor close enough to reliably observe the presence or absence of shrimps and gastropods, the observation was marked in the mosaics. Animal abundances were semi-quantitatively assessed. Shrimp abundance was categorized according to absence, low abundance (1-10 ind. m^{-2}) and high abundance (>10 ind. m^{-2}). Gastropods were present in all sites and therefore divided into two categories of low abundance (individuals are scattered, substrate is clearly visible between individuals) and high abundance (gastropods build closed groups, substrate not visible between individuals). This work was performed for all five sites but the amounts of observation points at Atos 10 and Marker 4 were too low (<5) for interpretation; therefore the results are not shown. However, data from every site were used for the analyses of abundance against distance to points of fluid emission. The resolution of the mosaic images did not allow an identification of shrimps and gastropods to species level. Therefore, our analyses only used the higher taxon levels 'shrimp' and 'gastropods'.

4.4.4 Estimations of *B. azoricus* biomass, methane and sulfide consumption

Total population and total biomass of *B. azoricus* were estimated for all sites (except Marker 4), based on our measured values of mussel coverage and on estimated mussel sizes and densities.

From our observations, mussel patches included various sizes from juveniles to largest individuals of ca. 12 cm shell length. We did not analyze representative values for population densities and size frequencies of the mussels, however, our collections revealed that small juveniles and very large individuals were rare, while the majority of the animals was medium sized. This corresponded to published data based on collections in several years and at different seasons. According to these data the shell lengths for the majority of individuals at Menez Gwen ranged between 40 and 80 mm (Comtet & Desbruyères 1998). Population density in *B. azoricus* mussel patches at Menez Gwen has been estimated 400 to 700 ind. m^{-2} (Colaço et al. 1998). Based on these estimates of *B. azoricus* shell size and population density, biomass estimations range between 0.71 and 5.3 kg wet wt m^{-2} (Martins et al. 2008).

Table 4.1: Ranges of values for all parameters concerning *Bathymodiolus azoricus* at Menez Gwen, which are used in this study; minimum and maximum calculated values are based respectively on the lowest and highest limits of assumed shell length and population density; refer to text of detailed explanations.

Parameter	Range	Type	Source
Shell length (mm)	40 - 80	Assumption	(Comtet & Desbruyères 1998)
Population density (ind m^{-2})	400 – 700	Assumption	(Colaço et al. 1998)
Weight (g wet wt ind^{-1})	1.78 – 7.56	Calculated	from Martins et al. (2008)
Biomass (kg wet wt m^{-2})	0.71 – 5.3	Calculated	from Martins et al. (2008)
Gill weight (g dry wt ind^{-1})	0.09 – 0.36	Calculated	from Martins et al. (2008)
CH_4 uptake (µmol d^{-1} ind^{-1})	5.9 – 96.1	Calculated	from Martins et al. (2008)
H_2S uptake (µmol d^{-1} ind^{-1})	36.5 – 604.1	Calculated	from Martins et al. (2008)

We used these values (Table 4.1) to estimate population sizes and total biomasses of *B. azoricus* for each site, except for Marker 4, for which the perspective distortion of the mosaic did not allow calculating areas. The population size estimations were based on the extents of mussel coverage measured on 2D images from the various sites. As these images do not account for the bottom relief, the calculated population sizes are possibly underestimated. Furthermore, as biomass estimations were additionally based on a range representative of the most frequent shell sizes and not on real size frequency distributions, the total areal biomasses are also very likely underestimated and represent minimum values.

Our calculations of methane and sulfide consumption by the mussels are based on published values of chemical uptake rates by *B. azoricus* at Menez Gwen. We followed the modeling results of Martins et al. (2008) and used uptake rates of 5.9 to 96.1 µmol CH_4 d^{-1} ind^{-1} and 36.5 to 604.1 µmol H_2S d^{-1} ind^{-1} (Table 4.1). These values were modeled based on estimated average volatile concentrations in Menez Gwen mussel habitats of 100 µM methane and 60 µM sulfide (Sarradin et al. 1998, Martins et al. 2008), and on maximum uptake rates of methane and sulfide of 742 and 4596.5 µmol g^{-1} gill dry wt d^{-1} (I. Martins personal comm.). According to Martins et al. (2008), maximum uptakes rates could only be reached by the largest mussel specimen (≥110 mm SL), and with CH_4 and H_2S concentrations about three times higher than those estimated within the Menez Gwen habitats. Therefore, in order to constrain our estimations, we chose ranges of uptake values that are representative of the majority of the mussel population, and do not consider under-represented extreme values (low and high).

4.4.5 Estimations of focused fluid flow rates

Focused fluid flow rates at Menez were estimated from the mosaics, the dive videos, and published estimations of fluid velocities (Sarrazin et al. 2009). Indeed, the imagery data gave a reasonable overview of the number and distribution of discrete fluid flow outputs at each site. At some of them, mainly with chimney structures, hot fluid vigorously discharged in the form of a distinct plume clearly visible on the images. However, in most cases we could neither visualize the contours nor estimate the basal diameters of the plumes of venting fluids. Moreover, observations showed that the height of the chimneys could not be used as a proxy for plume size. Therefore we were not able to assess the relative strength of focused discharges between sites. Nevertheless, based on our observations of high definition dive videos, we could conclude that a diameter of 2 cm is a likely low estimate of the average plume diameter. We arbitrarily chose this value for our calculations of fluid flow rates.

Unfortunately fluid flow velocity measurements do not exist for the Menez Gwen system. Published fluid velocity measurements in other hydrothermal systems give broad ranges of values: velocities range from 100 to 6200 mm/s in discrete sources and from 1.1 to 150 mm/s in diffuse sources (Sarrazin et al. 2009). We chose the low range limit velocity of 100 mm/s for discrete sources in our estimations of minimum fluid flows. Therefore, and assuming that

discrete outflows are circular, an average focused source is likely to yield a minimum of 991.4 $m^3 yr^{-1}$.

The values chosen for plume diameters and fluid velocities are aimed at providing a low range estimation of focused fluid flow rates. Furthermore, considering that some discrete fluid outflows may not have been spotted, final fluid flow estimates are likely to be underestimated.

4.5 Results

4.5.1 Visual and geophysical site descriptions

The high-resolution bathymetry data gathered during cruises POS402 and M82/3 in 2010 showed that the inner volcano is bisected by a fracture in a SW-NE direction similar to that of the graben (Figure 4.2a-b). According to visual exploration, several additional N-NE striking fractures across the eastern summit of the volcano, with few steep, meter-high slopes covered with broken pillow tubes. The dive videos also disclosed an inner volcano mostly covered by sediment-free pillow lavas (Figure 4.3a) likely resulting from recent volcanic events, while the grabens mainly are filled with talus material. These fractures suggest apparently that the topography in this area was shaped by a combination of volcanic and tectonic events. Furthermore, such fractures are likely to provide preferential pathways for the hydrothermal fluids.

Some parts of the eastern side of the young volcano, and particularly in the close vicinity of the sites of hydrothermal activity, are dominated by talus of broken pillows and areas of breccia. In general, the pillows were not or only sparsely covered by sediment; except at the sites of active venting, which were covered by sandy material.

The five sites investigated in the study are grouped spatially into two clusters (Figure 4.2c). The first cluster comprises Woody, Atos 10, and White Flames (Figures 4.4-4.6). This cluster also includes some minor sites of active venting, in particular between White Flames and Woody (Figure 4.3b). The alignment of some of these sites suggests that hydrothermal activity in this area is structurally controlled. The second cluster, which includes the sites Marker 4 and Cage Site, is located about 50 meters to the southwest and closer to the summit of the volcano (Figures 4.7-4.8). Mosaics were constructed for all five sites, and the full resolution GeoTIFF files of the corresponding geo-referenced mosaics are given as electronic supplements.

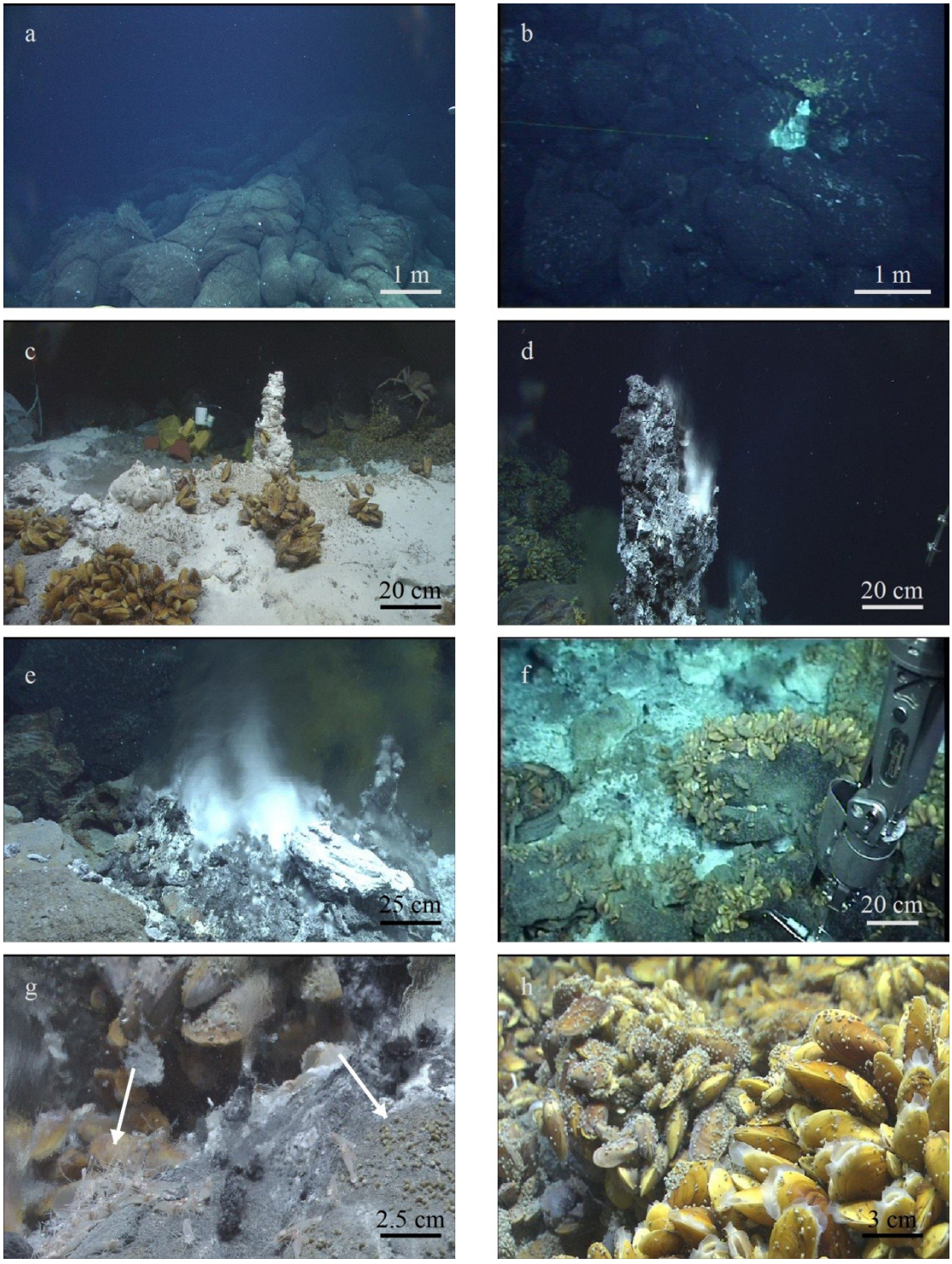

Figure 4.3: Seafloor images taken by ROV Quest (courtesy Marum). For all images scale bars apply to the foreground. (a) Pillow lava (dive 281); (b) unnamed mini-site of venting activity halfway between Woody and White Flames (dive 286); (c) center of the main mound at Woody covered with anhydrite precipitates; the chimney structure showed no active venting; the greyish speckle around the bottom of the chimney is caused by a high abundance of gastropods (dive 293); (d, e) chimney structure and hydrothermal fluid close to boiling point at the top of White Flames (dive 276); (f) basaltic rock covered with mussels on the side facing the hot fluid chimney, and bare on the opposite side (dive 295); (g) swarm of shrimps and gastropods on rocks around hot fluid emissions (dive 289); (h) *Bathymodiolus azoricus* with high (background) and low (foreground) gastropods abundance on their shells (dive 281).

Table 4.2: Characteristics of the sites and mussel covers.

Site	Approx. depth (m)	Area (m^2)	Discrete sources with chimneys	Discrete sources without chimney	Mussel cover (m^2)	Mussel cover (%)
Woody	829	69	1 (inactive?)	7	17	24.6
Atos 10	828	59	13	2	13.2	22.4
White Flames	835-850	199	43	4	29.1	14.6
Cage Site	813.5	100	16	7	12.3	12.3
Marker 4	812	20-30	?	?	-	-

4.5.1.1 Woody

The Woody site (Figure 4.4) is about 829 m deep and has a total area of 69 m² (Table 4.2). The site is composed of a main mound structure and two small areas of minor venting activity. The topography in this zone is dipping gently toward east to a break in slope and then flattening on the east of the site. The main mound is located in the slope and is characterized by an almost flat circular center dipping strongly down to the break in slope on its east side (Figure 4.4c). The break-in-slope could be the result of a normal fault running across the site in a north-south direction, and it is likely related to one of the larger fractures that cross the volcano. Based on the videos, the vertical displacement was estimated to less than two meters. Such a fault may provide preferred pathways for the hydrothermal fluids.

The main mound appeared devoid of boulders, and was covered by a sandy material and slabs and crusts. Its center was about 4.5 m in diameter and white precipitates covered large parts of it. The main chimney was about 50 cm high and was located on the center part. In contrast to the chimneys of the other study sites, the chimney at Woody did not seem recently active (Figure 4.3c). It was entirely white, likely due to anhydrite precipitates, and no vent fluid was observed coming out of the chimney during the cruise M82/3. The most active sites of fluid exit were observed around the chimney, from small fractures and from within the mussel patches.

Table 4.3: Minimum and maximum estimated mussel population, total biomass, and annual consumptions of methane and sulfide by *Bathymodiolus azoricus*; minimum estimates are based on the lowest limits of shell length (SL = 40 mm) and density (400 ind m^{-2}), whereas maximum estimates rely on the highest limits (SL = 80 mm, density = 700 ind m^{-2}).

Site	Population size (ind)	Total biomass (kg wet wt)	CH_4 uptake by *B. azoricus* (mol yr^{-1})	H_2S uptake by *B. azoricus* (mol yr^{-1})
Woody	6800 – 11900	12.1 – 90	15 – 418	91 – 2626
Atos 10	5280 – 9240	9.4 – 69.9	11 – 324	70 – 2039
White Flames	11640 – 20370	20.7 – 154.1	25 – 715	155 – 4494
Cage Site	4920 – 8610	8.7 – 65.1	11 – 302	66 – 1890
Total	28640 - 50120	50.9 – 379.1	62 - 1759	382 - 11059

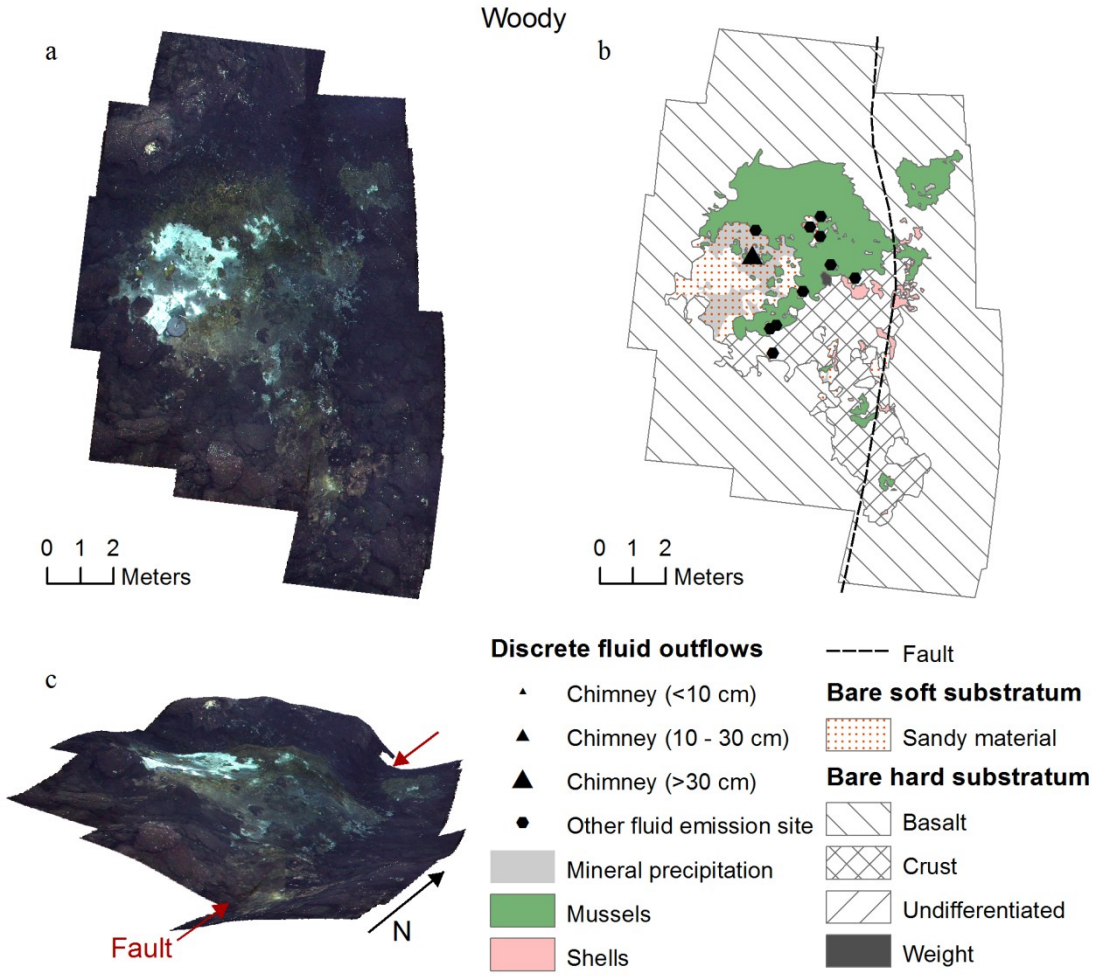

Figure 4.4: Representations of the Woody hydrothermal vent site: (a) photo-mosaic, (b) schematic, (c) three-dimensional representation; the relative dimensions of the 3D view are not to scale. The main chimney represented on the schematic was inactive at the time of the cruise M82/3. 'Other fluid emission site' refers to sites where localized emission of hot fluid was observed, but without a chimney structure. This site is characterized by a break-in-slope in the topography, likely related to a fault.

Bivalves were present in thick layers and they were mostly restricted to hard surfaces. Nevertheless, they did not cover every rock surface that surrounded the main mound; pillows on the western and southwestern sides were entirely bare, and rocky surfaces on the northeastern side supported most of the bivalve population (Figure 4.4a-c). In terms of surface, almost 25% of the total area was covered by mussels (Table 4.2). The maximum distance between the mussel beds and the hot fluid exits did not exceed 2.5 m. According to our estimations, the mussel population and total biomass at Woody range from 6800 to 11,900 ind. and from 12.1 to 90 kg wet wt respectively (Table 4.3).

The smaller active emission sites were located at 6 and 8 m from the center of the main mound. Both were very close to the break-in-slope and slightly off on its eastern side. They were characterized by a very small center covered with white precipitates surrounded by mussels *B. azoricus*. Sandy cover was not visible.

4.5.1.2 Atos 10

Atos 10 is located at a depth of 828 m, covered an area of 59 m² (Table 4.2), and is composed of a major eastern site and a minor western site, about 5 meters apart (Figure 4.5a-c). Experiments and colonization cages had been deployed at Atos 10 during the French/Portuguese/British Atos cruise in 2001 and earlier French/Portuguese research cruises (Dixon et al. 2001, Sarradin et al. 2001). The site was clearly identified by the presence of old mooring weights.

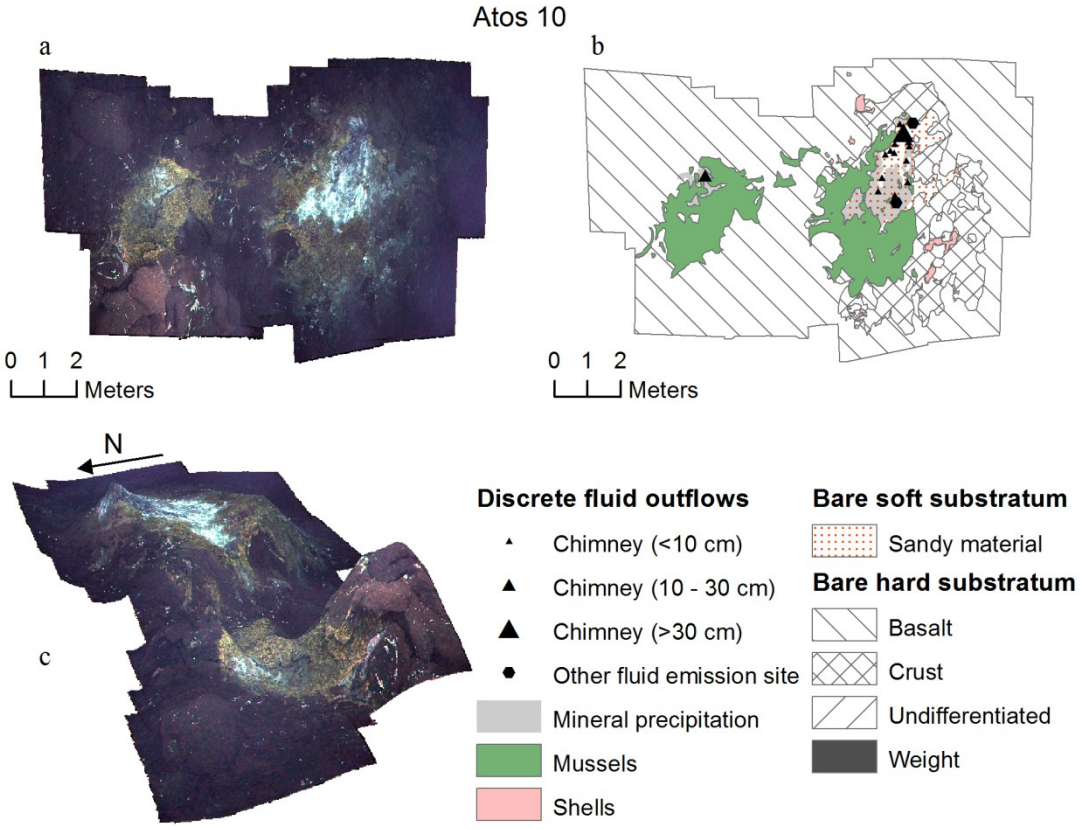

Figure 4.5: Representations of the Atos 10 hydrothermal vent site: (a) photo-mosaic, (b) schematic, (c) three-dimensional representation; for detailed explanations, see caption of Figure 4.4. Atos 10 is composed of two sites; the eastern site is characterized by a mound of sandy material, covered with abundant white precipitates and with focused outflows. The western site is devoid of soft sediments and developed around a single chimney; Mussels are abundant at both sites.

The major eastern site formed a circular mound of about 4 m in diameter, slightly elevated compared to the surrounding ground, and devoid of large pillows (Figure 4.5c). The central part was largely covered by white precipitates and scattered with 13 chimneys, most of them very small (less than 5 cm). One chimney on the northern edge of the mound was significantly larger, reaching up to about 50 cm in height.

Bathymodiolus azoricus covered the rim of the main mound, and the abundance of this species increased with the distance to the chimneys and to the main area of hot fluid

emission. The largest and thickest cover of bivalves was observed in the south and southwestern edges of the mound (Figure 4.5b). In total, this bivalve covered 22.4% of the total area of the Atos 10 site (Table 4.2).

The western site has developed only a location of fluid emission and did not form a mound. It consisted of a single 15-20 cm high chimney, which has grown between basaltic pillows. Sandy or crusty material was absent. White precipitates were visible on the pillows in the close vicinity of the chimney, over an area of about 0.5 m². Surrounding rocks were densely covered by *B. azoricus* over an area of about 6 m².

Bivalve aggregations at Atos 10 were never observed farther than 3.2 m from the hot fluid exits. According to our estimations, mussel population and total biomass at Atos 10 range from 5280 to 9240 ind. and from 9.4 to 69.9 kg wet wt respectively (Table 4.3).

4.5.1.3 White Flames

White Flames (Figure 4.6) is located about 20 meters to the west of Woody and it is the largest of the Menez Gwen sites investigated during the M82/3 cruise, with an area of 199 m^2 (Table 4.2). This site was characterized by several chimneys of various sizes (5 cm to 1 m high) expelling hot fluids and gas bubbles that are considered to represent the gaseous phase separated by subsurface boiling. These emissions brightly reflected ROV lights and gave the impression of burning flares (Figure 4.3d-e). The site extended over 25 meters in a west to east direction, and had an approximate width of 6 meters. The elevation decreased regularly from west to east with a relatively strong gradient (Figure 4.6c). The difference in altitude was estimated from the navigation data of the ROV to be 15 m, which corresponded to a mean slope gradient of 60% between the western/top and eastern/bottom ends of the site.

The highest chimney (about 0.8-1 m high) was located at a depth of 835 m and marked the western and top end of White Flames. More chimneys were observed downslope towards east. Their numbers and sizes decreased in a downslope direction. The site was mostly covered by sands and gravels with a few pillows of basalt. Barite-rich crusts were also visible. White mineral precipitates indicating diffuse fluid flow were present in many places around the chimneys and towards the bottom of the site (Figure 4.6a-b).

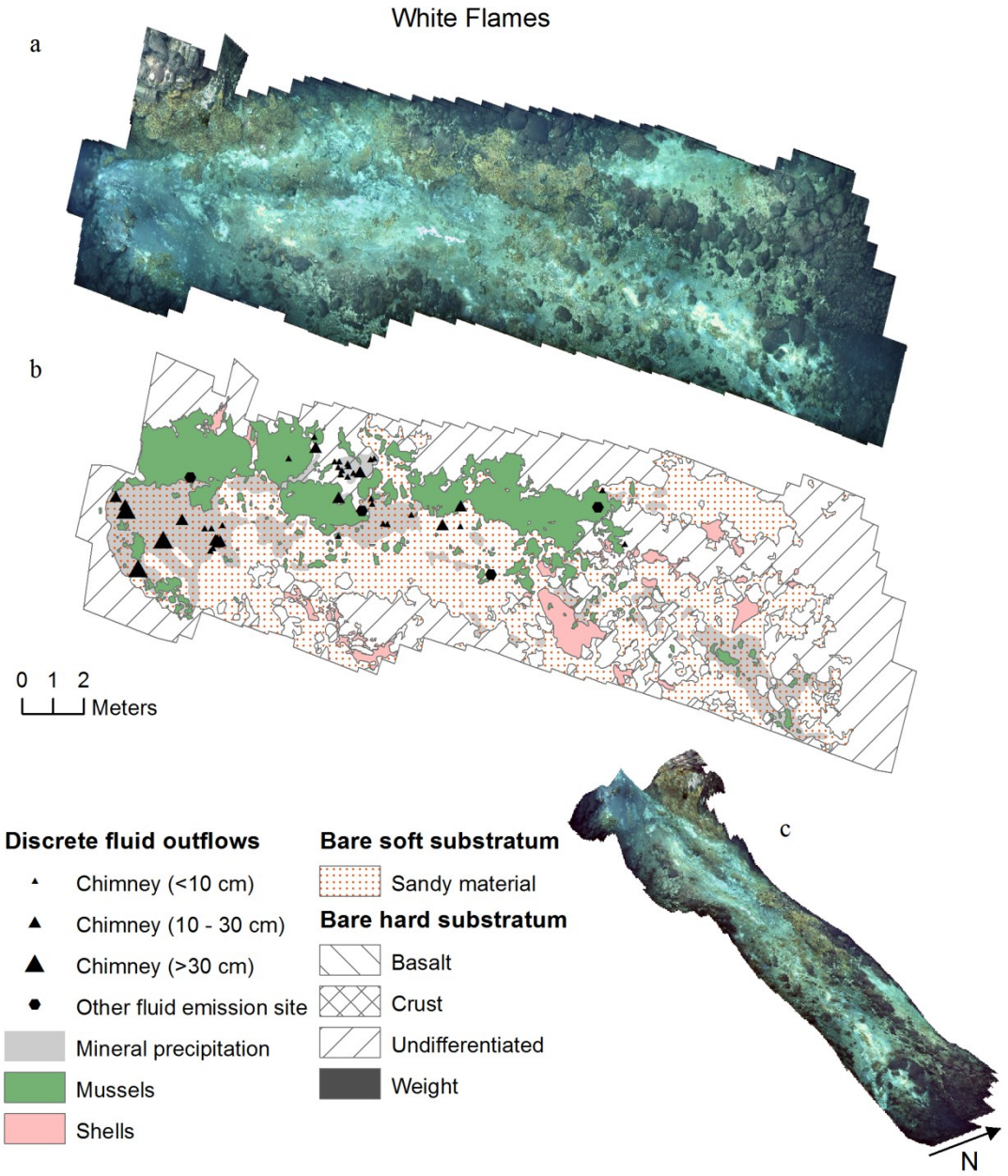

Figure 4.6: Representations of the White Flames hydrothermal vent site: (a) photo-mosaic, (b) schematic, (c) three-dimensional representation; for detailed explanations, see caption of Figure 4.4. The White Flames site developed along a steep slope and is topped by high chimneys; sandy material and white mineral precipitates are abundant; mussels are mostly distributed on basaltic boulders along the northern side of the site.

Bivalves covered 14.6% of the White flames area and this coverage was low compared to the other sites in the same cluster. (Table 4.2, Figure 4.6b). The bivalve distribution did not extend to all zones where diffuse fluid was expected to occur, and seemed limited to hard substrates, such as basaltic pillows and crusts that were in the upper two-thirds of the slope. In this area, the northern side of the site was bordered by large basaltic structures that grew larger and higher nearer the top of the site, thus creating jagged vertical surfaces that overlooked the main areas of hot fluid emission. Those structures were heavily covered by bivalves and,

based on the mosaics, represented more than 90% of the total bivalve cover at White Flames. The main aggregations of mussels were constantly observed within 2.8 m from a hot fluid exit. According to our estimations, mussel population and total biomass at White Flames range from 11,640 to 20,370 ind. and from 20.7 to 154.1 kg wet wt respectively (Table 4.3).

4.5.1.4 Marker 4

Marker 4, located in 812 m water depth, is the smallest of the five investigated sites (Table 4.2). The mosaics of Marker 4 were composed of images from the forward-looking cameras. They were strongly impacted by perspective distortion and GIS geo-referencing was therefore not possible (Figure 4.7). The size of the site was assessed at 20 – 30 m² from navigation data.

Hot fluid was emitted from small chimneys at the top of the site. From that point, a stripe of white hydrothermal deposits extended over about 4 meters down-slope towards the east. The slopes were partly covered by sandy deposits, and slabs of crusts were visible that stuck out around the top of the site. Iron oxides could be seen over the surrounding rocks.

This site harbored only a few mussels scattered individually or in patches of less than 20 animals over the white deposits. Their abundance was negligible compared to the other sites.

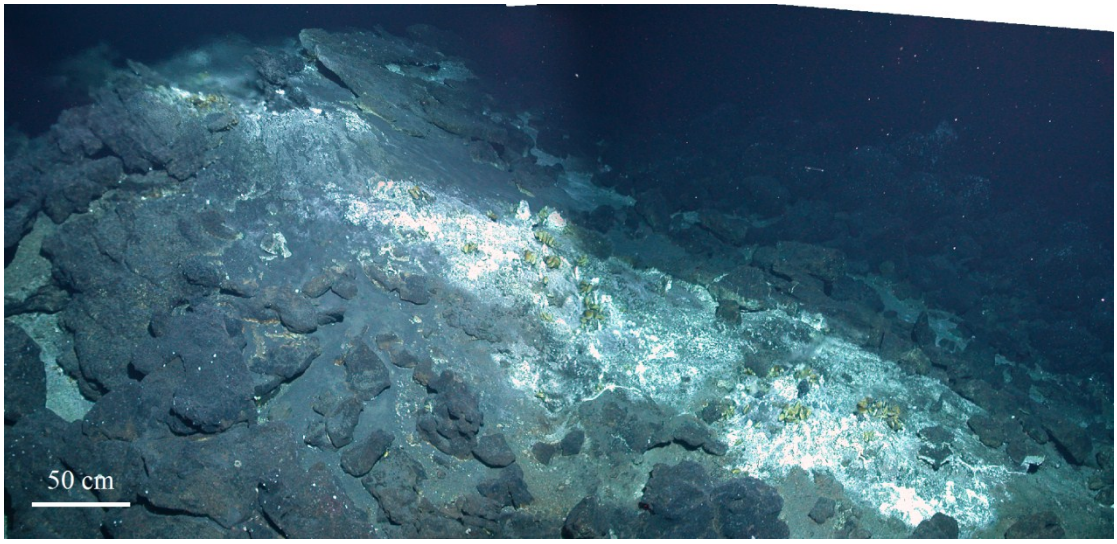

Figure 4.7: Photo-mosaic of Marker 4; Active venting occurs at the top of the site (indicated by blurry water). Downslope from there white precipitates form a 4 m-long and 1 m-wide stripe. Mussels are present in small aggregations (<20 ind) mostly located on the white precipitates.

4.5.1.5 Cage Site

Cage Site (Figure 4.8a) is located at 813.5 m water depth and covers 100 m² (Table 4.2). It was used for mooring deployments during earlier cruises, and was easily identified from remaining ground weights.

This site consisted mainly of a single W-NW dipping oval mound (9-9.5 m diam.) that was protruding slightly from the surrounding basaltic pillows. A few basaltic pillows were scattered

on the higher part, in the southeastern corner of the mound, while the rest was covered by sandy material and slabs of barite-rich crust. Located south-east of the mound center was a large (4 m^2) depression, less than 1 m deep and covered by soft sediments. On the western side the sediment cover extended up to 2 m away from the edge of the mound (Figure 4.8b-c).

White precipitates related to fluid flow were unevenly distributed on the mound surface. The most intense venting occurred on the highest part of the site. In this area, hot fluid was emitted from several chimneys, which were all located within an 8-m² large area of high mineral precipitation. In other areas of high mineral precipitation, hot fluid emission was only observed from fractures or from under slabs of barite (Figure 4.8b).

Bathymodiolus azoricus were concentrated within 2.8 m of hot fluid exits and covered about 12% of the site area (Table 4.2). Mussels settled predominantly on rock surfaces that were orientated towards the fluid emissions while the central depression was almost bare of bivalves (Figure 4.3f). Mussel patch sizes ranged from dense aggregations of hundreds of *B. azoricus* to single individuals. According to our estimations, mussel population and total biomass at Cage Site range from 4920 to 8610 ind. and from 8.7 to 65.1 kg wet wt respectively (Table 4.3).

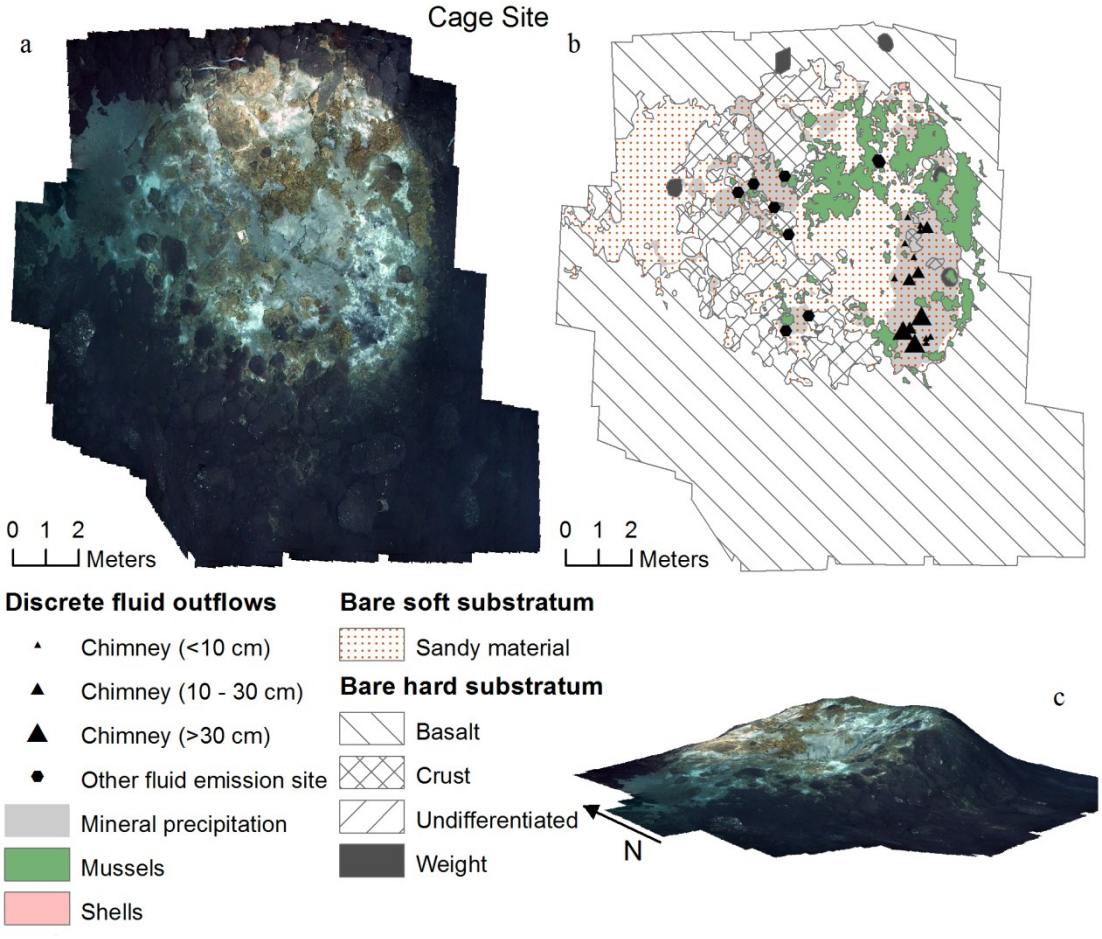

Figure 4.8: Representations of the Cage Site hydrothermal vent site: (a) photo-mosaic, (b)

schematic, (c) three-dimensional representation; for detailed explanations, see caption of Figure 4.4. Cage Site is a single W-NW dipping oval mound covered by sandy material and slabs of barite-rich crusts. The site is characterized by the presence of a depression (4 m^2) near its center. East of the depression is the most active area, as indicated by the presence of chimneys and abundant white precipitates.

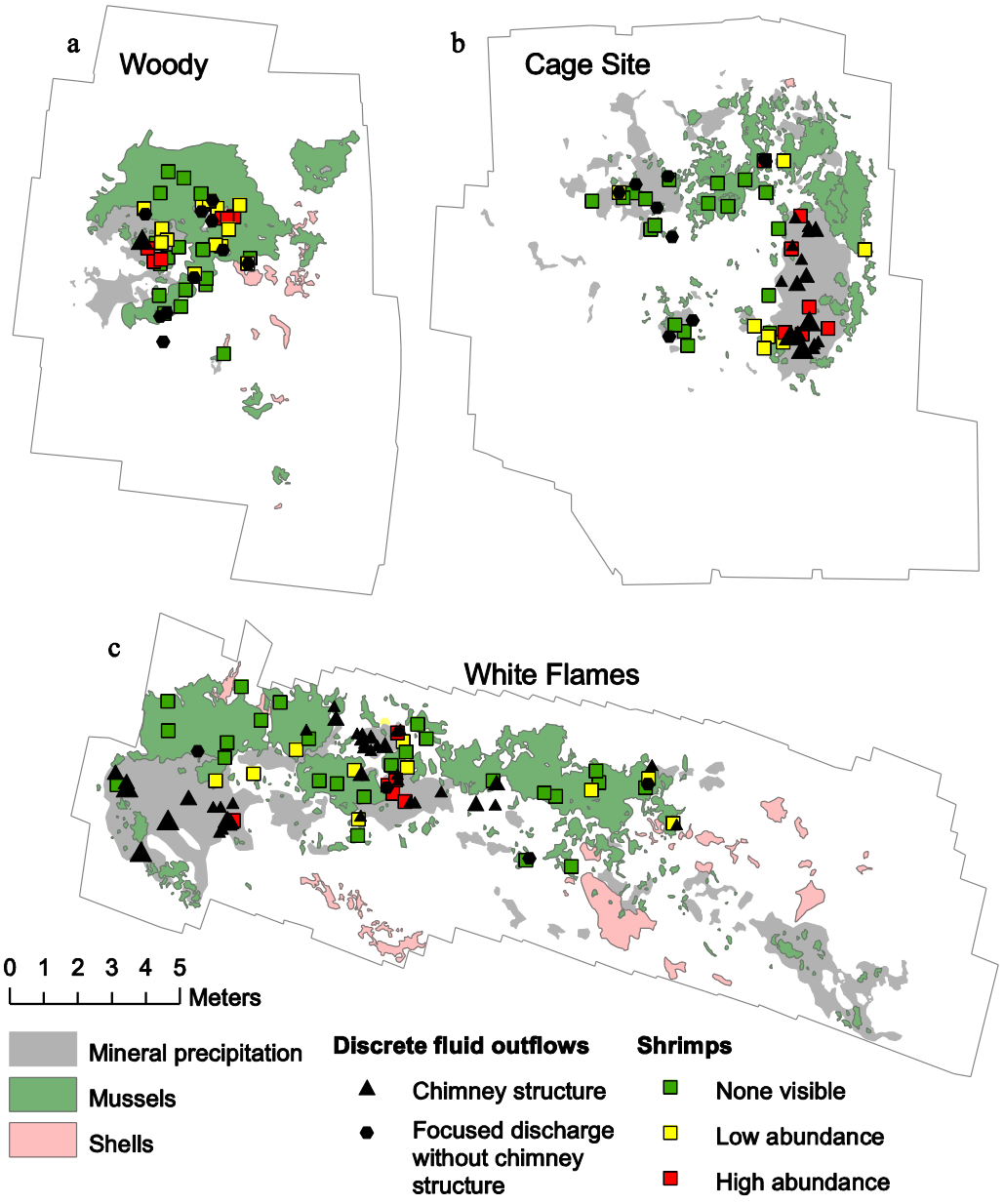

Figure 4.9: Shrimp distribution at (a) Woody, (b) Cage Site and (c) White Flames. The shrimp distribution pattern is similar at all sites, and shows a strong correlation with the presence of focused fluid outflows; high shrimp abundance occurs within 1 m of hot fluid outflows.

4.5.2 Occurrences of other fauna visible on video materials

Shrimps usually occurred at all sites around fluid emission and occasionally also in mussel beds. High shrimp densities (>10 ind. m^{-2}) were always related to hot fluid discharge and

occurred within a radius of 1 m around the fluid source during all observations (Figures 4.9, 4.10). Animals were concentrated in dense swarms in close proximity to single hot fluid emissions (Figure 4.3g) or spread more evenly over larger areas with several smaller point sources. These swarms were located next to hot fluid emissions at all sites (Figures 4.9, 4.10) and were particularly common nearby some chimneys of White Flames. However, shrimps were not present at each hot discharge locations; for instance, shrimps were not observed close to the larger chimneys at the top of White Flames. At Cage Site and Woody, the shrimp spread over larger areas where hot fluids were emitted from several small sources.

Gastropods were observed at all sites on mussel shells and hard rock surfaces (Figure 4.3h). While close-up photos revealed that they were also present on soft substrates, they were not reliably discernible on the mosaic images because the contrast resolution was not sufficient. Gastropods were patchily distributed. Dense aggregations were observed on rocks and mussel shells next to hot fluid emissions and along the path of the hot fluid flows (Figures 4.10, 4.11). Only a few centimeters to decimeters away, the density of gastropods dropped sharply. Videos showed that gastropods were constantly moving and that their distribution pattern was thereby very dynamic.

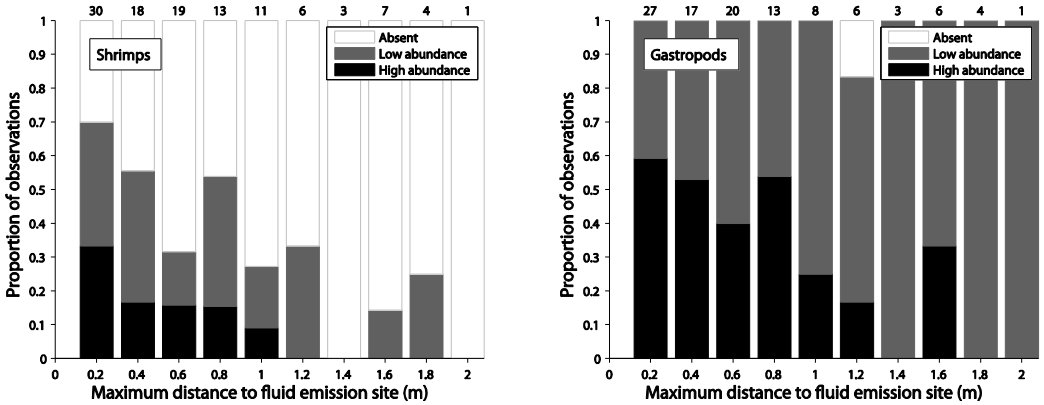

Figure 4.10: Variation of the abundance of shrimps (left) and gastropods (right) with the distance to the closest hot fluid exit; the values above the bars represent on the left plot the total amount of observations of abundance.

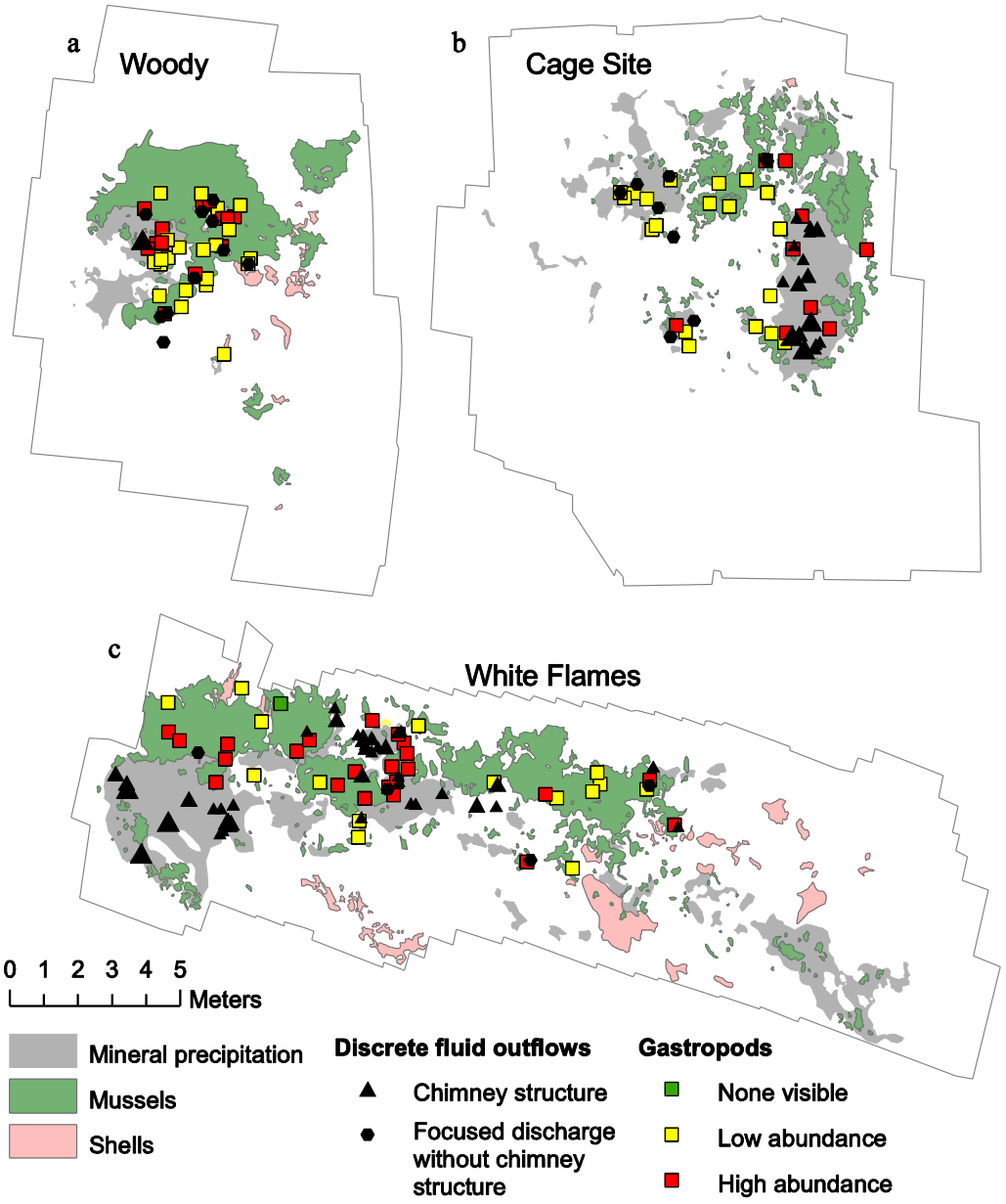

Figure 4.11: Gastropod abundance at (a) Woody, (b) Cage Site and (c) White Flames. The gastropod distribution pattern is similar at all sites, and is related to the presence of fluid flow; dive videos showed that the gastropod abundance drops sharply a few centimeters only away from the distance to hot fluid (see text).

4.6 Discussion

4.6.1 Mosaics for site identification

Hydrothermal activity at Menez Gwen has been described at two areas on the southern and eastern flanks of the inner volcano (Charlou et al. 2000, Desbruyères et al. 2001). The sites studied in this work correspond to the active vent area on the eastern flank that is referred to as marker PP30/31 in the literature (Desbruyères et al. 2001, Riou et al. 2010), but we were

not able to unequivocally relocate this site. Therefore our investigation sites may not be identical to the originally described marker positions, but it is also possible that the original markers were not anymore in place. Clear identification of bottom weights at Atos 10 and Cage Site that had been left from cage moorings deposited during the Atos cruise in 2001 indicated that these sites were identical to locations of earlier work.

In total, five sites were found on the eastern flank, and a mosaic was built for each of them. The area was intensively investigated during twenty dives and it is unlikely that other major sites were missed in the close vicinity.

We used USBL navigation which is known to suffer from temporary inaccuracies of up to tens of meters offset from the real positions. However, occasional outliers in our navigation data were leveled for a total of 20 dives at the investigation sites to guarantee reliable navigation data. The mosaics presented here provide an additional basis for future identification of the vent sites on the eastern flank of the young Menez Gwen volcano, and this information will compensate for possible inaccuracies of underwater navigation.

A loss of quality is commonly introduced during the mosaicking process. Indeed, where adjacent frames overlap, images are seamlessly blended together (Pizarro & Singh 2003). However, small registration errors may occur, which can cause some fuzziness in parts of the mosaics. The schematics of the sites (Figures 4.4b, 4.5b, 4.6b, 4.8b) compensate for this loss of quality by showing the most important features of each site.

4.6.2 Faunal distribution

Mussels preferentially settled on rock surfaces and they were rarely placed on hydrothermal deposits. This is in accordance with previous observations around the marker sites PP10/F11 on the southern volcano flank and PP32/33 on the eastern flank (Desbruyères et al. 2001). The mussels predominantly concentrated on rock surfaces exposed to the vent fluid flow. This was particularly obvious at Cage Site where only rock surfaces facing fluid emanations were densely covered by mussels while other surfaces of the same rocks were entirely bare of mussels (Figures 4.3f, 4.8b). The distribution of the bivalves was therefore highly controlled by site morphologies and exposure of rock surfaces to fluid flow. However, *B. azoricus* avoided close contact with focused vent fluids and were scarcely present in the immediate vicinity of the focused fluid discharge. Maximum distances between mussel aggregations and hot fluid exits ranged between 2.5 and 3.2 m. This matched earlier observations at the Eiffel Tower edifice in Lucky Strike where *B. azoricus* always kept a distance of at least 25 cm from hot fluid exits, and where mussel beds and clumps were never observed farther than about 3 m from black smokers (Cuvelier et al. 2009).

Conversely, shrimps occurred mostly within the hot fluid and in the very close vicinity of the emission sites. High abundances of shrimps were never observed farther than in 1 m distance from a fluid exit point. This is comparable to earlier observations at Lucky Strike. There, swarms of shrimps occurred within 1.25 m distance to black smokers and 50 cm distance to

flanges and diffusion zones (Cuvelier et al. 2009).

Shrimp species could not be identified from the images. However, *Chorocaris chacei*, *Mirocaris fortunata*, and *Alvinocaris* sp.aff. *stactophila* have been found in Menez Gwen before (Colaço et al. 1998, Gebruk et al. 2000b). All of them have different feeding behaviors (Gebruk et al. 2000b, Ramirez Llodra et al. 2000) and this certainly controls their distribution. *C. chacei* and *M. fortunata* have been observed on chimney walls in Lucky Strike before (Gebruk et al. 2000b, Cuvelier et al. 2009) and it is very likely that both species existed also among the shrimps we detected next to hot fluid discharge. *C. chacei* scavenges and also carries episymbiotic micro-organisms which are considered chemoautotrophic and most likely add to the nutrition of their hosts (Gebruk et al. 2000b, Ramirez Llodra et al. 2000). Therefore, it is reasonable that *C. chacei* aggregated next to hot fluids in Menez Gwen where the chemosynthetic bacteria should have good access to diluted sulfide. *M. fortunata* grazes on bacteria on sulfide surfaces and also feeds on detritus and fecal deposits of *Bathymodiolus* (Gebruk et al. 2000b, Ramirez Llodra et al. 2000). Accordingly, we may have observed this species among the dense shrimp aggregates around hot fluid discharge sites and also among the scattered shrimp individuals in the mussel beds. The feeding habits of *A.* sp. aff. *stactophila* are unknown, but *Alvinocaris* species in general are predators and opportunistic feeders and they are often observed at the peripheries of vent communities (Gebruk et al. 2000b). Hence, we assume that *Alvinocaris* sp. aff. *stactophila* were existent among the shrimps in the mussel beds.

4.6.3 *B. azoricus* area calculations

Bathymodiolus coverage was estimated at each site by delineating each individual patch of bivalves into a GIS. The smallest areas of mussel coverage were measured at Cage site and Atos 10, with respectively 12.3 m^2 and 13.2 m^2, while the largest coverage areas occurred at Woody with 17 m^2 and at White Flames with 29.1 m^2.

From those data, it is not clear whether the extent of the mussel coverage is correlated to the size of the sites (Table 4.2). Data from Atos 10, Woody and White Flames suggest that larger sites host a larger mussel population. However, data from Cage Site, the second largest of the studied sites, suggest otherwise. The comparatively low mussel coverage of Cage Site could be related to a different fluid chemistry than at Atos 10, Woody and White Flames. Although we do not have fluid chemistry data to support this hypothesis, we know that Cage Site and Marker 4 are located in a different cluster than the other sites (Figure 4.2c). Barreyre et al. (2012) proposed that the spatial distribution of active sites at Lucky Strike may reflect “the geometry of the underlying plumbing system”. Such interpretation implies that the larger the distance between outflows, the greater the differences in fluid composition. This would support the hypothesis that the fluid chemistry may be different between the two clusters described in this study.

Likewise, we could not correlate mussel coverage and fluid flow intensity from our data.

Although the imagery data gave a reasonable view of the distribution (Figures 4.4-4.6, 4.8) and amount (Table 4.2) of focused outflows at each site, it did not allow assessing the size of focused outflows reliably enough to compare fluid flow intensity between sites. Moreover, it appears that the number of discrete outflows alone may not be representative of the strength of fluid flow. Indeed, Woody, the second largest site in terms of mussel cover, has fewer discrete outflows than Atos 10, Cage Site, and White Flames.

Similarly, zones of diffuse fluids could not be defined and, therefore, a comparison of diffuse fluid occurrence between sites could not be done. Indeed, the main indicators for diffuse fluid flow that can be observed on imagery data of hydrothermal vents are bacterial mats and anhydrite precipitates (Barreyre et al. 2012). However, bacterial mats were rarely observed at the Menez Gwen sites, and diffuse fluid-related precipitates could not, in most cases, be unequivocally distinguished from precipitates related to focused fluid flow.

It is difficult to compare our estimations of mussel coverage to other hydrothermal vents because calculations of mussel coverage area are rarely available. An exception is the Logatchev hydrothermal vent field where *Bathymodiolus puteoserpentis* forms a large and continuous mussel bed of at least 100 m^2 at the base of the Irina-2 sulfide mound (Gebruk et al. 2000a). However, the extension of the Irina-2 mussel bed at Logatchev is controlled by the special underlying local geology. Logatchev is an ultramafic system characterized by serpentinization processes. The Irina-2 mussel bed is situated on silicified crusts that are underlain by sulfide fragments and chalcopyrite sand grading into serpentinite mud (Petersen et al. 2009). This incoherent underlying material provides many conduits for rising hydrothermal fluids that mix in the subsurface with entrained bottom water and exit the silicified crusts via many diffuse outlets spread over a large area (Petersen et al. 2009). Conversely, Menez Gwen is a basaltic-hosted system in which subsurface fluid conduits are controlled by basaltic rock. Fluid discharge is much more focused and colonization of mussels is predominantly confined to rock surfaces next to this focused discharge.

Other values of *Bathymodiolus* bottom coverage are available for two 50.3-m^2 and 40-m^2 large mosaics of diffuse flow areas at vents in the Eastern Lau Spreading Center of the western Pacific (Podowski et al. 2009). Here, the given values of site areas correspond to the mosaic areas. The dimensions of the actual sites of diffuse flow are not known and are potentially larger, thus, percentages of cover cannot be determined. However, the mussel *Bathymodiolus brevior* alone covered bottom areas of 3.8 m^2 and 0.72 m^2 and it is believed to be in competition with the provannid snail Ifremeria nautilei over additional areas of 3.8 m^2 and 0.6 m^2 (Podowski et al. 2009). The relation of the values to the size of the study areas is similar to this relation at Menez Gwen.

4.6.4 *B. azoricus* biomass estimations

Based on our measured values of mussel coverage (Table 4.2), population assessments (Table 4.3) ranged from about 4900 to 8600 ind at Cage Site (the least populated site) and

from 11,600 to more than 20,000 ind at White Flames (the most populated site). The smallest biomass values were calculated for Cage Site with between 9 and 65 kg wet wt, and the largest for White Flames with between 21 and more than 154 kg wet wt.

These are the first estimations of total mussel biomass on entire hydrothermal vent sites, while all other published values use the standardized unit kg m^{-2}. In the absence of data about the size of the mussel beds at the other sites, the total biomasses cannot be compared.

Published data for mussel biomass at hydrothermal vents or hydrocarbon seeps are rare and most of them range from 2.2 to 10 kg m^{-2} (Table 4.4), while a single peak value of 43.4 kg m^{-2} has been reported from the Oasis vent field on the Southern East Pacific Rise (Sarrazin et al. 2006). Compared to these values, a mussel biomass of 0.71 to 5.3 kg m^{-2} at Menez Gwen appears low. Nevertheless, this range is in accordance with the biomass estimation for *B. azoricus* at Lucky Strike (3.5 kg m^{-2}) (Dover et al. 1996).

Table 4.4: Published biomass estimations of mussels at hydrothermal vent and cold seep systems.

Site	Biomass (wet weight)	Reference
Galapagos	10.1 kg m^{-2}	(Hessler & Smithey 1983)
Galapagos Ridge	2.2 kg m^{-2}	(Fustec et al. 1988)
EPR	44.5 kg m^{-2} (tubeworms/mussels)	(Desbruyères & Laubier 1991)
Lucky Strike	3.5 kg m^{-2}	(Dover et al. 1996)
Barbados Prism	5.4-9 kg m^{-2}	(Olu et al. 1996b)
Oasis vent, SEPR	43.4 kg m^{-2}	(Sarrazin et al. 2006)
Menez Gwen	0.71-5.3 kg m^{-2}	Assessed from Martins et al. (2008)

4.6.5 Methane and sulfide consumption by *B. azoricus*

Hydrothermal fluids at Menez Gwen are relatively enriched in dissolved gas (Charlou et al. 2000), some of which are partly consumed by *B. azoricus*. Indeed, *Bathymodiolus* species are characterized by a great abundance of symbionts in their gills and by depleted isotopic carbon signatures in their tissues, which indicates that *Bathymodiolus* species from hydrothermal vents and hydrocarbon seeps primarily rely on the chemosynthetic production of the symbionts (Le Pennec et al. 1990, Raulfs et al. 2004). *Bathymodiolus azoricus* harbor sulfur oxidizing and methane oxidizing symbionts in their gills which provide the host with metabolites from chemosynthetic oxidation of both volatiles present in the Menez Gwen hydrothermal fluids (Fiala-Médioni et al. 2002, Duperron et al. 2006). However, *Bathymodiolus* can filter feed (Page et al. 1990, Riou et al. 2010), and although the relative contribution of filter feeding to the nutrition of hosts has never been evaluated experimentally, recent modeling results suggest that particulate organic matter (POM) contributes to 48% to the nutrition of *B. azoricus* at Menez Gwen. Consequently, 52% of their nutrition is derived by

symbiotic chemosynthesis that is fueled by oxidation of sulfide and methane (Martins et al. 2008).

Based on our assumptions of chemical uptake rates by the mussels (Table 4.1) and the calculated population size (Table 4.3), we provided minimum and maximum estimations of the annual methane and sulfide consumption at each study site (Table 4.3). The minimum estimates were obtained by combining the low limit (40 mm) of shell lengths range given by Comtet & Desbruyères (1998) with the lowest published estimation of mussel density at Menez Gwen (400 ind m^{-2}) (Colaço et al. 1998). The maximum estimate was using the corresponding upper limits of shell length and mussel density (SL = 80 mm, density = 700 ind m^{-2}) (Colaço et al. 1998, Comtet & Desbruyères 1998). Therefore, the minimum and maximum scenarios provide very broad ranges for the estimated annual consumption of methane and sulfide by *B. azoricus*. Indeed, according to these calculations, the annual methane and sulfide consumption of population of *B. azoricus* at the study sites was estimated to range between 62 and 1760 mol CH_4 and between 382 and 11,060 mol H_2S. Such ranges reflect the uncertainties of our assumptions. Future measurements of mussel size distribution, density and chemical uptake rates should help constraining these estimates further.

The estimation method for uptake rates of methane and sulfide by *B. azoricus* (Martins et al. 2008) does not take into account the recent discovery that hydrogen also fuels endosymbiosis in *Bathymodiolus* mussels on the MAR (Petersen et al. 2011). With an average value of 38 µmol kg^{-1} the hydrogen concentration of Menez Gwen fluids is considered to be low in comparison to other vent systems (Charlou et al. 2000). This could imply that hydrogen consumption by mussels at Menez Gwen is low in comparison to sulfide and methane consumption.

Nevertheless, these are the first estimates of total consumption of methane and sulfide by *B. azoricus* over entire sites of active venting. Hence we cannot provide a comparison with similar estimations from other hydrothermal vent systems, but these values could serve for future comparisons with other sites.

4.6.6 Methane and sulfide effluxes

In order to put these estimations of chemical consumption by the mussel population into a broader perspective, we need to look at the chemical fluxes that are potentially released via venting. Previous estimations of chemical fluxes at Menez Gwen do not exist but can, within orders of magnitude, be estimated from published fluid data (Charlou et al. 2000) and estimations of fluid flow rates.

Hydrothermal fluids at Menez Gwen are relatively enriched in dissolved gas. For instance, mean end-member methane and sulfide concentrations were estimated at 1.7 mmol CH_4/kg and 1.6 mmol H_2S/kg (Charlou et al. 2000). Considering a mean fluid flow rate of 990 m^3 yr^{-1} per discrete outflow, each focused source could yield 1685 mol CH_4 yr^{-1} and 1586 mol H_2S yr^{-}

^{1}. Based on the number of discrete fluid discharges (Table 4.2), we estimate the total focused discharge in the area of study at 91,000 m^3 yr^{-1}. This corresponds to total annual releases of methane and sulfide via discrete venting of 155 × 10^3 mol CH_4 yr^{-1} and 146 × 10^3 mol H_2S yr^{-1}. These values are based on low limit estimations of fluid velocity and of mean plume diameter; hence, they likely underestimate the actual chemical fluxes.

These estimations suggest that methane and sulfide consumption by the mussel population represents a small fraction of fluxes potentially released from the system into the water column. Indeed, considering that 92 active discrete outflows were observed (Figures 4.4-4.6, 4.8, Table 4.2), the mussel consumption would represent up to 1.1 % of the methane and 7.6 % of the sulfide fluxes released via focused venting.

Areas of diffuse outflow were not easily identified from the imagery data and could not be quantified. Based on mosaics of Lucky Strike, Barreyre et al. (2012) suggest several types of diffuse flow-related features. Some of these, such as bacterial mats and patches of hydrothermal precipitates, occurred in the studied sites. However, bacterial mats were rarely observed at the Menez Gwen sites, and diffuse fluid-related precipitates could not, in most cases, be unequivocally distinguished from precipitates related to focused fluid flow. For these reasons, we diffuse flow rates could not be quantified for the entire sites. Nevertheless, available data allow estimating order of magnitude of diffuse chemical fluxes. According to Sarrazin et al. (2009), existing velocity measurements of diffuse fluids in hydrothermal systems range from 1.1 to 150 mm s^{-1} in diffuse sources. Therefore, using the low range limit value of 1 mm s^{-1}, diffuse chemical fluxes could be in the order of at least 54 × 10^3 mol CH_4 m^{-2} yr^{-1} and 50 × 10^3 mol H_2S m^{-2} yr^{-1}.

Based on these values of diffuse chemical fluxes, diffuse venting over a 1 m^2 area could meet respectively 30 and 4.5 times the total mussel consumption of methane and sulfide in the entire studied area.

A few values of methane fluxes within hydrothermal plumes have been published for other vent fields with similarly high end-member methane concentrations. All are at least 3 orders of magnitude higher than our estimations of methane fluxes at Menez Gwen. For instance, methane fluxes of about 132 × 10^6 mol yr^{-1} were estimated in the plume 200 m above the Endeavor vent field on the Juan de Fuca Ridge (Rosenberg et al. 1988). Similarly, published estimations of helium isotope ^{3}He flux and of the $CH_4/^3$He ratio at the Rainbow hydrothermal vent on the MAR allow calculating a methane flux of 50.8 × 10^6 mol yr^{-1} for a plume that includes all hot fluid flow emanating from a 100 × 200 m^2-large area (Jean-Baptiste et al. 2004). Furthermore, for the same plume, German et al. (2010) inferred a methane flux of 31.6 × 10^6 mol yr^{-1} by establishing a linear relationship between methane concentrations and "plume-particle" fluxes from optical backscatter anomalies. Finally, Keir et al. (2008) calculated methane fluxes at the solitary "Drachenschlund" black smoker vent in the "Nibelungen" hydrothermal vent field on the Southern MAR ranging from 1.8 × 10^6 mol yr^{-1} at the vent itself to 15.8 × 10^6 mol yr^{-1} in the horizontal plume. All these systems emit hot fluids

with high methane concentrations (Lilley et al. 1993, Charlou et al. 2002, Melchert et al. 2008) similarly to those measured at Menez Gwen (Charlou et al. 2000), even though their geological settings are different.

This could imply that the Menez Gwen sites are minor in terms of chemical release. However, our estimations of fluid flow and chemical fluxes were purposely low estimations, which were aimed at assessing the relative importance of chemical consumption by the mussel. Indeed, according to available fluid velocity measurements (Sarrazin et al. 2009), actual fluid flow rates and chemical fluxes at Menez Gwen could be higher than our estimations by more than an order of magnitude.

4.7 Conclusions

The zones of active venting have very limited extents and are mainly concentrated on the flanks of a mini-volcano close to the center of the Menez Gwen volcano.

The faunal distribution at the studied sites is very similar to that at the Eiffel Tower structure in the neighboring Lucky Strike vent field (Cuvelier et al. 2009). The fauna at the studied Menez Gwen sites is dense and largely dominated by *Bathymodiolus azoricus*. Patches of mussels are mostly distributed on hard substrata on the pathway of the hot fluid but preferentially away from the chimney flanks. Populations of more mobile taxa such as shrimps and gastropods are clearly denser in the vicinity of points of fluid emission. Nevertheless, this behavior was not observed at every point of venting activity. Good examples are the large chimneys at the top of White Flames site, where the venting fluid appears as if boiling.

Despite the small extent of the sites of active venting, mussel population amounts to thousands of individuals and estimates of the minimum total biomass over the sites of study sum up to hundreds of kilograms. The estimations of total annual consumption of methane and sulfide by B. azoricus can be significant, and respectively up to 1760 mol CH_4 yr^{-1} and 11,060 mol H_2S yr^{-1}. The chemical consumption seems nevertheless low in comparison to estimations of vent-scale hydrothermal methane and sulfide effluxes. However, this work considered the consumption by mussels only, and the total consumption by all symbiotic fauna may be more substantial. Nevertheless, B. azoricus was the dominant species at these sites and, therefore, the total consumption by the fauna is likely to be in the same order of magnitude.

Geo-referenced photo-mosaics and geographic information systems constitute efficient tools to observe the faunal distribution and are amongst the most accurate tools available for areal calculations in such remote environments. Estimating the total biomass of B. azoricus at every site was only possible with accurate estimates of the extent of the mussel patches. The photo-mosaics presented in this work are also aimed at giving a snapshot of the situation at Menez Gwen in 2010 and can serve for future works as basemaps for planning or site

recognition purposes. They also are a good basis to observe the temporal evolution of the venting and faunal activity.

4.8 Acknowledgements

We would like to thank Nicole Dubilier, chief scientist of M82/3 cruise, the captain and crew of RV Meteor, and the ROV Quest team. Also thanks to Elizabeth L. Podowski, Charles R. Fisher and Stephanie Lessard-Pilon.

This work was supported by the European Commission under the EU Framework 7 funded Marie Curie Initial Training Network (ITN) SENSEnet (contract nº237868), and funded through DFG Research Center / Excellence Cluster "The Ocean in the Earth System".

Chapter 5

Distribution and temporal evolution of mega-fauna at the Regab pockmark (Northern Congo Fan), based on a comparison of video-mosaics and GIS analyses

Yann Marcon[1], Heiko Sahling[1], Anne-Gaëlle Allais[2], Gerhard Bohrmann[1], Karine Olu[3]

[1] *MARUM – Center for Marine Environmental Sciences and Faculty of Geosciences, University of Bremen, Klagenfurterstr. 2, D-28359 Bremen, Germany*

[2] *IFREMER, Centre de Méditerranée, Département Infrastructures Marines et Numériques, La Seyne sur Mer, France*

[3] *IFREMER, Centre de Bretagne, Département Études des Écosystèmes Profonds (DEEP), Plouzané, France*

MANUSCRIPT 3

In review at *Marine Ecology*.

5.1 Abstract

The Regab pockmark is a large cold seep area located 10-km north of the Congo deep sea channel at about 3160 m water depth. The associated ecosystem hosts abundant fauna, dominated by chemosynthetic species such as the mussel *Bathymodiolus* aff. *boomerang*, siboglinid polychaetes *Escarpia southwardae*, and vesicomyid clams *Laubiericoncha chuni* and *Christineconcha regab*. The pockmark was visited during the West African Cold Seeps (WACS) cruise with RV Pourquoi Pas? in February 2011, and a 14,000 m^2-large high-resolution video-mosaic was constructed to map the most populated area and to describe the distribution of dominant megafaunal species. The results are compared to previous published works, which also included a video-mosaic in the same area of the pockmark, based on images of the Biozaire cruise, in 2001. The 10-year evolution of the faunal distribution is described and reveals that the abundance and distribution of the dominant megafaunal populations at Regab did not change significantly, suggesting that the overall methane and sulfide fluxes that reach the faunal communities have been stable. Nevertheless, small and localized distribution changes in the clam community indicate that it is exposed to more transient fluxes than the other communities. Observations suggest that the main megafaunal aggregations at Regab are distributed around focused zones of high flux of methane–enriched fluids likely related to distinct smaller pockmark structures that compose the larger Regab pockmark. The results are generally consistent with the existing successional models for seep communities. However, we observe that the distribution of the Regab mussel population does not entirely fit into these models of successions, and we hypothesize that the mussel distribution at Regab could also be controlled by the occurrence of zones of both intense methane fluxes and reduced efficiency of the anaerobic oxidation of methane.

Keywords: temporal evolution, pockmark, cold seep, Regab, mosaic, fauna.

5.2 Introduction

Cold-seep ecosystems have been identified along active and passive margins worldwide, and are known to host rich and abundant chemosynthetic communities (Sibuet & Olu-Le Roy 2002). Many studies have described the distribution of the dominant faunal assemblages in relation to their environment in several cold seeps systems (Sibuet & Olu-Le Roy 2002, MacDonald et al. 2003, Olu-Le Roy et al. 2007a, Jerosch et al. 2007b, Lessard-Pilon et al. 2010b), and cold seeps are usually considered to provide more stable environments than hydrothermal vents. Indeed, numerous studies of temporal evolution of vent communities suggested that hydrothermal vents are highly dynamic environments (Hessler et al. 1988, Shanks 1995, Shank et al. 1998, Mullineaux et al. 2000, Cuvelier et al. 2011), whereas observations of individual taxonomic groups at cold seeps revealed very slow growth rates and extremely long lifetimes likely related to slow and steady fluxes of reduced compounds (Nix et al. 1995, Fisher et al. 1997, Smith et al. 2000, Bergquist et al. 2000). For instance, some tubeworm aggregations were estimated to be at least 250 years old (Fisher et al. 1997, Bergquist et al. 2000), and ages of several hundreds of years have been assessed for *Bathymodiolus childressi* (Smith et al. 2000).

Up to now, very few works focused on the temporal evolution of the faunal distribution (Lessard-Pilon et al. 2010b) in a cold seep environment. Such information is yet not only important to increase our knowledge about the community dynamics, but it also allows better understanding the dynamics of the venting activity. Indeed, chemosynthetic communities are highly dependent on their environment, primarily as distribution patterns of the dominant symbiont-bearing, habitat-creating taxa are linked to methane and sulfide levels and fluxes, and substrata (Sahling et al. 2002, MacDonald et al. 2003, Levin et al. 2003, Bergquist et al. 2005, Mau et al. 2006, Olu-Le Roy et al. 2007a). Distribution changes therefore could also reflect changes in the venting activity.

Bergquist et al. (2003b) and Cordes et al. (2005b) suggested that community changes could be also time-related, and proposed a succession model for Gulf of Mexico seep communities, in which mussel beds become replaced by tubeworm communities as carbonate precipitates in the sediments. With time, tubeworm communities then contribute to reducing methane and sulfide availability at the sediment/water interface, thus leading to changes in the associated communities, by allowing non-endemic species to venture and compete with chemosynthetic species.

Whichever the cause of flux change, mussel population mortality and movements is considered to reflect changes in seepage flow or chemistry (Roberts et al. 1990, Lessard-Pilon et al. 2010b), while tubeworms tend to increase their dominance when fluid flow declines and can persist for years (Bergquist et al. 2003a, b, Cordes et al. 2005b). Finally, Lessard-Pilon et al. (2010b) attributed succession patterns between tubeworm and mussel populations along a 15 years interval to renewed or redirected active seepage.

During the West African Cold Seeps (WACS) cruise in February 2011, the Regab pockmark was intensively surveyed and a 14,000 m^2-large video-mosaic was assembled to map the main populated area of the pockmark. A subset of this same area had already been described by Olu-Le Roy et al. (2007a), who provided a detailed description of the spatial patterns of the faunal assemblages, highlighting high degree of spatial heterogeneity. This work was based on imagery data, and in particular on video-mosaics, taken in 2001 during the Biozaire cruise.

Using geo-referenced mosaics and geographic information systems (GIS), we propose a description of the current faunal distribution and its ten-year evolution in one of the most densely populated areas of the Regab pockmark gathering siboglinid tubeworms, bathymodiolid mussels and vesicomyids that create the dominant habitats of the pockmark. This is to our knowledge the first study of the temporal evolution of the distribution of chemosynthetic fauna at this scale and including such diverse habitats.

5.3 Site description

The Regab pockmark is located on the passive Congo-Angola margin at 3160 m water depth and about 10 km to the north of the Congo deep-sea canyon. The pockmark is a circular-shaped depression on the seafloor that is less than 20 m deep and about 800 m wide (Charlou et al. 2004, Ondréas et al. 2005) (Figure 5.1). Regab has been described as a 'pockmark cluster' since it is considered to be composed of several smaller pockmarks (Ondréas et al. 2005). Those features are believed to result from seafloor collapses following the release of over-pressured interstitial fluids. This was suggested after seismic profiles showed the presence of an underlying 300 m-deep pipe rooted in a palaeo-channel that acts as a reservoir for the accumulating fluids (Ondréas et al. 2005, Gay et al. 2006c). Trapped fluids are mostly enriched in methane and are believed to be produced in deeper layers of sediment by microbial activity (Charlou et al. 2004). Presence of gas hydrates was observed both in hydrate outcrops at the sediment surface and in gravity cores down to a depth of 6 m (Charlou et al. 2004, Ondréas et al. 2005). Sulfide is produced from methane and sea-water sulfate in the subsurface sediment by anaerobic methane oxidation evidenced in the different habitats (Cambon-Bonavita et al. 2009).

The most active area in terms of fluid escape is a 600 m-long and 200 m-wide N70º-directed area located near the middle of the pockmark. This area corresponds to a zone of extensive carbonate crusts and it seems to host most of the fauna of the pockmark (Ondréas et al. 2005). The faunal communities present at Regab are dominated by symbiont-bearing species including Siboglinidae polychaetes (vestimentiferan tubeworms) of the species *Escarpia southwardae* (Andersen et al. 2004), two species of Vesicomyidae bivalves, *Laubiericoncha chuni* and *Christineconcha regab* (Cosel & Olu 2008, 2009, Krylova & Cosel 2011), and of the mussel *Bathymodiolus* aff. *boomerang* (Olu-Le Roy et al. 2007b). These foundation species create habitats that support associated heterotrophic macro- and meio-faunal communities

which vary in biomass and diversity among habitats (Gaever et al. 2009, Menot et al. 2009, Olu et al. 2009).

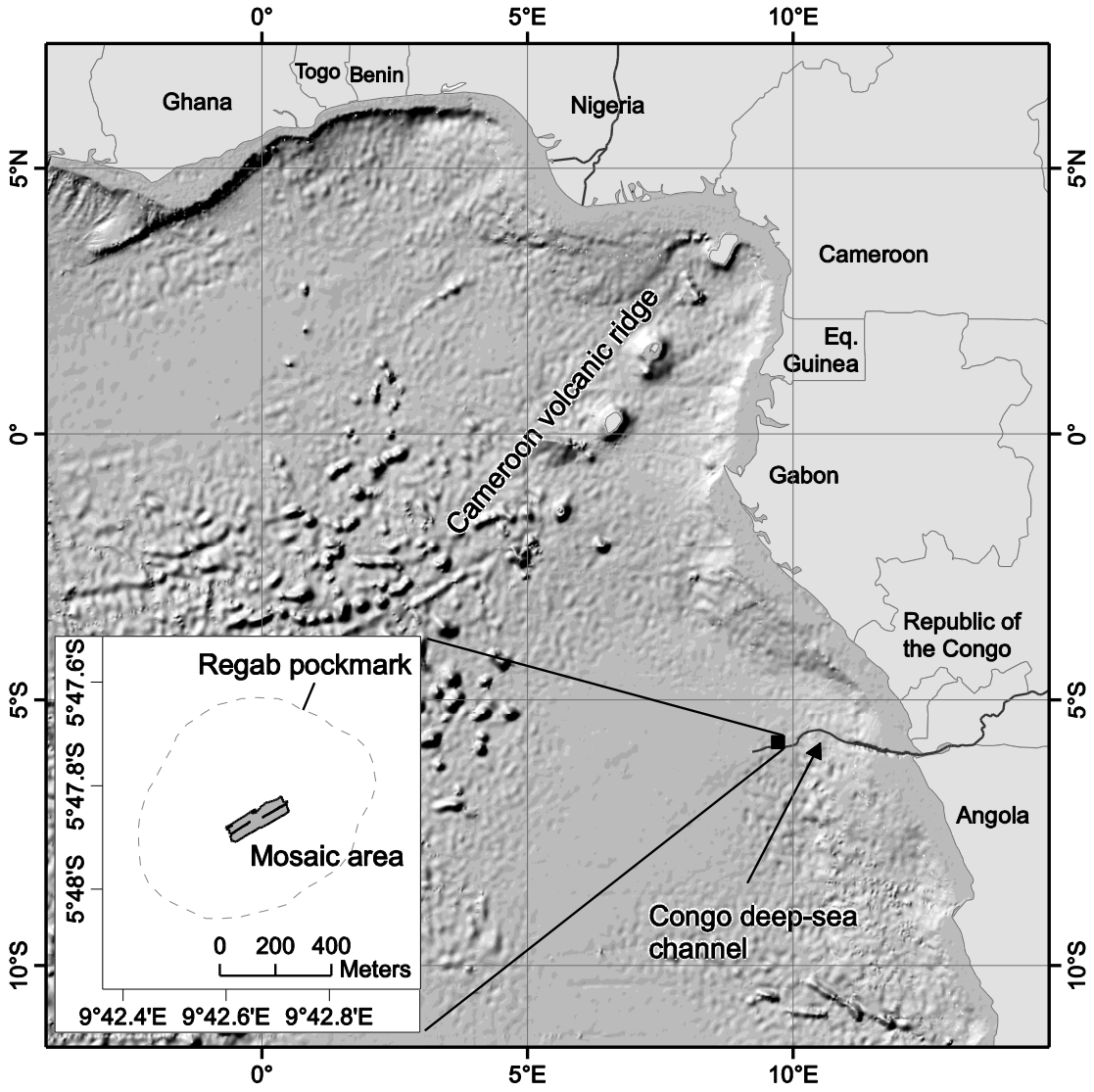

Figure 5.1: Location of the Regab pockmark; the insert map shows the approximate outline of the pockmark and the mosaic area.

5.4 Methods

5.4.1 WACS mosaic

5.4.1.1 Acquisition

Imagery used for the production of mosaics was acquired with a high-definition color video camera over two ROV dives during the WACS cruise with RV Pourquoi Pas?. The camera is mounted vertically on the ROV Victor 6000 and is dedicated to high-resolution mosaicking applications. The surveys were carried out in a structured way by performing parallel lines

separated by 3-meter intervals and from an average altitude of 3 meters, so as to ensure overlap between the mosaic lines. The total surveyed area covers a rectangular surface of about 65×220 m^2. The limits of this surface correspond to the limits of the 'mosaic 2' produced by Olu-Le Roy et al. (2007a) from images acquired during the BIOZAIRE cruise in 2001. The reason for this is to enable later comparison of the two mosaics. To minimize drift-induced positioning errors, the survey area was split into two equal subareas of 65×115 m^2 each. The survey required a total of twenty-one lines per subarea to cover the entire surface. Each line was 115 m long in order to ensure overlap between the two subareas. Moreover, the ROV position was reset onto a marker at the beginning of each line in order to eliminate any drifting error before starting a new line. During the survey, the maximum observed drift error at the end of a line was about 3 meters. The markers were also used to reset the ROV position when resuming the survey in another dive. Final navigation is therefore a hybrid navigation from USBL and dead-reckoning navigation reset with markers.

5.4.1.2 Construction of the video-mosaic

The lines of mosaic were constructed using the Ifremer in-house MATISSE program (Vincent et al. 2003, Allais et al. 2004). The MATISSE program was first designed for online-mosaicking, i.e. to build the mosaic while the survey is ongoing. However, due to compatibility issues between the program and the new camera and navigation systems of the ROV Victor 6000, building the mosaic involved numerous intermediate data manipulation steps and could not be performed in real-time. For instance, the HD-formatted video files (1920x1080 pixels) had to be converted into DVD-PAL format (720x576 pixels) before they could be read by MATISSE. This involved adding black bands on the image in order to preserve the 16/9-ratio of HD frames. Conversion to DVD format was done with the ConvertXtoDVD commercial program. Navigation files also had to be rewritten according to an older standard to ensure compatibility with MATISSE. The navigation was then replayed with the Ifremer TRIADE Software, a program that sends navigation entries to MATISSE at a real-time frequency in order to simulate an online mode. Mosaic lines were then constructed at a real-time pace.

Each line of mosaic was constructed separately instead of letting Matisse run straight from the beginning to the end of the survey. The reason was to keep size of files small, and to allow more flexibility in the construction of the final areal mosaic.

5.4.1.3 GIS and spatial analyses

The separate lines were imported and geo-referenced into ArcGIS. Geo-referencing was done with the ROV navigation data, but care was taken that corresponding features between overlapping segments would match on the same points.

For all mosaics, surficial features were delineated and polygons were created in ArcGIS to map the spatial distribution of each feature. Mapped features are similar to those used for the Biozaire mosaic (Olu-Le Roy et al. 2007a), and they include carbonate concretions, dense

and sparse patches of living and dead mussels, vesicomyid clams, and tubeworms, and zones of reduced sediment and microbial cover. Areas of coverage were computed for each non-sparse category.

Carbonate crusts were mapped only where concretions could clearly be seen on the images, and the mapped areas often do not include the carbonated crusts that underlie the tubeworm population or thin sediment covers. The dense Mytilidae category refers to areas where the living mussel distribution is almost continuous and where the substratum is rarely visible. Conversely, sparse mussel patches correspond to areas where the substratum is clearly visible between the individuals. Such distinction was not made for mussel shells, and only dense patches were mapped. The dense *E. southwardae* category refers both to single large bushes of adult tubeworms, and to fields of bushes of adult tubeworms, whereas the sparse category corresponds to areas where bushes of adult tubeworms are not closely distributed and contain relatively few tubes (roughly 10 or less). The young tubeworm category refers to bushes where tubeworms are of strikingly small size in comparison to the adult community. The recumbent tubeworm category designates bushes where the tubes are disposed horizontally, and senescent refers to dead and bad-conditioned individuals whose tubes lie on the seafloor. Patches of vesicomyid clams are categorized either as living, mixed or dead. Living clams are normally vertically disposed and half buried in the sediments, whereas clam shells are generally open and lying in the sediments. The ‘mixed’ categories refer to mussel or clam patches that contain both living and dead individuals.

The delineation process was supported by the use of the full HD resolution video files, particularly for differentiating clams from mussels and living bivalves from dead bivalves. Vesicomyid clams comprehend two species, *Laubiericoncha chuni* and *Christineconcha regab,* that cannot be separated on the images. However, both in 2001 and in 2011, *Christineconcha regab* was largely dominant in samples and on close-up views (Cosel & Olu 2009, Decker et al. 2012).

5.4.2 BIOZAIRE mosaic

The BIOZAIRE mosaic corresponds to the 'mosaic 2' described in the literature (Olu-Le Roy et al. 2007a). Due to the absence of navigation data, the BIOZAIRE mosaic was never geo-referenced. But surfaces could be calculated anyway from the altitude of survey and the camera parameters. In this work we used the new WACS mosaic to geo-reference each individual segment of the BIOZAIRE mosaic. The geo-referencing was done in ArcGIS by registering features common to both mosaics, such as unchanged carbonate concretions, dead shells, detritus and also bushes of tubeworms. The advantage of this technique is that it reduces the discrepancies between both mosaics, no matter how accurate the geo-referencing of the WACS mosaic is. In other words, a same polygon should have the same surface on both mosaics and patch sizes be directly comparable, with only a low relative error. However, differences in angles of perspective, in image quality, in visibility and in

contouring precision also occur and cause some discrepancies in the computed areas. Contours of living and dead mussel patches are the most affected by such discrepancies.

In order to keep consistency with the published work, BIOZAIRE contours were not redrawn. Instead, the original contours, drawn in Photoshop by Olu-Le Roy et al. (2007a), were reused. This implied exporting every contour layer from Photoshop. Contours were then imported as polygon features into ArcGIS and geo-referenced over the BIOZAIRE mosaic. The surfaces were recalculated according to the new geo-referencing data.

5.5 Results

5.5.1 WACS mosaic (2011)

The surveyed zone almost fully covers a 14,000 m²-large rectangular area directed in a southwest-to-northeast direction (Figure 5.1). Direct mapping of the main faunal assemblages and visible carbonate concretion areas is available for the entire study area (Figure 5.2a). It shows that the substratum is composed either of soft sediments or of harder carbonate concretions and that the faunal distribution is spatially non-uniform but instead is divided into areas of high and low faunal abundance. Areas of high faunal abundance can in turn be categorized based on the dominant type of fauna (Figure 5.2b).

Carbonate concretions were visible over a large portion of the survey area (Figure 5.2b). The total measured extent exceeds 4400 m^2. This is however a minimum estimation since it does not include carbonate concretions that were not directly visible at the surface, i.e. concretions covered by sediments or underlying the fields of tubeworms and mussels.

5.5.1.1 Mussel distribution

The map of faunal distribution (Figure 5.2a) shows that large mussel beds were round-shaped and always adjacent to the tubeworms fields. At the limit between the two aggregations, a transition zone with co-occurrence of mussels and tubeworms was often observed. In these transition zones mussels were present on the substratum between the tubeworms but they were also attached onto the tubeworms themselves. The mosaic and video material from ROV dives also indicated that areas of mussel occurrence tended to coincide with areas of hard substrata, i.e. of carbonate concretions, either bare or with thin sediment cover. Most of the mussel population within the study area was concentrated in two main (M2, M1) and one minor (M4) areas (Figure 5.2b).

The largest mussel area, known from the Biozaire mosaic as “M2”, stretched over 20 m and 26 m in the SW-NE and NW-SE directions respectively and had an approximate surface of 450 m^2. Observations of video footages showed that a large part of the population in this area was located at the bottom of a depression between boulders of carbonate concretions (Figure 5.2a). This mussel bed stretched further towards the north boundary of the mosaic and was

likely to extend beyond it.

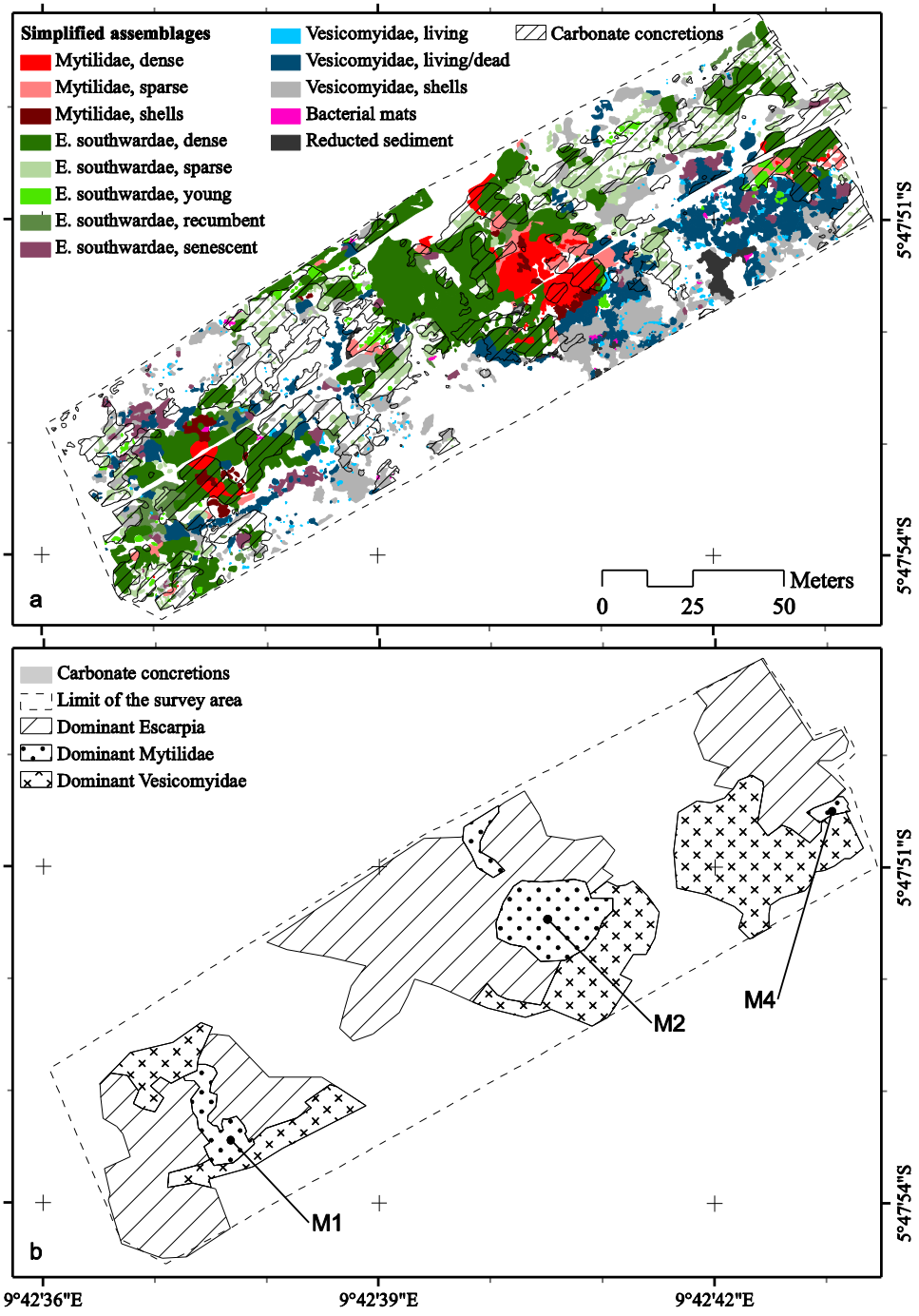

Figure 5.2: (a) Distribution of the main faunal assemblages and carbonate concretions based on the WACS mosaic; (b) Simplified areas of distribution of the main types of fauna according to the WACS mosaic.

The second main mussel area (“M1”) was located at about a hundred meters to the southwest

of the first one. It was composed of two beds of dense living mussels, one of about 45 m^2 and the other of about 30 m^2. The population was almost entirely surrounded by dense bushes of tubeworms but image material indicates that mussels were also present, although at a lower density. Patches of dead mussels seemed to be larger at M1, whereas the abundance of living mussels was believed to be lower than at M2.

Additionally a minor mussel patch was present at the northeastern limit of the mosaic. In this area, the densest mussel bed covered an area of less than 10 m^2, but was likely to extend over the limit of the mapped area. This area will be referred to as “M4”.

5.5.1.2 Tubeworm distribution

The majority of the tubeworm population within the area of study was concentrated in dense bushes. Bushes of tubeworms were solitary and isolated but were more commonly present in large and dense fields. In either case, tubeworms were mostly present on carbonate concretions and surrounded the main mussel areas.

The largest field with high tubeworms density was up to 1400 m^2-large and was located near the middle of the study area, west-northwest of M2. This area seemed more elevated than in the rest of the study area. This was due to the presence of blocks of hard concretions that gave the relief a rugged surface. A relatively high abundance of mussels was observed within the transition zone between mussel and tubeworm populations. In this area the transition zone was up to 7 m-wide.

The second largest field of tubeworms covered an area of about 600 m^2 and surrounded M1 almost entirely. In this field, the zone of co-occurrence between tubeworms and mussels was very small and it was not observed at every mussel/tubeworm limit. The field stretched farther towards the south-southwest and beyond the limits of the study area.

The next largest fields of dense tubeworms were located at the eastern and northeastern end of the mosaic. In this area, two fields of about 130 m^2 each were separated by a zone of soft sediments and low faunal abundance. A 55 m^2-large zone of co-occurrence between tubeworms and mussels could be observed in the vicinity of M4.

Juveniles were mostly observed as lonely bushes or as small fields in the periphery of the large aggregations of dense tubeworms. Mytilidae were also observed within populations of juvenile tubeworms, where those bordered the mussel beds.

Senescent/recumbent populations were rarely observed, and never within the main tubeworms aggregations. The main occurrences were located in the periphery of larger fields of tubeworms, and often over soft sediments and in the immediate vicinity of clam aggregations.

5.5.1.3 Vesicomyid clam distribution

Vesicomyids were observed in aggregates of very varied dimensions, and ranged from very

small clusters about 0.01 m^2-large to large fields of up to 400 m^2, gathering living, dead or mixed individuals. However, most aggregates contained mixed individuals, i.e. both living and dead, and it was hard to quantify the relative proportion of living and dead individuals from the images. In a few cases, small clusters of living clams could be observed and delineated within larger patches of mixed clams. Dimension of individual aggregates of living clams in the survey area did not exceed 1.5 m^2.

Clam communities seemed limited to the areas covered by soft sediments. For instance, clusters of living vesicomyids were scattered across the mosaic but were consistently observed in the areas covered with soft sediments. They were also often located in patches of dark reduced sediments.

This was also the case for the larger patches of vesicomyids, which were mostly present in the bottom half of the survey area and often in the periphery of the aggregations of mussels and tubeworms. The largest field of vesicomyids, located on the eastern side of the survey area, however did not appear to be restrained to the periphery of the other communities. Around this field were observed some areas of reduced sediments occurrence and, to a lesser extent some bacterial mats. Those areas were devoid of visible living fauna.

Patches of dead vesicomyids were also mainly observed in soft sediments, although sometimes in carbonate concretions too. Large fields of dead communities were present in the bottom part of the survey area, and particularly along the aggregates of mixed vesicomyids southeast of M2, where the field of clam shells exceeded 200 m^2 in surface.

5.5.1.4 Areas of lower faunal abundance

Areas of lower faunal abundance were not totally bare of fauna, but exhibited strikingly low numbers of tubeworms, clams, and mussels patches in comparison to the rest of the survey area (Figure 5.2a). Apart from the highly mobile fauna such as the galatheids, most of the fauna in those areas was composed mainly of sparse patches of tubeworms ($\leqslant$ 25 m^2) or of living and mixed clams ($\leqslant$ 20 m^2). Clam shells were also frequently observed.

The emptiest zone was located to the south of the large mussels and tubeworms communities located in the middle of the survey area. It covered an area of about 1000 m^2 and was mostly composed of soft, bioturbated sediments.

5.5.2 Comparison with BIOZAIRE mosaic (2001)

The Biozaire mosaic (2001) covers only a subset of the WACS (2011) survey area, and both mosaics overlap over a 4605 m^2-large area. In order to compare the trend in faunal distribution, this overlapping area is shown the Biozaire and WACS video-mosaics (Figure 5.3). Overall, there were only little changes in the spatial location of the main faunal assemblages.

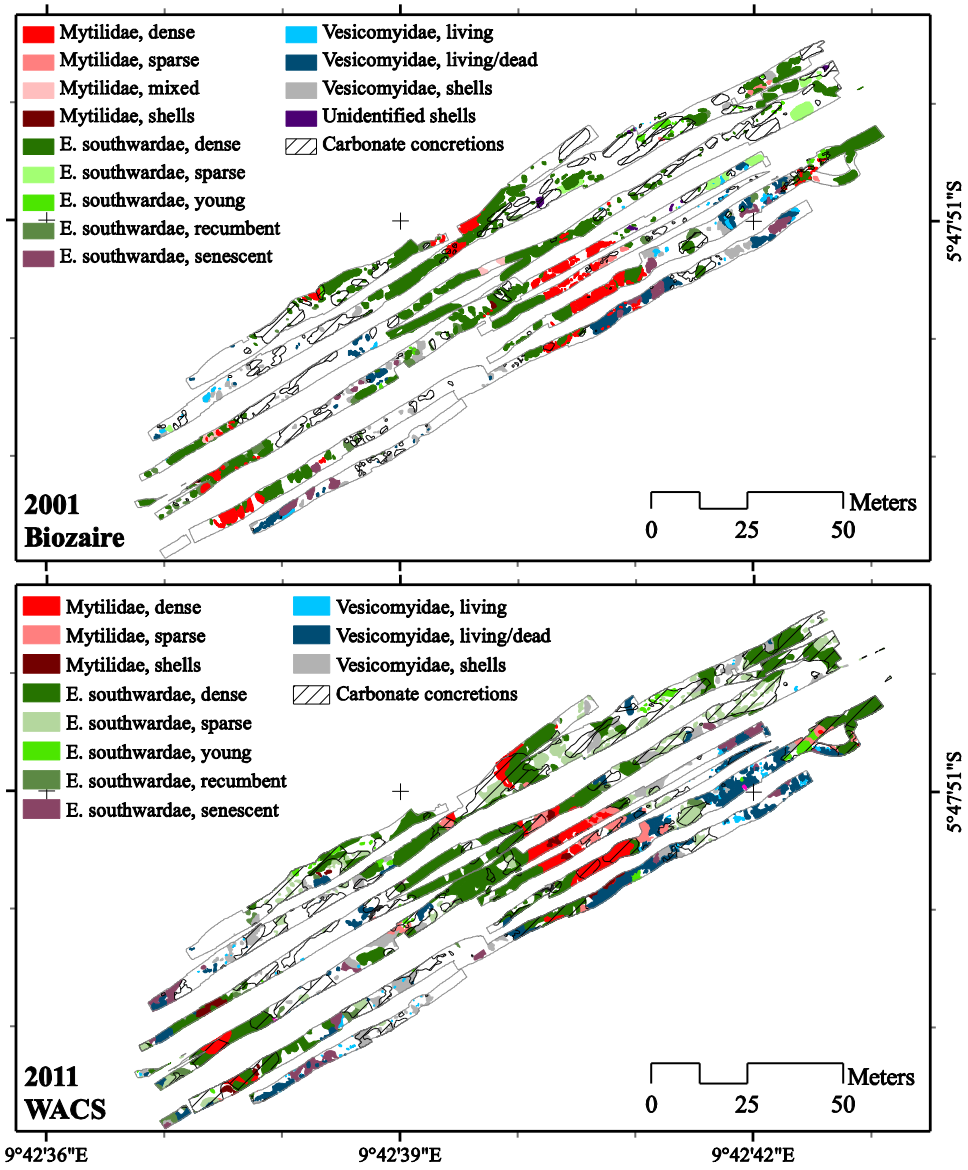

Figure 5.3: Distribution of the main faunal assemblages and carbonate concretions in the area of overlap between the Biozaire (2001) and the WACS (2011) mosaics.

The mussel distribution has remained mostly the same as it was during the Biozaire cruise. Although it is hard to compare the size of the patches due to the smaller coverage of the Biozaire mosaic, there is evidence that M2 contained a larger mussel population on the WACS mosaic than on the Biozaire map, with fewer gaps between the different patches (Figure 5.4a). Conversely, some small mussel beds at M1 seem to have disappeared and to have been replaced by mussel shells (Figure 5.4b). M4 is not covered by the Biozaire mosaic and cannot be compared.

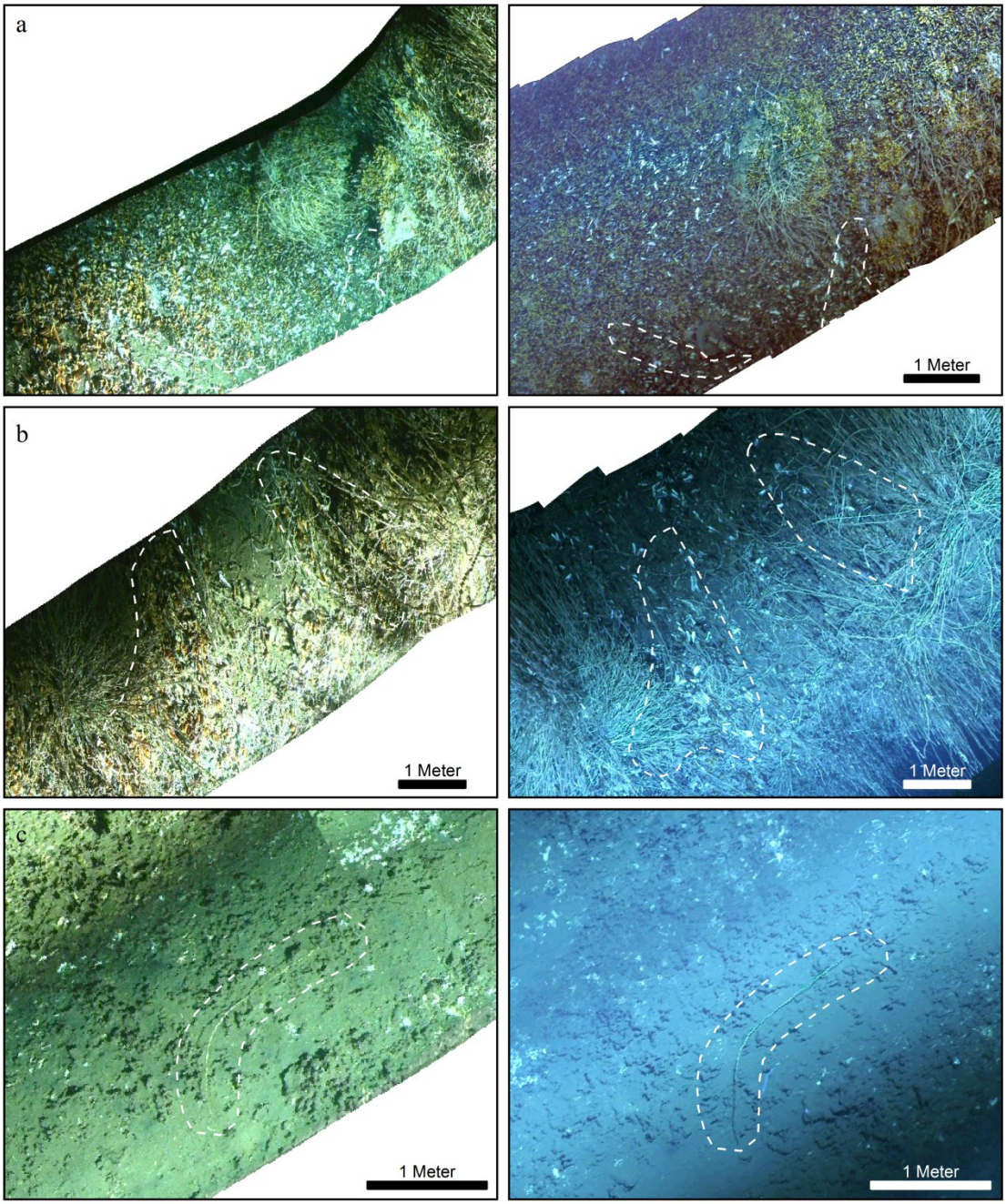

Figure 5.4: Images taken from the Biozaire (left) and WACS (right) mosaics, representing almost the same areas of the seafloor; (a) at M2, some areas previously devoid of mussels are now fully colonized by mussels; (b) at M1, small beds of living mussels on the Biozaire have been replaced by mussel shells on the WACS mosaic; (c) a recumbent tube of siboglinid polychaete showed no change in size and position between 2001 and 2011. Images taken by ROV Victor 6000 (© Ifremer, Biozaire 2001 and WACS 2011).

Tubeworm fields showed no change in distribution, the slight difference in polygon sizes being more due to the lower resolution of the Biozaire imagery data than on actual distribution changes. From these results, the tubeworm community is believed to be the one that changed the less across the study area. Most bushes or even single tubeworms were found unchanged and in some cases in the exact same position than in the older mosaic (Figures

4c, 5). Tubeworms were indeed the most reliable features when registering the Biozaire mosaic onto the WACS mosaic.

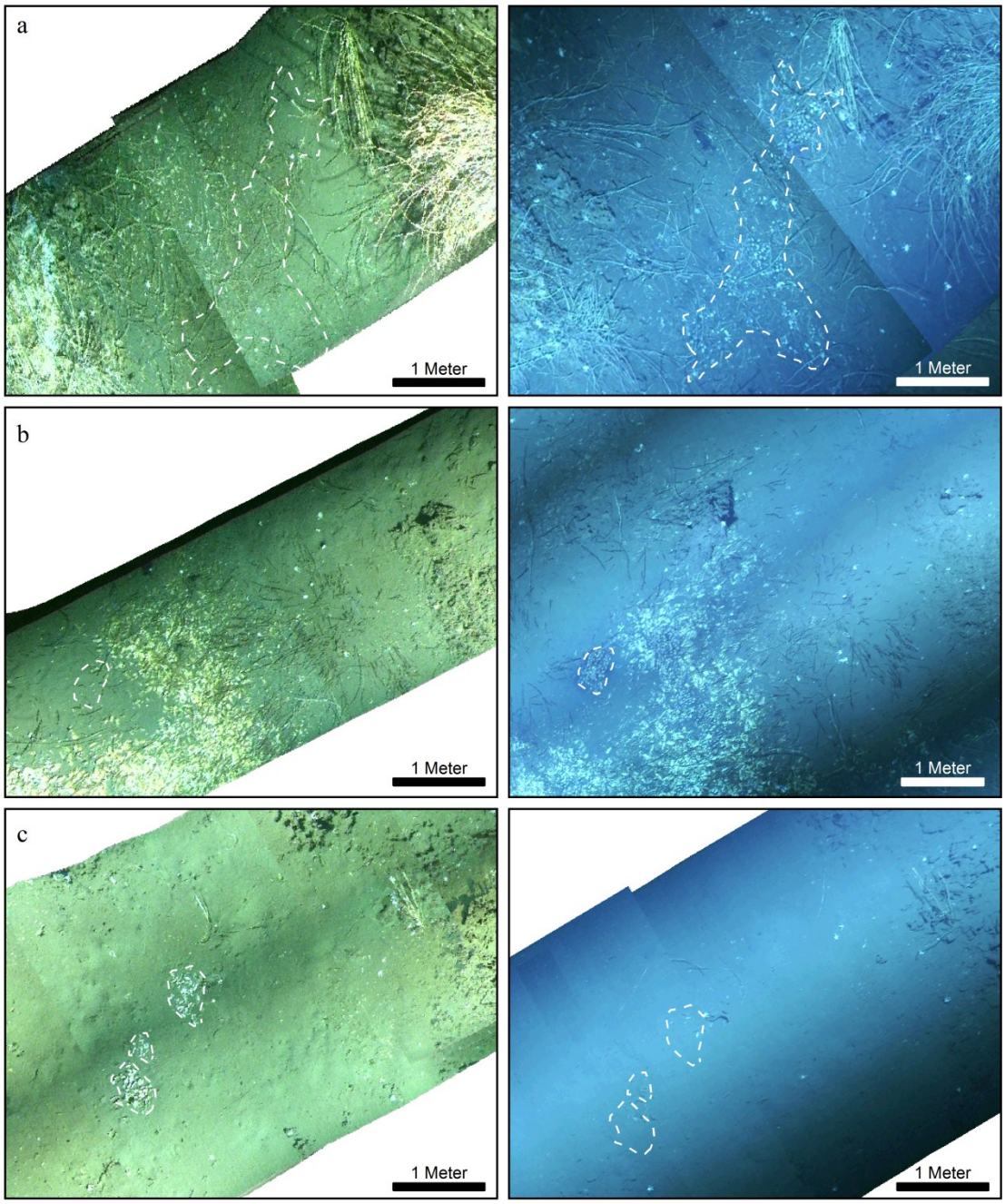

Figure 5.5: Images taken from the Biozaire (left) and WACS (right) mosaics, representing almost the same areas of the seafloor; (a,b) new patches of vesicomyids that did not exist at the time of the Biozaire cruise; b also shows that the patch of dead clams has been partly re-colonized; (c) a patch of mixed vesicomyids almost disappeared under sediment cover. Images taken by ROV Victor 6000 (© Ifremer, Biozaire 2001 and WACS 2011).

The vesicomyid clam population is the one that changed the most. Although the main fields have remained at the same locations, their sizes seem to have increased. In addition, new patches of living clams were observed that did not exist during the Biozaire cruise. Those new

patches were often in the close vicinity of older patches (Figure 5.5b), but were also in a few cases new settlements farther from previously existing patches (Figure 5.5a). Conversely, there were also a few patches that did not exist anymore or at least that were buried under some sediments (Figure 5.5c).

Extents of the areas of occurrence of dense mussels, tubeworms and clams were computed for both the Biozaire and the WACS faunal distribution maps (Table 5.1). Areas of sparse mussel and sparse tubeworm occurrence are not shown due to too large errors in contouring sparse aggregations. In addition, to keep consistency with previous work on the Biozaire mosaic, areas of zones of living mussel and tubeworm co-occurrence are given (Table 5.1). Given a total common area of 4605 m^2 between the Biozaire and the WACS mosaics, the areas can be expressed in percentage of cover of the mosaic. According to these calculations, patches of living siboglinid polychaetes, of siboglinid with mussels and of mixed (dead and living) clams underwent the most significant changes, with coverage increases of up to 1.5, 1.3 and 1.2% of the total area respectively. The total areal extent of the other assemblages showed almost no change.

Table 5.1: Areas of coverage of the different assemblages in both Biozaire (2001) and WACS (2011) mosaics. The percentages are relative to the total area (4605 m^2) covered by both mosaics.

Assemblage	Biozaire (m^2)	Biozaire (%)	WACS (m^2)	WACS (%)	Trend
Escarpia, living	716	15.5%	782	17.0%	+1.5%
Escarpia + *Bathymodiolus*	207	4.5%	268	5.8%	+1.3%
Escarpia, juveniles	25	0.5%	28	0.6%	+0.1%
Escarpia, recumbent	79	1.7%	60	1.3%	-0.4%
Escarpia, senescent	70	1.5%	95	2.1%	+0.6%
Mytilidae, living	194	4.2%	207	4.5%	+0.3%
Mytilidae, shells	2	0.04%	14	0.3%	+0.3%
Vesicomyidae, living	23	0.5%	27	0.6%	+0.1%
Vesicomyidae, mixed	141	3.1%	199	4.3%	+1.2%
Vesicomyidae, shells	112	2.4%	125	2.7%	+0.3%

Overall, the distribution of the carbonate concretions over the study area did not change between the Biozaire and the WACS cruises. The higher resolution of the new mosaic allowed better defining the contours of the concretions, especially in areas covered with vestimentiferans or mussels, and no major new area of occurrence was observed. On the contrary, in many places the carbonate concretions tended to slightly disappear under a thin sediment cover.

5.6 Discussion

5.6.1 Faunal and carbonate distribution

The mosaic and the distribution map of the megafaunal communities (Figure 5.2) give a very detailed view and full coverage of the entire study area. The results show that the megafauna at Regab is concentrated mainly in three distinct areas of high faunal abundance, separated by areas of relatively lower abundance (Figure 5.2b). Such distribution indicates that the chemical fluxes that are required to sustain these chemosynthetic communities are heterogeneous over the study area. Indeed, the distribution of the main faunal assemblages (Figure 5.2) showed a concentric spatial succession pattern starting from mussel beds in the middle to tubeworms and finally fields of vesicomyids towards the outside. In our study this spatial succession pattern from mussels to vesicomyid clams was observed, to various extents, around the three main mussel areas (M1, M2, M4).

A model presenting a concentric pattern has been proposed previously for the Regab pockmark (Gay et al. 2006c), but it considered both mussels and siboglinids as methane-dependant species inhabiting the same carbonate-dominated facies (Olu-Le Roy 2006). Although *Bathymodiolus* aff. *boomerang* contains both methanotrophic and thiotrophic symbionts (Duperron et al. 2005) and, for the populations living in the Regab pockmark, is known to rely on methane as dominant energy source (Olu et al. 2009, Duperron et al. 2011), siboglinid polychaetes are known to host sulphur-oxydizing symbionts (Dubilier et al. 2008) and to have very high demands in terms of sulfide supply (Cordes et al. 2003).

We postulate that the observed distribution is controlled by the strength of fluid advection and related methane fluxes, and propose a model in which the megafaunal distribution at Regab is structured by the presence of discrete zones of intense fluid advection and methane fluxes under the mussel beds. The distribution of the other communities would therefore be related to decreasing advection rates with distance from the mussel beds. The existence of such localized pathways of high fluid advection rate is compatible with the current understanding that the center of the pockmark is composed of several smaller pockmarks (Ondréas et al. 2005). In this section we discuss the concepts of this model, and confront them to more detailed observations of the faunal distribution and of the presence/absence of carbonate crusts.

Our observations show that the main mussel beds occur in areas where carbonates form blocs of indurated sediments and concretions within slight depressions, and that the main tubeworm aggregations occur in areas with extensive, continuous and prominent carbonate crusts. The formation of authigenic carbonates is a byproduct of the anaerobic oxidation of methane (AOM) in the sediment (Boetius et al. 2000, Aloisi et al. 2002) and is an indicator of methane fluxes and microbial activity within the sediments. However, the formation of continuous carbonate crusts impacts the porosity and permeability of the sediments and hence reduces the possible pathways for methane- and sulfide-rich fluid escapes and for

sulfate-rich seawater infiltration (Hovland 2002, Luff et al. 2004). Therefore, areas of mussel occurrence are likely to be characterized by higher fluxes between the sediments and the bottom water than the encrusted areas where tubeworms occur.

We propose that the three main mussel areas present in our study area are located on focused zones where the seepage activity is the strongest, and where fluid flow is intense enough for the methane fluxes to reach the sediment/water interface. Indeed, the distribution of mussels mainly in dense circular beds suggests the presence of localized areas of intense methane fluxes. This hypothesis was mentioned previously from the results of the Biozaire mosaic (Ondréas et al. 2005, Olu-Le Roy et al. 2007a). This is also supported by previous studies in other areas that showed that release of methane to the water column is indeed facilitated in high fluxes areas (Boetius & Suess 2004, de Beer et al. 2006, Niemann et al. 2006).

Co-occurrence of mussels and tubeworms is commonly observed at the transition between the two populations. In such zones, numerous mussels are observed onto the tubes of the siboglinid aggregations that directly border the mussel beds. This confirms that methane fluxes are higher in those areas than in the tubeworms aggregations located farther from the mussel beds. This is supported by previous studies that indicate that mussel beds at Regab are located in areas with the highest concentrations of methane in the water (Charlou et al. 2004, Olu-Le Roy et al. 2007a). Such behavior was also observed for methanotrophic mussel populations in the Southern Barbados prism (Olu et al. 1996b).

The distribution of the tubeworms aggregations around the mussel beds could be related to lower fluid advection rates than those under the mussel beds. Niemann et al. (2006) and De Beer et al. (2006) suggested that by preventing downward fluxes of sulfate-rich water into the sediments, intense fluid advection rates can hinder the efficiency of AOM. This could explain why tubeworms did not settle in place of the mussel bed.

Our observations show that those areas correspond to where the carbonate crusts are most prominent, and likely the thickest. Siboglinid polychaetes in seeps at the Gulf of Mexico have been shown to release sulfate through their roots into the sediments (Cordes et al. 2005a), thus preventing a potential sulfate-depletion of the sediments. This ability is believed to allow adult tubeworms to fuel or even enhance the AOM (Cordes et al. 2005a, Dattagupta et al. 2008) in order to maintain their supply in sulfide. As a corollary effect, the siboglinid population contributes to the formation of carbonates, which is supported by our observations that tubeworms are present where concretions form continuous and prominent crusts.

Juvenile tubeworms consistently occur near or at the limit between carbonate crusts and bare sediments. Sulfide fluxes and concentrations are likely to be higher in such areas with unsealed sediment/water interface than in areas covered by thick crusts, and thus to provide a suitable environment for the larvae to settle until they can self-maintain their supply in sulfide. According to Bergquist et al. (2002), the recruitment of new tubeworms is time-constrained and stops in older aggregations, due to the presence of thick carbonate

pavements and low concentrations of sulfide in the water (Bergquist et al. 2003a). Sulfide concentrations have indeed been reported to be higher around aggregations of juvenile than within older aggregations (Bergquist et al. 2003b).

This interpretation is further supported by the occurrence of bands of black reduced sediments along the limits of the siboglinids-hosting carbonate concretions (Figure 5.6), indicating that AOM and sulfide release occur in those areas. These features also suggest that part of the methane fluxes trapped beneath the carbonates could be redirected toward the sides of the carbonate crusts.

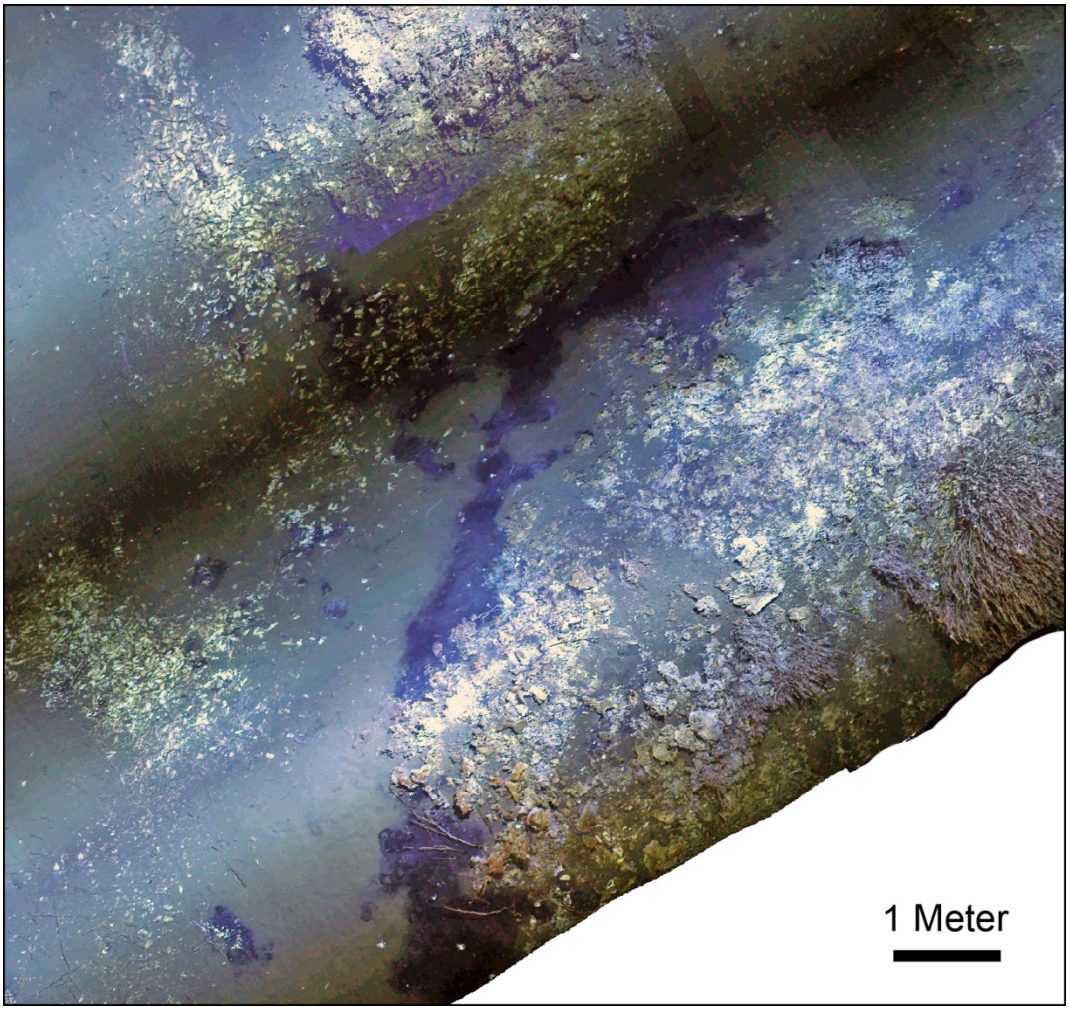

Figure 5.6: Excerpt from the WACS mosaic showing a band of reduced sediments along the border of carbonate crusts; juvenile siboglinid polychetes are visible on the right, and fields of vesicomyid clams can be seen in the sediment on the left. Images taken by ROV Victor 6000 (© Ifremer, WACS 2011).

The distribution of the vesicomyid population is likely related to even lower advection rates than the tubeworm aggregations. Results show indeed that the living vesicomyid clams are mainly located in the soft sediment areas surrounding the tubeworms and mussel aggregations, where methane and sulfide fluxes are lower. This is consistent with the current understanding that methane/sulfide availability shapes the structure of the microbial and

megafaunal communities (Olu et al. 1996a, b, 1997, Sahling et al. 2002, Sibuet & Olu-Le Roy 2002, Levin et al. 2003, Levin 2005, Ritt et al. 2011).

In search of a successional model, the vesicomyid clam environment is sometimes proposed as being a precursor stage towards a tubeworms/carbonate environment (Sahling et al. 2008a). This is partly supported by our observations of dead shells occurrences on some bare carbonate concretions. Also, the presence of shells within the concretions has been reported previously (Pierre & Fouquet 2007). These observations suggest that areas with vesicomyids are in some cases led towards the formation of carbonated crusts, either with or without siboglinids. However, we have also observed large patches of vesicomyid shells within the sediments, sometimes almost buried, that would suggest that seepage activity in these areas decreased or stopped and that living populations either died or moved away. Such areas might never turn into tubeworms/carbonate environments due to too low or too transient fluxes. Thus, vesicomyid populations might not be restricted to one particular successional stage of colonization, but be present in a range of areas representing different evolution stages of the seeping activity and the observed patterns of distribution reflect the spatial heterogeneity of fluid flux.

Bergquist et al. (2003b) and Cordes et al. (2005b) suggested that the relative distribution of mussels and tubeworms could be related to different stages of succession, and explain that mussel beds indicate an earlier stage of colonization that would later be replaced by tubeworms, when the formation of carbonate concretions reduces the methane supply to the water column.

However, we propose that the situation at Regab is somehow different and that it could also be partly related to spatial heterogeneity of the fluid advection regime. If the relative mussel/tubeworm distribution was solely related to different colonization stages, the mussel population would expectedly be observed mainly together with, or in the vicinity of, juvenile tubeworm aggregations. Although we do observe juveniles around some small mussel clusters, the larger mussel beds present in the study area are predominantly bordered by large adult tubeworm aggregations (Figure 5.2a). Considering the extreme slow growth rate of tubeworms (Fisher et al. 1997, Bergquist et al. 2000), this indicates that fluid advection in those areas has been going on for a relatively long time, but that recruitment of juvenile has not occurred or has been hindered.

5.6.2 Temporal comparison

The comparison of the maps of faunal distribution and of the computed areas reveals that the size of the areas of faunal occurrence has remained globally the same between the Biozaire (2001) and the WACS (2011) cruises (Figure 5.3, Table 5.1). We consider the discrepancies in computed values (Table 5.1) and mapped areas (Figure 5.3) to be largely caused by uncertainties in the method. First, images for each mosaic have been taken with different camera and lighting setups, which results in different resolutions and visibilities between the

Biozaire and WACS mosaics. Furthermore, small perspective distortions can, in places, impact the precision of the relative geo-referencing of the mosaics, or make a same feature look larger on one mosaic than on the other. Finally, the contouring process is a manual step that highly depends on the interpretation and precision of the observer. For all these reasons, mapped features may look different (Figure 5.3) and discrepancies in the computed areas (Table 5.1) may arise that are difficult to evaluate. However, based on qualitative observations described below, we consider that the calculated areas are due to error of the method and cannot be used to analyze the temporal changes in the areas of faunal cover. Nevertheless, considering the possible causes for uncertainty and the large size of the study area, the computed areas are remarkably consistent between the two mosaics.

For instance, our observations confirm that no change occurred in the population of tubeworms within the studied area over the past 10 years. Indeed, an increase of the area covered by tubeworms would signify that recruitment occurred. However, we did not observe new juvenile aggregations, possibly because the observation period was too short and that juveniles are still too small to be seen, or that the recruitment in the area covered by the mosaics was somehow limited. Overall, the absence of changes in the siboglinid population is in accordance with the findings that tubeworms can be very slow-growing and long-living (Fisher et al. 1997, Bergquist et al. 2000), and such observations were somewhat expected.

Conversely, some changes in size of individual beds of living and dead mussels were observed (Figure 5.4a-b), which suggest that localized variations of methane fluxes or carbonate precipitation might have occurred. For instance, small scale visual observations suggest that the dense mussel bed in M2 could sustain a greater abundance of mussels in 2011 than in 2001 (Figure 5.4a), and that some minor mussel beds at M1 disappeared (Figure 5.4b). This could indicate that the intensity of the fluxes increased in M2 and decreased in M1. A decrease in activity in M1 would be consistent with the findings of Olu-Le Roy et al. (2007a), who also hypothesized that a decreasing methane flux occurs in this area, based on the lower density of the mussel beds.

Overall, the mussel population showed very little changes. These findings are only partly consistent with observations of the temporal evolution of discrete seep communities in the Gulf of Mexico (Lessard-Pilon et al. 2010b). Both studies agree that only little change was observed on the total area covered by foundation fauna. However, Lessard-Pilon et al. (2010b) observed significant changes in distribution of mussel populations, and reported that about 50% of the area originally covered by living mussels at one site had been, after a period of 15 years, either replaced by mussel shells or colonized by tubeworms. Although we did observe minor changes in the mussel distribution, we did not observe the settlement of new siboglinid aggregations.

Indeed, no change was observed in the tubeworm aggregations surrounding these areas. Expectedly mussel populations are more dynamic and respond faster to environmental changes than siboglinid polychaetes (Lessard-Pilon et al. 2010b), which may be insensitive to

small variations of seepage activity. Alternatively, the increased dead mussels occurrence in M1 could reflect a late stage of the successional model developed by (Bergquist et al. 2003b), characterized by a decrease of mussel population due to a decrease of methane and maybe of sulfide in the water column. Indeed mussels are associated to areas of vigorous seepages and high methane concentrations (Nix et al. 1995, Bergquist et al. 2005).

Changes in the population of vesicomyid clams were more frequently observed than for the mussel population. Although we cannot conclude if the total living population globally did change, the location of the aggregates of living individuals shows relatively more differences in comparison to the other populations studied. Indeed, several patches of living individuals observed in the 2011 mosaic did not exist in 2001 (Figure 5.5a-b). Conversely some patches of Vesicomyid clams that existed in 2001 did not exist anymore in 2011 (Figure 5.5c). Also, in some cases, old patches of dead clams were re-colonized by living clams (Figure 5.5b). However, changes in the patches distribution of living/dead clams are difficult to apprehend since the relative proportion of living and dead clams cannot be estimated from the images. Overall, the distribution of living vesicomyid clams is very patchy (Figure 5.2a) and is difficult to understand.

Sahling et al. (2008a) proposed a model where the distribution of the tubeworm and clam assemblages is controlled by the depth of the gas hydrate deposits. The model considers that gas hydrates deposits act as “capacitors” (Dickens 2003) that buffer the transient influxes of methane from below and that ensure a more stable diffusion of methane into the pore water above, thus allowing sustaining long-living seep communities. We believe that a similar control mechanism occurs at Regab. Indeed, the presence of gas hydrates at Regab is known both from direct observation of outcrops on the sediment surface and from sediment cores (Charlou et al. 2004, Ondréas et al. 2005).

However, although this model is supported by the presence of such large populations of long-living seep communities and by their spatial patterns of distribution, it does not fully explain the temporal changes observed within the clam populations. At Regab, most aggregates of living individuals are indeed located within patches of black sediments, indicating the occurrence of AOM, and changes in areas of distribution must somehow reflect changes of sulfide availability. One possible explanation could be that gas hydrate deposits under clam communities are either absent or too thin to buffer the transient methane fluxes. The observed changes in clam distribution would therefore be the response to the transient release of methane and subsequent sulfide production. Clearly, some monitoring of sulfide concentrations and some geological sampling under the clam aggregates would be required to further refine this interpretation. However, this is in accordance with other studies that suggest that vesicomyid clams are supported by diffuse or transient fluxes (Olu et al. 1996a, b).

5.7 Conclusion

This study is the first to describe the 10-year evolution of the distribution of the megafauna in a cold seep environment over a 4600 m^2-large area. Changes in areas of faunal coverage appeared to be well below the precision limit of our methodology. Therefore, at such a scale, a mosaic-based comparison does not allow accurately quantifying small changes in faunal distribution.

Nevertheless, the study revealed that the overall size of the dominant megafaunal populations of Regab did not change, indicating an overall unchanged intensity of the methane and sulfide fluxes that reach the faunal communities. Such continuity could be related to the presence of gas hydrate deposits acting as “capacitors” for the methane fluxes. This study also shows that the small-scale distribution of the living population of vesicomyid clams changed more than the other populations studied, suggesting that the clam community is exposed to more transient fluxes.

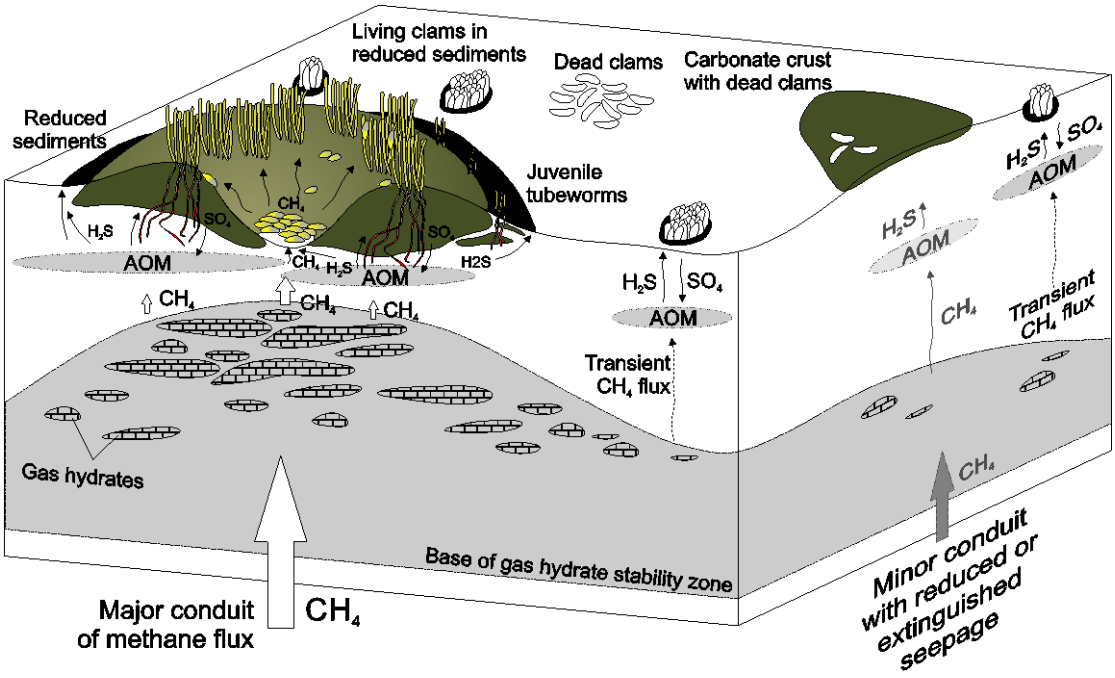

Figure 5.7: Summary schematic model (not to scale). The main aggregations are distributed in concentric patterns with the mussels in the middle, then the siboglinid polychaetes on thick concretions, and finally the vesicomyid clams in the sediments around. Mussels are present in an area of intense flux with significant release of methane in the water column. A transition zone is observed where mussels are present at the bottom and on the tubes of the siboglinids. Siboglinid polychaetes are present on carbonate concretions but reach the sediments with their roots. Through sulfate release, they maintain the AOM and the sulfide production. Juvenile tubeworms are distributed near the limit of the crusts where the sulfide fluxes from the sediments are likely higher. The presence of dark reduced sediments around the concretions indicate that part of the methane and sulfide fluxes are redirected from under the crusts towards more sulfate-rich zones where AOM occurs. Populations of vesicomyid clams occur in the sediments around. Their patchy distribution suggests that it is controlled by discrete and transient fluxes from below.

In addition, our mosaic-based observations of the faunal distribution over a 14,000 m^2-large area show that the main megafaunal aggregations at Regab are distributed according to spatial patterns with the methanotrophic mussels in the middle, then the siboglinid polychaetes and finally the vesicomyid clams on the outer zone. We interpret that each of these patterns is centered on a zone of high flux of methane–enriched fluids (Figure 5.7). Such zones of high fluid flow are responsible for the spatial variation of intensity of the fluxes reaching the upper sediments, and hence structure the distribution of the chemosynthetic megafauna in the pockmark.

5.8 Acknowledgements

We would like to thank the captain and the crew of RV Pourquoi Pas?, and the ROV Victor 6000 team. Also thanks to Olivier Soubigou, Christophe Bayle and Michaël Aron for their technical help and advices. We are grateful to the entire team of the LEP for receiving me in their team.

This work was supported by the Ifremer and by the European Commission under the EU Framework 7 funded Marie Curie Initial Training Network (ITN) SENSEnet (contract nº237868).

Chapter 6

Fluid flow regimes and growth of a giant pockmark

Yann Marcon[1], Hélène Ondréas[2], Heiko Sahling[1], Gerhard Bohrmann[1], Karine Olu[3]

[1] *MARUM – Center for Marine Environmental Sciences and Faculty of Geosciences, University of Bremen, Klagenfurterstr., D-28359 Bremen, Germany*

[2] *IFREMER, Centre de Bretagne, Laboratoire Géochimie et Métallogénie (REM/GM), Plouzané, France.*

[3] *IFREMER, Centre de Bretagne, Laboratoire Environnement Profond (REM/EEP), Plouzané, France.*

MANUSCRIPT 4

In preparation for submission to *Geology*.

6.1 Abstract

Pockmarks are seafloor depressions commonly associated to fluid escape from the seabed. They have been observed in many different areas and geological contexts, and can greatly vary in size and shape. Nevertheless the global mechanisms of pockmark growth are still largely unclear.

The giant complex Regab pockmark, located at 3160 m water depth near the Congo deep-sea channel, was investigated during the West African Cold Seeps (WACS) cruise with RV Pourquoi Pas? using current state of the art mapping devices mounted on the Ifremer's remotely operated vehicle (ROV) Victor 6000. ROV-borne micro-bathymetry and backscatter data of the entire structure, 105,000 m^2-large high-resolution photo-mosaic of the most active area, sidescan mapping of gas emissions, and maps of fauna distribution as well as of carbonate crust occurrence are combined to provide an unprecedented detailed view of a giant pockmark.

All datasets suggest that the pockmark is composed of two very distinctive zones in terms of seepage intensity. We postulate that these zones are the surface expression of two distinct fluid flow regimes in the sub-surface: focused flow through a fractured medium and diffuse flow through a porous medium. We conclude that the growth of giant pockmarks is controlled by self-sealing processes and lateral spreading of rising fluids. In particular, partial redirection of fluids through fractures in the sediments can anisotropically drive the pockmark growth into preferential directions.

6.2 Introduction

The term “pockmark” commonly refers to a seafloor depression and is considered to be one surficial expression type of fluid (i.e. liquid or gas) seepage processes, as well as mud volcanoes or gas hydrate pingoes (Judd & Hovland 2007, Serié et al. 2012). However, observations of pockmarks in various areas and settings show great differences in terms of sizes, morphologies, and frequencies of occurrence (Hovland et al. 2002, Judd & Hovland 2007, Gay et al. 2007). Such differences suggest that the term “pockmark” is loosely constrained and applies to a broad range of seafloor features (Hovland et al. 2002). For instance, reports of pockmarks on the Scotian Shelf mention diameters ranging from a few meters up to 150 m and spatial densities sometimes exceeding 40 km^{-2} (Judd & Hovland 2007). By contrast, pockmarks up to 1 km in diameter have been observed on the West African continental margin and with a distribution density of about 20.4 per 100 km^2 (Gay et al. 2007, Sahling et al. 2008a).

The shape of a pockmark is the result of local conditions and the processes involved in the formation and growth of pockmarks are likely to vary between settings. Several mechanisms have been proposed for the formation of individual pockmarks: fine sediment lifting by ascending gas (Hovland et al. 1984), drainage and escape of pore water (Harrington 1985), sudden fluid flow release following pressure buildup (Hovland et al. 2005), or collapse depression caused by hydrate dissolution (Sultan et al. 2010). All the different hypotheses confirm that several processes could apply and that the main mechanisms involved in the formation and growth of pockmarks remain largely unclear.

In this study we present for the first time the results of high-resolution acoustic and optical surveys of the giant ‘Regab’ pockmark in the lower Congo basin. Surveys were conducted using the Ifremer’s remotely operated vehicle (ROV) Victor 6000 during the West African Cold Seeps (WACS) cruise on the RV Pourquoi Pas? in January-February 2011. The dataset is fully comprehensive and includes in particular ROV-borne micro-bathymetry and backscatter maps together with detailed sidescan-based mapping of seafloor gas emissions over the entire pockmark. This is completed by a 105,000 m^2-large high-resolution photo-mosaic and fauna mapping of the most populated and active area of the pockmark in terms of seepage intensity.

To date such a comprehensive dataset of a pockmark feature is unique and gives unprecedented insights on the detailed morphology of complex pockmarks. In particular, the results provide valuable clues to decipher the functioning of giant pockmarks, which are discussed in this study.

6.3 Study area

The Regab pockmark is located on the Gabon-Congo-Angola margin about 10 km north of

the Congo deep-sea channel at about 3160 m water depth (Ondréas et al. 2005). In this area, muddy hemipelagic sediments cover turbiditic channel/levee bodies of the Congo fan (Droz et al. 1996, Gay et al. 2003). Seismic data show that the pockmark is linked to a deep palaeochannel/levee system that could act as reservoir for the seeping fluids (Ondréas et al. 2005, Gay et al. 2006c).

The pockmark was described as being composed of a cluster of 50-100 m-large sub-pockmarks aligned in a N70 direction (Ondréas et al. 2005, Gay et al. 2006c). Advecting fluids are enriched in methane of biogenic origin (Charlou et al. 2004) and sustain an abundant population of chemosynthetic fauna (Olu-Le Roy et al. 2007a) within the pockmark. Crusts of authigenic carbonates are extensive (Ondréas et al. 2005, Olu-Le Roy et al. 2007a) and widespread presence of shallow gas hydrates was inferred from seafloor observations and sediment cores (Charlou et al. 2004, Pierre et al. 2012).

6.4 Data and methods

Bathymetry data were acquired with a multibeam echosounder (MBES) Reson Seabat 7125 running at 400 kHz. The main survey was conducted from a 30 m altitude over a 1.2 km^2-large area and allowed mapping the entire pockmark. An additional survey was conducted from an 8 m altitude over a 0.175 km^2-large subarea of the pockmark. The data was processed with CARAIBES (Le Gal & Edy 1997) and the final bathymetry and backscatter maps include both datasets.

Imagery data were acquired simultaneously to the second bathymetry survey with the Victor 6000's high sensitivity OTUS photo-camera (Simeoni et al. 2007), and the photo-mosaic was constructed using an the ROV navigation data. Both datasets having been acquired simultaneously, an excellent match of the photo-mosaic onto the bathymetry was obtained. The mosaic was used to map the extent of carbonate crusts and the fauna distribution. Mapped fauna include siboglinid polychaetes (tubeworms), mussels and vesicomyid clams.

Seabed gas emissions in the water column were mapped using the CARIS program to visualize the sidescan data. Sidescan data from the 30 m altitude survey allowed identifying presence of gas in the water column as far as 40 to 60 m on each side of the ROV depending on the seabed morphology. Due to the dense track line spacing this ensured full coverage of the pockmark.

6.5 Results

6.5.1 Bathymetry

The bathymetry (Figure 6.1) shows that the pockmark is a large elliptical structure with

diameters ranging between 700 and 950 m. Its stretches in the N70 direction along an elongated feature, possibly related to a fracture. Elongated appendices can be observed in several places at the edge of the pockmark. The largest of these occur in the northeastern side and seem to be extensions of the N70 fracture expression. The pockmark boundary shows a sharp edge in the northeastern half, and becomes softer towards the southwestern side. The bathymetry also reveals that Regab is composed of numerous (>1000) rounded depressions, or sub-pockmarks, of very various sizes (from less than 5 m to 100 m in diameter) and depths (from 0.5 to 15 m).

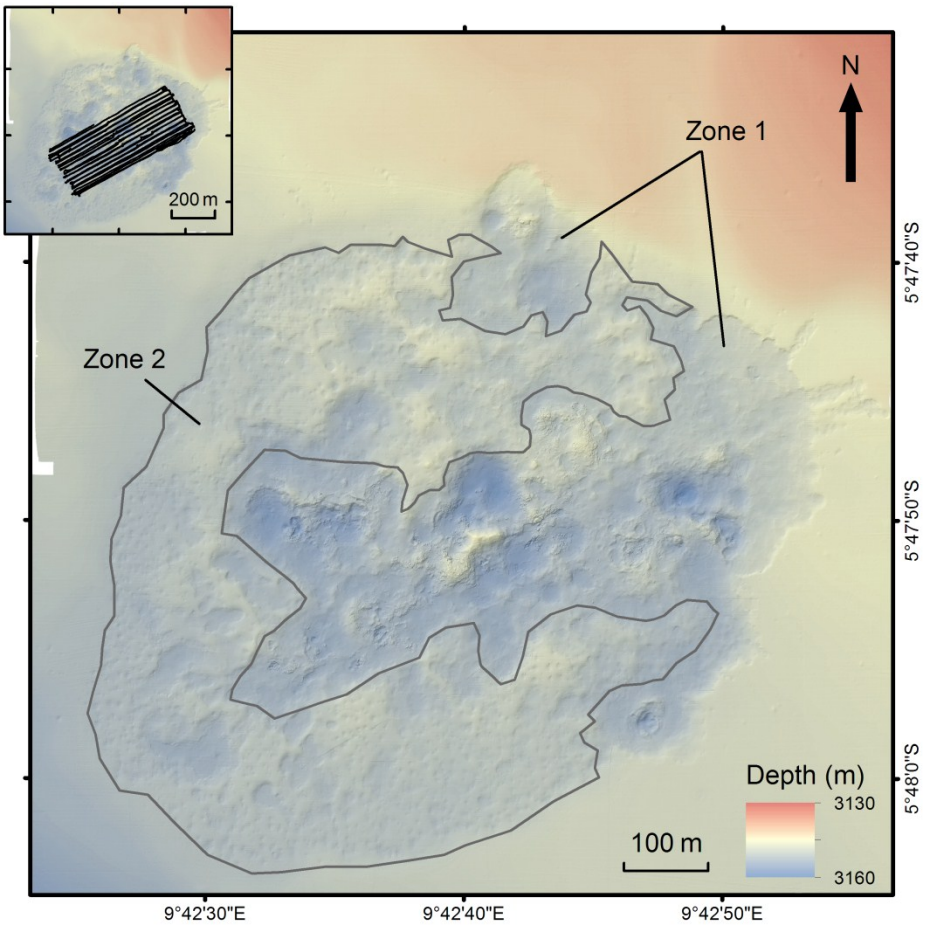

Figure 6.1: Micro-bathymetry of the Regab pockmark, and extent of the photo-mosaic (insert). Regab is about 800m in diameter and stretches slightly in the N70 direction along an elongated feature. The pockmark boundary shows a sharp edge in the northeastern half, and becomes softer towards the southwestern side. Zone 1 is characterized by a very rugged surface with relatively deep (>3 m) and large (>20 m) depressions; zone 2 has a smoother appearance and is scattered by numerous (>1000) very small- (<5 m) to medium- (up to 60 m) size shallow (<3 m) depressions.

Those depressions are not randomly distributed and two zones can be clearly distinguished (Figure 6.1): zone 1 is composed of relatively large (>20 m) and deep (>3 m) sub-pockmarks, and is characterized by a very rugged surface and the presence of carbonated elevations and slabs; zone 2 has a smoother appearance but is scattered by more than a thousand very small (<5 m) to medium (up to 60 m) and shallow (<3 m) pockmarks.

6.5.2 Backscatter and gas plumes

The signal reflectivity and gas plume distribution show a very characteristic pattern over the pockmark area (Figure 6.2).

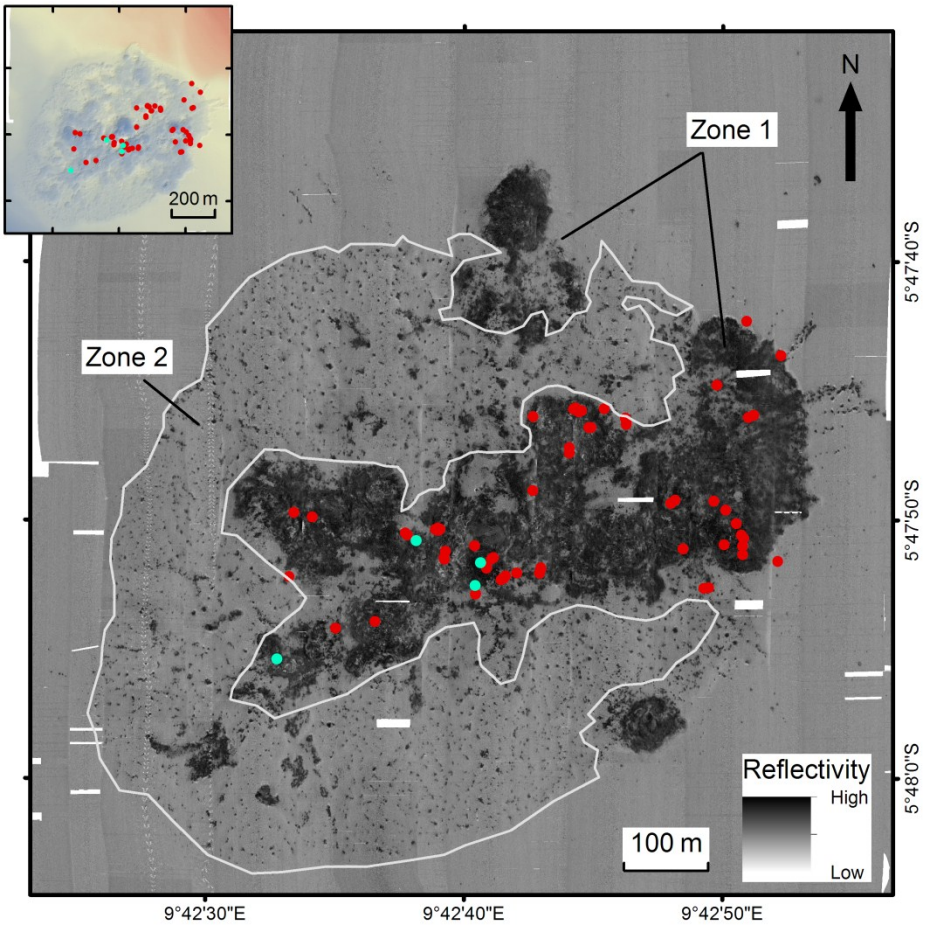

Figure 6.2: Seabed gas emissions (red dots) and gas hydrate outcrops (blue dots) in relation to backscatter intensity (large map) and to micro-bathymetry (insert). The signal reflectivity shows a very characteristic pattern over the pockmark area. Zone 1 is almost entirely characterized by high-reflectivity areas; the largest of them is located along and around the N70 longitudinal feature identified from the bathymetry, while the other two areas are located precisely on the boundary of the Regab pockmark, respectively on the northern and southern edges, and are associated to large individual sub-pockmarks (80-100 m in diameter). Zone 2 has a comparatively low-backscatter signature, but is scattered by a myriad of high-reflectivity anomalies of various sizes (up to 50 m in width) and shapes, which are consistently located within the numerous shallow sub-pockmarks identified from the bathymetry. Gas emissions occurred exclusively within the high-reflectivity area of zone 1.

Zone 1 is almost entirely characterized by high-reflectivity areas. The largest of them is located around the N70 longitudinal feature identified on the bathymetry; it stretches up to and along the eastern edge of Regab. Two additional areas of high backscatter occur precisely on the boundary of the pockmark, respectively on the northern and southern edges; they are associated to distinct and relatively large sub-pockmarks (80-100 m in diameter).

In contrast, zone 2 has a comparatively low-backscatter signature, but is scattered by a myriad of high-reflectivity anomalies of various sizes (up to 50 m in width) and shapes; these anomalies are consistently located within the numerous shallow unit pockmarks identified from the bathymetry. Vice versa, zone 2 unit pockmarks are always associated to high-reflectivity anomalies.

Gas emissions occurred exclusively within the largest high-reflectivity area of zone 1. They were generally observed in the slopes surrounding the main depressions or right at the edge of Regab, but never in the center of depressions.

6.5.3 OTUS and video imagery

The faunal and carbonate mapping from the photo-mosaic reveals a clear segregation between zones 1 and 2, and a clear causal link with backscatter data (Figure 6.3).

The rugged morphology of zone 1 is shaped by massive carbonate crusts that form thick elevations around sediment-covered depressions. Gas hydrates occur at the surface in several places (Figure 6.2) under carbonated crusts. Near the most active areas in terms of gas emissions, carbonate elevations host abundant mussel and tubeworm populations (Figure 6.2, Figure 6.3). Generally, mussel beds are located closer to active gas emissions and in areas of disturbed seafloor, where carbonate crusts seem broken or displaced. Clams are generally distributed in sediment-covered areas, but rarely within the deepest depressions of zone 1. Conversely, carbonate crusts, mussels and tubeworms are never observed in zone 2, and the imagery data only reveals soft sediments and clams presence. However, the clam distribution is very distinctive and shows that clams are only present in the center of the zone 2 unit pockmarks (Figure 6.3, Figure 6.4).

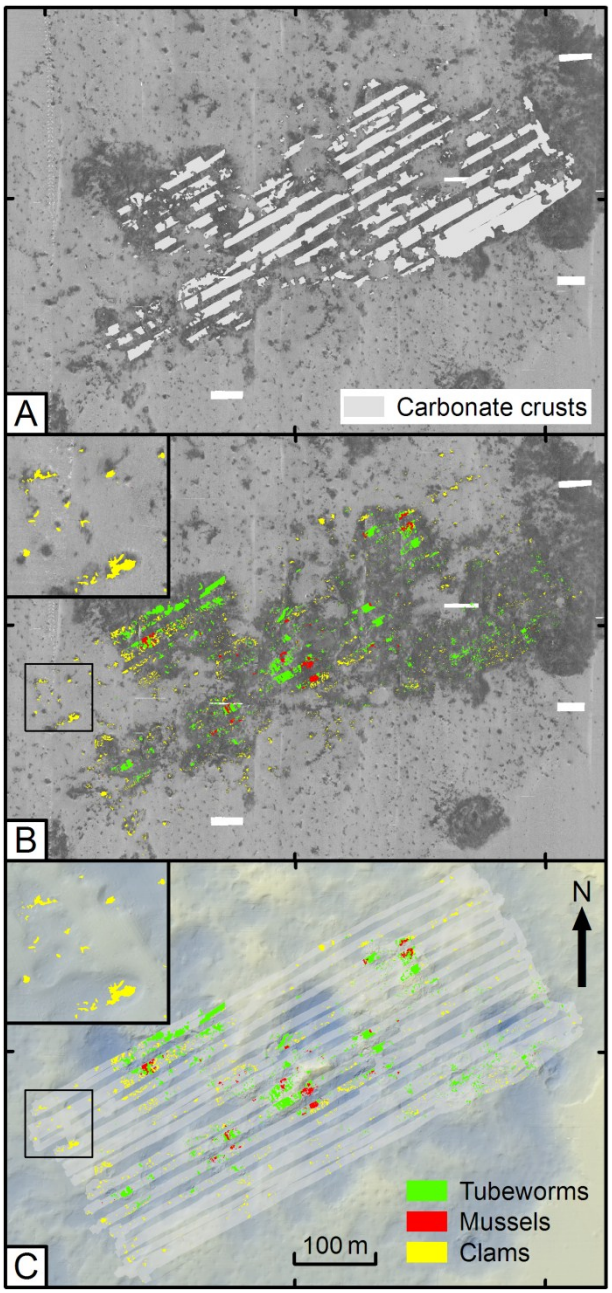

Figure 6.3: A: Carbonate distribution and backscatter; the good spatial correlation indicates that carbonates cause most high-backscatter anomalies. B: Fauna distribution and backscatter; tubeworms and mussels occur in high-backscatter areas related to carbonate presence; conversely clams generate their own high-backscatter anomalies, which are not related to carbonates. C: Fauna distribution and micro-bathymetry; the gray lines show the extent of the photo-mosaic; tubeworms and mussels occur mainly on elevated areas; clams are present in comparatively lower areas, but rarely in the deepest depressions. B and C: Inserts represent magnifications of the same area (shown by black rectangles) of zone 2; in this zone, clams occur exclusively within shallow sub-pockmarks of various size.

6.6 Discussion

Previous studies showed that the activity at Regab is linked to the presence of a vertical chimney under the pockmark that is rooted into a palaeo-channel (Ondréas et al. 2005, Gay et al. 2006c) and that the advection of fluid through the gas hydrate stability area is possibly related to a fault (Gay et al. 2006a). Such interpretation is supported by the elliptical shape of the pockmark and the linear feature evidenced from the bathymetry (Figure 6.1). However, although a fracture is likely the main feature controlling the fluid expulsion pattern at Regab (Figure 6.2), the new high-resolution data revealed two very distinctive zones within the pockmark. These two zones show strikingly different morphologies and distributions of

carbonates, fauna and gas emissions, and are clearly the expressions of very distinct fluid flow regimes.

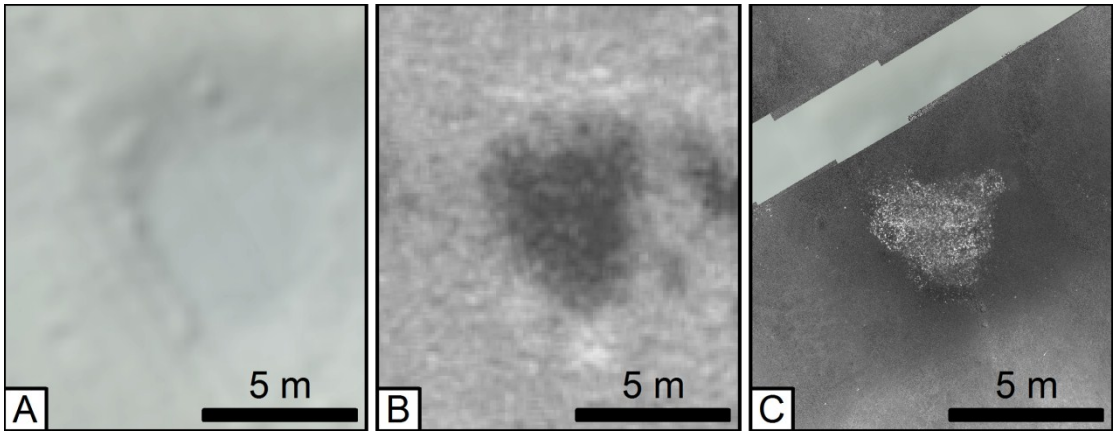

Figure 6.4: A-C: Bathymetry, backscatter and photo-mosaic of the same close-up view of a middle-size eyed-pockmark. A large aggregation of vesicomyid clams causes a high backscatter.

6.6.1 Zone 1: Intense and focused fluid flow

At zone 1, thick carbonate elevations, rich fauna and intense gas venting are many indications for high, focused and long-term seepage activity. First, the abundance of thick crusts of authigenic carbonates at the surface suggests that the anaerobic oxidation of methane (AOM) occurs close to the sediment surface (Aloisi et al. 2002) and has been active for a long period of time (Luff & Wallmann 2003, Teichert et al. 2003). A shallow AOM front would therefore indicate an intense upward flux of methane from below (Borowski et al. 1999).

Next, patterns in the distribution of mussels and tubeworms (Olu-Le Roy et al., 2007, Figure 6.3b-c) indicate that the chemical fluxes are heterogeneous across the zone. Regab mussels are strongly dependent on methane as energy source (Olu et al. 2009, Duperron et al. 2011) and tubeworms are known to be high sulfide consumers (Cordes et al. 2003, Dubilier et al. 2008); in particular, mussels and gas emissions were often observed together. Therefore, their occurrence could reflect areas of intense fluid flow where chemical supply is locally high. This is consistent with the distribution of bottom seawater methane concentrations, which is very heterogeneous in this zone (Charlou et al. 2004, Ondréas et al. 2005).

Finally, the faunal distribution (Ondréas et al. 2005), the backscatter signal, and the overall shape of zone 1 show a strong correlation with the N70 axis identified from the bathymetry. It is likely that such fracture provides the main pathways for focused fluid flow in this zone. Additional pathways for intense fluid flow may exist at sediment discontinuities along pockmark edge; this is supported by the presence of two large sub-pockmarks right on the boundary of Regab.

6.6.2 Zone 2: Diffuse and homogeneous fluid flow

We postulate that the relatively smooth surface of zone 2 is the expression of a more diffuse and uniform fluid flow pattern than in zone 1. Results show that carbonates, gas emissions, and hard substratum fauna, such as mussels and tubeworms were never observed in zone 2. Instead, a myriad of small and medium shallow sub-pockmarks are scattered across the zone; backscatter anomalies are present in each sub-pockmark (Figure 6.2), which are likely generated by the presence of clams (Figure 6.3). This supports findings from previous works in the Congo basin that correlated the distribution of clams to low seepage activity areas (Olu-Le Roy et al. 2007a, Sahling et al. 2008a).

The formation of unit pockmarks is not yet fully understood and could be related to various mechanisms such as sediment lifting by ascending gas (Hovland et al. 1984), volume loss caused by pore fluid drainage (Harrington 1985), rafting of small hydrate clumps (MacDonald et al. 1994, Paull et al. 1995), or hydrate dissolution (Sultan et al. 2010). Mechanisms involving free gas escape in this zone are not supported by our observations of gas flare distribution, whereas those involving presence of shallow subsurface gas hydrates deposits are not supported by backscatter data and the observed scarcity of faunal communities (Figure 6.2, Figure 6.3), which suggests low seepage activity.

However, pore fluid advection is known to occur at Regab, with rates up to 2.3 mm/a at the western edge of the pockmark (Chaduteau et al. 2009). This would favors the model by Harrington (1985), according to which advecting pore water is retained in fine sediments until it is released due to pressure buildup. Subsequent sediment winnowing and water drainage ultimately leads to the formation of pits, or unit pockmarks, at the surface.

Finally, the presence of clams in every unit pockmark of Regab brings the chicken-and-egg question of which appeared first. Clams are known to be water-pumping animals and to noticeably influence the water flow at seep sites (Wallmann et al. 1997). Such bioirrigation could also contribute to pit formation according to the pore fluid drainage model (Harrington 1985).

6.6.3 Possible mechanisms controlling the pockmark growth

We propose that self-sealing processes and subsequent fluid flow redirection control the pockmark growth. The formation of authigenic carbonates at methane seeps causes the sediment permeability to decrease, and may ultimately form a natural seal for rising fluids (Hovland 2002). Assuming that the overall seepage intensity is not decreasing, such permeability loss would result in an increase of pore fluid pressure; thus, excess fluids would spread laterally within the sediments until sufficient pathways to the surface become available and that uniform flow at hydrostatic pressure is restored. This is similar to the concept of ‘shortest and most permeable vertical pathway’ used to explain the migration of petroleum

fluids in rocks and sediments (Mackenzie & Quigley 1988, Floodgate & Judd 1992).

Furthermore, the interpretation that fluid overpressure may occur under carbonate crusts is supported by our observations of gas emissions and outcropping hydrates in areas of broken crusts or of displaced blocs; such features are evidences for catastrophic events and could be related to the sudden release of pressured free gas from under the crusts (Hovland et al. 2005) or to the formation and rafting of gas hydrates (MacDonald et al. 1994).

Redirected fluids may transit as diffuse (Darcy) flow through non-fractured porous sediments or as focused flow along discontinuities or fractures in the sediments. Regab provides evidences for both flow types: mainly focused in zone 1 and mainly diffuse in zone 2. The distribution of high backscatter areas and gas emissions within zone 1 suggests that rising fluids were partly redirected from the center towards the northeastern boundary of Regab, likely along a fracture, thus giving an elliptical shape to the pockmark. This hypothesis is supported by previous findings that southwesterly tubeworm and mussel assemblages may be older than northeasterly assemblages, and may be related to decreasing methane fluxes (Olu-Le Roy et al. 2007a). In the absence of similar preferential fluid pathways, fluid flow in zone 2 spreads over a relatively large area and reaches the surface with a lower intensity than in zone 1.

6.7 Conclusion

This is the first study to present such a high resolution and comprehensive mapping dataset of an entire giant complex pockmark. It demonstrates that current modern techniques exist that allow for detailed and large-scale investigations of the deep-seafloor. The value of such comprehensive datasets goes beyond the mere production of high quality maps. By giving full sight of the area of study it allows getting a deeper understanding of the system and the long-term processes involved. In this study, it allowed identifying zones with distinct fluid flow regimes, and inferring a growth model for giant pockmarks.

The proposed model is based on strong indications that the fluid flow at Regab occurs both as focused and diffuse flow. Self-sealing processes constrain rising fluids to redirect laterally until ways to the surface become available. In the case of Regab, fluids are primarily driven through fractures or discontinuities within the sediments, thus leading the pockmark growth into one preferential direction. However, fluids also partially redirect through non-fractured porous sediments, and reach the surface is a more isotropic way.

6.8 Acknowledgements

We would like to thank the captain and the crew of RV Pourquoi Pas?, and the ROV Victor 6000 team. We are grateful to the entire team of the LEP for receiving me in their team. This

work was supported by the Ifremer and by SENSEnet, a Marie Curie Initial Training Network (ITN) funded by the European Commission 7th Framework Programme, Contract No. PITN-GA-2009-237868.

Chapter 7 Conclusion and outlook

The three case studies, which are the major milestones of this work, investigated different aspects of seabed fluid flow processes, in various environments. The strong focus on high-resolution imaging techniques allowed mapping deep-sea sites in more detail and at larger scales than what is commonly done (Figure 7.1). In the two study areas, the Menez Gwen hydrothermal vent and the Regab pockmark, zones of active venting or seeping were mapped almost entirely, either with optical or acoustic imaging methods. Such datasets allowed measuring the dimensions of active areas and faunal coverage, quantifying related processes such as chemical fluxes and biomasses, and getting a better understanding of the spatial and temporal variation of fluid flow activity.

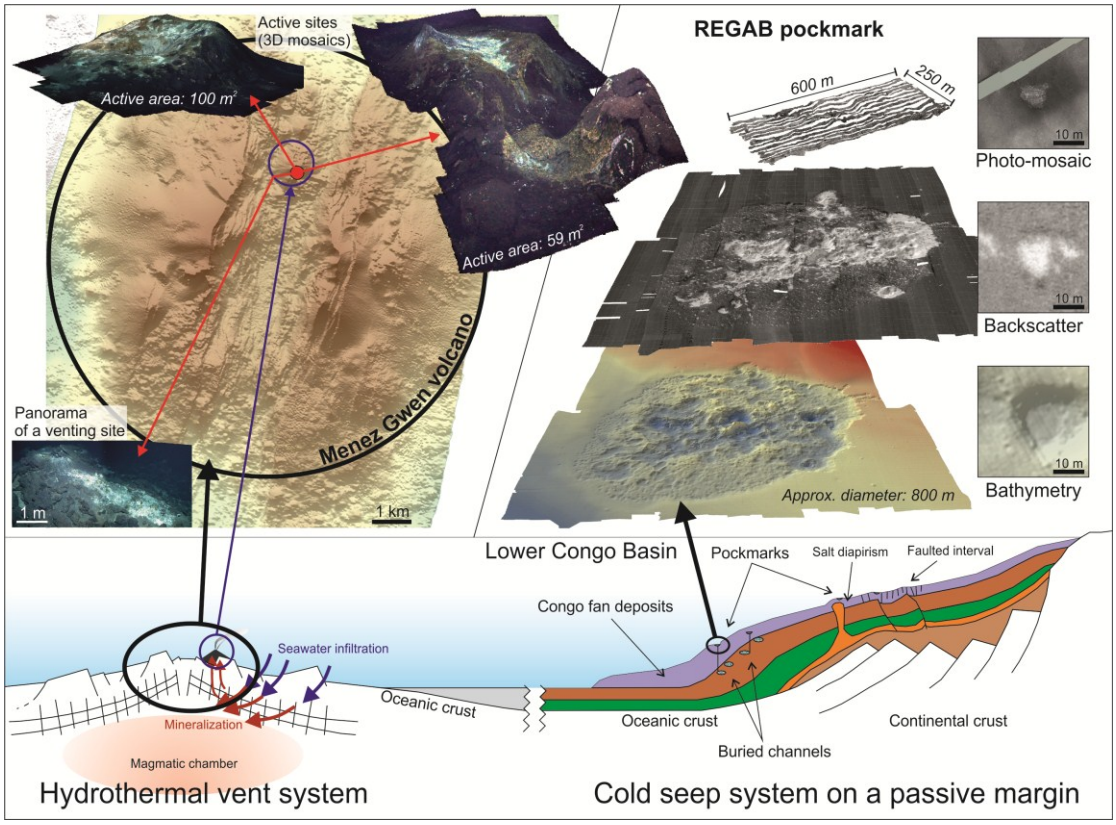

Figure 7.1: Summary of the main datasets and imaging methods used in this work, together with schematics (not to scale) of the geological contexts. The Menez Gwen volcano system occurs on the Mid-Atlantic Ridge (MAR); in this system, the hydrothermal activity is located almost right on the axis of the MAR; the dataset includes mainly a comprehensive bathymetry map of the volcano and several photo-mosaics and 3D views (not all shown). The Regab pockmark is located in the Congo deep-sea fan; seeping fluids originate from a shallow buried channel that acts as a reservoir for biogenic fluids; the pockmark was imaged with ROV-bathymetry, backscatter and large-area photo-mosaics and video-mosaics (not shown); the high data quality allowed detailed comparison of the different datasets.

The first case study focused on five venting sites of the Menez Gwen hydrothermal vent

system. A photo-mosaic was constructed for each of them, using an ROV-mounted underwater camera. These photo-mosaics provided full geo-referenced overviews of four of the sites and a partial panorama-view of the fifth and smallest site. Based on GIS analyses and area calculations, the distribution of the dominant megafauna species was described and population densities and biomasses were assessed at the scale of entire sites of active venting. The total population density over the four largest sites ranges between 28,640 and 50,120 individuals, which corresponds to a total biomass of 50 to 380 kg wet wt. Such estimations are so far unique, in the sense that similar estimations for entire sites of venting activity could not be found in current scientific litterature. Indeed, comparable studies generally use standardized units of density (individuals m^{-2}) and biomass (kg m^{-2}), but do not provide area measurements. The estimated total biomasses were used to infer the total consumption in dissolved gases by the fauna at different sites of active venting.

The second case study was based on two overlapping video-mosaics, which represent the most populated area of the Regab pockmark with a 10-year interval (2001-2011). It allowed studying the large-scale distribution of the megafauna and authigenic carbonates and its temporal variations. Seep fauna and methane-derived authigenic carbonates (MDAC) are indications for past or present seepage activity; hence, a model linking the fauna and MDAC occurrences to the subsurface plumbing system was proposed. Furthermore, the temporal evolution of the fauna and MDAC was used to discuss the evolution of the seepage activity.

The third case study presented a ROV-bathymetry and backscatter map of the entire Regab pockmark, together with a large-scale photo-mosaic and a comprehensive survey of gas emissions across the pockmark. This unprecedented dataset gave a new view of the entire pockmark morphology and of the actively venting areas, as well as a detailed mapping of the areas of occurrence of the megafauna and crusts of MDAC. It was shown that the pockmark is composed of two distinct areas in term of seepage activity. One area was associated to strong fluid seepage, enabled by the occurrence of preferred fluid pathways such as fractures in the subsurface; conversely, the second area was characterized by comparatively lower seepage activity, likely related to slowly rising fluids through low- or un-disturbed sediments. It was evidenced that the growth of the pockmark is driven by self-sealing processes and by the formation of new pathways for focused and diffuse fluid flow.

These three case studies allowed answering the initial questions:

(1) At the scale of a hydrothermal vent site, how significant is the chemical consumption by vent fauna in comparison to the natural release in dissolved gas? Do benthic vent fauna exert a noticeable control on the methane and sulfide effluxes to the hydrosphere?

This work concludes that the faunal consumption in dissolved gases is low in comparison to the natural gases from the system. Total consumption in methane and sulfide by the dominant fauna over the four largest active sites of the study was estimated to be about ten (sulfide)

and a hundred (methane) times lower than the minimum estimations of the focused release from the system. Similarly, a one-square meter area of diffuse venting could meet at least 30 and 4.5 times the total consumption of methane and sulfide in the four largest sites together.

This conclusion was reached based on the most optimistic scenario, i.e. by comparing the maximum estimations of faunal consumption with the minimum estimations of gas effluxes. Therefore, it is likely that the faunal consumption is even less significant in comparison to the total natural gas release from the system. Considering this, the control of vent benthic fauna on diffuse methane and sulfide effluxes to the hydrosphere is relatively poor at Menez Gwen. As a comparison, this is unlike seep fauna, which was shown to act as an efficient benthic filter for dissolved methane (Sommer et al. 2006).

(2) Is there any distinct pattern in the distribution of seep fauna? If so, what does it reveal about the seepage activity and plumbing system of the pockmark?

Distinct distribution patterns of seep fauna were observed, in which the megafaunal communities of Regab were distributed more or less concentrically; the most methane consuming fauna (mussels) occurred towards the center of the circular patterns, and were surrounded by the rather sulfide-dependent fauna. Tubeworms occurred associated to carbonate crusts directly around the main mussel aggregations, while clams were generally present on the outer side, within soft sediments.

Such pattern was observed in three different places and provided information to understand subsurface seeping activity. Indeed, this particular distribution suggested that the seeping activity is very heterogeneous and discrete, with several localized zones of high methane advection. The faunal patterns are centered on such zones, and reflect the spatial variability of the methane fluxes. The plumbing system must, therefore, be characterized by the presence of preferential pathways for seeping fluids, such as fractures or zones of higher-permeability. Different advection rates result in different depths of the gas hydrate deposits and of the sulfate-methane interface zone, and, thus, control the distribution of the chemosynthetic fauna and MDAC.

(3) How dynamic are cold seep communities? What can be inferred about the temporal evolution of the seepage activity?

Results of the case study 2 showed that the distribution and overall size of the dominant megafaunal populations globally remained unchanged over the 10-year period of the study. In particular, the same distribution patterns were observed on both video-mosaics, what suggests that the main pathways for fluid advection did not change. This is in accordance with the general understanding that cold seep systems provide rather stable environments to chemosynthetic communities.

However, some small and localized distribution changes were observed, especially within the clam population. They consisted mostly in small-scale re-organization of some clam aggregates, and they did not put back in question the general distribution of the clam population. Nevertheless, such rearrangement indicates that the chemical fluxes reaching the surface within the clam population, i.e. within soft sediments, are locally variable.

(4) What are the main mechanisms driving the growth of the Regab pockmark?

Self-sealing processes and formation of new pathways for focused fluid flow are likely the main mechanisms that control the evolution of the pockmark. In this work, two areas with distinct fluid flow regimes could be identified at the Regab pockmark. One area is characterized by relatively large and deep depressions (sub-pockmarks) associated to thick carbonate crusts, abundant and diverse fauna, and gas ebullition. This area is the most active in terms of seepage and is related to the presence of preferential pathways for focused fluid flow, such as fractures, in the shallow sub-surface. The second area is composed of a myriad of unit shallow depressions (‘pits’ or ‘unit pockmarks’) of various dimensions and aspects. This area is associated to comparably low seepage intensity, related to diffuse fluid flow through sediment pores, and occur mostly on the outer side of the pockmark. The formation of unit pockmarks could be related to drainage of pore water, either triggered by fluid advection or by bio-irrigation of the fauna.

It is postulated that the formation of extensive carbonate crusts in the focused flow area, and the subsequent permeability loss (self-sealing), cause fluids to redirect until pathways become available for focused or diffuse flow. Focused flow would occur following the reopening of a former pathway through breakup of the carbonate seal, or when a new preferential pathway is found on the side of the sealed area. With time, a new focused fluid pathway will lead to the formation of a sub-pockmark at the surface, as well with carbonate crusts and diverse fauna. Conversely, diffuse flow occurs as long as sufficient pathways for focused flow are not available. In the absence of focused pathways, seepage continues through a continuous and porous medium, and rising fluids disperse over a larger area; at the surface, such seepage is associated with small and shallow sub-pockmarks and low faunal diversity.

(5) To what extent do high-resolution acoustic and optical datasets allow understanding vent- and seep-related processes?

This work showed that geo-referenced mosaics are so far the best tools currently available to perform spatial analyses of fluid flow-related features. By enabling area measurements they allow quantifying vent- and seep-related processes at the scale of entire structures. In particular, this has been shown in this work with the quantification of the faunal consumption in dissolved gases, and of fluid flows at the Menez Gwen hydrothermal vent. The value of

mosaics was also shown in case studies 2 and 3, where they allowed (1) identifying spatial distribution patterns for the fauna and the carbonate crusts, (2) comparing mosaics from different years to study the temporal evolution of the system, and (3) identifying distinct zones with different fluid flow regimes.

It is interesting to note that, although many institutes have been working on improving mosaicking techniques since the first discovery of hydrothermal vents in 1977, these techniques are still marginally used, and most known seabed fluid flow systems have not been fully imaged so far. Very few works provide such large-scale mosaics or quantify fluxes over entire sites.

Similarly, micro-bathymetry maps, either alone or in combination with mosaics and local observations, are still under-represented in studies about seabed fluid flow systems. So far, only few large vent and seep features have been mapped with ROV-mounted multibeam echosounders. However, when available, those datasets are very valuable assets for the understanding of the formation and evolution of the studied structures. The third study case of this work confirms that detailed seafloor topography does give a deeper insight on the mechanisms involved. Indeed, it allowed identifying features that could not be seen on previous datasets of the same pockmark; thus, from morphology differences, different sub-surface fluid flow regimes could be inferred.

Therefore, high-resolution mapping techniques contribute in various ways to the understanding deep-sea processes. However, the benefits gained from such techniques could be much strengthened by combining such maps with other datasets. For instance, additional information about the pore water chemistry or the depth of hydrate deposits and of carbonate concretions in the different zones of the Regab pockmark would be crucial to constrain and support the interpretation of the subsurface processes, and could help assessing chemical and mass fluxes at the scale of the pockmark.

About the technical aspect, this entire work highlighted the need for reliable mosaicking tools that could be used by end-users, without any in-depth knowledge of the mathematics and physics involved. It was mentioned that mosaicking techniques are generally developed by experts in informatics, robotics and computer vision sciences who are often aimed at improving known techniques rather than on developing a robust product for potential end-users. For instance, most recent mosaicking works concentrate on 3-dimensional imaging and mosaicking techniques, but no freely available tool exists for end-users to easily produce 2-dimensional areal mosaics. To palliate this lack, the MATLAB toolbox for large-area photo-mosaicking (LAPM toolbox) that was developed in this work for the third case study will ultimately be freely available on the Internet. This tool is not designed to compete with the most advanced mosaicking techniques, and it is certainly not the fastest either; but it does allow a potential end-user scientist to build a large-scale and geo-referenced photo-mosaic easily, with relatively low knowledge of the technical background involved.

Nevertheless, faster and more robust tools will be required in the future, in order to make mosaics the routine and not the exception. Indeed, the growing interest of the marine scientific community in the field of mosaicking and the increasing number of studies that use photo-mosaics, confirm that underwater mosaics have a huge potential in improving our understanding of deep-sea processes.

Acknowledgements

I would like to thank Prof. Dr. Gerhard Bohrmann for giving me the opportunity to work on this project in his working group. During these three years, Gerhard fully supported my work and provided me with multiple opportunities to carry out the project effectively. He especially gave me the chance to participate in several research cruises, from which I benefited a lot. Many thanks also to Dr. Christoph Waldmann and Dr. Heiko Sahling, who set up this project within the Marie Curie SENSEnet initial training network. I am also thankful to Prof. Dr. Achim J. Kopf, who kindly agreed to spend his Christmas holidays reviewing this thesis.

I greatly thank Dr. Heiko Sahling for his advices and guidance during this project. Heiko significantly contributed to this work with many reviews and comments, and with the very constructive discussions we had.

I am very grateful to Paul Wintersteller and Christian dos Santos Ferreira for their unfailing and enthusiastic technical help and support.

I thank all my colleagues Jan-Hendrik Körber, David Fischer, Tobias Himmler, Stephan Klapp, Thomas Pape, Miriam Römer, Michal Tomczyk, Jiangong Wei, and Tingting Wu, who were always available to help, and with whom it was a pleasure to work. Especially thanks to Jan-Hendrik Körber who shared the office with me for more than three years. It involved extra work for him: apart from patiently listening to my morning blathering, he spent countless hours of his PhD time doing translation work and answering all my questions. Also thanks to Tobias Himmler and David Fischer for telling me all about carbonates or bio-irrigation processes. Further, I would like to thank Angelika Rinkel and Greta Ohling for their constant support and without whom's help I would be long drown in the administrative paperwork.

Special thanks to Dr. Karine Olu and Dr. Hélène Ondréas, who greatly contributed to this thesis by providing me with enormous amounts of data. In particular, Karine gave me the chance to join the WACS cruise and received me at the Ifremer for a long-term secondment. Her support and advices were very helpful.

I would like to thank Prof. Dr. Charles Fisher, Elizabeth Podowski, and Stephanie Lessard-Pilon for receiving me at Penn State College, sharing their knowledge and methods, and for hosting me!

Also thanks to Dr. Doug Connelly and Carla Sands, who did a great job managing the SENSEnet project, and who never forgot to remind project members about deadlines!

I thank my friends for all the good times and for always trying (often successfully) to divert me from work: Michaël Aron, Christophe Bayle, Inge Van Den Beld, William Brocas, Claudia Sofia Burbano, James Collins, Jaime Davies, Yann Ferret, Nicolas Gayet, Cyril Giry, Angélique Gobet, Aline Govin, Jeroen Groeneveld, Gerald Herrling, Julien Herreros, Tobias Himmler, Sebastian Hötzel, Chia-I Huang, Eva Kwoll, Hendrik Lantzsch, Alice Lefebvre, Jérôme Locastro, Eric Meineri, Julien Michel, Jean Nizou, Enoma Omoregie, Arnaud Richard,

Domenico Romano, Mariem Saavedra, Zsuzsanna Tóth, Francesca Valle, Ines Voigt, Laura Wagenknecht, Gunter Wegener, Stefan Wenau, Henry Wu, Marcel Zarrouk.

My greatest thanks go to my parents and my brother for they invaluable support. They always questioned my choices, but also always supported them…and me.

Finally, my apologies to Christina, who had to put up with me and particularly with my 'I-have-a-thesis-to-write' mood of the last months of the project. Thank you Christina for being here and for supporting me.

References

Abramoff MD, Magalhães PJ, Ram SJ (2004) Image processing with ImageJ. *Biophotonics international*, **11**, 36–42.

Allais AG, Borgetto M, Opderbecke J, Pessel N, Rigaud V (2004) Seabed video mosaicking with MATISSE: a technical overview and cruise results. In: *Proceedings of The Fourteenth International Offshore and Polar Engineering Conference*. Toulon, France

Aloisi G, Bouloubassi I, Heijs SK, Pancost RD, Pierre C, Sinninghe Damsté JS, Gottschal JC, Forney LJ, Rouchy JM (2002) CH4-consuming microorganisms and the formation of carbonate crusts at cold seeps. *Earth and Planetary Science Letters*, **203**, 195–203.

Andersen AC, Hourdez S, Marie B, Jollivet D, Lallier FH, Sibuet M (2004) *Escarpia southwardae* sp. nov., a new species of vestimentiferan tubeworm (Annelida, Siboglinidae) from West African cold seeps. *Canadian Journal of Zoology*, **82**, 980–999.

Archer D, Buffett B (2005) Time-dependent response of the global ocean clathrate reservoir to climatic and anthropogenic forcing. *Geochemistry Geophysics Geosystems*, **6**, 13 pp.

Baker PA, Burns SJ (1985) Occurrence and Formation of Dolomite in Organic-Rich Continental Margin Sediments. *AAPG Bulletin*, **69**, 1917–1930.

Ballard B (1977) Notes on a major oceanographic find. *Oceanus*, **20**, 35–44.

Barnes RO, Goldberg ED (1976) Methane production and consumption in anoxic marine sediments. *Geology*, **4**, 297–300.

Baross JA, Hoffman SE (1985) Submarine hydrothermal vents and associated gradient environments as sites for the origin and evolution of life. *Origins of Life and Evolution of Biospheres*, **15**, 327–345.

Barreyre T, Escartín J, Garcia R, Cannat M, Mittelstaedt E, Prados R (2012) Structure, temporal evolution, and heat flux estimates from the Lucky Strike deep-sea hydrothermal field derived from seafloor image mosaics. *Geochemistry Geophysics Geosystems*, **13**, 29 pp.

Bayon G, Loncke L, Dupré S, Caprais JC, Ducassou E, Duperron S, Etoubleau J, Foucher JP, Fouquet Y, Gontharet S, Henderson GM, Huguen C, Klaucke I, Mascle J, Migeon S, Olu-Le Roy K, Ondréas H, Pierre C, Sibuet M, Stadnitskaia A, Woodside J (2009) Multi-disciplinary investigation of fluid seepage on an unstable margin: The case of the Central Nile deep sea fan. *Marine Geology*, **261**, 92–104.

Beer D de, Sauter E, Niemann H, Kaul N, Foucher JP, Witte U, Schlüter M, Boetius A (2006) In situ fluxes and zonation of microbial activity in surface sediments of the Håkon Mosby Mud Volcano. *Limnology and Oceanography*, **51**, 1315–1331.

Bell KLC, Nomikou P, Carey SN, Stathopoulou E, Polymenakou P, Godelitsas A, Roman C, Parks M (2012) “Continued Exploration of the Santorini Volcanic Field and Cretan Basin, Aegean Sea” in New Frontiers in Ocean Exploration: The E/V *Nautilus* and NOAA Ship *Okeanos Explorer* 2011 Field Season by Bell, K.L.C., K. Elliott, C. Martinez, and S.A. Fuller, eds. 2012. *Oceanography*, **25**, 30–31.

Bergquist DC, Andras JP, McNelis T, Howlett S, Horn MJ Van, Fisher CR (2003a) Succession in Gulf of Mexico cold seep vestimentiferan aggregations: the importance of spatial variability. *Marine Ecology*, **24**, 31–44.

Bergquist DC, Fleckenstein C, Knisel J, Begley B, MacDonald IR, Fisher CR (2005) Variations

in seep mussel bed communities along physical and chemical environmental gradients. *Marine Ecology Progress Series*, **293**, 99–108.

Bergquist DC, Urcuyo IA, Fisher CR (2002) Establishment and persistence of seep vestimentiferan aggregations on the upper Louisiana slope of the Gulf of Mexico. *Marine Ecology Progress Series*, **241**, 89–98.

Bergquist DC, Ward T, Cordes EE, McNelis T, Howlett S, Kosoff R, Hourdez S, Carney R, Fisher CR (2003b) Community structure of vestimentiferan-generated habitat islands from Gulf of Mexico cold seeps. *Journal of Experimental Marine Biology and Ecology*, **289**, 197–222.

Bergquist DC, Williams FM, Fisher CR (2000) Longevity record for deep-sea invertebrate. *Nature*, **403**, 499–500.

Boetius A, Beer D de, Felden J, Viehweger M, Asendorf V, Weiz E, Stiens R, Eicken G, Wetzel G, Harmegnies F, Dussud L, Ferré B, Campenhout J Van, Albrecht S, German CR, Camilli R, Billings A, Kinsey JC, Duester A, Yoerger DR, Versteeg W, Vercruysse J, Rycker K de (2010) *Short Cruise Report - MERIAN MSM16/2 - "LOOME"- Long Term Observatory of Mud Volcano Eruptions*. Alfred Wegener Institut für Polar und Meeresforschung, Bremerhaven

Boetius A, Ravenschlag K, Schubert CJ, Rickert D, Widdel F, Gieseke A, Amann R, Jørgensen BB, Witte U, Pfannkuche O (2000) A marine microbial consortium apparently mediating anaerobic oxidation of methane. *Nature*, **407**, 623–626.

Boetius A, Suess E (2004) Hydrate Ridge: a natural laboratory for the study of microbial life fueled by methane from near-surface gas hydrates. *Chemical Geology*, **205**, 291–310.

Bohrmann G, Blinova V, Dehning K, Evtushenko D, Friese C, Hiruta A, Hüttich D, Ivanov M, Klapp SA, Körber JH, Komakhidze G, Kopiske E, Lange K, Mai HA, Malakhova T, Marcon Y, Meinecke G, Pape T, Ratmeyer V, Rehage R, Renken J, Reuter C, Reuter M, Römer M, Sahling H, Sakvarelidze E, Wintersteller P, Zarrouk M (2011) *Report and preliminary results of RV MARIA S. MERIAN Cruise MSM 15/2, Istanbul (Turkey) - Piraeus (Greece), 10 May - 2 June 2010. Origin and structure of methane, gas hydrates and fluid flows in the Black Sea.* Geowissenschaften, Universität Bremen, Bremen

Bohrmann G, Greinert J, Suess E, Torres M (1998) Authigenic carbonates from the Cascadia subduction zone and their relation to gas hydrate stability. *Geology*, **26**, 647–650.

Bohrmann G, Ivanov M, Foucher JP, Spiess V, Bialas J, Greinert J, Weinrebe W, Abegg F, Aloisi G, Artemov Y, Blinova V, Drews M, Heidersdorf F, Krabbenhöft A, Klaucke I, Krastel S, Leder T, Polikarpov I, Saburova M, Schmale O, Seifert R, Volkonskaya A, Zillmer M (2003) Mud volcanoes and gas hydrates in the Black Sea: new data from Dvurechenskii and Odessa mud volcanoes. *Geo-Marine Letters*, **23**, 239–249.

Bohrmann G, Torres ME (2006) Gas Hydrates in Marine Sediments. In: Schulz HD, Zabel M (eds) *Marine Geochemistry*. Springer Berlin Heidelberg, p481–512.

Borowski WS, Paull CK, Ussler III W (1999) Global and local variations of interstitial sulfate gradients in deep-water, continental margin sediments: Sensitivity to underlying methane and gas hydrates. *Marine Geology*, **159**, 131–154.

Brandou V, Allais AG, Perrier M, Malis E, Rives P, Sarrazin J, Sarradin PM (2007) 3D reconstruction of natural underwater scenes using the stereovision system IRIS. In: *Proceedings of the MTS/IEEE Oceans 2007 Conference*. p1–6.

Buffett B, Archer D (2004) Global inventory of methane clathrate: sensitivity to changes in the deep ocean. *Earth and Planetary Science Letters*, **227**, 185–199.

Burt PJ, Adelson EH (1983) A multiresolution spline with application to image mosaics. *ACM Transactions on Graphics*, **2**, 217–236.

Burton EA (1993) Controls on marine carbonate cement mineralogy: review and reassessment. *Chemical Geology*, **105**, 163–179.

Butterfield DA, Jonasson IR, Massoth GJ, Feely RA, Roe KK, Embley RE, Holden JF, McDuff RE, Lilley MD, Delaney JR, Pyle D (1997) Seafloor Eruptions and Evolution of Hydrothermal Fluid Chemistry [and Discussion]. *Philosophical Transactions: Mathematical, Physical and Engineering Sciences*, **355**, 369–386.

Butterfield DA, McDuff RE, Mottl MJ, Lilley MD, Lupton JE, Massoth GJ (1994) Gradients in the composition of hydrothermal fluids from the Endeavour segment vent field: Phase separation and brine loss. *Journal of Geophysical Research*, **99**, 9561–9583.

Cambon-Bonavita MA, Nadalig T, Roussel E, Delage E, Duperron S, Caprais JC, Boetius A, Sibuet M (2009) Diversity and distribution of methane-oxidizing microbial communities associated with different faunal assemblages in a giant pockmark of the Gabon continental margin. *Deep Sea Research Part II: Topical Studies in Oceanography*, **56**, 2248–2258.

Campbell KA (2006) Hydrocarbon seep and hydrothermal vent paleoenvironments and paleontology: Past developments and future research directions. *Palaeogeography, Palaeoclimatology, Palaeoecology*, **232**, 362–407.

Caress DW, Chayes DN (2001) Improved management of large swath mapping datasets in MB-System Version 5. *AGU Fall Meeting Abstracts*.

Chaduteau C, Jean-Baptiste P, Fourré E, Charlou JL, Donval JP (2009) Helium transport in sediment pore fluids of the Congo-Angola margin. *Geochemistry Geophysics Geosystems*, **10**, 12 pp.

Charlou JL, Donval JP (1993) Hydrothermal methane venting between 12°N and 26°N along the Mid-Atlantic Ridge. *Journal of Geophysical Research*, **98**, 9625–9642.

Charlou JL, Donval JP, Douville E, Jean-Baptiste P, Radford-Knoery J, Fouquet Y, Dapoigny A, Stievenard M (2000) Compared geochemical signatures and the evolution of Menez Gwen (37°50'N) and Lucky Strike (37°17'N) hydrothermal fluids, south of the Azores Triple Junction on the Mid-Atlantic Ridge. *Chemical Geology*, **171**, 49–75.

Charlou JL, Donval JP, Fouquet Y, Jean-Baptiste P, Holm N (2002) Geochemistry of high H2 and CH4 vent fluids issuing from ultramafic rocks at the Rainbow hydrothermal field (36°14′N, MAR). *Chemical Geology*, **191**, 345–359.

Charlou JL, Donval JP, Fouquet Y, Ondréas H, Knoery J, Cochonat P, Levaché D, Poirier Y, Jean-Baptiste P, Fourré E, Chazallon B (2004) Physical and chemical characterization of gas hydrates and associated methane plumes in the Congo–Angola Basin. *Chemical Geology*, **205**, 405–425.

Charlou JL, Fouquet Y, Bougault H, Donval JP, Etoubleau J, Jean-Baptiste P, Dapoigny A, Appriou P, Rona PA (1998) Intense CH4 plumes generated by serpentinization of ultramafic rocks at the intersection of the 15°20′N fracture zone and the Mid-Atlantic Ridge. *Geochimica et Cosmochimica Acta*, **62**, 2323–2333.

Charlou JL, Fouquet Y, Donval JP, Auzende JM, Jean-Baptiste P, Stievenard M, Michel S (1996) Mineral and gas chemistry of hydrothermal fluids on an ultrafast spreading ridge: East Pacific Rise, 17° to 19°S (Naudur cruise, 1993) phase separation processes controlled by volcanic and tectonic activity. *Journal of Geophysical Research*, **101**, 15,899–15,919.

Claypool GE, Kvenvolden KA (1983) Methane and other hydrocarbon gases in marine sediment. *Annual Review of Earth and Planetary Sciences*, **11**, 299–327.

Clennell MB, Judd A, Hovland M (2000) Chapter 9. Movement and Accumulation of Methane in Marine Sediments: Relation to Gas Hydrate Systems. In: Max MD (ed) *Gas Hydrates in Oceanic and Permafrost Environments*. p105–122.

Colaço A, Desbruyères D, Comtet T, Alayse AM (1998) Ecology of the Menez Gwen hydrothermal vent field (Mid-Atlantic Ridge/Azores Triple Junction). *Cahiers de Biologie Marine*, **39**, 237–240.

Collett TS (2002) Energy Resource Potential of Natural Gas Hydrates. *AAPG Bulletin*, **86**, 1971–1992.

Comtet T, Desbruyères D (1998) Population structure and recruitment in mytilid bivalves from the Lucky Strike and Menez Gwen hydrothermal vent fields (37°17'N and 37°50'N on the Mid-Atlantic Ridge). *Marine Ecology Progress Series*, **163**, 165–177.

Copley J, Tyler PA, Murton BJ, Dover CL van (1997) Spatial and interannual variation in the faunal distribution at Broken Spur vent field (29°N, Mid-Atlantic Ridge). *Marine Biology*, **129**, 723–733.

Cordes EE, Arthur MA, Shea K, Arvidson RS, Fisher CR (2005a) Modeling the mutualistic interactions between tubeworms and microbial consortia. *PLoS Biology*, **3**, 497–506.

Cordes EE, Bergquist DC, Fisher CR (2009) Macro-ecology of Gulf of Mexico cold seeps. *Annual Review of Marine Science*, **1**, 143–168.

Cordes EE, Bergquist DC, Shea K, Fisher CR (2003) Hydrogen sulphide demand of long-lived vestimentiferan tube worm aggregations modifies the chemical environment at deep-sea hydrocarbon seeps. *Ecology Letters*, **6**, 212–219.

Cordes EE, Hourdez S, Predmore BL, Redding ML, Fisher CR (2005b) Succession of hydrocarbon seep communities associated with the long-lived foundation species *Lamellibrachia luymesi*. *Marine Ecology Progress Series*, **305**, 17–29.

Corliss JB, Dymond J, Gordon LI, Edmond JM, Herzen RP von, Ballard RD, Green K, Williams D, Bainbridge A, Crane K, Andel TH van (1979) Submarine Thermal Springs on the Galapagos Rift. *Science*, **203**, 1073–1083.

Cosel R von, Comtet T, Krylova EM (1999) *Bathymodiolus* (Bivalvia : Mytilidae) from hydrothermal vents on the Azores Triple Junction and the Logatchev hydrothermal field, Mid-Atlantic Ridge. *VELIGER*, **42**, 218–248.

Cosel R von, Olu K (2008) A new genus and new species of Vesicomyidae (Mollusca, Bivalvia) from cold seeps on the Barbados accretionary prism, with comments on other species. *Zoosystema*, **30**, 929–944.

Cosel R von, Olu K (2009) Large Vesicomyidae (Mollusca: Bivalvia) from cold seeps in the Gulf of Guinea off the coasts of Gabon, Congo and northern Angola. *Deep Sea Research Part II: Topical Studies in Oceanography*, **56**, 2350–2379.

Cuvelier D, Sarrazin J, Colaço A, Copley J, Desbruyères D, Glover AG, Tyler P, Serrão-Santos R (2009) Distribution and spatial variation of hydrothermal faunal assemblages at Lucky Strike (Mid-Atlantic Ridge) revealed by high-resolution video image analysis. *Deep Sea Research Part I: Oceanographic Research Papers*, **56**, 2026–2040.

Cuvelier D, Sarrazin J, Colaço A, Copley JT, Glover AG, Tyler PA, Serrão Santos R, Desbruyères D (2011) Community dynamics over 14 years at the Eiffel Tower hydrothermal edifice on the Mid-Atlantic Ridge. *Limnology and Oceanography*, **56**, 1624–1640.

Damm KL von (1995) Controls on the chemistry and temporal variability of seafloor hydrothermal fluids. *Geophysical Monograph Series*, **91**, 222–247.

Dattagupta S, Arthur MA, Fisher CR (2008) Modification of sediment geochemistry by the hydrocarbon seep tubeworm *Lamellibrachia luymesi*: A combined empirical and modeling approach. *Geochimica et Cosmochimica Acta*, **72**, 2298–2315.

Decker C, Caprais JC, Khripounoff A, Olu K (2012) First respiration estimates of cold-seep vesicomyid bivalves from in situ total oxygen uptake measurements. *Comptes Rendus Biologies*, **335**, 261–270.

Delaney JR, Robigou V, McDuff RE, Tivey MK (1992) Geology of a vigorous hydrothermal system on the Endeavour segment, Juan de Fuca Ridge. *Journal of Geophysical Research*, **97**, 663–682.

Desbruyères D, Biscoito M, Caprais JC, Colaço A, Comtet T, Crassous P, Fouquet Y, Khripounoff A, Bris N Le, Olu K, Riso R, Sarradin PM, Segonzac M, Vangriesheim A (2001) Variations in deep-sea hydrothermal vent communities on the Mid-Atlantic Ridge near the Azores plateau. *Deep Sea Research Part I: Oceanographic Research Papers*, **48**, 1325–1346.

Desbruyères D, Laubier L (1991) Systematics, phylogeny, ecology and distribution of the Alvinellidae (Polychaeta) from deep-sea hydrothermal vents. *Ophelia*, **5**, 31–45.

Desbruyères D, Segonzac M, Bright M (2006) *Handbook of deep-sea hydrothermal vent fauna*. Biologiezentrum der Oberösterreichisches Landesmuseen: 544 pp. pp.

Devol AH, Ahmed SI (1981) Are high rates of sulphate reduction associated with anaerobic oxidation of methane? *Nature*, **291**, 407–408.

Dickens GR (2003) Rethinking the global carbon cycle with a large, dynamic and microbially mediated gas hydrate capacitor. *Earth and Planetary Science Letters*, **213**, 169–183.

Dixon DR, Dando PR, Santos RS, Gwynn JP, VENTOX C (2001) Retrievable cages open up new era in deep-sea vent research. *InterRidge News*, **10**, 21–23.

Douville E, Charlou J., Oelkers E., Bienvenu P, Jove Colon C., Donval J., Fouquet Y, Prieur D, Appriou P (2002) The rainbow vent fluids (36°14′N, MAR): the influence of ultramafic rocks and phase separation on trace metal content in Mid-Atlantic Ridge hydrothermal fluids. *Chemical Geology*, **184**, 37–48.

Dover CL van (2000) *The Ecology of Deep-Sea Hydrothermal Vents*. Princeton Univ. Press, Princeton, N.J.

Dover CL van, Desbruyères D, Segonzac M, Comtet T, Saldanha L, Fiala-Médioni A, Langmuir C (1996) Biology of the Lucky Strike hydrothermal field. *Deep Sea Research Part I: Oceanographic Research Papers*, **43**, 1509–1529.

Dover CL van, Humphris SE, Fornari D, Cavanaugh CM, Collier R, Goffredi SK, Hashimoto J, Lilley MD, Reysenbach AL, Shank TM, Damm KL von, Banta A, Gallant RM, Götz D, Green D, Hall J, Harmer TL, Hurtado LA, Johnson P, McKiness ZP, Meredith C, Olson E, Pan IL, Turnipseed M, Won Y, Young CR, Bolles RC (2001) Biogeography and Ecological Setting of Indian Ocean Hydrothermal Vents. *Science*, **294**, 818–823.

Droz L, Rigaut F, Cochonat P, Tofani R (1996) Morphology and recent evolution of the Zaire turbidite system (Gulf of Guinea). *Geological Society of America Bulletin*, **108**, 253–269.

Dubilier N, Bergin C, Lott C (2008) Symbiotic diversity in marine animals: the art of harnessing chemosynthesis. *Nature Reviews Microbiology*, **6**, 725–740.

Duperron S, Bergin C, Zielinski F, Blazejak A, Pernthaler A, McKiness ZP, DeChaine E, Cavanaugh CM, Dubilier N (2006) A dual symbiosis shared by two mussel species, *Bathymodiolus azoricus* and *Bathymodiolus puteoserpentis* (Bivalvia: Mytilidae), from

hydrothermal vents along the northern Mid-Atlantic Ridge. *Environmental Microbiology*, **8**, 1441–1447.

Duperron S, Guezi H, Gaudron SM, Pop Ristova P, Wenzhöfer F, Boetius A (2011) Relative abundances of methane- and sulphur-oxidising symbionts in the gills of a cold seep mussel and link to their potential energy sources. *Geobiology*, **9**, 481–491.

Duperron S, Nadalig T, Caprais JC, Sibuet M, Fiala-Medioni A, Amann R, Dubilier N (2005) Dual symbiosis in a *Bathymodiolus* sp. mussel from a methane seep on the Gabon continental margin (Southeast Atlantic): 16S rRNA phylogeny and distribution of the symbionts in gills. *Applied and Environmental Microbiology*, **71**, 1694–1700.

Dupré S, Buffet G, Mascle J, Foucher JP, Gauger S, Boetius A, Marfia C (2008) High-resolution mapping of large gas emitting mud volcanoes on the Egyptian continental margin (Nile Deep Sea Fan) by AUV surveys. *Marine Geophysical Researches*, **29**, 275–290.

Durand B (1980) *Kerogen: Insoluble organic matter from sedimentary rocks*. Editions technip

Durand S, Bel M Le, Juniper SK, Legendre P (2002) The use of video surveys, a Geographic Information System and sonar backscatter data to study faunal community dynamics at Juan de Fuca Ridge hydrothermal vents. *Cahiers de Biologie Marine*, **43**, 235–240.

Edmond JM, Damm KL von, McDuff RE, Measures CI (1982) Chemistry of hot springs on the East Pacific Rise and their effluent dispersal. *Nature*, **297**, 187–191.

Escartín J, García R, Delaunoy O, Ferrer J, Gracias N, Elibol A, Cufi X, Neumann L, Fornari DJ, Humphris SE, Renard J (2008) Globally aligned photomosaic of the Lucky Strike hydrothermal vent field (Mid-Atlantic Ridge, 37°18.5′N): Release of georeferenced data, mosaic construction, and viewing software. *Geochemistry Geophysics Geosystems*, **9**, 17 pp.

Etiope G, Martinelli G (2002) Migration of carrier and trace gases in the geosphere: an overview. *Physics of the Earth and Planetary Interiors*, **129**, 185–204.

Eustice R, Pizarro O, Singh H, Howland J (2002) UWIT: Underwater Image Toolbox for optical image processing and mosaicking in MATLAB. In: *Proceedings of the 2002 International Symposium on Underwater Technology, 2002.* p141–145.

Ferrer J, Elibol A, Delaunoy O, Gracias N, Garcia R (2007) Large-area photo-mosaics using global alignment and navigation data. In: *Proceedings of the MTS/IEEE Oceans 2007 Conference*. p1–9.

Feseker T, Brown K, Blanchet C, Scholz F, Nuzzo M, Reitz A, Schmidt M, Hensen C (2010) Active mud volcanoes on the upper slope of the western Nile deep-sea fan—first results from the P362/2 cruise of R/V <i>Poseidon</i> *Geo-Marine Letters*, **30**, 169–186.

Fiala-Médioni A, McKiness ZP, Dando P, Boulegue J, Mariotti A, Alayse-Danet AM, Robinson JJ, Cavanaugh CM (2002) Ultrastructural, biochemical, and immunological characterization of two populations of the mytilid mussel *Bathymodiolus azoricus* from the Mid-Atlantic Ridge: evidence for a dual symbiosis. *Marine Biology*, **141**, 1035–1043.

Fischer D, Sahling H, Nöthen K, Bohrmann G, Zabel M, Kasten S (2011) Interaction between hydrocarbon seepage, chemosynthetic communities and bottom water redox at cold seeps of the Makran accretionary prism: insights from habitat-specific pore water sampling and modeling. *Biogeosciences Discuss*, **8**, 9763–9811.

Fisher CR, Urcuyo IA, Simpkins MA, Nix E (1997) Life in the slow lane: Growth and longevity of cold-seep vestimentiferans. *Marine Ecology*, **18**, 83–94.

Fleischer SD, Rock SM (1998) Experimental validation of a real-time vision sensor and navigation system for intelligent underwater vehicles. In: *IEEE International Conference on Intelligent Vehicles*.

Fleischer SD, Rock SM, Burton R (1997) Global position determination and vehicle path estimation from a vision sensor for real-time video mosaicking and navigation. In: *OCEANS'97. MTS/IEEE Conference Proceedings*. p641–647.

Fleischer SD, Wang HH, Rock SM, Lee MJ (1996) Video mosaicking along arbitrary vehicle paths. In: *Proceedings of the 1996 Symposium on Autonomous Underwater Vehicle Technology, 1996. AUV'96.* p293–299.

Floodgate GD, Judd AG (1992) The origins of shallow gas. *Continental Shelf Research*, **12**, 1145–1156.

Fort X, Brun JP, Chauvel F (2004) Salt tectonics on the Angolan margin, synsedimentary deformation processes. *AAPG Bulletin*, **88**, 1523–1544.

Fouquet Y, Charlou JL, Costa I, Donval JP, Radford-Knoery J, Pellé H, Ondréas H, Lourenco N, Segonzac M, Tivey MK (1994) A detailed study of the Lucky Strike hydrothermal site and discovery of a new hydrothermal site: Menez Gwen; preliminary results of the DIVA1 cruise (5-29 May, 1994). *InterRidge News*, **3**, 14–17.

Fouquet Y, Ondréas H, Charlou JL, Donval JP, Radford-Knoery J, Costa I, Lourenco N, Tivey MK (1995) Atlantic lava lakes and hot vents. *Nature*, **377**, p. 201.

Fouquet Y, Schultz A, Fouquet Y, Herrington R, Nesbitt RW (1997) Where are the large hydrothermal sulphide deposits in the oceans? *Philosophical Transactions: Mathematical, Physical and Engineering Sciences*, **355**, 427–441.

Foustoukos DI, Seyfried Jr. WE (2007) Fluid Phase Separation Processes in Submarine Hydrothermal Systems. *Reviews in Mineralogy and Geochemistry*, **65**, 213–239.

Fustec A, Desbruyères D, Laubier L (1988) Estimation de la biomasse des peuplements associés aux sources hydrothermales profondes de la dorsale du Pacifique oriental à 13^{o}N. *Oceanologica Acta*, **8**, 15–21.

Gaever S van, Galéron J, Sibuet M, Vanreusel A (2009) Deep-sea habitat heterogeneity influence on meiofaunal communities in the Gulf of Guinea. *Deep Sea Research Part II: Topical Studies in Oceanography*, **56**, 2259–2269.

Gal L Le, Edy C (1997) CARAIBES: an integrated software for multibeam echosounder and sidescan sonar data mapping. In: *OCEANS '97. MTS/IEEE Conference Proceedings*. p1242–1245.

Galkin SV, Goroslavskaya EI (2010) Bottom fauna associated with *Bathymodiolus azoricus* (Mytilidae) mussel beds in the hydrothermal fields of the Mid-Atlantic Ridge. *Oceanology*, **50**, 51–60.

Gay A, Lopez M (2004) Polygonal faults-furrows system related to early stages of compaction - upper Miocene to present sediments of the Lower Congo Basin. *Basin Research*, **16**, 101–116.

Gay A, Lopez M, Berndt C, Séranne M (2007) Geological controls on focused fluid flow associated with seafloor seeps in the Lower Congo Basin. *Marine Geology*, **244**, 68–92.

Gay A, Lopez M, Cochonat P, Levaché D, Sermondadaz G, Seranne M (2006a) Evidences of early to late fluid migration from an upper Miocene turbiditic channel revealed by 3D seismic coupled to geochemical sampling within seafloor pockmarks, Lower Congo Basin. *Marine and Petroleum Geology*, **23**, 387–399.

Gay A, Lopez M, Cochonat P, Séranne M, Levaché D, Sermondadaz G (2006b) Isolated seafloor pockmarks linked to BSRs, fluid chimneys, polygonal faults and stacked Oligocene–Miocene turbiditic palaeochannels in the Lower Congo Basin. *Marine Geology*, **226**, 25–40.

Gay A, Lopez M, Cochonat P, Sultan N, Cauquil E, Brigaud F (2003) Sinuous pockmark belt as indicator of a shallow buried turbiditic channel on the lower slope of the Congo basin, West African margin. *Geological Society, London, Special Publications*, **216**, 173–189.

Gay A, Lopez M, Ondréas H, Charlou JL, Sermondadaz G, Cochonat P (2006c) Seafloor facies related to upward methane flux within a Giant Pockmark of the Lower Congo Basin. *Marine Geology*, **226**, 81–95.

Gebruk AV, Chevaldonné P, Shank T, Lutz RA, Vrijenhoek RC (2000a) Deep-sea hydrothermal vent communities of the Logatchev area (14°45′N, Mid-Atlantic Ridge): diverse biotopes and high biomass. *Journal of the Marine Biological Association of the United Kingdom*, **80**, 383–393.

Gebruk AV, Southward EC, Kennedy H, Southward AJ (2000b) Food sources, behaviour, and distribution of hydrothermal vent shrimps at the Mid-Atlantic Ridge. , **80**, 485–499.

German CR, Thurnherr AM, Knoery J, Charlou JL, Jean-Baptiste P, Edmonds HN (2010) Heat, volume and chemical fluxes from submarine venting: A synthesis of results from the Rainbow hydrothermal field, 36°N MAR. *Deep Sea Research Part I: Oceanographic Research Papers*, **57**, 518–527.

Gracias N, Mahoor M, Negahdaripour S, Gleason A (2009) Fast image blending using watersheds and graph cuts. *Image and Vision Computing*, **27**, 597–607.

Gracias N, Santos-Victor J (2001) Underwater mosaicing and trajectory reconstruction using global alignment. *Proceedings of the MTS/IEEE Oceans 2001 Conference*, 7 pp.

Grehan AJ, Juniper SK (1996) Clam distribution and subsurface hydrothermal processes at Chowder Hill (Middle Valley), Juan de Fuca Ridge. *Marine Ecology Progress Series*, **130**, 105–115.

Greinert J, Artemov Y, Egorov V, Batist M De, McGinnis D (2006) 1300-m-high rising bubbles from mud volcanoes at 2080 m in the Black Sea: Hydroacoustic characteristics and temporal variability. *Earth and Planetary Science Letters*, **244**, 1–15.

Haas A, Little CTS, Sahling H, Bohrmann G, Himmler T, Peckmann J (2009) Mineralization of vestimentiferan tubes at methane seeps on the Congo deep-sea fan. *Deep Sea Research Part I: Oceanographic Research Papers*, **56**, 283–293.

Haas A, Peckmann J, Elvert M, Sahling H, Bohrmann G (2010) Patterns of carbonate authigenesis at the Kouilou pockmarks on the Congo deep-sea fan. *Marine Geology*, **268**, 129–136.

Harrington P (1985) Formation of pockmarks by pore-water escape. *Geo-Marine Letters*, **5**, 193–197.

Hessler RR, Smithey WM (1983) *Hydrothermal processes at seafloor spreading centers*. Plenum Press, New York, N.Y.

Hessler RR, Smithey WM, Boudrias MA, Keller CH, Lutz RA, Childress JJ (1988) Temporal change in megafauna at the Rose Garden hydrothermal vent (Galapagos Rift; eastern tropical Pacific). *Deep Sea Research Part A Oceanographic Research Papers*, **35**, 1681–1709.

Hinrichs KU, Boetius A (2002) The anaerobic oxidation of methane: new insights in microbial

ecology and biogeochemistry. In: *Ocean Margin Systems*. Springer-Verlag, Berlin, p457–477.

Hoehler TM, Alperin MJ, Albert DB, Martens CS (1994) Field and laboratory studies of methane oxidation in an anoxic marine sediment: Evidence for a methanogen-sulfate reducer consortium. *Global Biogeochemical Cycles*, **8**, 451–463.

Hovland M (2002) On the self-sealing nature of marine seeps. *Continental Shelf Research*, **22**, 2387–2394.

Hovland M, Gardner JV, Judd AG (2002) The significance of pockmarks to understanding fluid flow processes and geohazards. *Geofluids*, **2**, 127–136.

Hovland M, Judd AG, King LH (1984) Characteristic features of pockmarks on the North Sea Floor and Scotian Shelf. *Sedimentology*, **31**, 471–480.

Hovland M, Svensen H (2006) Submarine pingoes: Indicators of shallow gas hydrates in a pockmark at Nyegga, Norwegian Sea. *Marine Geology*, **228**, 15–23.

Hovland M, Svensen H, Forsberg CF, Johansen H, Fichler C, Fosså JH, Jonsson R, Rueslåtten H (2005) Complex pockmarks with carbonate-ridges off mid-Norway: Products of sediment degassing. *Marine Geology*, **218**, 191–206.

Huene R von, Scholl DW (1991) Observations at convergent margins concerning sediment subduction, subduction erosion, and the growth of continental crust. *Reviews of Geophysics*, **29**, 279–316.

Iversen N, Jørgensen BB (1985) Anaerobic Methane Oxidation Rates at the Sulfate-Methane Transition in Marine Sediments from Kattegat and Skagerrak (Denmark). *Limnology and Oceanography*, **30**, 944–955.

Jansen JHF, Giresse P, Moguedet G (1984) Structural and sedimentary geology of the Congo and Southern Gabon continental shelf; a seismic and acoustic reflection survey. *Netherlands Journal of Sea Research*, **17**, 364–384.

Jean-Baptiste P, Charlou JL, Stievenard M, Donval JP, Bougault H, Mevel C (1991) Helium and methane measurements in hydrothermal fluids from the mid-Atlantic ridge: The Snake Pit site at 23°N. *Earth and Planetary Science Letters*, **106**, 17–28.

Jean-Baptiste P, Fourré E, Charlou JL, German CR, Radford-Knoery J (2004) Helium isotopes at the Rainbow hydrothermal site (Mid-Atlantic Ridge, 36°14′N). *Earth and Planetary Science Letters*, **221**, 325–335.

Jerosch K, Lüdtke A, Schlüter M, Ioannidis GT (2007a) Automatic content-based analysis of georeferenced image data: Detection of Beggiatoa mats in seafloor video mosaics from the Håkon Mosby Mud Volcano. *Computers & Geosciences*, **33**, 202–218.

Jerosch K, Schlüter M, Foucher JP, Allais AG, Klages M, Edy C (2007b) Spatial distribution of mud flows, chemoautotrophic communities, and biogeochemical habitats at Håkon Mosby Mud Volcano. *Marine Geology*, **243**, 1–17.

Jerosch K, Schlüter M, Pesch R (2006) Spatial analysis of marine categorical information using indicator kriging applied to georeferenced video mosaics of the deep-sea Håkon Mosby Mud Volcano. *Ecological Informatics*, **1**, 391–406.

Judd AG (2003) The global importance and context of methane escape from the seabed. *Geo-Marine Letters*, **23**, 147–154.

Judd AG, Hovland M (2007) *Seabed fluid flow: the impact of geology, biology and the marine*

environment. Cambridge University Press, Cambridge: 387 pp. pp.

Juniper SK, Sarrazin J, Grehan A (1998) Remote sensing of organism density and biomass at hydrothermal vents. *Cahiers de biologie marine*, **39**, 245–247.

Keir RS, Schmale O, Walter M, Sültenfuß J, Seifert R, Rhein M (2008) Flux and dispersion of gases from the “Drachenschlund” hydrothermal vent at 8°18’ S, 13°30’ W on the Mid-Atlantic Ridge. *Earth and Planetary Science Letters*, **270**, 338–348.

Kelley DS (1996) Methane-rich fluids in the oceanic crust. *Journal of Geophysical Research*, **101**, 2943–2962.

Kelley DS, Baross JA, Delaney JR (2002) Volcanoes, Fluids, and Life at Mid-Ocean Ridge Spreading Centers. *Annual Review of Earth and Planetary Sciences*, **30**, 385–491.

Kelley DS, Karson JA, Blackman DK, Früh-Green GL, Butterfield DA, Lilley MD, Olson EJ, Schrenk MO, Roe KK, Lebon GT, Rivizzigno P, Party the A-60 S (2001) An off-axis hydrothermal vent field near the Mid-Atlantic Ridge at 30° N. *Nature*, **412**, 145–149.

King LH, MacLean B (1970) Pockmarks on the Scotian Shelf. *Geological Society of America Bulletin*, **81**, 3141–3148.

Klaucke I, Sahling H, Weinrebe W, Blinova V, Bürk D, Lursmanashvili N, Bohrmann G (2006) Acoustic investigation of cold seeps offshore Georgia, eastern Black Sea. *Marine Geology*, **231**, 51–67.

Knittel K, Boetius A (2009) Anaerobic Oxidation of Methane: Progress with an Unknown Process. *Annual Review of Microbiology*, **63**, 311–334.

Krylova EM, Cosel R von (2011) A new genus of large Vesicomyidae (Mollusca, Bivalvia, Vesicomyidae, Pliocardiinae) from the Congo margin, with the first record of the subfamily Pliocardiinae in the Bay of Biscay (northeastern Atlantic). *Zoosystema*, **33**, 83–99.

Kulm LD, Suess E, Moore JC, Carson B, Lewis BT, Ritger SD, Kadko DC, Thornburg TM, Embley RW, Rugh WD, Massoth GJ, Langseth MG, Cochrane GR, Scamman RL (1986) Oregon subduction zone: venting, fauna, and carbonates. *Science*, **231**, 561–566.

Kvenvolden KA (1993) Gas hydrates—geological perspective and global change. *Reviews of Geophysics*, **31**, 173–187.

Lessard-Pilon SA, Podowski EL, Cordes EE, Fisher CR (2010a) Megafauna community composition associated with *Lophelia pertusa* colonies in the Gulf of Mexico. *Deep Sea Research Part II: Topical Studies in Oceanography*, **57**, 1882–1890.

Lessard-Pilon SA, Porter MD, Cordes EE, MacDonald IR, Fisher CR (2010b) Community composition and temporal change at deep Gulf of Mexico cold seeps. *Deep Sea Research Part II: Topical Studies in Oceanography*, **57**, 1891–1903.

Levin LA (2005) Ecology of cold seep sediments : Interactions of fauna with flow, chemistry and microbes. *Oceanography and Marine Biology*, **43**, 1–46.

Levin LA, Ziebis W, Mendoza GF, Growney VA, Tryon MD, Brown KM, Mahn C, Gieskes JM, Rathburn AE (2003) Spatial heterogeneity of macrofauna at northern California methane seeps: influence of sulfide concentration and fluid flow. *Marine Ecology Progress Series*, **265**, 123–139.

Lilley MD, Butterfield DA, Lupton JE, Olson EJ (2003) Magmatic events can produce rapid changes in hydrothermal vent chemistry. *Nature*, **422**, 878–881.

Lilley MD, Butterfield DA, Olson EJ, Lupton JE, Macko SA, McDuff RE (1993) Anomalous CH4 and NH4+ concentrations at an unsedimented mid-ocean-ridge hydrothermal system. *Nature*, **364**, 45–47.

Lilley MD, Olson EJ (2001) Methane and Hydrogen in Active Hydrothermal Systems. In: *Eleventh Annual V. M. Goldschmidt Conference*.

Lirman D, Gracias N, Gintert BR, Gleason AC., Reid RP, Negahdaripour S, Kramer P (2007) Development and application of a video-mosaic survey technology to document the status of coral reef communities. *Environmental Monitoring and Assessment*, **125**, 59–73.

Loncke L, Mascle J, Fanil Scientific Parties (2004) Mud volcanoes, gas chimneys, pockmarks and mounds in the Nile deep-sea fan (Eastern Mediterranean): geophysical evidences. *Marine and Petroleum Geology*, **21**, 669–689.

Lowe DG (1999) Object recognition from local scale-invariant features. In: *The Proceedings of the Seventh IEEE International Conference on Computer Vision, 1999*. p1150–1157.

Lowe DG (2004) Distinctive image features from scale-invariant keypoints. *International Journal of Computer Vision*, **60**, 91–110.

Luff R, Wallmann K (2003) Fluid flow, methane fluxes, carbonate precipitation and biogeochemical turnover in gas hydrate-bearing sediments at Hydrate Ridge, Cascadia Margin: numerical modeling and mass balances. *Geochimica et Cosmochimica Acta*, **67**, 3403–3421.

Luff R, Wallmann K, Aloisi G (2004) Numerical modeling of carbonate crust formation at cold vent sites: significance for fluid and methane budgets and chemosynthetic biological communities. *Earth and Planetary Science Letters*, **221**, 337–353.

Lutz RA, Kennish MJ (1993) Ecology of deep-sea hydrothermal vent communities: A review. *Rev Geophys*, **31**, 211–242.

MacDonald GJ (1990) Role of methane clathrates in past and future climates. *Climatic Change*, **16**, 247–281.

MacDonald IR, Guinasso NL, Sassen R, Brooks JM, Lee L, Scott KT (1994) Gas hydrate that breaches the sea floor on the continental slope of the Gulf of Mexico. *Geology*, **22**, 699–702.

MacDonald IR, Sager WW, Peccini MB (2003) Gas hydrate and chemosynthetic biota in mounded bathymetry at mid-slope hydrocarbon seeps: Northern Gulf of Mexico. *Marine Geology*, **198**, 133–158.

Mackenzie AS, Quigley TM (1988) Principles of Geochemical Prospect Appraisal. *AAPG Bulletin*, **72**, 399–415.

Makogon YF, Holditch SA, Makogon TY (2007) Natural gas-hydrates — A potential energy source for the 21st Century. *Journal of Petroleum Science and Engineering*, **56**, 14–31.

Marks RL, Rock SM, Lee MJ (1994) Real-time video mosaicking of the ocean floor. In: *Proceedings of the 1994 Symposium on Autonomous Underwater Vehicle Technology, 1994. AUV '94.* p21–27.

Martens CS, Berner RA (1977) Interstitial Water Chemistry of Anoxic Long Island Sound Sediments. 1. Dissolved Gases. *Limnology and Oceanography*, **22**, 10–25.

Martins I, Colaço A, Dando PR, Martins I, Desbruyères D, Sarradin PM, Marques JC, Serrão-Santos R (2008) Size-dependent variations on the nutritional pathway of *Bathymodiolus*

azoricus demonstrated by a C-flux model. *Ecological Modelling*, **217**, 59–71.

Marton LG, Tari GC, Lehmann CT (2000) Evolution of the Angolan passive margin, West Africa, with emphasis on post-salt structural styles. In: Mohriak W, Taiwani M (eds) *Atlantic Rifts and Continental Margins*, AGU. Washington, D.C., p129–149.

Mascle A, Moore JC (1990) ODP Leg 110; tectonic and hydrologic synthesis. *Proceedings of the Ocean Drilling Program, 110 Scientific Results*, **110**, 409–425.

Maslin M, Owen M, Betts R, Day S, Jones TD, Ridgwell A (2010) Gas hydrates: past and future geohazard? *Philosophical Transactions of the Royal Society A: Mathematical, Physical and Engineering Sciences*, **368**, 2369–2393.

Maslin M, Owen M, Day S, Long D (2004) Linking continental-slope failures and climate change: Testing the clathrate gun hypothesis. *Geology*, **32**, 53–56.

Mau S, Sahling H, Rehder G, Suess E, Linke P, Soeding E (2006) Estimates of methane output from mud extrusions at the erosive convergent margin off Costa Rica. *Marine Geology*, **225**, 129–144.

Melchert B, Devey CW, German CR, Lackschewitz KS, Seifert R, Walter M, Mertens C, Yoerger DR, Baker ET, Paulick H, Nakamura K (2008) First evidence for high-temperature off-axis venting of deep crustal/mantle heat: The Nibelungen hydrothermal field, southern Mid-Atlantic Ridge. *Earth and Planetary Science Letters*, **275**, 61–69.

Menot L, Crassous P, Desbruyères D, Galéron J, Khripounoff A, Sibuet M (2009) Colonization patterns along the equatorial West African margin: Implications for functioning and diversity maintenance of bathyal and abyssal communities. *Deep Sea Research Part II: Topical Studies in Oceanography*, **56**, 2313–2325.

Milkov A. (2000) Worldwide distribution of submarine mud volcanoes and associated gas hydrates. *Marine Geology*, **167**, 29–42.

Moore JC (1989) Tectonics and hydrogeology of accretionary prisms: role of the décollement zone. *Journal of Structural Geology*, **11**, 95–106.

Moulin M, Aslanian D, Olivet JL, Contrucci I, Matias L, Géli L, Klingelhoefer F, Nouzé H, Réhault JP, Unternehr P (2005) Geological constraints on the evolution of the Angolan margin based on reflection and refraction seismic data (ZaïAngo project). *Geophysical Journal International*, **162**, 793–810.

Mullineaux LS, Fisher CR, Peterson CH, Schaeffer SW (2000) Tubeworm succession at hydrothermal vents: use of biogenic cues to reduce habitat selection error? *Oecologia*, **123**, 275–284.

Naehr TH, Eichhubl P, Orphan VJ, Hovland M, Paull CK, Ussler III W, Lorenson TD, Greene HG (2007) Authigenic carbonate formation at hydrocarbon seeps in continental margin sediments: A comparative study. *Deep Sea Research Part II: Topical Studies in Oceanography*, **54**, 1268–1291.

Naudts L, Greinert J, Poort J, Belza J, Vangampelaere E, Boone D, Linke P, Henriet JP, Batist M De (2010) Active venting sites on the gas-hydrate-bearing Hikurangi Margin, off New Zealand: Diffusive- versus bubble-released methane. *Marine Geology*, **272**, 233–250.

Nicosevici T, Gracias N, Negahdaripour S, Garcia R (2009) Efficient three-dimensional scene modeling and mosaicing. *Journal of Field Robotics*, **26**, 759–788.

Nicosevici T, Negahdaripour S, Garcia R (2006) Monocular-based 3-D seafloor reconstruction and ortho-mosaicing by piecewise planar representation. In: *Proceedings of the MTS/IEEE Oceans 2005 Conference*. p1279–1286.

Niemann H, Lösekann T, Beer D de, Elvert M, Nadalig T, Knittel K, Amann R, Sauter EJ, Schlüter M, Klages M, Foucher JP, Boetius A (2006) Novel microbial communities of the Haakon Mosby Mud Volcano and their role as a methane sink. *Nature*, **443**, 854–858.

Nikolovska A, Sahling H, Bohrmann G (2008) Hydroacoustic methodology for detection, localization, and quantification of gas bubbles rising from the seafloor at gas seeps from the eastern Black Sea. *Geochemistry Geophysics Geosystems*, **9**, 13 pp.

Nix ER, Fisher CR, Vodenichar J, Scott KM (1995) Physiological ecology of a mussel with methanotrophic endosymbionts at three hydrocarbon seep sites in the Gulf of Mexico. *Marine Biology*, **122**, 605–617.

Olu K, Caprais JC, Galéron J, Causse R, Cosel R von, Budzinski H, Ménach KL, Roux CL, Levaché D, Khripounoff A, Sibuet M (2009) Influence of seep emission on the non-symbiont-bearing fauna and vagrant species at an active giant pockmark in the Gulf of Guinea (Congo–Angola margin). *Deep Sea Research Part II: Topical Studies in Oceanography*, **56**, 2380–2393.

Olu K, Duperret A, Sibuet M, Foucher JP, Fiala-Médioni A (1996a) Structure and distribution of cold seep communities along the Peruvian active margin: relationship to geological and fluid patterns. *Marine Ecology Progress Series*, **132**, 109–125.

Olu K, Lance S, Sibuet M, Henry P, Fiala-Médioni A, Dinet A (1997) Cold seep communities as indicators of fluid expulsion patterns through mud volcanoes seaward of the Barbados accretionary prism. *Deep Sea Research Part I: Oceanographic Research Papers*, **44**, 811–841.

Olu K, Sibuet M, Harmegnies F, Foucher JP, Fiala-Médioni A (1996b) Spatial distribution of diverse cold seep communities living on various diapiric structures of the southern Barbados prism. *Progress In Oceanography*, **38**, 347–376.

Olu-Le Roy K (2006) Comments on: the paper of Gay et al. (2006) Seafloor facies related to upward methane flux within a giant pockmark of the Lower Congo Basin. Marine Geology 226:81-95 by Gay et al. Author's reply. *Marine Geology*, **232**, 101–104.

Olu-Le Roy K, Caprais JC, Fifis A, Fabri MC, Galéron J, Budzinsky H, Ménach K Le, Khripounoff A, Ondréas H, Sibuet M (2007a) Cold-seep assemblages on a giant pockmark off West Africa: spatial patterns and environmental control. *Marine Ecology*, **28**, 115–130.

Olu-Le Roy K, Cosel R von, Hourdez S, Carney SL, Jollivet D (2007b) Amphi-Atlantic cold-seep Bathymodiolus species complexes across the equatorial belt. *Deep-Sea Research Part I: Oceanographic Research Papers*, **54**, 1890–1911.

Ondréas H, Fouquet Y, Voisset M, Radford-Knoery J (1997) Detailed study of three contiguous segments of the Mid-Atlantic Ridge, south of the Azores (37 N to 38 30′ N), using acoustic imaging coupled with submersible observations. *Marine Geophysical Researches*, **19**, 231–255.

Ondréas H, Olu K, Fouquet Y, Charlou JL, Gay A, Dennielou B, Donval JP, Fifis A, Nadalig T, Cochonat P, Cauquil E, Bourillet JF, Moigne M le, Sibuet M (2005) ROV study of a giant pockmark on the Gabon continental margin. *Geo-Marine Letters*, **25**, 281–292.

Page HM, Fisher CR, Childress JJ (1990) Role of filter-feeding in the nutritional biology of a deep-sea mussel with methanotrophic symbionts. *Marine Biology*, **104**, 251–257.

Pape T, Bahr A, Klapp SA, Abegg F, Bohrmann G (2011) High-intensity gas seepage causes rafting of shallow gas hydrates in the southeastern Black Sea. *Earth and Planetary Science Letters*, **307**, 35–46.

Parnell J (2002) Fluid Seeps at Continental Margins: towards an Integrated Plumbing System.

Geofluids, **2**, 57–61.

Parson L, Grācia E, Coller D, German C, Needham D (2000) Second-order segmentation; the relationship between volcanism and tectonism at the MAR, 38° N-35° 40'N. *Earth and Planetary Science Letters*, **178**, 231–251.

Paull CK, Normark WR, Ussler III W, Caress DW, Keaten R (2008) Association among active seafloor deformation, mound formation, and gas hydrate growth and accumulation within the seafloor of the Santa Monica Basin, offshore California. *Marine Geology*, **250**, 258–275.

Paull CK, Ussler W, Borowski WS, Spiess FN (1995) Methane-rich plumes on the Carolina continental rise: Associations with gas hydrates. *Geology*, **23**, 89–92.

Peckmann J, Reimer A, Luth U, Luth C, Hansen BT, Heinicke C, Hoefs J, Reitner J (2001) Methane-derived carbonates and authigenic pyrite from the northwestern Black Sea. *Marine Geology*, **177**, 129–150.

Pennec M Le, Donval A, Herry A (1990) Nutritional strategies of the hydrothermal ecosystem bivalves. *Progress In Oceanography*, **24**, 71–80.

Petersen S, Kuhn K, Kuhn T, Augustin N, Hékinian R, Franz L, Borowski C (2009) The geological setting of the ultramafic-hosted Logatchev hydrothermal field (14°45′N, Mid-Atlantic Ridge) and its influence on massive sulfide formation. *Lithos*, **112**, 40–56.

Petersen JM, Zielinski FU, Pape T, Seifert R, Moraru C, Amann R, Hourdez S, Girguis PR, Wankel SD, Barbe V, Pelletier E, Fink D, Borowski C, Bach W, Dubilier N (2011) Hydrogen is an energy source for hydrothermal vent symbioses. *Nature*, **476**, 176–180.

Pichon X Le, Henry P, Lallemant S (1993) Accretion and Erosion in Subduction Zones: The Role of Fluids. *Annual Review of Earth and Planetary Sciences*, **21**, 307–331.

Pierre C, Blanc-Valleron MM, Demange J, Boudouma O, Foucher JP, Pape T, Himmler T, Fekete N, Spiess V (2012) Authigenic carbonates from active methane seeps offshore southwest Africa. *Geo-Marine Letters*, 13 pp.

Pierre C, Fouquet Y (2007) Authigenic carbonates from methane seeps of the Congo deep-sea fan. *Geo-Marine Letters*, **27**, 249–257.

Pilcher R, Argent J (2007) Mega-pockmarks and linear pockmark trains on the West African continental margin. *Marine Geology*, **244**, 15–32.

Pizarro O, Eustice R, Singh H (2009) Large area 3D reconstructions from underwater surveys. *IEEE Journal of Oceanic Engineering*, **34**, 150–169.

Pizarro O, Singh H (2003) Toward large-area mosaicing for underwater scientific applications. *IEEE Journal of Oceanic Engineering*, **28**, 651–672.

Podowski EL, Moore TS, Zelnio KA, Luther III GW, Fisher CR (2009) Distribution of diffuse flow megafauna in two sites on the Eastern Lau Spreading Center, Tonga. *Deep Sea Research Part I: Oceanographic Research Papers*, **56**, 2041–2056.

Ramirez Llodra E, Shank TM, German CR (2007) Biodiversity and biogeography of hydrothermal vent species : thirty years of discovery and investigations. *Oceanography*, **20**, 30–41.

Ramirez Llodra E, Tyler PA, Copley J (2000) Reproductive biology of three caridean shrimp, *Rimicaris exoculata*, *Chorocaris chacei* and *Mirocaris fortunata* (Caridea: Decapoda), from hydrothermal vents. *Journal of the Marine Biological Association of the United Kingdom*, **80**, 473–484.

Ranero CR, Grevemeyer I, Sahling H, Barckhausen U, Hensen C, Wallmann K, Weinrebe W, Vannucchi P, Huene R von, McIntosh K (2008) Hydrogeological system of erosional convergent margins and its influence on tectonics and interplate seismogenesis. *Geochemistry Geophysics Geosystems*, **9**, 18 pp.

Raulfs EC, Macko SA, Dover CL van (2004) Tissue and symbiont condition of mussels (*Bathymodiolus thermophilus*) exposed to varying levels of hydrothermal activity. *Journal of the Marine Biological Association of the United Kingdom*, **84**, 229–234.

Reagan MT, Moridis GJ (2007) Oceanic gas hydrate instability and dissociation under climate change scenarios. *Geophysical Research Letters*, **34**, L22709.

Reeburgh WS (1976) Methane consumption in Cariaco Trench waters and sediments. *Earth and Planetary Science Letters*, **28**, 337–344.

Reeburgh WS (2007) Oceanic methane biogeochemistry. *Chemical Reviews*, **107**, 486–513.

Riou V, Duperron S, Halary S, Dehairs F, Bouillon S, Martins I, Colaço A, Serrão-Santos R (2010) Variation in physiological indicators in *Bathymodiolus azoricus* (Bivalvia: Mytilidae) at the Menez Gwen Mid-Atlantic Ridge deep-sea hydrothermal vent site within a year. *Marine Environmental Research*, **70**, 264–271.

Ritger S, Carson B, Suess E (1987) Methane-derived authigenic carbonates formed by subduction-induced pore-water expulsion along the Oregon/Washington margin. *Geological Society of America Bulletin*, **98**, 147–156.

Ritt B, Pierre C, Gauthier O, Wenzhöfer F, Boetius A, Sarrazin J (2011) Diversity and distribution of cold-seep fauna associated with different geological and environmental settings at mud volcanoes and pockmarks of the Nile Deep-Sea Fan. *Marine Biology*, **158**, 1187–1210.

Roberts H, Aharon P, Carney R, Larkin J, Sassen R (1990) Sea floor responses to hydrocarbon seeps, Louisiana continental slope. *Geo-Marine Letters*, **10**, 232–243.

Rogers AD, Tyler PA, Connelly DP, Copley JT, James R, Larter RD, Linse K, Mills RA, Garabato AN, Pancost RD, Pearce DA, Polunin NVC, German CR, Shank T, Boersch-Supan PH, Alker BJ, Aquilina A, Bennett SA, Clarke A, Dinley RJJ, Graham AGC, Green DRH, Hawkes JA, Hepburn L, Hilario A, Huvenne VAI, Marsh L, Ramirez-Llodra E, Reid WDK, Roterman CN, Sweeting CJ, Thatje S, Zwirglmaier K (2012) The Discovery of New Deep-Sea Hydrothermal Vent Communities in the Southern Ocean and Implications for Biogeography. *PLoS Biol*, **10**, 17 pp.

Römer M, Sahling H, Pape T, Bahr A, Feseker T, Wintersteller P, Bohrmann G (2012) Geological control and magnitude of methane ebullition from a high-flux seep area in the Black Sea—the Kerch seep area. *Marine Geology*, **319–322**, 57–74.

Rosenberg ND, Lupton JE, Kadko D, Collier R, Lilley MD, Pak H (1988) Estimation of heat and chemical fluxes from a seafloor hydrothermal vent field using radon measurements. *Nature*, **334**, 604–607.

Sahling H, Bohrmann G, Artemov YG, Bahr A, Brüning M, Klapp SA, Klaucke I, Kozlova E, Nikolovska A, Pape T, Reitz A, Wallmann K (2009) Vodyanitskii mud volcano, Sorokin trough, Black Sea: Geological characterization and quantification of gas bubble streams. *Marine and Petroleum Geology*, **26**, 1799–1811.

Sahling H, Bohrmann G, Spiess V, Bialas J, Breitzke M, Ivanov M, Kasten S, Krastel S, Schneider R (2008a) Pockmarks in the Northern Congo Fan area, SW Africa: Complex seafloor features shaped by fluid flow. *Marine Geology*, **249**, 206–225.

Sahling H, Masson DG, Ranero CR, Hühnerbach V, Weinrebe W, Klaucke I, Bürk D,

Brückmann W, Suess E (2008b) Fluid seepage at the continental margin offshore Costa Rica and southern Nicaragua. *Geochemistry Geophysics Geosystems*, **9**, 22 pp.

Sahling H, Rickert D, Lee RW, Linke P, Suess E (2002) Macrofaunal community structure and sulfide flux at gas hydrate deposits from the Cascadia convergent margin, NE Pacific. *Marine Ecology Progress Series*, **231**, 121–138.

Sarradin PM, Caprais JC, Riso R, Comtet T, Aminot A (1998) Brief account of the chemical environment at hydrothermal vent mussel beds on the MAR. *Cahiers de Biologie Marine*, **39**, 253–254.

Sarradin PM, Caprais JC, Riso R, Kerouel R, Aminot A (1999) Chemical environment of the hydrothermal mussel communities in the Lucky Strike and Menez Gwen vent fields, Mid Atlantic Ridge. *Cahiers de Biologie Marine*, **40**, 93–104.

Sarradin PM, Desbruyères D, Dixon DR, Almeida A, Briand P, Caprais JC, Colaço A, Company R, Cosson R, Cueff V, Dando P, Etoubleau J, Fabri MC, Fiala-Medioni A, Gaill F, Godfroy A, Gwynn JP, Hourdez S, Jollivet D, Khripounoff A, Lallier FH, Laulier M, Bris N Le, Martins I, Mestre N, Pruski A, Rodier P, Serrão-Santos R, Shillito B, Zal F, Zbinden M (2001) ATOS cruise R/V L'Atalante, ROV Victor, June 22nd - July 21st 2001. *InterRidge News*, **10**, 18–20.

Sarrazin J, Juniper SK (1998) The use of video imagery to gather biological information at deep-sea hydrothermal vents. *Cahiers de biologie marine*, **39**, 255–258.

Sarrazin J, Robigou V, Juniper SK, Delaney JR (1997) Biological and geological dynamics over four years on a high-temperature sulfide structure at the Juan de Fuca Ridge hydrothermal observatory. *Marine Ecology Progress Series*, **153**, 5–24.

Sarrazin J, Rodier P, Tivey MK, Singh H, Schultz A, Sarradin PM (2009) A dual sensor device to estimate fluid flow velocity at diffuse hydrothermal vents. *Deep Sea Research Part I: Oceanographic Research Papers*, **56**, 2065–2074.

Sarrazin J, Walter C, Sarradin PM, Brind'Amour A, Desbruyères D, Briand P, Fabri MC, Gaever S van, Vanreusel A, Bachraty C, Thiebaut E (2006) Community structure and temperature dynamics within a mussel assemblage on the Southern East Pacific Rise. *Cahiers de Biologie Marine*, **47**, 483–490.

Savoye B, Cochonat P, Apprioual R, Bain O, Baltzer A, Bellec V, Beuzart P, Bourillet JF, Cagna R, Cremer M, Crusson A, Dennielou B, Diebler D, Droz L, Ennes JC, Floch G, Guiomar M, Harmegnies F, Kerbrat R, Klein B, Kuhn H, Landuré JY, Lasnier C, Drezen E Le, Formal JP Le, Lopez M, Loubrieu B, Marsset T, Migeon S, Normand A, Nouzé H, Ondréas H, Pelleau P, Saget P, Séranne M, Sibuet JC, Tofani R, Voisset M (2000) Structure et évolution récente de l'éventail turbiditique du Zaïre : premiers résultats scientifiques des missions d'exploration Zaïango1 & 2 (marge Congo–Angola). *Comptes Rendus de l'Académie des Sciences - Series IIA - Earth and Planetary Science*, **331**, 211–220.

Serié C, Huuse M, Schødt NH (2012) Gas hydrate pingoes: Deep seafloor evidence of focused fluid flow on continental margins. *Geology*, **40**, 207–210.

Shank TM, Fornari DJ, Damm KL von, Lilley MD, Haymon RM, Lutz RA (1998) Temporal and spatial patterns of biological community development at nascent deep-sea hydrothermal vents (9°50′N, East Pacific Rise). *Deep Sea Research Part II: Topical Studies in Oceanography*, **45**, 465–515.

Shank TM, Martin JW (2003) A new caridean shrimp of the family Alvinocarididae from thermal vents at Menez Gwen on the Mid-Atlantic Ridge. *Proceedings of the Biological Society of Washington*, **116**, 158–167.

Shanks WC (1995) Rebirth of a sea-floor vent. *Nature*, **375**, 18–19.

Shanks WC, Böhlke JK, Seal RR (1995) Stable isotopes in mid-ocean ridge hydrothermal systems: Interactions between fluids, minerals, and organisms. *Geophysical Monograph Series*, **91**, 194–221.

Sibuet M, Olu K (1998) Biogeography, biodiversity and fluid dependence of deep-sea cold-seep communities at active and passive margins. *Deep Sea Research Part II: Topical Studies in Oceanography*, **45**, 517–567.

Sibuet M, Olu-Le Roy K (2002) Cold seep communities on continental margins: Structure and quantitative distribution relative to geological and fluid venting patterns. In: *Ocean Margin Systems*. Springer-Verlag, Berlin, p235–251.

Simeoni P, Sarrazin J, Nouze H, Sarradin PM, Ondréas H, Scalabrin C, Sinquin JM (2007) Victor 6000: new high resolution tools for deep sea research. “Module de Mesures en Route”. In: *Proceedings of the MTS/IEEE Oceans 2007 Conference*. IEEE, p6 pp.

Sloan ED (1998) Physical/chemical properties of gas hydrates and application to world margin stability and climatic change. In: *Gas Hydrates - Relevance to World Margin Stability and Climate Change*. Geological Society, London, Special Publications, p31–50.

Sloan ED (2003) Fundamental principles and applications of natural gas hydrates. *Nature*, **426**, 353–363.

Smith CR, Baco AR (2003) Ecology of whale falls at the deep-sea floor. *Oceanography and marine biology*, **41**, 311–354.

Smith EB, Scott KM, Nix ER, Korte C, Fisher CR (2000) Growth and condition of seep mussels (*Bathymodiolus childressi*) at a Gulf of Mexico brine pool. *Ecology*, **81**, 2392–2403.

Sommer S, Pfannkuche O, Linke P, Luff R, Greinert J, Drews M, Gubsch S, Pieper M, Poser M, Viergutz T (2006) Efficiency of the benthic filter: Biological control of the emission of dissolved methane from sediments containing shallow gas hydrates at Hydrate Ridge. *Global Biogeochemical Cycles*, **20**, 14 pp.

Somoza L, Díaz-del-Río V, León R, Ivanov M, Fernández-Puga MC, Gardner JM, Hernández-Molina FJ, Pinheiro LM, Rodero J, Lobato A, Maestro A, Vázquez JT, Medialdea T, Fernández-Salas LM (2003) Seabed morphology and hydrocarbon seepage in the Gulf of Cádiz mud volcano area: Acoustic imagery, multibeam and ultra-high resolution seismic data. *Marine Geology*, **195**, 153–176.

Suess E (2010) Marine Cold Seeps. In: *Handbook of Hydrocarbon and Lipid Microbiology*. Springer Berlin Heidelberg, p185–203.

Suess E, Torres ME, Bohrmann G, Collier RW, Greinert J, Linke P, Rehder G, Trehu A, Wallmann K, Winckler G, Zuleger E (1999) Gas hydrate destabilization: enhanced dewatering, benthic material turnover and large methane plumes at the Cascadia convergent margin. *Earth and Planetary Science Letters*, **170**, 1–15.

Suess E, Torres M, Bohrmann G, Collier R, Rickert D, Goldfinger C, Linke P, Heuser A, Sahling H, Heeschen K, Jung C, Nakamura K, Greinert J, Pfannkuche O, Trehu A, Klinkhammer G, Whiticar M, Eisenhauer A, Teichert B, Elver M (2001) Sea floor methane hydrates at Hydrate Ridge, Cascadia margin. In: *Natural Gas Hydrates: Occurrence, Distribution, and Detection*, AGU. Washington, D.C., p87–98.

Sultan N, Cochonat P, Foucher JP, Mienert J (2004) Effect of gas hydrates melting on seafloor slope instability. *Marine Geology*, **213**, 379–401.

Sultan N, Marsset B, Ker S, Marsset T, Voisset M, Vernant AM, Bayon G, Cauquil E, Adamy J, Colliat JL, Drapeau D (2010) Hydrate dissolution as a potential mechanism for pockmark formation in the Niger delta. *Journal of Geophysical Research*, **115**, B08101.

Talukder AR (2012) Review of submarine cold seep plumbing systems: leakage to seepage and venting. *Terra Nova*, **24**, 255–272.

Teichert BMA, Bohrmann G, Suess E (2005) Chemoherms on Hydrate Ridge — Unique microbially-mediated carbonate build-ups growing into the water column. *Palaeogeography, Palaeoclimatology, Palaeoecology*, **227**, 67–85.

Teichert BMA, Eisenhauer A, Bohrmann G, Haase-Schramm A, Bock B, Linke P (2003) U/Th systematics and ages of authigenic carbonates from Hydrate Ridge, Cascadia Margin: recorders of fluid flow variations. *Geochimica et Cosmochimica Acta*, **67**, 3845–3857.

Tissot BP, Welte DH (1978) The Origin of Petroleum in the Marine Environment. In: *Petroleum. Formation and Occurrence: A New Approach to Oil and Gas Exploration*. Springer-Verlag, p33 pp.

Treude T, Niggemann J, Kallmeyer J, Wintersteller P, Schubert CJ, Boetius A, Jørgensen BB (2005) Anaerobic oxidation of methane and sulfate reduction along the Chilean continental margin. *Geochimica et Cosmochimica Acta*, **69**, 2767–2779.

Ussler III W, Paull CK, Boucher J, Friederich GE, Thomas DJ (2003) Submarine pockmarks: a case study from Belfast Bay, Maine. *Marine Geology*, **202**, 175–192.

Vedaldi A, Fulkerson B (2008) VLFeat: An open and portable library of computer vision algorithms. *www.vlfeat.org*.

Vedaldi A, Fulkerson B (2010) VLFeat: An open and portable library of computer vision algorithms. In: *Proceedings of the international conference on Multimedia*. p1469–1472.

Vincent AG, Pessel N, Borgetto M, Jouffroy J, Opderbecke J, Rigaud V (2003) Real-time geo-referenced video mosaicking with the MATISSE system. In: *Proceedings of the MTS/IEEE Oceans 2003 Conference*. San Diego, USA, p2319–2324.

Vogt PR, Gardner J, Crane K (1999) The Norwegian–Barents–Svalbard (NBS) continental margin: Introducing a natural laboratory of mass wasting, hydrates, and ascent of sediment, pore water, and methane. *Geo-Marine Letters*, **19**, 2–21.

Wallmann K, Linke P, Suess E, Bohrmann G, Sahling H, Schlüter M, Dählmann A, Lammers S, Greinert J, Mirbach N von (1997) Quantifying fluid flow, solute mixing, and biogeochemical turnover at cold vents of the eastern Aleutian subduction zone. *Geochimica et Cosmochimica Acta*, **61**, 5209–5219.

Welhan JA (1988) Origins of methane in hydrothermal systems. *Chemical Geology*, **71**, 183–198.

Westbrook GK, Thatcher KE, Rohling EJ, Piotrowski AM, Pälike H, Osborne AH, Nisbet EG, Minshull TA, Lanoisellé M, James RH, Hühnerbach V, Green D, Fisher RE, Crocker AJ, Chabert A, Bolton C, Beszczynska-Möller A, Berndt C, Aquilina A (2009) Escape of methane gas from the seabed along the West Spitsbergen continental margin. *Geophysical Research Letters*, **36**, L15608.

Whiticar MJ (1999) Carbon and hydrogen isotope systematics of bacterial formation and oxidation of methane. *Chemical Geology*, **161**, 291–314.

Yoerger DR, Bradley AM, Jakuba M, Tivey MA, German CR, Shank TM, Embley R. (2007) Mid-ocean ridge exploration with an Autonomous Underwater Vehicle. *Oceanography*, **20**, 52–61.

Appendix A: Review of commonly used mosaicking techniques

A.1 Introduction

The deep marine environment is hardly accessible and most part has remained largely unknown. One reason is that available underwater vehicles for deep ocean exploration have limited range and that surveys and investigations are still much localized, and focus on small areas of the seafloor only. But another main reason is that light in the deep-sea environment undergoes strong attenuation and high backscattering, which constrains optical surveys of the seafloor to be carried out from few meters only above the bottom. Such low altitudes severely limit the field of view of the cameras and representing extended scenes of the seafloor requires several images to be taken and assembled together.

This creates the need for mosaicking. Video- or photo-mosaicking consists in aligning and stitching images together to form a large composite picture. The mosaics are usually 2D representations of a 3D scene, and hence rely on the assumption that the scene is planar. Several uncertainties and inaccuracies impact the data acquisition and quality. The main technical issues as regards the acquisition of images for mosaicking purposes are related to the accuracy of the positioning data and to the presence of tilt and drift in the submersible's motion.

Frame alignment can therefore hardly rely solely on the navigation data and must be complemented with pictorial correlations. This is the main step in the creation of mosaics, i.e. to match the points in areas of overlap between consecutive pictures. This step is commonly called image registration, and is the base of most accurate methods for relative positioning between two pictures. Such correspondence mapping between adjacent images not only allows to align the images but also to determine the geographic transformation between them. This information is critical, as images generally need to be resized and wrapped in order to compensate for distortions and to match with the reference image or mosaic.

The main transformation between two images depends chiefly on the motion of the camera. For instance transformations between consecutive images taken that were with a camera moving on a 2D plan should consist mostly in translation and/or rotation. In practice however, the camera's motion can be subject to pitch, roll, yaw and heave, and the transformations get more complex. Moreover, the planar scene assumption is not always verified and more scaling discrepancies can occur. Other sorts of distortion also impact the images, such as the lens distortion and the radial distortion caused by the water/air interface. Determining and compensating for the main distortions and motion transforms between consecutive frames is a key step towards precise registration and accurate rendering.

There are additional difficulties that are related to the environment itself. First, due to strong attenuation of light, photo-imaging techniques must rely on powerful lighting systems, including strobes; such systems have the side effect of non-uniformly illuminating the scene

and of generating light backscattering towards the camera. Next, the seafloor can be relatively featureless and show little contrasts, which impacts both data acquisition and image registration phases. Those difficulties are very challenging in terms of mosaicking and algorithms must be robust enough to cope with all of these peculiarities.

The present document reviews the main mosaicking techniques (Table A.1), and is structured as follow; section A.2 describes the data acquisition, sections A.3 to A.5 present the mosaicking workflow and review the main techniques and algorithms, section A.6 tackles the limitations related to the lighting or lens distortions, and section A.7 details the advances that have been made in three dimensional mosaicking.

Table A.1: Overview of most cited mosaicking methods.

Source	Underwater application	Type	Real-time	Method relying on navigation data
Haywood (1986)	yes	photo	no	LBL
Marks et al. (1995)	yes	video	yes	no
Sawhney & Kumar (1997)	no	photo	no	no
Fleischer et al. (1997)	yes	video	yes	DVL
Gracias & Santos-Victor (2000)	yes	video	no	no
Rzhanov et al. (2000, 2002)	yes	video	yes	no
Eustice et al. (2002)	yes	photo	no	no
Vincent et al. (2003)	yes	video	yes	USBL and DVL, mainly for geo-referencing
Pizarro & Singh (2003)	yes	photo	no	no
Maki et al. (2006)	yes (AUV)	photo	possible	Profiling sonar to detect acoustic reflectors
Ferrer et al. (2007)	yes	photo	no	USBL and DVL
Caccia et al. (2009)	yes	video	possible	no
Nicosevici et al. (2009)	yes	any	no	no
Bülow et al. (2009)	yes	photo	yes	no

A.2 Data acquisition

A.2.1 Material

Work in the deep sea relies mostly on the use of remotely operated underwater vehicles. According to the literature, several of them have been equipped with cameras and lighting systems for the exploration of the seafloor. One can cite the ROVs Victor 6000 (Vincent et al. 2003, Simeoni et al. 2007), Jason II (Podowski et al. 2009), Minerva (Ludvigsen et al. 2007),

Quest (Sahling et al. 2009), and the AUVs SeaBED (Singh et al. 2004a), Tri-Dog 1 (Maki et al. 2006), and Sirius (Johnson-Roberson et al. 2009).

Cameras for seafloor mapping purposes must be facing downwards and can be either video or still cameras. Video cameras produce images at a high frequency rate, with high overlap between each frame. This is very useful for mosaicking algorithms that rely on pictorial information. Conversely still cameras generally produce higher resolution images, but must rely on the use of powerful strobes; for mosaicking applications, strobe charging times limit the acquisition frequency, hence photo-images show low overlap areas. Therefore, mosaicking techniques must be more robust to align and stitch images in order to form a mosaic. However, areas for pictorial correspondence between images are smaller and transformations between consecutive frames are likely to be more complex or of higher amplitude than between video-frames.

Underwater platforms also integrate positioning and navigation sensors. Ultra-short-baseline (USBL) is a positioning system that is commonly used onboard underwater vehicles. It allows absolute positioning of the vehicle in relation to the ship. Accuracy of USBL systems can be in the order of a few meters and experience and literature has shown that USBL data cannot be used for precise vehicle tracking and image-mosaicking (Eustice et al. 2005). Other systems, such as long-baseline (LBL) can offer sub-meter precision but rely on the deployment of acoustic landmarks.

Doppler velocity log (DVL) sensors provide relative positioning data. Those sensors are also called dead-reckoning sensors. DVL relative positioning is more precise than with USBL but is impacted by drift. Drift between consecutive measurements is generally small but grows unbounded with each new measurement and can lead to larger positioning errors. Eustice et al. (2005) shows that DVL data can be complemented with visually augmented navigation (VAN) to compute accurate positioning. Visually augmented navigation is based on the concept of simultaneous localization and mapping (SLAM), which for an autonomous vehicle consists in simultaneously building a map and keeping track of its current position.

A.2.2 Trajectories for areal mapping

Due to the limited vision in the deep sea, seafloor imaging is done from very low altitude and has limited field of view. For this reason, imaging areas of the seafloor requires taking several images and assembling them into a mosaic of the scene. It is important to ensure that images are sufficiently overlapping and that no gap occurs in the dataset, i.e. that every point of the scene appears on one image at least. Therefore, images must be acquired in a consistent and structured way.

A common trajectory for areal mapping is the lawn-mower pattern (Figure A.1), which consists in doing several parallel and overlapping transects.

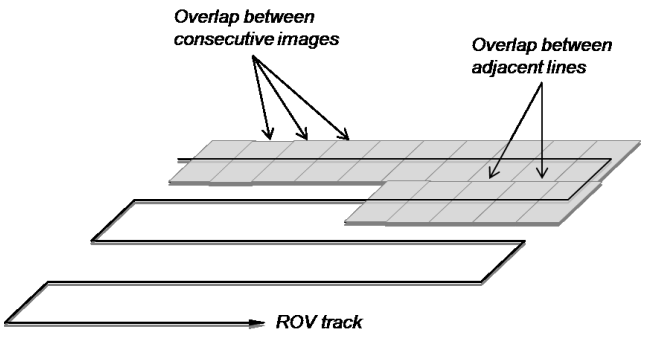

Figure A.1: Lawn-mower pattern for areal mapping.

In order to reduce drift and orientation errors between transects, it can be beneficial to keep a constant heading during the entire survey. This can be achieved by moving alternatively forward and backward without altering the heading between two transects (Marks et al. 1995). An alternative is to rely on high accuracy positioning data. For instance, (Maki et al. 2006, 2007a, b) proposed a navigation system that relies on the use of a profiling sonar to position the underwater vehicle in relation to artificial and natural acoustic landmarks.

However, accurate positioning data is not always available, and it is important to limit the effect of the drifting. Bottom currents or compass imprecisions can be source of drift, and methods exists that propose to include crossover points, i.e. points where the ROV crosses its own trajectory in order to survey a same area twice, as complement to the lawn-mower pattern (Fleischer et al. 1996, 1997, Fleischer & Rock 1998, Garcia Campos 2001, Vincent et al. 2003, Borgetto 2005). When the camera passes over a same area twice, its relative position can be re-estimated accurately and compensated for drift.

Vincent et al. (2003) take advantage of crossover points, called *rendezvous* points, and DVL data (relative positioning) to estimate an optimized trajectory, prior to its fusion with the mosaic. This is done by iteratively calculating the shortest path between two extreme positions, implementing some “retiming positions”, gained from information from the crossover points, and then re-calculating the shortest path.

Fleischer et al. (1996, 1997) propose to use the information from crossover data on the image alignment directly, instead of applying it to the navigation data. He explains it is not sufficient to simply use such information to update the current position and to go on with the image alignment. He asserts that additional information can be used to propagate the error correction back through the chain of images. Whenever the camera path crosses itself, a closed loop is formed. Using a filter, called *smoother-follower*, the image alignment along the loop is re-estimated, thus reducing the general registration errors.

Although it is not explicitly mentioned as such, Pizarro & Singh (2003) perform a similar correction based on rendezvous points. Using the images pre-alignment based on the time sequence to detect further overlaps between non-consecutive images enables the algorithm to detect possible crossover points. The correction of alignment errors is done during the

global registration phase (Section A.4) by minimizing a cost function, which uses all overlap information.

A.3 Image registration

Image registration is the process of aligning and matching two images in the same plane. It is considered as the first step in image mosaicking and can be seen as the combination of image alignment, overlap detection and image matching. Zitová & Flusser (2003) propose a thorough survey of registration methods in the wider field of image mosaicking, i.e. not only for areal mapping but also for medical imaging or landscape planning. The registration process follows a four-step workflow: feature detection, feature matching, transform model estimation, and image re-sampling and transformation. Garcia Campos (2001) also presented an overview of the registrations methods with a focus on underwater applications. He described a common frame for mosaic construction that is similar to the one proposed by Zitová & Flusser (2003). Feature detection consists in extracting from each image the salient features such as points, lines, or regions. This is usually done by edge or corner detectors (Harris & Stephens 1988, Lowe 1999, Bay et al. 2008). Feature matching is the process of finding a correspondence between adjacent images. Numerous methods exist, some matching the frames based on the spatial distribution or on the description of the features, while others do not even rely on feature detection. These methods are discussed in more details in section A.3.1. After the matching step, a mapping function can be estimated from the control points to relate one frame to the next. The mapping function somehow models the transformation between the frames. In underwater imagery it is commonly assumed that simple geometric deformations applied to the entire image can compensate for most of the distortion. One reason is to find the right balance between quality of the mosaic and speed of execution. Last, images are re-sampled and transformed to compensate for the distortion and be matched to the previous image. This is the actual registration of the image.

A.3.1 Feature detection and matching

Feature detection can be done over the entire image area. Feature matches are then looked for among any pair of images. To speed up the process however, some techniques generate a pre-alignment of the frames in order to focus the image matching process on overlapping images only. It also prevents wrong matches between non-adjacent images. Ferrer et al. (2007) rely on navigation data of the camera's platform to produce a preliminary frame alignment. This pre-alignment is then used to detect overlaps not only on consecutive frames but also on any adjacent images. Gracias & Santos-Victor (2000) proposed to use the time sequence of the frames instead of relying on navigation sensors to pre-align the images. By correlating feature points between one image and the next, they align images chronologically. In this approach, matching inaccuracies and alignment errors between consecutive frames

are small but build up with every new image. This can lead to a large error in the global alignment. To palliate this problem they extended the technique by directly matching the images with the mosaic being constructed. Pizarro & Singh (2003) adopted a similar approach to pre-align low-overlapping images (in the order of 30%). The main improvement lies in the fact that the pre-alignment is then used to detect overlapping areas between non-consecutive frames. Marks et al. (1994) used image correlation to determine the displacement of every image and to allow for real-time video mosaicking. To prevent gaps in the mosaic, the images are selected based on their spatial offset instead of their time-intervals. Fleischer et al. (1997) constructed a real-time mosaic from DVL positioning data, and implemented a filter smoother algorithm (named *smoother-follower*) to iteratively detect closed loops in the trajectory. Such information about crossover points is used to update the current position and to recalculate and improve the global placement of all previous images in the mosaic. Such method is highly demanding in terms of computation resources but yields noticeable improvements. Maki et al. (2006) successfully generated mosaics without using any image-based correlations. The system was implemented on an autonomous underwater vehicle (AUV), and relied on accurate and drift-free positioning of the vehicle. The AUV used a profiling sonar to estimate its position in relation to pre-deployed acoustic reflectors. Finally, Haywood (1986), a pioneer in the creation of underwater photo-mosaics, used pre-defined positional coordinates, to acquire and align the images. Good accuracy was obtained using LBL positioning system, which also enabled taking and scaling stereo photographs.

A.3.2 Image matching techniques

Image matching techniques have been extensively described in the literature and are commonly divided into two major categories: Featureless and feature-based methods (Garcia Campos 2001, Pizarro & Singh 2003, Zitová & Flusser 2003, Bülow et al. 2009, Caccia et al. 2009).

A.3.2.1 Featureless methods

In the literature, featureless methods are also referred to as direct methods, or intensity-based methods (Pizarro et al. 2003). These methods use the pixels intensity values to estimate the motion between images and their accuracy depends highly on the percentage of overlap between consecutive frames; this makes them more suited for video-mosaicking than photo-mosaicking. The most common direct methods are (1) cross-correlation of image intensities and (2) Fourier methods, i.e. correlation of images in the frequency domain (Zitová and Flusser 2003). The latter method is generally more robust, faster and less noise-sensitive.

Techniques using cross-correlation use directly the pixels intensities and require a fixed light source. The fact that in underwater imagery the light source moves together with the camera generates moving shadows and significant variations in intensity across the images, and directly affects the efficiency of cross-correlation techniques. Another drawback of these

techniques is that translation is assumed to be the main transform between consecutive frames, and images with significant rotation, scaling or affine transforms are not successfully registered. Therefore those methods are efficient for mosaicking of planar scenes where the motion between frames can be assimilated to a translation, but do not cope well with rapidly changing topography, and areas with relief and moving shadows are not always well rendered. To improve robustness of the technique, most methods are based on a “coarse-to-fine” strategy, estimating the parameters of the flow vector at each level of the Gaussian pyramid, successively moving from the coarsest level to the finest level (Odobez & Bouthemy 1995, Sawhney & Kumar 1999, Vincent et al. 2003, Singh et al. 2004b).

Frequency-based techniques, also called Fourier methods, are generally more efficient and cope better with scale and orientation differences. For instance, in the frequency domain, scaling and rotation transforms can be represented as translations and ,thus, be easily registered (Rzhanov et al. 2000, Eustice et al. 2002, Singh et al. 2004b, Bülow & Birk 2009, Bülow et al. 2009).

Featureless methods are effective in relating images with large overlapping areas and can be well suited for applications on video imagery. Especially their computing times are usually short, what makes them a good option for real-time applications. However, these techniques usually fail to successfully register low overlapping still images.

A.3.2.2 Feature-based methods

Feature-based methods rely on feature extraction and matching techniques, and proved efficiency with low overlapping imagery (Pizarro & Singh 2003). The technique consists in recognizing and mapping a set of features over consecutive images. Point-to-point mapping between two frames is done via the use of control points. Therefore, accuracy of those methods highly depends on the efficiency of the feature extraction and matching method. Indeed, low contrasts, terrain relief, heterogeneous lighting, perspective distortions, rotation and scaling changes represent many challenges. Feature-based methods rely on corner detectors to detect features or contours across images (Harris & Stephens 1988, Marks et al. 1994, Lowe 1999, Bay et al. 2008).

Marks et al. (1994) used the signum of the “Laplacian of the Gaussian” (S-LoG) operator to generate a binary version of the original image, which highlights the main contours in the image. The LoG operator allows detecting high image gradients in the image (*i.e.* contours). Image registration is then done by correlating sections of the binary image with sections of the previous image. This method is somewhat similar a featureless cross-correlation technique, but differs in that it is less impacted by illumination heterogeneities. This technique enabled real-time mosaicking applications, but it requires a powerful hardware to meet the computing demands (Marks et al. 1994, 1995). Although this method was successful in generating mosaics, it could not cope with rotation or scale changes.

A same feature can appear distorted on a next image if it has undergone some rotation,

scaling or non-linear transforms and be hardly identifiable. As motion is not always known and cannot always be compensated for beforehand, identification of such features on several images relies on the use of invariant descriptors. The idea behind is to describe features in a way that is invariant to changes such as translation, rotation, scaling, affine or even perspective transforms.

The Harris corner detector (Harris & Stephens 1988) is often used in underwater imagery. Gracias & Santos-Victor (2000) implemented a simplified version without Gaussian filtering (Gracias 1998) for feature detection. Ferrer et al. (2007) used the Harris detector to validate registration of each pair of images, whereas the detection and matching is performed with the more recent SURF algorithm (Bay et al. 2008). Pizarro & Singh (2003) used a modified version of the Harris corner detector (Harris & Stephens 1988), that can recognize a same point in the presence of rotation and scale changes. In their method, moment invariants (Zernike moments) are used to describe image patches around each detected feature.

The real-time video mosaicking MATISSE program (Vincent et al. 2003) can perform the motion estimation either with a featureless method or a feature-based method (Section A.3.2). The latter is based on the Shi-Tomasi-Kanade tracker (Shi & Tomasi 1994). This detector can cope with affine changes in the feature window, i.e. translation, rotation, scaling and even shear (Garcia Campos 2001).

More recently, other powerful algorithms have been developed, two of which are commonly used in commercial or open source programs to detect and describe features: the scale-invariant feature transform (SIFT) descriptor (Lowe 1999, 2004), and the Speeded Up Robust Features (SURF) descriptor (Bay et al. 2008). These detectors are now commonly used for underwater mosaicking (Ferrer et al. 2007, Escartín et al. 2008, Bülow et al. 2009, Caccia et al. 2009, Nicosevici et al. 2009), and are considered as being the most robust detectors currently available. The more recent SURF descriptor is faster than the SIFT descriptor for a comparable efficiency.

A major source of errors in feature-based registration methods is the occurrence of false matches in the sets of detected features and it is primordial that feature-based methods integrate detection and filtering capabilities to remove mismatches. Commonly used mismatch removal techniques are: Least Median of Squares (LMS or LMedS) (Pizarro & Singh 2003), MEDian Set Reduction (MEDSERE) (Gracias & Santos-Victor 2000) or RANdom SAmple Consensus (RANSAC) (Fischler & Bolles 1981, Vincent et al. 2003, Ferrer et al. 2007, Escartín et al. 2008).

A.3.3 Homography estimation

Feature matching is used to determine the motion between consecutive images. Not only it is used to position an image relatively to another but it also allows calculating the homography, i.e. the planar transformation, which best explains the motion between two images. The planar transformation, also called mapping function (Zitová & Flusser 2003) or motion model

(Garcia Campos 2001), is used to project an image onto the 2D plan of the mosaic. This projected image can also be called an *homography*. Briefly, the creation of the mosaic consists in stitching the homographies together.

Motion of the camera is impacted by multidirectional tilt and heave; hence, distortions between images do not always consist in mere translations but often comprehend a combination of rotation, scaling, and perspective deformations.

Planar transforms can be divided in several types based on the number of parameters that define them, i.e. based on the number of degrees of freedom (DOF). The different types of planar transformations are listed below, starting from the simplest to the most general:

- Translation (2 DOF).
- Euclidean (3 DOF): translation and rotation.
- Similarity (4 DOF): translation, rotation, and scaling change.
- Affine transform (6 DOF): same as the similarity but also includes the shear.
- Projective transform (8 DOF): same as the affine transform but it also includes perspective deformation. This is the most general planar transformation.

For the creation of a mosaic, it is important to choose the type of motion model based on the assumed deformation. The most general transform, with 8 degrees of freedom, might not always return the best results, and in some cases a restricted transformation may be less sensitive to noise. For instance, for a set of images acquired with a translating camera that is free of adverse motion, a transform with 2 DOF will explain the motion as a translation only; Conversely, a transform with more degrees of freedom will try to estimate more parameters and might not explain the motion with a mere translation. Hence, prior knowledge of the camera's motion is valuable to assume the geometric deformation.

As stable as they may be, underwater remotely operated vehicles are never entirely free of pitch and roll and perspective deformations do occur. Rzhanov et al. (2001) suggested to rely on the attitude sensor to correct images for pitch and roll and, thus, to reduce the complexity of the transform from projective to affine. He showed that registration and mosaic quality can be greatly improved, even with approximate values of pitch and roll. Pizarro & Singh (2003) proposed to first estimate the topology, i.e. the spatial relation between images, by registering all the images with an affine transform. Then, new overlaps between non-consecutive images are detected and a global solution is recomputed. This step is done iteratively until no new overlap is detected. The purpose is to identify overlaps and to accurately position the frames together before the final global registration phase, which is done assuming a projective transform. Finally, Vincent et al. (2003) estimate the motion entirely with an affine model.

A.4 Global registration

The global registration phase consists in registering all the images together. Most methods described so far have allowed estimating the motion between every consecutive image. This technique is known as pairwise registration (Pizarro & Singh 2003) or image-to-image registration (Marks et al. 1994, Rzhanov et al. 2000, Gracias & Santos-Victor 2000). However small registration errors between consecutive images accumulate during mosaic construction and can lead to a large global registration error, as the registration error grows unbounded with every new image added to the mosaic.

An alternative is to directly register new images with the mosaic being constructed. This technique is known as image-to-mosaic registration or also as online-mosaicking, since it is a very common strategy for real-time applications. Registering an image to the mosaic allows bounding the registration error. The registration is not performed only with the previous image, but also takes into account other overlaps with adjacent pictures (Gracias & Santos-Victor 2000). (Pizarro & Singh 2003) proposed a very consistent approach by considering every overlaps of the mosaic simultaneously. Rather than concatenating pairwise homographies, the homographies are determined considering the overlap areas with both the previous and the following image. Then further overlaps with non-consecutive frames are detected and the homographies are recomputed. This process is done during the topology estimation phase using affine transforms, and serves as a starting point to the global registration step, which is performed with projective transforms. Such a technique cannot be used for real-time applications but yields remarkable results. Rzhanov et al. (2002) described a similar method but with the possibility to include additional positioning and attitude data in the cost function calculation. The use of weighting coefficients allows considering the modest accuracy of such data. Ferrer et al. (2007) proposed to select a subset of the correspondence points that were used to compute the pairwise homographies, and to compute a global solution for the entire mosaic, also called bundle adjustment. This is less demanding in terms of computing resources, but the subset of point must be well spread and representative of the homography, in order to yield good results. Vincent et al. (2003) proposed a radically different approach, in which pairwise homographies are used to compute the mosaic, which in turn is fused with the dead-reckoning data (DVL data). This involves some pre-processing of the positioning data to improve the trajectory, and then some warping of the mosaic to match the trajectory.

A.5 Mosaic rendering

After registration, images are merged together to compose the mosaic. Methods to render the overlapping areas are manifold and can be divided in two categories: blending and clipping.

The blending approach consists in combining the overlapping pixels. This can be done for instance by averaging the colors or taking the temporal median. Depending on the technique,

moving objects such as fish can be more or less well rendered. According to Garcia Campos (2001), a temporal average strategy usually creates a slight blurring where the object has moved. Alternatively, a temporal median strategy can solve this issue much more effectively, but only if moving objects cover background pixels over less than half the frames. Therefore, the use of a temporal median strategy is more sensible for video-mosaicking applications, for which single mosaic pixels appear on many frames. Images used in photo-mosaicking are generally low-overlapping and most mosaic pixels do not appear on more than two images. In such a case, use of the average is more suited. More complex blending methods exist; among those, the use of *multi-resolution pyramidal based blending* (Burt & Adelson 1983, Eustice et al. 2002, Pizarro & Singh 2003) and of wavelets and graph cuts (Gracias et al. 2009) produced very promising results.

The clipping approach consists in taking into account one image only. Usually the first image (less recent) or the last image (more recent) is chosen (Marks et al. 1994, Ferrer et al. 2007). But similarly, a variant exists, which is to choose the pixel that is the closest from the image center (Lirman et al. 2007). This method can minimize the effects of uncorrected lens distortions, which are larger close to the image boundaries (Gracias 2002).

Requirements in terms quality of image alignment differ between the two approaches. The blending strategy requires a good pixel alignment over the entire overlap area, in order to get a mosaic free of blurred patches, whereas the clipping strategy requires accurate alignment along the seams only. The clipping is not as memory demanding as blending the pixels, and is commonly chosen for real-time applications.

A.6 Limitations

A.6.1 Scene Lighting and image processing

Lighting represents one of the main limitations in underwater imagery. Light in the deep sea undergoes strong absorption and attenuation, and seafloor imagery techniques must integrate powerful artificial lighting systems. The main difficulties related to the lighting are (1) non-uniform illumination of the scene and (2) backscattering of light towards the camera. Judicious positioning of the lights and thorough survey planning can help to reduce adverse lighting effects (Ludvigsen et al. 2007); however images often require being pre-processed prior to stitching, so as to enhance the contrasts and to compensate for the lighting heterogeneities.

A.6.1.1 Non-uniformity of illumination

Quality of most underwater images is impacted by non-uniform illumination. Images present a bright halo in their center and become darker towards the border of the frame (e.g. see Figure 2.1). This phenomenon is sometimes called vignetting, and affects the whole set of images in a similar fashion. Vignetting is a known issue in imagery techniques that is usually caused by

lens's failure to properly render a uniform illumination. However, it is accentuated in the deep sea due to light being rapidly attenuated, and its intensity depends on several factors such as the altitude of the camera, the position of the light system, or also the relief of the scene.

Vignetting is an important issue in image-mosaicking applications, and can be a hindrance to feature tracking and matching algorithms. Since the lighting systems moves along with the camera, scene illumination varies between consecutive images, and a well-lit feature in one image can appear dark in the next frame; hence image registration algorithms must be robust enough to cope with intensity variations. Although vignetting generally cannot be totally prevented, its intensity can be limited by optimizing the setup of the lighting system. It is commonly accepted that using several lights and moving them away from the camera can achieve better illumination (Ludvigsen et al. 2007). The idea behind this is to hamper the occurrence of a bright halo by combining several light sources and to produce a more even lighting over the scene.

A.6.1.2 Light backscattering

This is another common issue of underwater imagery that light is being scattered back to the camera. Light backscattering is caused by suspended particles, known as marine snow, and impacts the overall quality of the images by generating some high frequency artifacts. Increasing the intensity of the light also increases the backscatter-induced noise, resulting in a lower contrast.

An effective way to limit light backscattering is to increase the distance between the light sources and the camera. This has the effect of reducing the quantity of light that is scattered back towards the camera (Jaffe 1990, Singh et al. 2004b).

A.6.1.3 Images processing for lighting correction and contrast enhancement

Processing images for lighting, colors, and contrast compensation can enhance the overall quality of a mosaic and ease the stitching process. However, there is a limit to the quality of improvement that can be achieved with image processing, and information cannot always be recovered if for instance the scene has been insufficiently lit. It is therefore important to get the best illumination and quality from the acquisition stage and not to rely on image processing only.

Several processing methods are described in the literature, to improve the illumination of the images and to reduce the backscatter-induced noise. Marks et al. (1995) used the Laplacian of the Gaussian operator to reduce effects of lighting biases and low contrast. From there, filtered versions of the images are created and used for finding correspondences. This technique can also be used to improve the visual quality of the final mosaic; however, this step is not detailed in the publication. The Laplacian of the Gaussian is considered to be efficient in removing backscatter-induced noise to a certain extent; but, it can also destroy some information. Rzhanov et al. (2000) presented an approach called de-trending. A low-

order polynomial spline is fitted to the frames and subtracted from the image. Such method is efficient in removing dark edges and darkening bright spots. Also, it can be applied as a batch processing to the whole set of frames. Eustice et al. (2002) applied a technique called contrast-limited adaptive histogram specification (CLAHS). It is based on the contrast-limited adaptive histogram equalization (CLAHE) technique (Zuiderveld 1994). The idea is to divide an image in a set of sub-regions and to equalize the histogram of each region separately, according to the desired distribution. Bi-linear interpolation is then used to smooth the transition between the sub-regions. According to Eustice et al. (2002), the Rayleigh distribution yields better results with underwater imagery. Pizarro & Singh (2003) applied a radiometric correction on every image and showed remarkable improvement on the final mosaic. The radiometric correction is calculated for each pixel and is based on the inverse of the average of intensities. Ludvigsen et al. (2007) explained that light of an underwater scene can be divided into an illumination component and a reflectance component, and that both components can be separated easily in the frequency domain. By applying a de-trending technique on the illumination component, a more uniformly lit image can be obtained.

To complete this brief overview, several comprehensive reviews of image processing methods for lighting, color and contrast enhancement can be found in the literature (Garcia Campos 2001, Garcia et al. 2002, Borgetto 2005, Schettini & Corchs 2010).

A.6.2 Geometric distortion and camera calibration

A.6.2.1 Geometric distortion

Due to the behavior of the camera sensor and to imperfections in the design and alignment of the optical elements of the camera, images are usually impacted by geometric distortion. It may not be immediately distinguishable on single images but can be a problem when attempting to compose a mosaic with several images (Sawhney & Kumar 1999). This phenomenon is known as lens distortion. It is a common problem in video or photo imagery and it is accentuated in underwater applications, where different refractive indexes of light in the water and the air media generate additional distortion at the air/water interface, i.e. between the camera pressure housing and the water.

The global distortion is mostly a combination of two main components: a radial distortion and a tangential distortion (Elibol et al. 2008). The effect of the tangential component is commonly considered as negligible in comparison to the radial distortion, and most works focus on the correction of radial distortion. Radial distortion can be of two types: pincushion or barrel distortion, or a combination of both and is considered to be more prominent with wide-angle lenses, such as fish-eye objectives.

For this reason, some techniques (Marks et al. 1995, Ludvigsen et al. 2007) use narrow angle objectives, or long focal lenses, to reduce the distortion to a level where it can be considered as negligible. However, this has the effect of reducing the camera’s field of view and more

images are needed to compose a mosaic. Other methods use full or partial camera calibration, i.e. use the extrinsic and intrinsic parameters of the camera (Gracias & Santos-Victor 2000, Pizarro et al. 2003, Gracias & Negahdaripour 2005, Eustice et al. 2008). This way, images can be warped prior to mosaicking in order to compensate for the distortion. However, camera calibration is not the only way to compensate for the distortion. Pizarro & Singh (2003) showed the gain in quality of registration obtained by correcting the lens distortion. In this method, a simple radial distortion correction is estimated from the matched features of a subset of adjacent images of a planar scene, and then applied to the whole set of frames. The correction is only approximate but yields relatively good results. The advantage of such technique is that it can be calculated from the survey imagery and does not require a camera calibration.

A.6.2.2 Camera calibration

Nevertheless, most methods rely on camera calibration to eliminate the distortion. Several methods have been described to fully or partially calibrate a camera. Zhang (2000) proposes a technique to fully calibrate the camera, using an underwater target. Bryant et al. (2000) developed a camera calibration scheme using an algorithm based on point detection and a 3D calibration pattern. Heikkila & Silven (1997) developed a MATLAB toolbox to fully calibrate a camera and compensate for both radial and tangential distortions. Rzhanov et al. (2002) performs the calibration with the Camera Calibration Toolbox for MATLAB (Bouguet 2010), which is freely available on the internet. Then the distortion correction is applied as a pre-processing step prior to mosaicking. (Vincent et al. 2003) uses a self-calibration method that is based on feature tracking across a sequence of images, i.e. without resorting to external target. This method is likely to be efficient mainly for high-overlapping images.

A.7 3D mosaicking

Several attempts at three-dimensional mosaicking have been proposed, often with very different approaches.

Haywood (1986) was one of the firsts to propose a 3D mosaicking technique. His approach consists in using stereo-photography to generate stereo-photographic mosaics. Information about the camera setup is used to estimate the vertical scale. (Negahdaripour & Madjidi 2003) also uses stereo-images to produce 3D mosaics. The mosaicking algorithm relies on the optic flow and works with video-imagery. The algorithm allows for some real-time applications such as trajectory following to ease the data acquisition step. Some other methods rely on the fusion of the mosaic and the bathymetry data (Singh et al. 2000, Johnson-Roberson et al. 2009).

But impressive results have been obtained by methods based on pictorial information. These methods generally assume that the camera system is calibrated and use an algorithm that

extracts 3D information directly from the pictures (Pizarro et al. 2003, 2004, 2009). The algorithm relies on the concept of structure from motion (SFM) reconstruction. This consists in first recovering the vehicle motion to infer the relation between consecutive images, in order to better render the 3D information. Their method also takes advantage of the available navigation data from other sensors to constrain the solution. Nicosevici et al. (2009) described a similar technique but without relying on navigation priors. Their methods can be applied to both high-overlap video imagery and low-overlap photographs.

A.8 Conclusion

The topic of underwater mosaicking has been subject to extensive research, and impressive results have been achieved both in video-mosaicking and photo-mosaicking.

Photo-mosaics generally achieve better resolutions than video-mosaics, due to the higher definition of photo-cameras. Photo-mosaicking techniques based on feature detection and mapping must cope with more constraints than video-mosaicking techniques, especially in terms of size of overlaps and lighting peculiarities caused by the use of strobes. However, they also allow more flexibility and better rendering for the production of *areal* mosaics, i.e. mosaics that follow a lawn-mower pattern. Indeed, by enabling feature matching between distinct lines, instead of between consecutive frames only, photo-mosaicking methods generally achieve a better global registration, with comparably low error.

The use of video-mosaicking is therefore very efficient for the production, on- or off-line, of *linear* mosaics. It is both fast and yields good results (Allais et al. 2004). Conversely, feature-based photo-mosaics are more accurate for *areal*-mapping applications.

Several mosaicking techniques have been proposed for underwater applications (Gracias & Santos-Victor 2000, Eustice et al. 2002, Vincent et al. 2003, Pizarro & Singh 2003, Allais et al. 2004, Ferrer et al. 2007, Nicosevici et al. 2009), some of which could successfully construct mosaics of the seabed. However, very few led to the development of a final end-user product that could be easily used by marine scientists interested in seafloor mapping, without requiring extensive background in mathematics and physics, and programming skills. The MATISSE program (Vincent et al. 2003, Allais et al. 2004) is one of the few programs available for the construction of geo-referenced video-mosaics. No such equivalent exists for the production of feature-based photo-mosaics. This constitutes an issue, especially since techniques that are described in the literature are not always easy to initiate for the end-user of deep-sea mosaics. Moreover, photo-mosaics are currently among the most accurate ways of mapping the seafloor and a robust end-user underwater photo-mosaicking tool would be of great benefit to the marine scientific community.

A.9 References

Allais AG, Borgetto M, Opderbecke J, Pessel N, Rigaud V (2004) Seabed video mosaicking with MATISSE: a technical overview and cruise results. In: *Proceedings of The Fourteenth International Offshore and Polar Engineering Conference*. Toulon, France

Bay H, Ess A, Tuytelaars T, Gool L Van (2008) Speeded-up robust features (SURF). *Computer Vision and Image Understanding*, **110**, 346–359.

Borgetto M (2005) Contribution à la construction de mosaïques d'images sous-marines géo-référencées par l'introduction de méthodes de localisation. PhD Thesis, Université du Sud, Toulon, France

Bouguet JY (2010) Camera Calibration Toolbox for Matlab. *http://www.vision.caltech.edu/bouguetj/calib_doc/*.

Bryant M, Wettergreen D, Abdallah S, Zelinsky A (2000) Robust camera calibration for an autonomous underwater vehicle. In: *Proceedings of the Australian Conference on Robotics and Automation*. p111–116.

Bülow H, Birk A (2009) Fast and robust photomapping with an Unmanned Aerial Vehicle (UAV). In: *IEEE/RSJ International Conference on Intelligent Robots and Systems, 2009. IROS 2009.* p3368–3373.

Bülow H, Birk A, Unnithan V (2009) Online generation of an underwater photo map with improved Fourier Mellin based registration. In: *Proceedings of the MTS/IEEE Oceans 2009 Conference*. p1–6.

Burt PJ, Adelson EH (1983) A multiresolution spline with application to image mosaics. *ACM Transactions on Graphics*, **2**, 217–236.

Caccia M, Bruzzone G, Ferreira F, Veruggio G (2009) Online video mosaicing through SLAM for ROVs. In: *Proceedings of the MTS/IEEE Oceans 2009 Conference*. p1–6.

Elibol A, Moller B, Garcia R (2008) Perspectives of auto-correcting lens distortions in mosaic-based underwater navigation. In: *23rd International Symposium on Computer and Information Sciences ISCIS '08*. p1–6.

Escartín J, García R, Delaunoy O, Ferrer J, Gracias N, Elibol A, Cufi X, Neumann L, Fornari DJ, Humphris SE, Renard J (2008) Globally aligned photomosaic of the Lucky Strike hydrothermal vent field (Mid-Atlantic Ridge, 37°18.5′N): Release of georeferenced data, mosaic construction, and viewing software. *Geochemistry Geophysics Geosystems*, **9**, 17p.

Eustice R, Pizarro O, Singh H (2005) Visually augmented navigation in an unstructured environment using a delayed state history. In: *Proceedings of the IEEE International Conference on Robotics and Automation, 2004. ICRA'04.* p25–32.

Eustice RM, Pizarro O, Singh H (2008) Visually Augmented Navigation for Autonomous Underwater Vehicles. *IEEE Journal of Oceanic Engineering*, **33**, 103–122.

Eustice R, Pizarro O, Singh H, Howland J (2002) UWIT: Underwater Image Toolbox for optical image processing and mosaicking in MATLAB. In: *Proceedings of the 2002 International Symposium on Underwater Technology, 2002.* p141–145.

Ferrer J, Elibol A, Delaunoy O, Gracias N, Garcia R (2007) Large-area photo-mosaics using global alignment and navigation data. In: *Proceedings of the MTS/IEEE Oceans 2007 Conference*. p1–9.

Fischler MA, Bolles RC (1981) Random sample consensus: a paradigm for model fitting with applications to image analysis and automated cartography. *Communications of the ACM*, **24**, 381–395.

Fleischer SD, Rock SM (1998) Experimental validation of a real-time vision sensor and navigation system for intelligent underwater vehicles. In: *IEEE International Conference on Intelligent Vehicles*.

Fleischer SD, Rock SM, Burton R (1997) Global position determination and vehicle path estimation from a vision sensor for real-time video mosaicking and navigation. In:

OCEANS'97. MTS/IEEE Conference Proceedings. p641–647.

Fleischer SD, Wang HH, Rock SM, Lee MJ (1996) Video mosaicking along arbitrary vehicle paths. In: *Proceedings of the 1996 Symposium on Autonomous Underwater Vehicle Technology, 1996. AUV'96.* p293–299.

Garcia Campos R (2001) A proposal to estimate the motion of an underwater vehicle through visual mosaicking. PhD Thesis, Universitat de Girona, Girona, Spain

Garcia R, Nicosevici T, Cufí X (2002) On the way to solve lighting problems in underwater imaging. In: *Proceedings of the MTS/IEEE Oceans 2002 Conference*. p1018–1024.

Gracias N (1998) Application of robust estimation to computer vision: video mosaics and 3-D reconstruction. MSc Thesis, Universidade Technica de Lisboa, Instituto Superior Tecnico, Lisbon, Portugal

Gracias N (2002) Mosaic–based visual navigation for Autonomous Underwater Vehicles. PhD Thesis, Universidade Technica de Lisboa, Instituto Superior Tecnico, Lisbon, Portugal

Gracias N, Mahoor M, Negahdaripour S, Gleason A (2009) Fast image blending using watersheds and graph cuts. *Image and Vision Computing*, **27**, 597–607.

Gracias X, Negahdaripour S (2005) Underwater mosaic creation using video sequences from different altitudes. In: *Proceedings of the MTS/IEEE Oceans 2005 Conference*. p1295–1300.

Gracias N, Santos-Victor J (2000) Underwater video mosaics as visual navigation maps. *Computer Vision and Image Understanding*, **79**, 66–91.

Harris C, Stephens M (1988) A combined corner and edge detector. *Proceedings of the Fourth Alvey Vision Conference*, 147–151.

Haywood R (1986) Acquisition of a micro scale photographic survey using an autonomous submersible. In: *OCEANS 1984*. p1423–1426.

Heikkila J, Silven O (1997) A four-step camera calibration procedure with implicit image correction. In: *Proceedings of the IEEE Computer Society Conference on Computer Vision and Pattern Recognition, 1997.* p1106–1112.

Jaffe JS (1990) Computer modeling and the design of optimal underwater imaging systems. *IEEE Journal of Oceanic Engineering*, **15**, 101–111.

Johnson-Roberson M, Pizarro O, Willams S (2009) Towards large scale optical and acoustic sensor integration for visualization. In: *Proceedings of the MTS/IEEE Oceans 2009 Conference*. p1–4.

Lirman D, Gracias N, Gintert BR, Gleason AC., Reid RP, Negahdaripour S, Kramer P (2007) Development and application of a video-mosaic survey technology to document the status of coral reef communities. *Environmental Monitoring and Assessment*, **125**, 59–73.

Lowe DG (1999) Object recognition from local scale-invariant features. In: *The Proceedings of the Seventh IEEE International Conference on Computer Vision, 1999*. p1150–1157.

Lowe DG (2004) Distinctive image features from scale-invariant keypoints. *International Journal of Computer Vision*, **60**, 91–110.

Ludvigsen M, Sortland B, Johnsen G, Singh H (2007) Applications of geo-referenced underwater photo mosaics in marine biology and archaeology. *Oceanography*, **20**, 10.

Maki T, Kondo H, Ura T, Sakamaki T (2006) Photo mosaicing of Tagiri shallow vent area by the AUV. In: *Proceedings of the MTS/IEEE Oceans 2006 Conference*. p1–6.

Maki T, Kondo H, Ura T, Sakamaki T (2007a) Positioning method for an AUV using a profiling sonar and passive acoustic landmarks for close-range observation of seafloors. In: *Proceedings of the MTS/IEEE Oceans 2007 Conference*. p1–6.

Maki T, Kondo H, Ura T, Sakamaki T (2007b) Navigation of an autonomous underwater vehicle for photo mosaicing of shallow vent areas. In: *Proceedings of the MTS/IEEE Oceans 2006 Conference*. p1–7.

Marks RL, Rock SM, Lee MJ (1994) Real-time video mosaicking of the ocean floor. In: *Proceedings of the 1994 Symposium on Autonomous Underwater Vehicle Technology, 1994. AUV '94.* p21–27.

Marks RL, Rock SM, Lee MJ (1995) Real-time video mosaicking of the ocean floor. *IEEE Journal of Oceanic Engineering*, **20**, 229–241.

Negahdaripour S, Madjidi H (2003) Stereovision imaging on submersible platforms for 3-D mapping of benthic habitats and sea-floor structures. *IEEE Journal of Oceanic Engineering*, **28**, 625–650.

Nicosevici T, Gracias N, Negahdaripour S, Garcia R (2009) Efficient three-dimensional scene modeling and mosaicing. *Journal of Field Robotics*, **26**, 759–788.

Odobez JM, Bouthemy P (1995) Robust multiresolution estimation of parametric motion models. *Journal of Visual Communication and Image Representation*, **6**, 348–365.

Pizarro O, Eustice R, Singh H (2003) Relative pose estimation for instrumented, calibrated imaging platforms. In: *Proceedings of the VIIth Digital Image Computing: Techniques and Applications*. Sydney, Australia, p601–612.

Pizarro O, Eustice R, Singh H (2004) Large area 3D reconstructions from underwater surveys. In: *Proceedings of the MTS/IEEE Oceans 2004 Conference*. p678–687.

Pizarro O, Eustice R, Singh H (2009) Large area 3D reconstructions from underwater surveys. *IEEE Journal of Oceanic Engineering*, **34**, 150–169.

Pizarro O, Singh H (2003) Toward large-area mosaicing for underwater scientific applications. *IEEE Journal of Oceanic Engineering*, **28**, 651–672.

Podowski EL, Moore TS, Zelnio KA, Luther III GW, Fisher CR (2009) Distribution of diffuse flow megafauna in two sites on the Eastern Lau Spreading Center, Tonga. *Deep Sea Research Part I: Oceanographic Research Papers*, **56**, 2041–2056.

Rzhanov Y, Cutter GR, Huff L (2001) Sensor-assisted video mosaicing for seafloor mapping. In: *Proceedings of the 2001 International Conference on Image Processing, 2001.* p411–414.

Rzhanov Y, Huff L, Cutter GR, Mayer L (2002) Sensor-assisted video mapping of the seafloor. In: *Proceedings of the MTS/IEEE Oceans 2002 Conference*. p1562–1568.

Rzhanov Y, Linnett LM, Forbes R (2000) Underwater video mosaicing for seabed mapping. In: *Image Processing, 2000. Proceedings. 2000 International Conference on*. p224–227.

Sahling H, Bohrmann G, Artemov YG, Bahr A, Brüning M, Klapp SA, Klaucke I, Kozlova E, Nikolovska A, Pape T, Reitz A, Wallmann K (2009) Vodyanitskii mud volcano, Sorokin trough, Black Sea: Geological characterization and quantification of gas bubble streams. *Marine and Petroleum Geology*, **26**, 1799–1811.

Sawhney HS, Kumar R (1997) True multi-image alignment and its application to mosaicing and lens distortion correction. In: *Proceedings of the IEEE Computer Society Conference on Computer Vision and Pattern Recognition, 1997.* p450–456.

Sawhney HS, Kumar R (1999) True multi-image alignment and its application to mosaicing and lens distortion correction. *IEEE Transactions on Pattern Analysis and Machine Intelligence*, **21**, 235–243.

Schettini R, Corchs S (2010) Underwater image processing: state of the art of restoration and image enhancement methods. *EURASIP Journal on Advances in Signal Processing*, **2010**, 14p.

Shi J, Tomasi C (1994) Good features to track. In: *Proceedings of the IEEE Computer Society Conference on Computer Vision and Pattern Recognition, 1994. CVPR '94.* p593–600.

Simeoni P, Sarrazin J, Nouze H, Sarradin PM, Ondréas H, Scalabrin C, Sinquin JM (2007) Victor 6000: new high resolution tools for deep sea research. "Module de Mesures en Route". In: *Proceedings of the MTS/IEEE Oceans 2007 Conference*. IEEE, p1–6.

Singh H, Armstrong R, Gilbes F, Eustice R, Roman C, Pizarro O, Torres J (2004a) Imaging

Coral I: Imaging coral habitats with the SeaBED AUV. *Subsurface Sensing Technologies and Applications*, **5**, 25–42.

Singh H, Howland J, Pizarro O (2004b) Advances in large-area photomosaicking underwater. *IEEE Journal of Oceanic Engineering*, **29**, 872–886.

Singh H, Roman C, Whitcomb L, Yoerger DR (2000) Advances in fusion of high resolution underwater optical and acoustic data. In: *Proceedings of the 2000 International Symposium on Underwater Technology, 2000. UT 00.* p206–211.

Vincent AG, Pessel N, Borgetto M, Jouffroy J, Opderbecke J, Rigaud V (2003) Real-time geo-referenced video mosaicking with the MATISSE system. In: *Proceedings of the MTS/IEEE Oceans 2003 Conference*. San Diego, USA, p2319–2324.

Zhang Z (2000) A flexible new technique for camera calibration. *IEEE Transactions on Pattern Analysis and Machine Intelligence*, **22**, 1330–1334.

Zitová B, Flusser J (2003) Image registration methods: a survey. *Image and Vision Computing*, **21**, 977–1000.

Zuiderveld K (1994) Contrast limited adaptive histogram equalization. In: *Graphics gems IV*. Academic Press Professional, Inc., p474–485.

Yann Marcon

Bismarckstraße 122

28203 Bremen

Erklärung

Hiermit versichere ich, dass ich

1. die Arbeit ohne unerlaubte fremde Hilfe angefertigt habe,

2. keine anderen als die von mir angegebenen Quellen und Hilfsmittel benutzt habe und

3. die den benutzten Werken wörtlich oder inhaltlich entnommenen Stellen als solche kenntlich gemacht habe.

Bremen, den 06.12.2012

Yann Marcon